UNIVERSITY
OF HULL

Schiff-base Macrocycles: Coordination Chemistry and

potential applications

being a thesis submitted in fulfilment of the

requirements for the degree of

Doctor of

Philosophy

at the University of Hull

by

Kuiyuan Wang

July 2021

Acknowledgements

Firstly, I would like to say thank you to my academic supervisor, Prof. Carl Redshaw, for his excellent supervision, valuable suggestions and patience during the past four years. He always gives us support and good suggestions when we met some difficulties. I feel very lucky and happy to study in Prof. Carl's group.

Also, I want to thank my second supervisor Dr. Tim Prior for the help with X-ray crystallography of this department and analysis and Dr. Xing Feng (Guangdong University of Technology) for DFT studies. We thank the EPSRC National Crystallographic Service at Southampton and National Mass Spectrometry Centre at Swansea, for X-ray diffraction data collection and mass spectrometry data, respectively.

I would like to thank Dr. Kai Chen for his suggestions about both lab work and life, it is so nice to meet Dr. Chen in Hull. I want to thank Dr. Rob Lewis for help with NMR spectroscopy and the departmental technical staff for help with the GPC, Mass Spectrometry and DSC.

Moreover, I want to thank my colleagues Tian Xing, Xin Zhang, Abdullah, everyone in the group is very friendly and they teach me a lot over the past four years. I am also very grateful to my friends Anheng Wang and Yu Liu in the chemistry department, they give me lots of help and support. I also want to thank CSC (China Scholarship Council) for financial support for my PhD project.

Lastly, I would appreciate my parents and friends who have always supported me and have always give me firm support whenever I encountered difficulties and hardships.

Publications and Conferences

K. Wang, T. J. Prior, C. Redshaw, Turning on ROP activity in a bimetallic Co/Zn complex supported by a [2+ 2] Schiff-base macrocycle. *Chemical Communications*, 2019, 55(75): 11279-11282. **https://doi.org/10.1039/C9CC04494A** (Chapter 2)

K. Wang, K. Chen, T. Bian, Y. Chao, T. Yamato, X. Feng, T. J. Prior, C. Redshaw, Emission and theoretical studies of Schiff-base [2+ 2] macrocycles derived from 2, 2′-oxydianiline and zinc complexes thereof. *Dyes and Pigments*, 2021, 190: 109300. **https://doi.org/10.1016/j.dyepig.2021.109300** (Chapter 3)

K. Wang, T. J. Prior, D. L. Hughes, A. Arbaoui, C. Redshaw. Coordination chemistry of [2+2] Schiff-base macrocycles derived from the dianilines [(2-NH$_2$C$_6$H$_4$)$_2$X](X= CH$_2$CH$_2$, O): structural studies and ROP capability towards cyclic esters. *Dalton Transactions*, 2021. **https://doi.org/10.1039/D1DT00711D** (Chapter 4)

K. Wang, C. Redshaw, Global Research and Innovation in Plastics Sustainability, 16th-18th March 2021, UK, Poster.

Abstract

In this thesis, a number of Schiff base compounds and their complexes have been synthesized and fully characterized. Moreover, some applications including their use in catalysis, specifically the ring opening polymerization of cyclic esters, is disclosed.

Chapter 1. This chapter presents an introduction of the synthesis of macrocyclic Schiff bases together with their coordination chemistry. Applications of these Schiff base ligands and metal complexes are discussed. Topics include: photoluminescence studies; peroxidase-like mimetics; ring-opening polymerization of cyclic esters.

Chapter 2. In this chapter, the catalytic behaviour of homo binuclear *versus* mixed-metal analogues is discussed. In particular, homo-dinuclear Co and Zn complexes derived from the macrocycle LH_2, $\{[2\text{-}(OH)\text{-}5\text{-}(R)\text{-}C_6H_2\text{-}1,3\text{-}(CH)_2][CH_2CH_2(2\text{-}C_6H_4N)_2]\}_2$ (R = Me, *t*Bu), revealed near inactivity for the ring opening polymerization (ROP) of the cyclic esters δ-valerolactone (δ-VL) and ε-caprolactone (ε-CL). By contrast, the hetero-bimetallic complexes $[LCo(NCMe)(\mu\text{-}Br)ZnBr]\cdot nMeCN$ (n=3 or 3.25) were found to be efficient catalysts for the ROP of ε-CL and δ-VL.

Chapter 3. This chapter looks at the emission properties of some of the macrocycles and their complexes. Specifically, the emission properties of a number of solvates of the [2+2] Schiff-base macrocycles $\{[2\text{-}(OH)\text{-}5\text{-}(R)\text{-}C_6H_2\text{-}1,3\text{-}(CH)_2][O(2\text{-}C_6H_4N)_2]\}_2$ (R = Me L^1H_2, *t*Bu L^2H_2, Cl L^3H_2), formed by reacting 2,6-dicarboxy-4-R-phenol with 2,2′-oxydianiline (2-aminophenylether), $(2\text{-}NH_2C_6H_4)_2O$, have been investigated. The macrocycle $L^{1\text{-}3}H_2$ exhibited the different maximum emission wavelengths in different solvents, from λ_{max} at 508 nm (in acetonitrile) to 585 nm (in dichloromethane). DFT studies on systems $L^{1\text{-}3}H_2$ involving solvents of different polarity (DMF *versus* *n*-hexane) indicated that the energy level gap increases with solvent polarity in line with the observed hypochromic shifts. Reaction of macrocycle L^1H_2 with three equivalents of

ZnBr$_2$, in the presence of Et$_3$N, affords the complex [(ZnBr)(ZnNCMe)**L^1**]$_2$[ZnBr$_4$]·2.5MeCN (**9**·2.5MeCN). In the case of **L^2**H$_2$, reaction with two equivalents of ZnBr$_2$ affords [(ZnBr)**L^2**H$_2$][ZnBr$_3$NCMe]·3MeCN (**10**·3MeCN), whilst in the presence of two equivalents of Et$_3$N, work-up led to the isolation of the complex [(ZnBr)$_2$**L^2**]·4.5MeCN (**11**·4.5MeCN). The molecular structures of **9-11** are reported, together with their emission behaviour.

Chapter 4. In this chapter, the coordination chemistry of the macrocycles is extended to iron, cobalt and copper. Reaction of the [2+2] Schiff-base macrocycles {[2-(OH)-5-(R)-C$_6$H$_2$-1,3-(CH)$_2$][CH$_2$CH$_2$(2-C$_6$H$_4$N)$_2$]}$_2$ (R = Me, **L^{Me}**H$_2$; tBu, **L^{tBu}**H$_2$) with FeBr$_2$ afforded the complexes [FeBr(**L^1/L^2**H$_2$)][X] (X = 0.5(FeBr$_3$)$_2$O, **L^{Me}**·2MeCN, **12**·2MeCN; **L^{tBu}**, **13**·0.5MeCN, X = Br, **L^{tBu}** **14**·3MeCN), respectively. Reaction of **L^{tBu}**H$_2$ with [KFe(OtBu)$_3$(THF)] (formed *in-situ* from FeBr$_2$ and KOtBu), following work-up, led to the isolation of the complex [Fe(**L^{tBu}**)(**L^{tBu}**H)]·3MeCN (**15**·3MeCN), whilst with [CuBr$_2$] afforded [CuBr(**L^{tBu}**H$_2$)][Br$_3$]·2MeCN (**16**·2MeCN). Attempts to form mixed Co/Ti species by reaction of [CoBr**L^2**][CoBr$_3$(NCMe)] with [TiCl$_4$] resulted in [**L^2**H$_4$][CoBr$_4$]·2MeCN (**17**·2MeCN). Use of the related oxy-bridged Schiff-base macrocycles {[2-(OH)-5-(R)-C$_6$H$_2$-1,3-(CH)$_2$][O(2-C$_6$H$_4$N)$_2$]}$_2$ (R = Me, **L^1**H$_2$; tBu, **L^2**H$_2$) with CoBr$_2$ led to the isolation of the complexes [(CoBr)$_2$(**L^1**)]·4C$_3$H$_6$O (**18**·4C$_3$H$_6$O), [Co(NCMe)$_2$(**L^2**H$_2$)][CoBr$_4$]·5MeCN (**19**·5MeCN), [Co(NCMe)$_6$][CoBr$_3$(MeCN)]$_2$·2MeCN (**20**·2MeCN). For comparative structural/polymerization studies, the complexes {CoBr(NCMe)**L^4**}$_2$·2MeCN (**21**·2MeCN) and [Co(NCMe)$_2$**L^4**]$_2$[CoBr$_3$(NCMe)]$_2$ (**22**), [FeBr(NCMe)**L^4**]$_2$·2MeCN (**23**·2MeCN) where **L^4**H = 2,6-(CHO)$_2$-4-tBu-C$_6$H$_2$OH, as well as the chelate-free salt [Fe(NCMe)$_6$][FeBr$_3$OFeBr$_3$] (**24**) have been isolated and structurally characterized. The ability of these complexes to act as catalysts for

the ring opening polymerization (ROP) of ε-caprolactone (ε-CL) and δ-valerolactone (δ-VL) has been investigated, as well as the co-polymerization of γ-CL with *rac*-lactide (γ-LA) and *vice-versa*.

Chapter 5. This chapter discusses the formation of a large macrocycle and how its' coordination chemistry with iron. The iron complex was evaluated for peroxidase-like catalytic activity. The [2+2] Schiff-base macrocycle {[2-(OH)-5-(CH$_3$)-C$_6$H$_2$-1,3-(CH)$_2$][O(2-C$_6$H$_4$N)$_2$]}$_2$ (**L^{1}H$_2$**) was reacted the with two equivalents of FeBr$_2$ afforded either the salt complex [**L^{1}H$_2$FeBr$_2$**]$_2$[FeBr$_3$OFeBr$_3$]·7MeCN (**25**·7MeCN) or, in the presence of Et$_3$N, [**L^1(FeBr)$_2$**]·3MeCN (**26**·3MeCN). The new larger [6+6] macrocycle {[2-(OH)-5-(CH$_3$)-C$_6$H$_2$-1,3-(CH)$_2$][O(2-C$_6$H$_4$N)$_2$]}$_6$ (**L^{5}H$_6$**) reacts with four equivalents of FeBr$_2$ to afford [Fe$_2$(**L^{2}H$_2$**)][FeBr$_3$OFeBr$_3$]·4MeCN (**27**·4MeCN). For the first time, we have evaluated such iron Schiff-base complexes for peroxidase-like catalytic activity. The electron transfer and the formation of hydroxyl radical were investigated in order to probe the mechanism of the peroxidase-like activity. Moreover, these Fe complexes were utilized for the determination of H$_2$O$_2$ using the colorimetric method. The linear range of H$_2$O$_2$ detection was 0.5-5 mM and 6-10 mM with a detection limit (LOD) of 0.05 mM. The method has good selectivity against interferents including glucose, urea, uric acid and metal ions.

Chapter 6 This chapter discuss the facile preparation, molecular structures and DFT studies of [2+2] [2+3] and [2+4] double layer macrocyclic Schiff-base compounds. The [2+3] compound has been used for the immobilization of Pd, and the morphology of the resulting composite was analyzed by PXRD and SEM. The Pd@Schiff base composite was employed as a peroxidase-like mimetic using 3,3′,5,5′-tetramethylbenzidine (TMB) as the substrate, and a colorimetric method for determining H$_2$O$_2$ was established.

Chapter 7 This chapter presents the experimental procedures.

Contents

IX

X

List of Figures

XIV

List of Tables

Abbreviations

Å	Angstrom
Ar	Aryl
tBu	$tert$-Butyl
h	Hour
min	Minute
MeCN	Acetonitrile
Me	Methyl
M_n	Number average
M_w	Weight average
PDI	Polydispersity index
THF	Tetrahydrofuran
°C	Degree
NMR	Nuclear magnetic resonance
br	Broad
δ	Chemical shift
d	Doublet
J	Coupling constant
ppm	Parts per million
s	Singlet

t	Triplet
MS	Mass spectrometry
EI	Electron impact
MALDI	Matrix-assisted laser desorption ionization
IR	Infra-red
m	Medium
s	Strong
PCL	Polycaprolactone
PVL	Polyvalerolactone
PLA	Polylactide
ROP	Ring opening polymerization
ε-CL	ε-Caprolactone
δ-VL	δ-Valerolactone
r-LA	*rac*-Lactide
GPC	Gel Chromatography Permeation
PXRD	Powder X-Ray diffraction
BnOH	Benzyl alcohol
DOS	*trans*-4-Dimethylamino-4′-(1-oxybutyl)stilbene
FWHM	Full width at half maximum
DMSO	Dimethyl sulfoxide

DFT	Density function theory
HOMO	Highest occupied molecular orbital
LOMO	Lowest unoccupied molecular orbital
ICT	Intermolecular charge transfer
ΔE	Energy gap
DMF	Dimethylformamide
TICT	Twisted intramolecular charge transfer
SEM	Scanning electron microscopy
UV-vis	Ultraviolet–visible
CIE	Commission Internationale de L'Eclairage
AIEE	Aggregation-induced emission enhancement
Et_3N	Triethylamine
MOFs	Metal organic frameworks
HRP	Horseradish peroxidase
TMB	3,3′,5,5′-Tetramethylbenzidine
ABTS	2,2'-Azino-bis(3-ethylbenzothiazoline-6-sulfonic acid)
K_m	Michaelis–Menten constant
V_{max}	Maximal reaction velocity
V_0	Initial velocity
GCE	Glassy carbon electrode

TA	Terephthalic acid
TAOH	Hydroxyterephthalate
LOD	Limit of detection
GO	Graphene oxide
COSY	Correlated Spectroscopy
HBMC	Heteronuclear Multiple Bond Correlation
OAc	Acetate

Chapter 1 . Introduction

1.1 Macrocyclic Schiff-bases and their metal complexes

1.1.1 Synthesis of macrocyclic Schiff base metal complexes

A Schiff base is an organic compound containing an imine structure (-RC=N-), and was first synthesised in 1864 by the German chemist Hugo Schiff using salicylaldehyde, aniline and copper ions. Schiff bases are usually formed by the condensation of the active carbonyl group of an aldehyde or ketone with an aliphatic or aromatic amine. The presence of nitrogen lone electron pairs in the structure of Schiff bases allows them to coordinate with metal ions. Schiff base compounds have a wide range of applications due to their simple synthesis, high yields, the diversity of raw material sources and, in particular, their good coordination properties.[1-5] This has resulted in Schiff bases receiving much attention in a number of research areas.

The synthesis of Schiff bases is a condensation reaction involving the addition, rearrangement and elimination:[6]
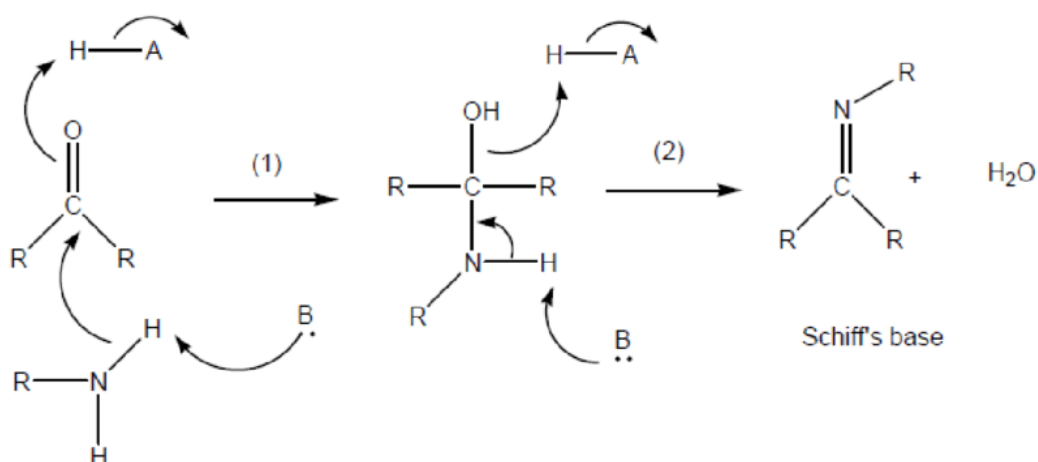
Figure 1-1. Mechanism of the synthesis of Schiff bases.

1) [2+2] Structures

In recent years, a number of [2+2] macrocyclic systems have been synthesized. For instance, the anthracenyl-hinge Schiff base macrocycle H_4L can form a bimetallic zinc complex by using $ZnEt_2$ (Figure 1-2). Interestingly, the obtuse Zn-Cl-Zn angles [150.54(9)°] and Zn-OH-Zn [157.4(3)°] illustrate these weak interactions and the importance of the cleft preorganization to stabilize the host.[7]
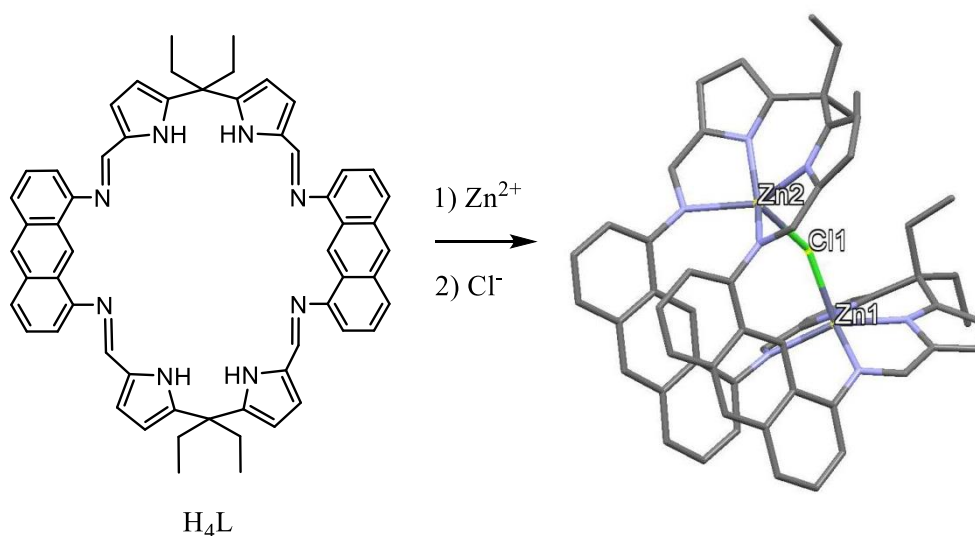
Figure 1-2. Synthesis of the binuclear Pacman complex.[7]

A macrocycle and its dinuclear Ag(I) complex were synthesized in 92% yield by using AgOAc in an argon atmosphere (Figure 1-3).[8] The coordination behaviour of Ag(I) is different from that of related Cu(II), Zn(II) complexes; no evidence of cooperative binding was found.
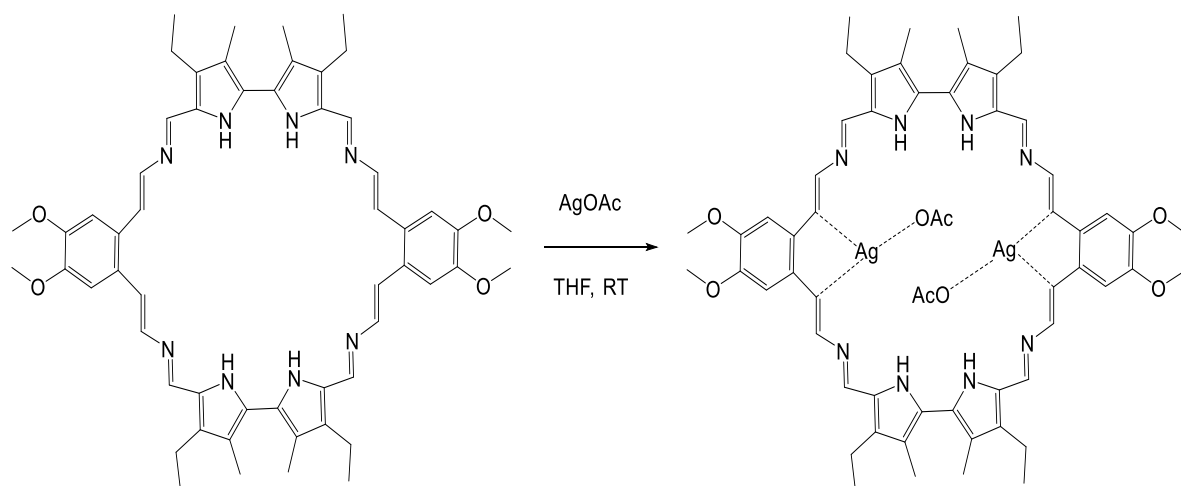
Figure 1-3. Synthesis of the bis-Ag(I) complex.[8]

2) [3+3] Structures

Two new conjugated Schiff base macrocycles incorporating phenanthrene have been reported, which possess 66 (left in Figure 1-4) and 78-membered ring systems (right in Figure 1-4), respectively. These macrocycles with isomeric backbones illustrate the potential use of Schiff base chemistry for constructing nanoscale macrocycles.[9]
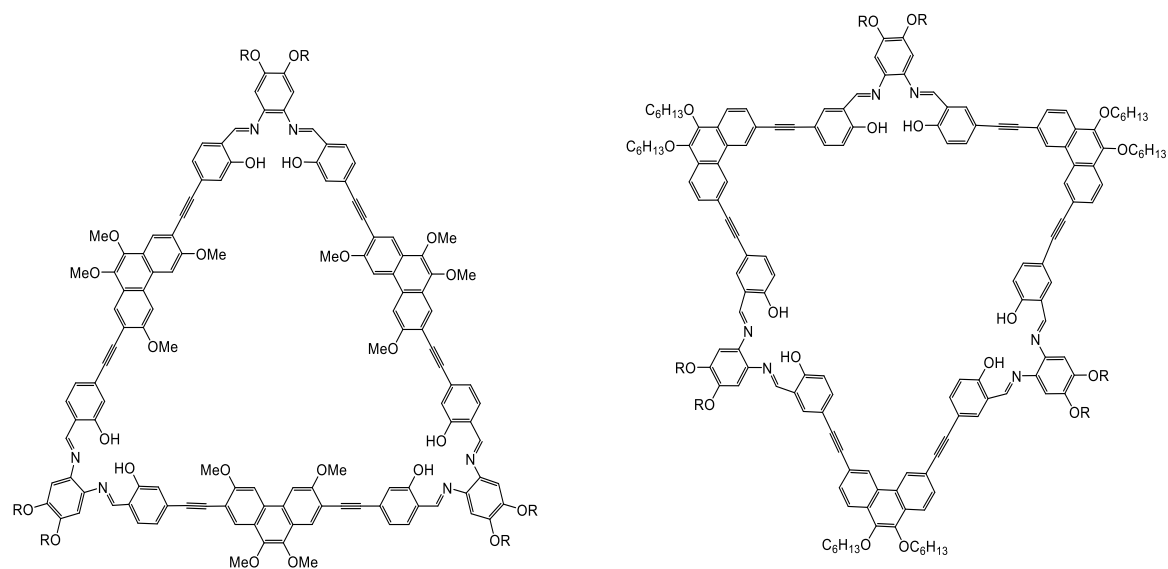
Figure 1-4. [3+3] Macrocyclic structures.[9]

Symmetric [3+3] macrocycles (Figure 1-5) have been synthesized under supercritical carbon dioxide (scCO$_2$) conditions as the "green solvent" instead of organic solvents.[10]

The above-mentioned Schiff bases possess an empty core, hence, these compounds can be used in host-guest chemistry or as selective probe materials. This research opens up the potential of using scCO$_2$ for the preparation of Schiff-base materials.
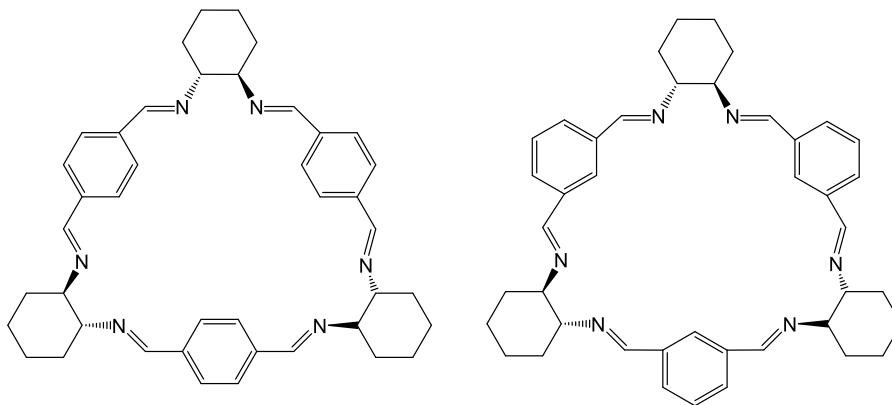
Figure 1-5. Structures of [3+3] macrocycles synthesized under scCO$_2$ conditions.[10]

Similarly, when the related fully conjugated macrocycles are reacted with Zn(OAc)$_2$, orange microcrystalline Zn complexes are isolated (Figure 1-6).[11]

R=OC$_2$H$_5$

R=O^{n}C$_5$H$_{11}$

R=O^{n}C$_6$H$_{13}$
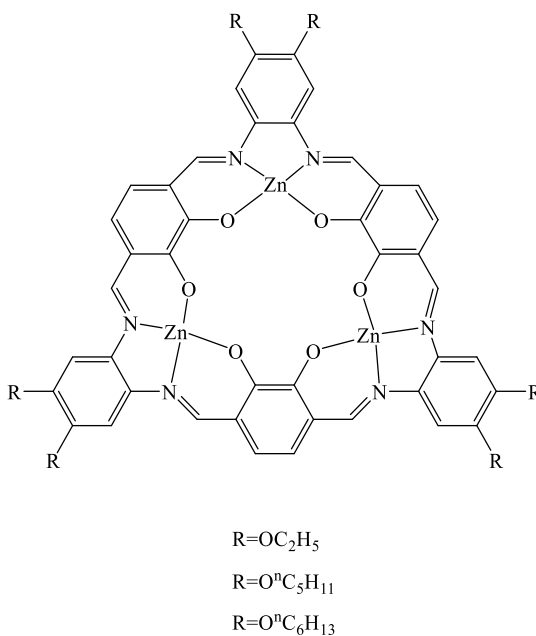
Figure 1-6. Structure of the Zn [3+3] Schiff-base macrocyclic complexes.[11]

2) [6+6] Structures

In 2006, [6+6] Schiff-base macrocycles were first published by MacLachlan's group (shown in Figure 1-7). A one-pot condensation procedure was used to prepare these large macrocycles. Semi-empirical calculations using a macrocycle with Ni^{2+} were carried out and it was found that the minimum energy conformation will be a boat and chair conformation. This research gives preliminary guidance on the coordination chemistry of such [6+6] big macrocycles.[12]

$R=OnC_6H_{13}$
$R=OnC_5H_{11}$
$R=H$

$R=OnC_6H_{13}$
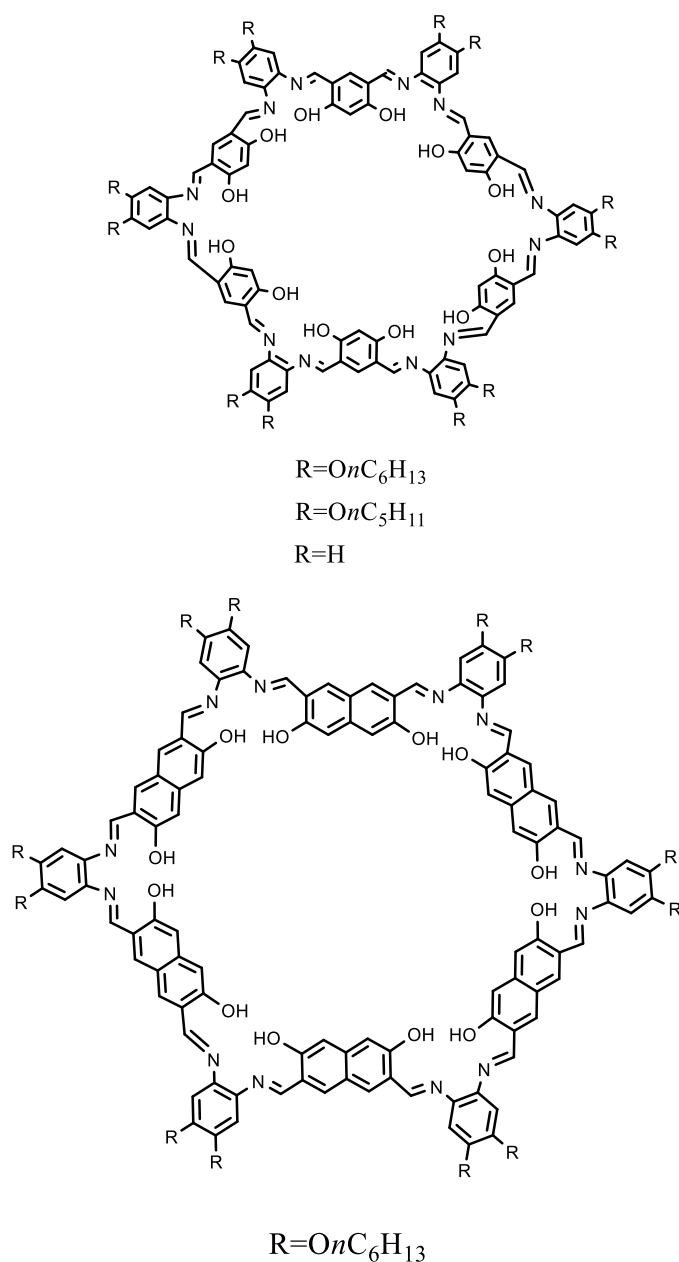
Figure 1-7. Structures of the [6+6] macrocycles.[12]

3) Other macrocycles

In addition, there are many other non-centrosymmetric Schiff base macrocycles. Jiang and MacLachlan synthesized a series of unsymmetrical triangular Schiff-base macrocycles (Figure 1-20).[13] From the NMR results, it was observed that the macrocycle is dominantly in the ketoenamine form. 2,6-Diacetylpyridine, tdmtn and hexamine were reacted in ethanol in a 1:1:1 ratio, in the presence of the metal salt, affording new

a   b

Figure 1-8. Synthesis of unsymmetrical Schiff-base macrocycles.[13]

M=Mg, Zn, Mn, Cd

Figure 1-9. Synthesis of unsymmetrical Schiff-base metal complexes.[14]

macrocyclic Mg, Mn, Zn and Cd complexes (Figure 1-9). These complexes adopt a pentagonal bipyramidal geometry at the metal in each case, and theoretical studies for the above-mentioned complexes were also carried out.[14]

1.1.2 Applications of macrocyclic Schiff bases Ligands and metal complexes

Schiff bases contain nitrogen lone electron pairs and one can introduce heteroatoms such as O and S, as well as other special functional groups, making them susceptible to coordination with metal ions to form metal complexes.[15] This makes Schiff bases of wide use in coordination chemistry, analytical chemistry, materials chemistry and many other applications.

1) Application in the Catalytic Field

Schiff bases and their metal complexes are excellent catalysts with applications in many areas of catalysis. For example, oxidation of olefins,[16] oxidation of alcohols or phenols, [17] polymerization of esters,[18] etc. They have become popular in the catalytic area because of the high catalytic activity exhibited by the resulting the metal complexes, selectivity and stability, and because they can also be recycled several times without any significant decrease in catalytic activity.

For instance, cobalt, iron, manganese and zinc complexes with a pentaaza-macrocyclic Schiff base ligand were synthesized. These complexes all adopted distorted pentagonal bipyramid geometry with metal centers which are all hepta-coordinated. The catalytic activity of light-driven hydrogen evolution was tested, and only the cobalt complex (shown in Figure 1-10) exhibited efficient hydrogen production activity.[19]
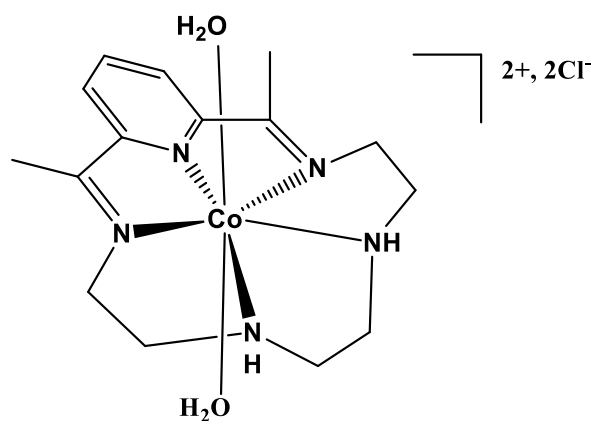
Figure 1-10. The Co pentaaza-macrocyclic Schiff base used in H_2 production.[19]

Pd(II) Pt(II) and Ru(II) complexes using tetraaza Schiff base ligand were synthesized (Figure 1-11). The Ru(II) centres are six-coordinate bound by four nitrogen atoms and two chloride ions, whereas the Pd(II) and Pt(II) centres are four coordinate bound by four nitrogen atoms. Moreover, these macrocyclic complexes were used as catalysts in the oxidation of pharmaceutical drug didanosine.[20] The above-mentioned method is simple, environmentally friendly, time-saving, highly efficient and does not need a co-oxidant.

M=Ru(II)   M=Pd(II) Pt(II)

X=

Y=Cl
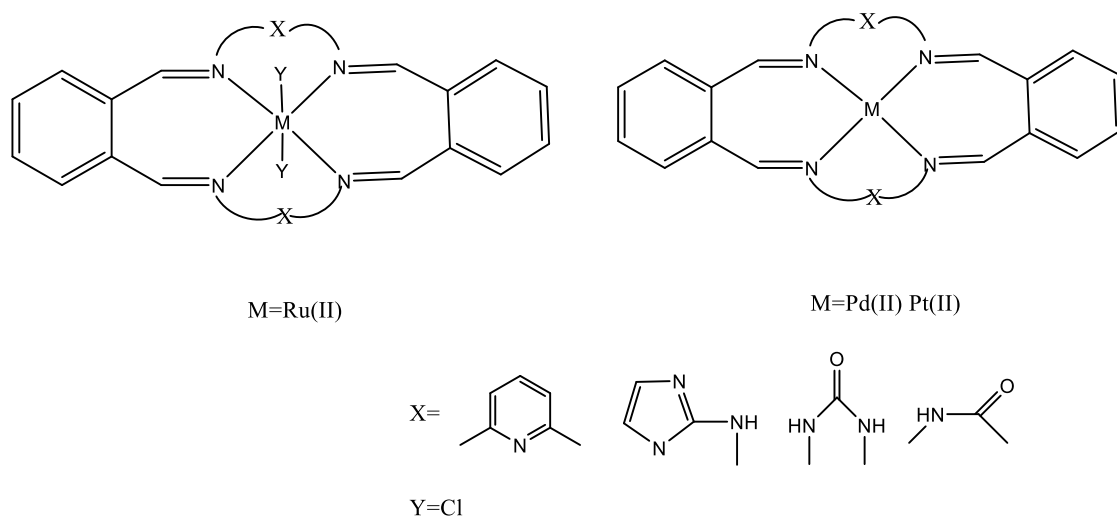
Figure 1-11. Ru(II), Pd(II) and Pt(II) Schiff base [2+2] macrocyclic complexes.[20]

2) Application in Analytical Chemistry

Schiff bases have shown promise in the field of metal ion analysis due to their ease of acquisition and facile coordination with metals. Xie and colleagues synthesized a macrocyclic ligand (Figure 1-12) and Zn(II) was coordinated to afford orange crystals. When coordinate to Zn^{2+}, the fluorescence intensity is enhanced, therefore, based on this, a Zn^{2+} sensor is established using the macrocyclic ligand.[21]

R=OMe; Me; *t*Bu
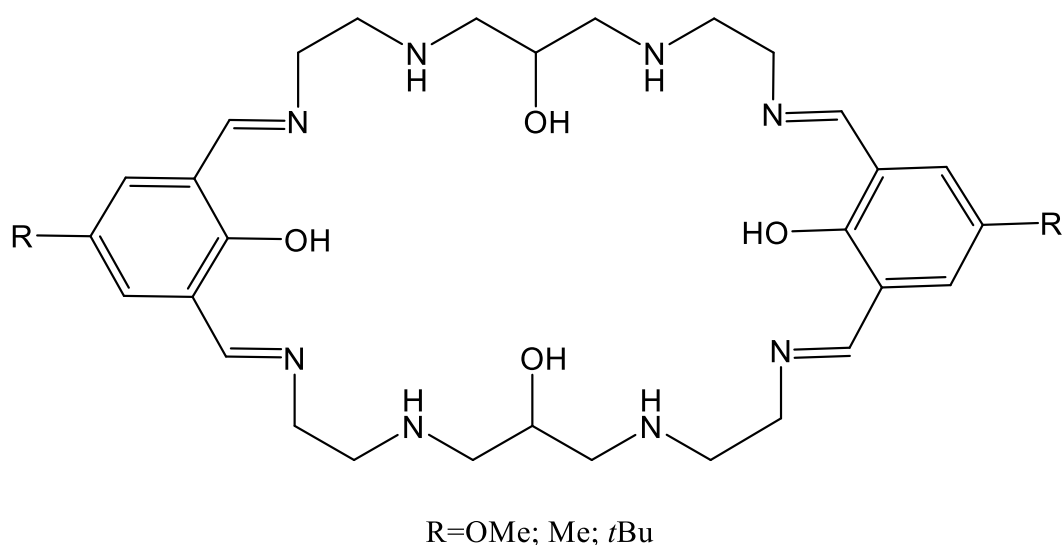
Figure 1-12. [2+2] Schiff base macrocycle used for Zn^{2+} detection.[21]

3) Application in Biochemistry

Studies have shown that some Schiff bases have good bactericidal, antibacterial and anticancer properties. For example, a range of five-coordinate Cr(III), Mn(III), Fe(III) were prepared, and were tested for antiinflammation and antimicrobial activity (Figure 1-13). The Cr complex revealed the best antimicrobial activity, whereas the Fe complex exhibited the best antiinflammation activity.[22]

M=Cr(III); Mn(III); Fe(III)

X=Cl⁻; NO₃⁻; CH₃COO⁻
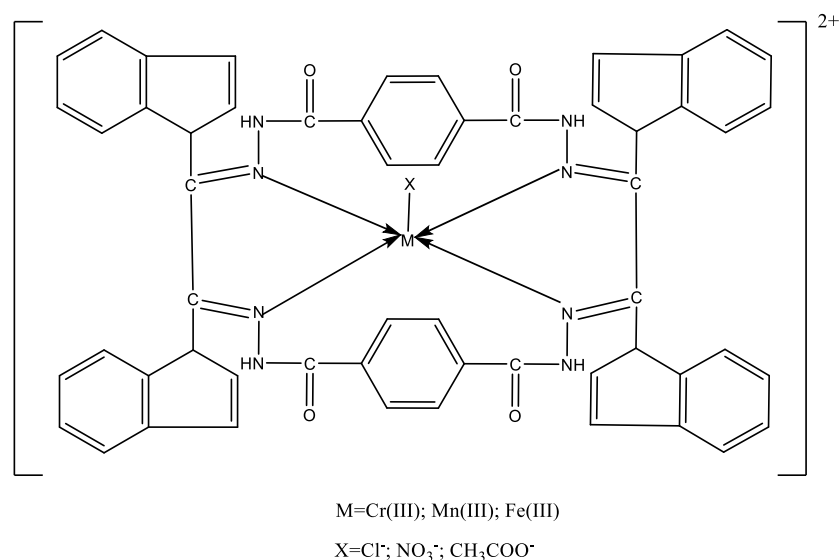
Figure 1-13. Structure of Cr(III), Mn(III), Fe(III) macrocyclic Schiff-base complexes.[22]

4) Application in Functional Materials

Schiff bases have also found application in the field of functional materials. Because Schiff bases contain C=N double bonds, they can be used as optical materials in OLEDs.[23] Moreover, some Schiff bases can be incorporated into materials as functional fillers to reduce the radiation emissivity of coatings, a property that has important applications in the military.[24]

A series of thermally stable zinc salphen macrocyclic complexes (Figure 1-14) has been synthesized and were shown to exhibit solid-state light emission. Moreover, some also exhibited Aggregation-Induced Enhanced Emission (AIEE), and therefore such Zn complexes have the potential to be utilized in OLEDs.[25]

$R_1 = t\text{Bu}/\text{NO}_2$ $R_2 = \text{H}/\text{Me}/\text{OCH}_2(\text{CH}_3)_3$ $X = \text{O}_2\text{C-Me}/\text{O}_2\text{C-Hex}$
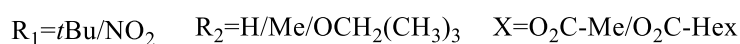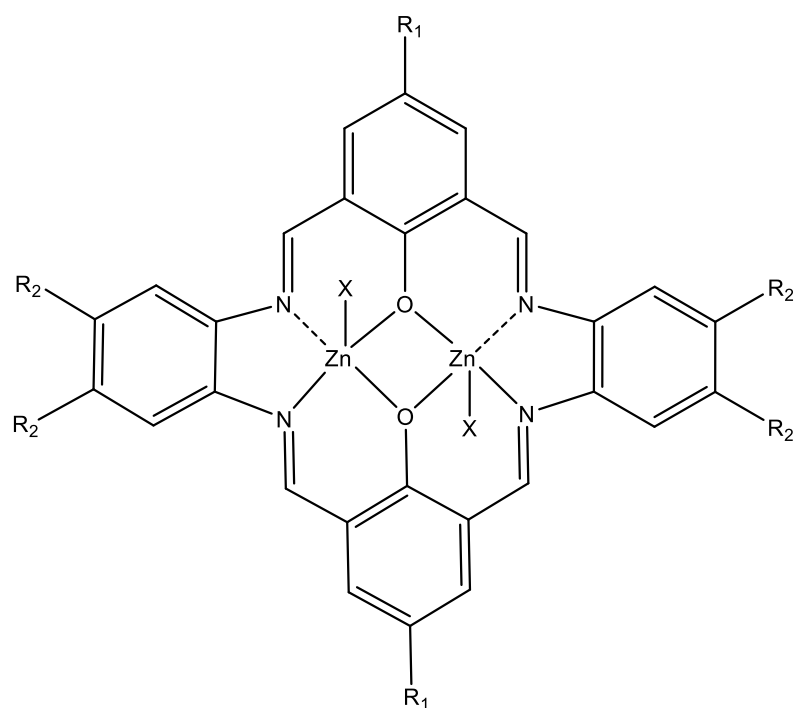
Figure 1-14. Thermally stable zinc disalphen macrocycles.[25]

1.2 Ring-opening polymerization of cyclic esters using Schiff base metal complexes.

1.2.1 Current status of plastic research

1.2.1.1 Problem with plastics

In recent years, the widespread use of polymer materials has brought great convenience to our daily life, but at the same time, it has also resulted in serious environmental problems since plastic products are difficult to decompose (e.g. white pollution). If plastic products are combusted in the soil, the groundwater and soil will be polluted and food production will decrease. Moreover, with the exhaustion of non-renewable resources such as fossil fuels and natural gas, there is an urgent demand for new environmental friendly, renewable degradable polymer materials to replace the traditional polymer materials

(polyethylene, polystyrene, polyvinyl chloride, etc.). Thus, biodegradable polymeric materials have become a recent hot topic of research. These materials can be degraded by microbial or chemical decomposition into environmentally friendly water and carbon dioxide molecules in a relatively short period. Therefore, it is urgent to find a cost-effective and energy-saving method to produce such biodegradable polyester materials.

Figure 1-15. Current pollution situation.

1.2.1.2 Application of biodegradable polymers

In recent years, biodegradable polymer materials have been widely used in agriculture, biomedicine, disposables, electronics, textiles, based on their environmentally friendly and excellent physical and chemical properties.

a.   Application in the field of disposables

Biodegradable polymers have good mechanical and physical processing properties. If they are under certain conditions, such as high temperature, high oxygen concentration or a large number of microorganisms exist, they will degrade in an environmentally friendly manner. Thus, such biodegradable polymers are currently mainly used for the production of packaging materials for food and beverage products, including food packaging bags, disposable lunch boxes, cups and other products.

b.   Application in agriculture

The good toughness of some biodegradable polymer materials such as polylactic acid derived materials makes them suitable for the production of thin film products. One of its outstanding advantages is that it will be degraded into environmentally friendly carbon dioxide and water molecules in the soil after a long time of use, therefore the fragile agricultural mulch film can be replaced by these biodegradable new products. This can effectively solve the problem of pollution caused by the agricultural film made of polyethylene at present.

c.   Application in the textile field

Synthetic fibers account for a large proportion of textile fibers, but most of the raw materials they are comprised of are produced by oil and coal which are non-renewable resources and difficult to degrade after being discarded.

d.   Application in the field of electronics

The application in the electronics field is mainly to use the physical and chemical properties of polylactide, which can be used to produce accessories for electronic products. The advantages in this area are mainly reflected in less CO_2 emissions after product disposal. The Nippon Electric Corporation (NEC) has developed a plant-derived bioplastic that is mainly based on PLA. It exhibits excellent fire resistance and widely used in many kinds of electronic products. In addition, these materials have good heat resistance and processing strength, so they can be used in the production of the outer case of items such as a business laptop.

e.   Application in the field of biomedicine

Currently, medical polymer materials mainly use PTFE (poly tetra fluoroethylene), silicone oil and silicone rubber, but these materials have certain side effects. With the continuous development and advancement in the field of medicine, people put forward higher requirements on medical polymer materials. Polylactide has good biocompatibility,

biodegradability and excellent physical and mechanical properties. It has been widely used in the field of biomedicine. Currently, it is mainly used for surgical sutures, drug sustained-release, orthopedic materials, infusion tools and other aspects.

1.2.2 Ring-opening polymerization of cyclic esters

Polyester materials are biodegradable, biocompatible and have other advantages that is why they have become a hot topic of research in the preparation of new polymer materials, which can replace traditional plastics. The depolymerization of biodegradable polymer materials will occur under the action of tissues, cells, enzymes and body fluids of animals or microorganisms in the environment. At present, polylactide (PLA), poly ε-caprolactone (PCL) and other copolymers (Figure 1-16) which are made from cyclic esters are attracting much attention. The main reason for the research on these materials is that they have unique advantages. On the one hand, the raw materials for the synthesis of these polyesters are renewable resources, such as corn starch and sugar beets. On the other hand, such polymers have very good biological properties such as biodegradability and biocompatibility.
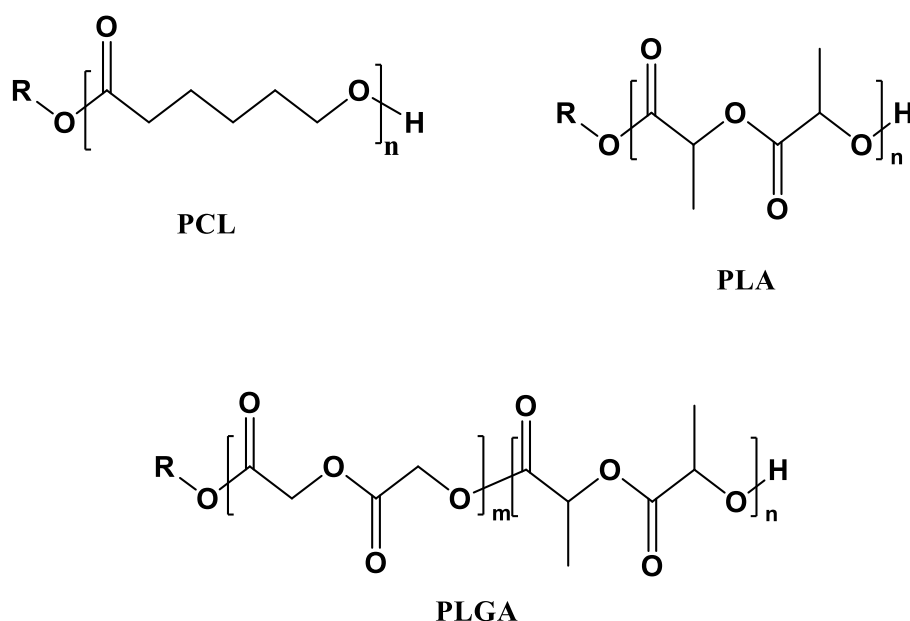
Figure 1-16. Structures for different kinds of polymer made via ROP.

14

Polycaprolactone has become an important polymer due to its good mechanical properties, biodegradability and compatibility with other polymers. Among many polymer materials, polycaprolactone has become an ideal application material for biomedicine and pharmaceuticals. The production of ε-caprolactone is still produced mainly by Baeyer-Williger oxidation reaction (Figure 1-18) with oxygen as the oxidant.[26] However, the recent patent literature reports on the method of synthesizing ε-caprolactone from starch as a raw material,[27] and the method of synthesizing ε-caprolactone from renewable resources to industrialize the production of polycaprolactone becomes possible. There are generally two methods for the synthesis of polycaprolactone (PCL): one is self-condensation of 6-hydroxyhexanoic acid, and the other is ring-opening polymerization from ε-caprolactone.[28] Compared to the polycondensation reaction, ring-opening polymerization has several advantages: Firstly, ε-caprolactone can be obtained from renewable resources such as starch. Secondly, no water is formed during the ring-opening polymerization, so the obtained polycaprolactone (PCL) has a larger molecular weight. Last but not least, the occurrence of side reactions such as chain transfer is reduced, and the obtained PCL has a low PDI.
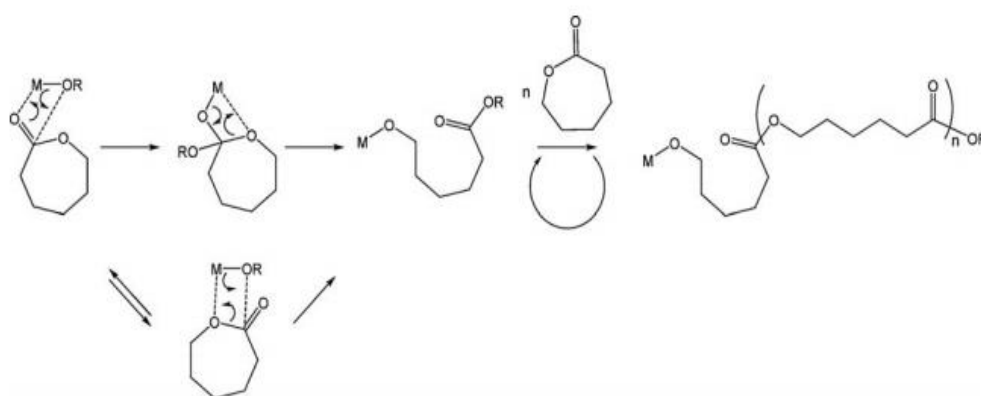
Figure 1-17. The mechanism of ROP reaction towards ε-caprolactone by using metal alkoxide species (M-OR). [30]

The use of ring-opening polymerization to obtain high-performance polymer poly *rac-*

lactide has become a hot research topic in recent years. There are currently two main synthetic methods: condensation polymerization from linear monomers,[29] and ROP of cyclic esters.[30] In the early stage, poly*rac*-lactide was generally obtained by direct condensation polymerization of *rac*-lactide. The advantage of this method is that the operation is simple, and the disadvantage is that the reaction temperature is high and the reaction time is very long, and the water generated during the reaction inhibits the forward progress of the reaction. This results in a polymer that cannot be obtained with a high molecular weight. Further, the polymer has a broad polydispersity index (PDI). In order to overcome such drawbacks, a method of catalytic ring-opening polymerization of a cyclic ester is generally employed to obtain a poly *rac*-lactide having a high molecular weight and a narrow molecular weight distribution. For example, the copper Schiff base complex (Figure 1-19) was synthesized and used to initiate the ROP of *L*-lactide in the presence of benzyl alcohol.[31]
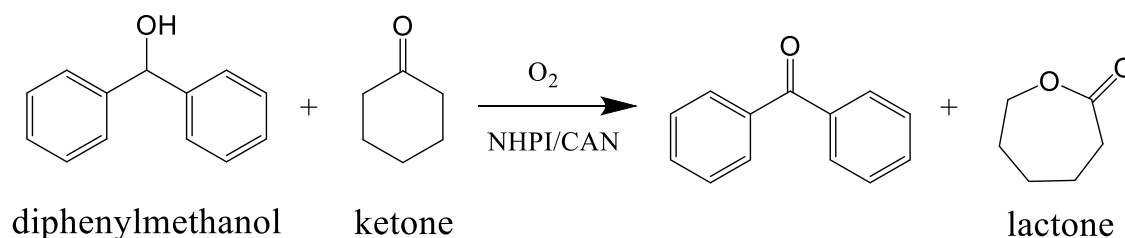
Figure 1-18. Baeyer-Williger oxidation of cyclohexanone to ε-caprolactone.[26]
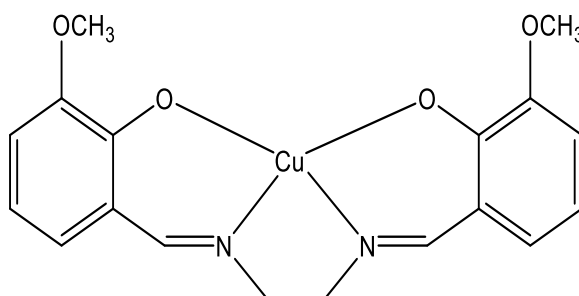
Figure 1-19. Structure of Cu Schiff-base complex reported by Routaray.[31]

1.2.3 Synthesize of block co-poly(cyclic esters).

A copolymer is a polymer derived from more than one type of monomer. The polymerization of monomers into copolymers is called copolymerization. Schiff base complexes are often used as catalysts for the synthesis of copolymers. For instance, Darensbourg and Karroonnirun have reported zinc Schiff base complexes derived from the natural amino acid phenylalanine as catalysts for random co-polymerization of *L*-lactide and ε-caprolactone.[32]

Yasuniwa and colleagues developed a process for the homopolymerization and copolymerization of lactones and DLLA (DL-Lactide) using Schiff-base aluminium complexes as catalysts (shown in Figure 1-20).[33] The copolymerization reactions of BL, CL or VL with DLLA gave the block-copolymers Figure 1-21.
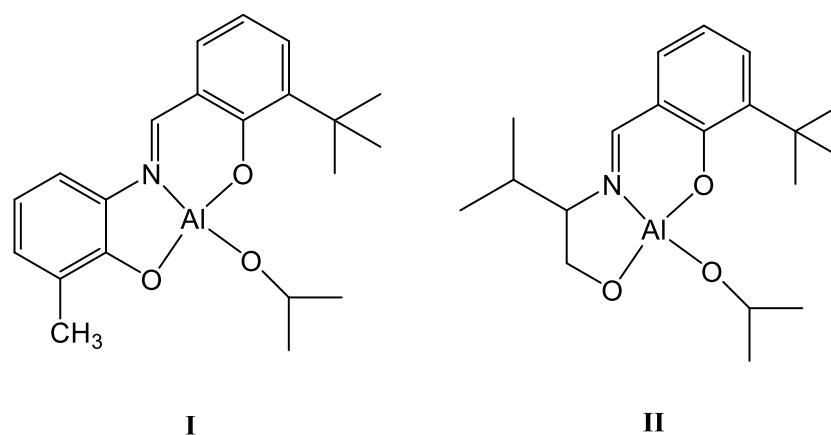
Figure 1-20. Structures of the tridentate aluminium complexes.[33]
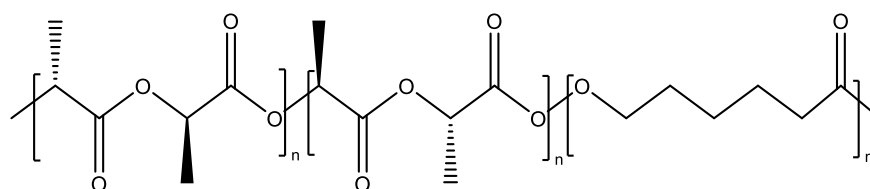
PDLLA-co-PCL
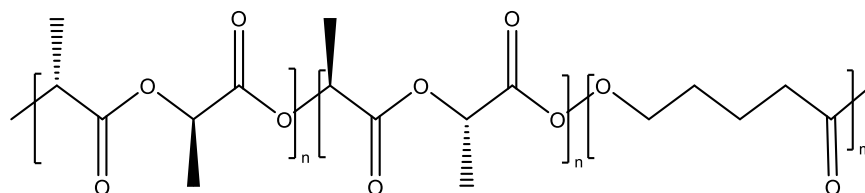
PDLLA-co-PVL
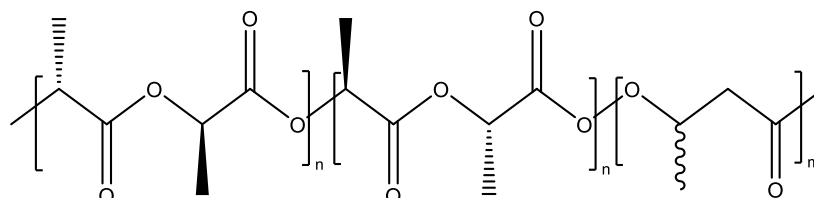
PDLLA-co-PBL

Figure 1-21. Copolymerization of *DL*-lactide with lactones initiated by **I** and **II**.[33]

1.3 Photolumincence studies of Schiff bases and their metal complexes

In recent years, the demand for fluorescent materials has increased, given they have good prospects for applications, such as fluorescent probes, sensors, anti-counterfeit markers. The development of economical fluorescent materials with good fluorescence properties has been a hot topic of research. Schiff-bases and their complexes are cost effective and have a wide range of applications due to their photochromic, photoconductive and other luminescent properties, so they are of interest as fluorescent materials.

1.3.1 Photolumincence studies of transition metal Schiff base complexes

The Schiff base TPE-An-Py compound (Figure 1-22) exhibits good fluorescent characterization in solvents. Based on this, a determination method for Cu(II) ion was established as the fluorescence intensity reduced proportionally with the addition of $Cu^{2+\cdot}$

18

This investigation provides a potential application for using Schiff base systems to detect Cu(II) ions in real samples.[34]
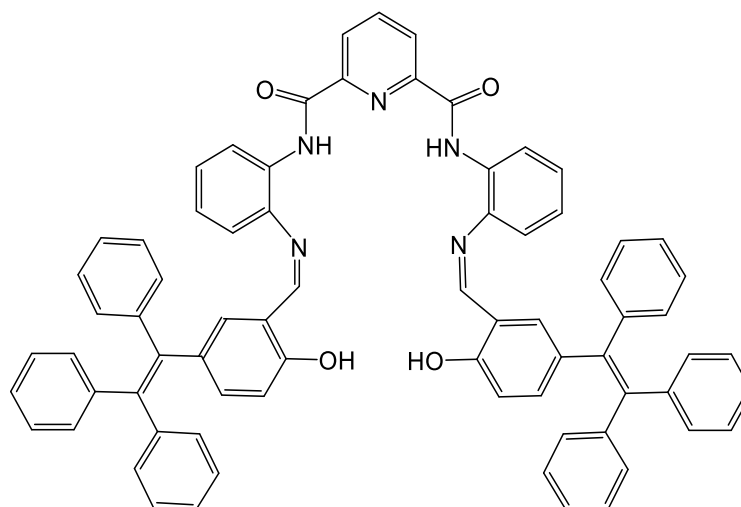
Figure 1-22. Structure of the Schiff base TPE-An-Py compound reported by Xie.[34]

In 2019, Chen's group synthesized several zinc (II) Schiff base complexes that exhibited robust AIEE (aggregation-induced emission enhancement) activity in acetonitrile and ether mixtures. Noteworthy, the AIEE performance can be enhanced by joining the two quinoline units using an alkoxy chain (Figure 1-23). Moreover, the introduction of the –OCH$_3$ group (Figure 1-23) can also improve the luminescence behaviour. The potential application of such complexes as smart fluorescent materials is worthy of exploration.[35]

R=H **III**,
R=OCH$_3$ **IV**

V
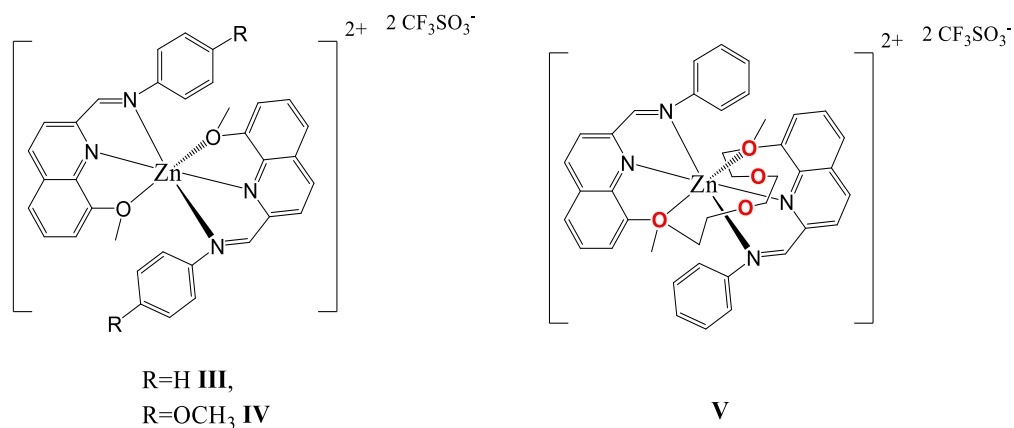
Figure 1-23. Structures of quinoline-based zinc(II)–Schiff base complexes **III**–**V**.[35]

19

In 2019, a new zinc complex bearing a Schiff base ligand (Figure 1-24) exhibited deep blue fluorescence, and was used in organic light-emitting devices (OLEDs). What is more, the optical characteristics of the fabricated OLEDs were also outstanding, and therefore this study may open up a new possibility for the commercialisation of deep blue OLEDs.[36]
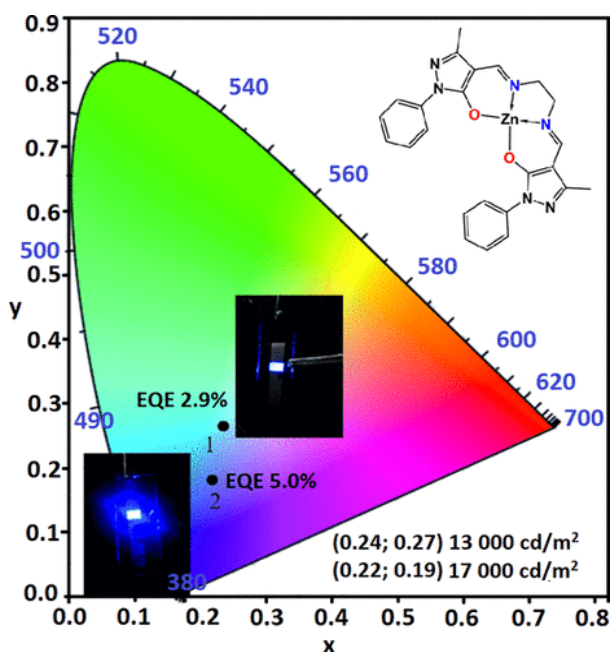
Figure 1-24. CIE1931 chromaticity coordinates.[36]

Not only zinc, but also many other transition metal Schiff base complexes exhibit fluorescent properties, for instance, azo-Schiff bases copper(II) or zinc(II) metal complexes were synthesized and show photoluminescence properties.[37]

Moreover, Cd(II) and Zn(II) complex using *N,N,O-* donor Schiff base ligation have been synthesized and their photoluminescent properties discussed. Interestingly, the quantum yields of the Cd(II) complex is higher than Zn(II) complexes probably due to the heavy atom perturbation effect.[38]

Klimant and co-workers synthesized Zn(II), Pd(II) and Pt(II) Schiff base complexes using a one-step condensation method (Figure 1-25). Noteworthy, the Pt(II) and Pd(II) complexes exhibited room temperature phosphorescence, whereas the Zn(II) complex

exhibited thermally-activated delayed fluorescence and they all possessed good photostability.[39]
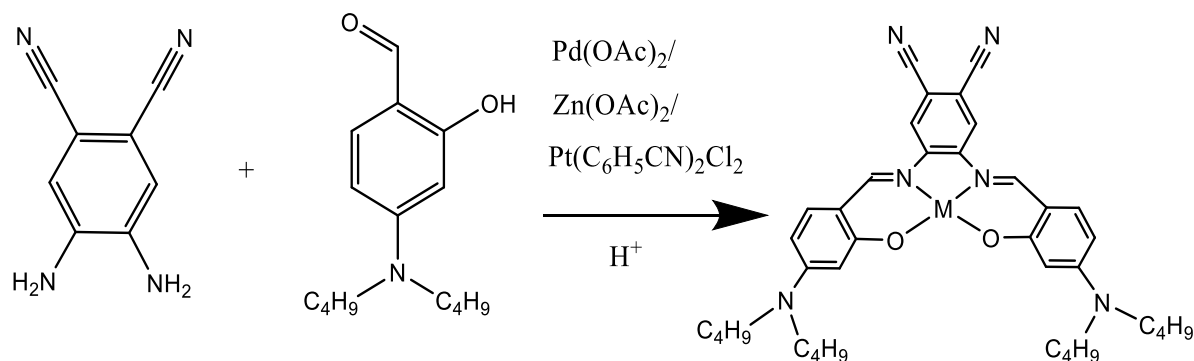
Figure 1-25. Synthesis of the Zn(II), Pd(II) and Pt(II) Schiff base complexes.[39]

1.3.2 Photoluminescent studies of lanthanide metal Schiff base complexes

Nowadays, lanthanide complexes are of great interest because they show good emission properties, for example, long lifetimes and large Stokes· shifts.[40] Because of these above-mentioned advantages, more and more Ln Schiff base complexes have been made and used as luminescent materials. For instance, the Ln(III) and Co(II) mononuclear and heterodinuclear complexes using the N_4O_4 macrocyclic ligand H_4L (Figure 1-26) were successfully synthesized, and all Eu(III), Yb(III), Er(III), Nd(III) exhibited good luminescent properties. Noteworthy, the Yb(III) complex can convert visible light to infrared radiation at 77 and 293 K. Moreover, the emission of the Eu(III) complex is temperature dependent, and is caused by the low lying ligand triplet state.[41]

H_2L

$[Ln(H_4L)]^{3+}$

$[LnCo(H_2L)]^{3+}$

$[LnCo(HL)]^{2+}$
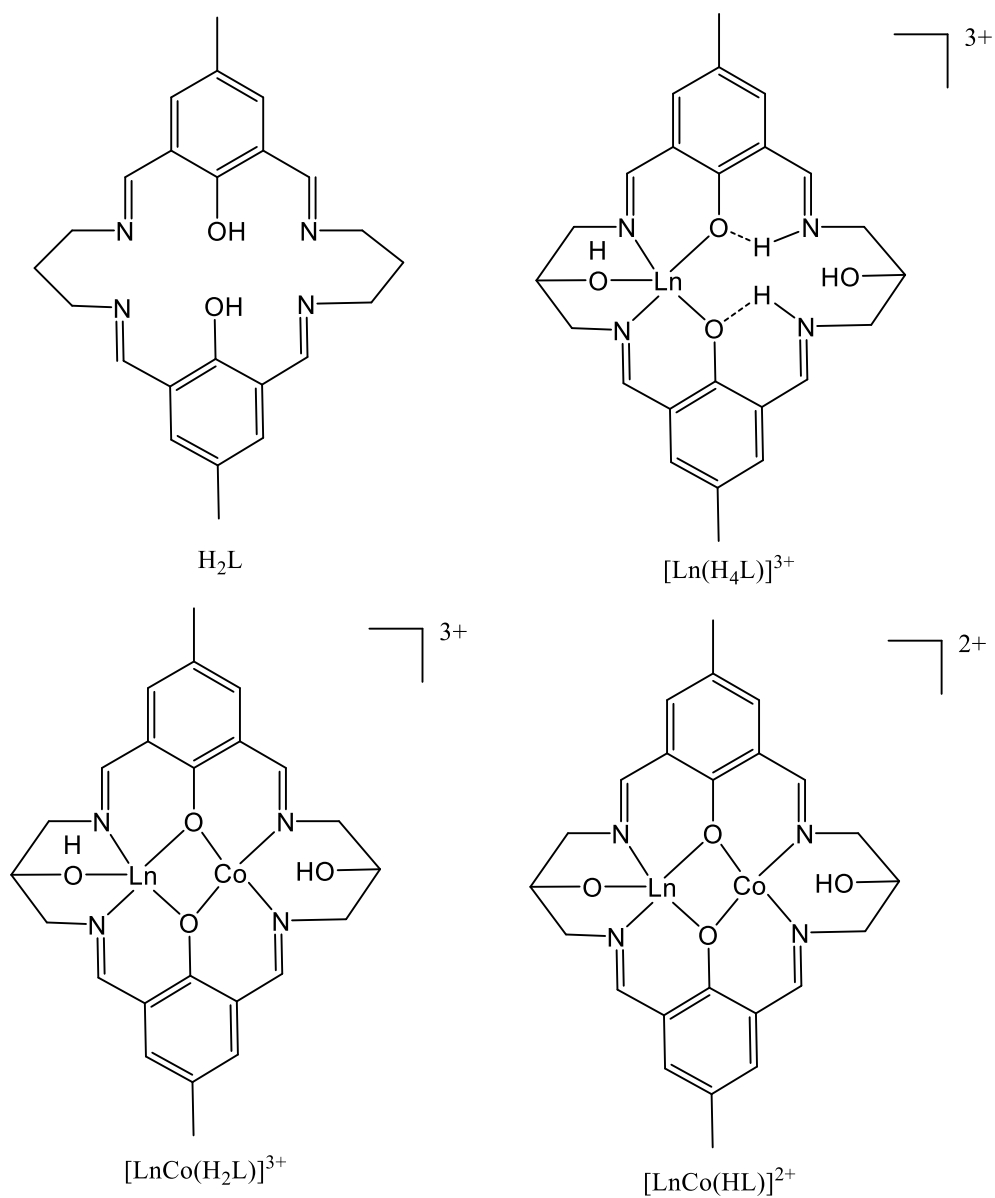
Figure 1-26. Structures of discussed macrocycles and complexes.[41]

FakhrEldin and coworkers discussed the structures and photophysical properties of Eu(III), Tb(III) and Gd(III) Schiff base complexes. Interestingly, the Eu(III) complex exhibited a white-light, whereas the Tb(III) complex emitted green light. Such findings may provide opportunities for designing flat panel displays.[42]

1.4 Coordination complexes as Peroxidase-like mimetics.

1.4.1 Materials used as peroxidase-like mimetics

Enzymes are biocatalysts in living cells, most of them are proteins and a few are RNA. They can catalyze various biological and chemical reactions efficiently by reducing the activation energy of chemical reactions under mild conditions. The limitations of natural enzymes, such as high cost, low stability and storage difficulties, have led to the emergence of various artificial enzymes. Types of artificial enzymes include catalase, peroxidase, superoxide dismutase, DNAzymes and oxidase. Over the last decade, iron complexes have been used as peroxidase-like mimetics especially iron porphyrin complexes,[43] for example, the group of Abhishek described a biomimetic iron porphyrin complex present in the active site of HRP.[44] Moreover, an iron(III) tetradentate monoamido complex was found to catalyse the oxidation of Orange II, guaiacol, ABTS and Amplex Red in the presence of H_2O_2.[45] Besides Fe complexes, peroxidase-like and catalase-like activities of manganese-Schiff base complexes also have been reported.[46] In recent years, the use of transition metal oxides (Fe_3O_4, Co_3O_4) [47,48] precious metals (Au, Pt) [49,50] composite materials,[51] heme,[52] porphyrin,[53] metal organic frameworks (MOFs) [54] and their derivatives [55] have also been investigated. Given their ease of acquisition, high efficiency and stability, such artificial mimetics have become an increasingly researched topic.

1.4.2 The applications for peroxidase-like activity

A) Application in analytical chemistry

The properties of mimicking peroxidase can be used for H_2O_2 and glucose determination.[56] In 2016, Wang and colleagues established an assay for glucose using Cu-MOFs. Firstly, glucose oxidase can decompose glucose into hydrogen peroxide and

gluconic acid, and then an organic substrate (TMB) is added. Cu-MOFs can catalyse the redox reaction between the above-mentioned hydrogen peroxide produced and the organic substrate (TMB), forming a colour change. Based on this, the colorimetric glucose detection method with a detection limit of 6.9 μM detection with a linear range of 10 μM-3 mM was established.

Moreover, the interference of lactose, glucose and fructose for glucose detection is tiny and can be ignored, therefore, this method has a low detection limit and good selectivity.
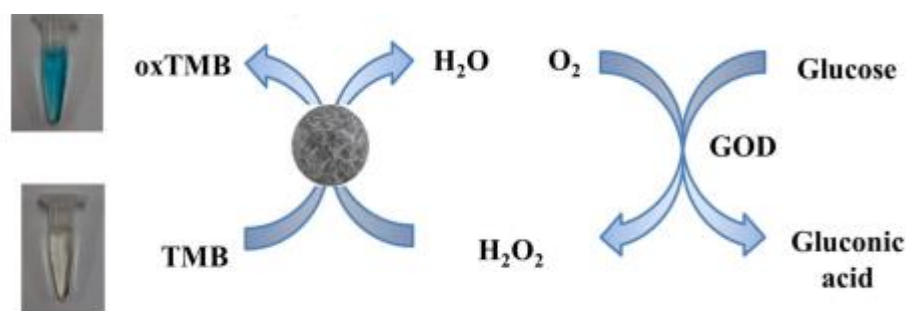
Figure 1-27. The mechanism for glucose sensing.[57]

The peroxidase-like activity can also be used for dopamine determination. The addition of dopamine reduces the oxidised TMB, resulting in a lower colour change and absorbance. Based on this principle, the colorimetric detection of dopamine was established using [Cu(PDA)(DMF)] with good selectivity and high sensitivity by Wang et al.[58]

In addition, enzyme mimetics can also be used to create assays for substances such as cholesterol, [59] cancer cells,[60] metal ions,[61] melamine,[62] pesticides,[63] etc. Thus, the above-mentioned assays provide simple, economical, and highly effective platforms for biosensor and other novel applications.

B）Application in Biomedical and diagnoses

Materials with intrinsic peroxidase-like activities are found to enhance the antibacterial performance of H_2O_2 and can avoid toxicity in high H_2O_2 levels. Nowadays, Pt nanocrystals hollow Nanodendrites with peroxidase-like activity can catalyze the decomposition of H_2O_2 and form •OH.[64] Based on this property, Ge and coworkers combined the material with low concentrations of H_2O_2 to achieve an antibacterial mixture that exhibited broad spectrum bactericidal properties against bacteria *in vitro*. Such breakthroughs can be used to guide the future design of novel enzyme-mimetics and antibacterial systems.

C）Application in degradation

Artificial peroxidase has shown great potential for the degradation of pollutants. Using peroxidases-like catalytic ability, organic dyes can be degraded in the presence of hydrogen peroxide, and the degradation rate can reach over 90%.[65]

For example, a peroxidase-like material Ni@Mil-100(Fe) @Ag nanowires (NMAs) was developed, which can detect cationic dyes. Moreover, a hydroxyl radical (•OH) can be produced in the presence of H_2O_2, and the pollution can be degraded within 1 min.[66]

What is more, Co(II) and Cu(II) Schiff-base complexes were used as mimetic peroxidase in the catalytic oxidation of phenol in H_2O_2-buffered solution.[67] Such peroxidase mimics exhibited good catalytic properties of the peroxidase in the catalytic oxidation of phenol by H_2O_2 under different conditions. In conclusion, peroxidases mimetics generate good catalytic activity towards the degradation of dyes or other pollutants in the presence of H_2O_2.

1.4.3 Mechanism studies for peroxidase mimic activity

1) Electron transfer mechanism

In 2011, Wang and coworkers discussed the electron transfer process for a Co_3O_4 nanoenzyme. The electron transfer between the 3,3',5,5'-tetramethylbenzidine (TMB) substrate and H_2O_2 can be accelerated by the artificial peroxidase-like mimetics,[48] and in 2015, similar behaviour for the perovskite $LaCoO_3$ peroxidase-like material (Figure 1-28) was observed.[68]
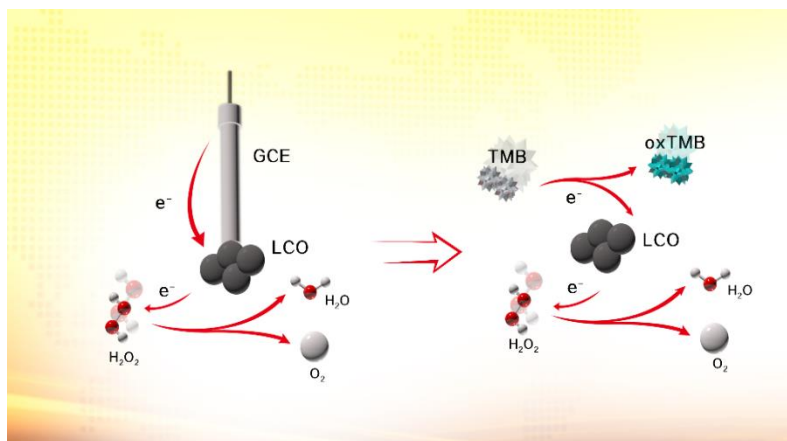
Figure 1-28. Schematic illustration of the electron transfer process between TMB-LCO-H_2O_2 system. [68]

2)·OH Radical

The ·OH radical is found to be an intermediate in the catalytic process in the presence of H_2O_2. Some peroxidase mimetics can break up the O–O bond of H_2O_2 into two hydroxyl radicals (Figure 1-29).[69] Then, the resulting hydroxyl radicals react with TA (Titratable acid) to form highly fluorescent hydroxyterephthalate (TAOH).
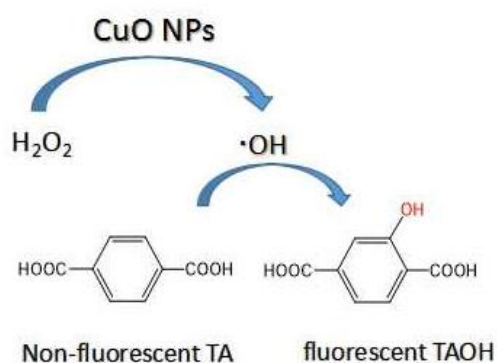
Figure 1-29. Schematic illustration of the cupric oxide nanoparticles-based fluorescent sensor for hydrogen peroxide.[69]

1.5 Characterization methods

Nuclear Magnetic Resonance spectroscopy (NMR)

Nuclear Magnetic Resonance spectroscopy is a technique using the nuclear magnetic resonance phenomenon to determine the molecular structure. At present, NMR spectroscopy has focused on the spectra of two types ^{1}H (hydrogen spectrum) and ^{13}C (carbon spectrum). Similar to infrared spectroscopy, NMR spectroscopy can provide information on the number and type of chemical functional groups in a molecule, but in addition, it can provide much information that infrared spectroscopy cannot. In this thesis, the techniques ^{1}H NMR, 2D-J resolved ^{1}HNMR, ^{1}H-^{1}H COSY NMR, ^{1}H-^{13}C COSY NMR, ^{13}C NMR spectroscopy are utilized.

Evans balance

The magnetic moment is a physical property of a magnet that can be expressed as a vector, and is related to the force experienced by a substance in the external magnetic field. The magnetic moment for the Fe and Co compounds in this thesis were tested by an Evans

balance (also known as a Johnson-Matthey balance).

Elementary analysis

Elementary analysis is a method for determining the elemental composition and percentage content of a compound using chemical reactions. There are two types: qualitative and quantitative. The former is used to identify which elements are present in the compound; the latter is used to determine the percentage content of these elements. For example, the content of elements such as carbon, hydrogen and sulfur can be determined quantitatively after the substance has been burned.

Mass spectrometry

Mass spectrometry is a technique that can ionize chemical substances and ranks them according to their mass-to-charge ratio (mass-to-charge ratio). These are used to determine the molecular masses of a sample and to explain the chemical structure of molecules.

X-ray diffraction analysis

Single crystal X-ray diffraction is an experimental method that uses the diffraction effect of single crystals on X-rays to determine the crystal structure. Whereas, powder X-ray diffraction analysis (PXRD) is mainly used to analyse the phase composition of a sample.

Fourier Transform Infrared Spectroscopy (FT-IR)

Fourier transform infrared spectroscopy (FT-IR) is an analytical method for identifying the functional groups of compounds and determining the molecular structure of substances based on information such as the relative vibrations and molecular rotation.

Scanning Electron Microscopy (SEM)

Scanning electron microscopy uses electron imaging to study the structure, morphology,

and particle size of a sample.

UV-Vis spectrophotometry

UV-Vis spectrophotometry is a qualitative, quantitative and structural analysis method based on the absorption of a range of electromagnetic waves, and is a measurement of the absorption at different wavelengths by molecules. The Lambert-Beer law is the basis for quantitative analysis by spectrophotometry.

Fluorescence spectrum

Fluorescence is the emission of light by a substance that has absorbed light or other electromagnetic radiation. The fluorescence spectrum includes both excitation and emission spectra. The fluorescence spectra in this thesis are all emission spectra.

Fluorescence lifetime

The fluorescence lifetime refers to the average time the molecule stays in its excited state before emitting a photon.[70] It is an important parameter for practical applications of fluorescence and is often expressed as τ.

Fluorescence quantum yield

The quantum yield (Y_f) is the ratio of the number of photons emitted by a fluorescent substance to the number of photons absorbed. Its value is normally always less than 1. The larger the value of Y_f, the more fluorescent the compound, whereas the fluorescence quantum yield of a non-fluorescent substance is equal to or very close to zero. The fluorescence quantum yields covered in this thesis are all absolute fluorescence quantum yields.

Gel permeation chromatography

Gel permeation chromatography (GPC) was first investigated by J.C. Moore in 1964 and

can be used not only for the separation and identification of small molecules but also for the analysis of polymers.[71] In this thesis, the main application of GPC is to determine the relative molecular mass and the molecular weight distribution of the polymers.

1.6   References

[1] C. Redshaw, *Catalysts*, 2017, 7, 165.

[2] W. Yang, K. -Q. Zhao, B. -Q. Wang, C. Redshaw, M. R. J. Elsegood, J. -L. Zhao and T. Yamato, *Dalton Trans.*, 2016, 45, 226-236.

[3] A. Arbaoui, C. Redshaw and D. L. Hughes, *Chem. Commun.,* 2008, 4717-4719.

[4] A. Arbaoui, C. Redshaw and D. L. Hughes, *Supramol. Chem.,* 2009, 21, 35-43.

[5] W. Yang, K.-Q. Zhao, T. J. Prior, D. L. Hughes, A. Arbaoui, T. Bian, M. R. J. Elsegood and C. Redshaw, *Dalton Trans.*, 2016, 45, 11990-12005.

[6] W. Qin, S. Long, M. Panunzio and S. Biondi, *molecules*, 2013, 18, 12264-12289.

[7] A. M. J. Devoille, P. Richardson, N. L. Bill, J. L. Sessler and J. B. Love, *Inorg. Chem.*, 2011, 50, 3116.

[8] J. L. Sessler, E. Tomat, V. M. Lynch., *J. Am. Chem. Soc.*, 2006, 128(13), 4184-4185.

[9] B. N. Boden, J. K. H. Hui, M. J. MacLachlan, *J. Org. Chem.*, 2008, 73(20), 8069-8072.

[10] A. M. Lopez-Periago, C. A. Garcia-Gonzalez and C. Domingo, *Chem. Commun.*, 2010, 46, 4315.

[11] H. L. C. Feltham, F. Klower, S. A. Cameron, D. S. Larsen, Y. H. Lan, M. Tropiano, S. Faulkner, A. K. Powell and S. Brooker, *Dalton Trans.*, 2011, 40, 11425–11432.

[12] J.K. Hui and M.J. MacLachlan, *Chem Commun.*, 2006, 23, 2480-2482.

[13] J. Jiang and M. J. MacLachlan, *Org. Lett.*, 2010, 12(5): 1020-1023.

[14] M. Rezaeivala and H. Keypour, *Coord. Chem. Rev.*, 2014, 280, 203-253.

[15] M. K. Taylor, K. D. Trotter, J. Reglinski, L. E. A. Berlouis, A. R. Kennedy, C. M. Spickett, R. J. Sowden, *Inorg. Chim. Acta*, 2008, 361, 2851-2862.

[16] D. M. Boghaei and S. Mohebi, *J. Mol. Catal. A Chem.*, 2002, 179, 41-51.

[17] M. M. Tamizh, K. Mereiter, K. Kirchner and R. Karvembu, *J. Organomet. Chem.*, 2012, 700, 194-201.

[18] H. Du, A. H. Velders, P. J. Dijkstra, Z. Zhong, X. Chen and J. Feijen, *Macromolecules*, 2009, 42, 1058-1066.

[19] R. Gueret, C.E. Castillo, M. Rebarz, F. Thomas, M. Sliwa, J. Chauvin, B. Dautreppe, J. Pécaut, J. Fortage and M. N. Collomb, *Inorg. Chem.*, 2019, 58, 9043-9056.

[20] P. M. Reddy, M. Sarangapani, G. Hanmanthu, B. Geeta, K.S. Rani and V. Ravinder, *Spectrochim. Acta A Mol. Biomol. Spectrosc.*, 2012, 97, 189-196.

[21] C. X. Ding, C. H. He and Y. S. Xie, *Chin. Chem. Lett.*, 2013, 24, 463-466.

[22] G. Kumar, S. Devi, R. Johari and D. Kumar, *Eur. J. Med. Chem.*, 2012, 52 , 269-274.

[23] L. Yan, R. Li, W. Shen and Z. Qi, *J. Lumin.*, 2018, 194, 151-155.

[24] C. M. Yeng, S. Hussiensyah and S. S. Ting, *Adv. Environ. Biol.*, 2014, 2609-2615.

[25] J. A. Marafie, D. D. Bradley and C. K. Williams, *Inorg. chem.*, 2017, 56, 5688-5695.

[26] D. Renfeng, Y. Haoran, Z. Chenxuan, W. Yongtao, Y. Jia, L. Haoran, Mol. Catal., 2020, 490, 110947.

[27] S. M. Thomas, R. Dicosimo and V. Nagarajan , *Trends Biotechnol.*, 2002, 20, 238 - 242.

[28] T. Xing, T. J. Prior, M. R. Elsegood, N. V. Semikolenova, I. E. Soshnikov, K. Bryliakov, K. Chen and C. Redshaw, *Catal. Sci. Technol.*, 2021, 11, 624-636.

[29] J. Gay-Lussac and J. Pelouze, *Ann. Pharm.*, 1833, 7, 40–44.

[30] A. Arbaoui, C. Redshaw, *Polym. Chem.*, 2010, 1(6), 801-826.

[31] A. Routaray, S. Mantri, N. Nath, A.K. Sutar and T. Maharana, *Chin. Chem. Lett.*, 2016, 27, 1763-1766.

[32] D. J. Darensbourg and O. Karroonnirun, *Macromolecules*, 2010, 43 (2010) 8880-8886.

[33] K. Matsubara, K. Eda, Y. Ikutake, M. Dan, N. Tanizaki, Y. Koga, M. Yasuniwa, *J. Polym. Sci. A Polym. Chem.*, 2016, 54, 2536-2544.

[34] H.-F. Xie, C.-J. Yu, Y.-L. Huang, H. Xu, Q.-L. Zhang, X.-H. Sun, X. Feng and C. Redshaw, *Mater. Chem. Front.*, 2020, 4, 1500-1506.

[35] D. Qiao, J. Y. Wang, L. Y. Zhang, F. R. Dai and Z. N. Chen, *Dalton Trans.*, 2019, 48, 11045-1105.

[36] A. N. Gusev, M. A. Kiskin, E. V. Braga, M. Chapran, G. Wiosna-Salyga, G. V. Baryshnikov, V. A. Minaeva, B. F. Minaev, K. Ivaniuk, P. Stakhira, H. Ågren and W. Linert, *J. Phys. Chem. Lett.*, 2019, 123, 11850-11859.

[37] F. Purtas, K. Sayin, G. Ceyhan, M. Kose and M. Kurtoglu, *J. Mol. Struct.*, 2017, 1137, 461-475.

[38] I. Majumder, P. Chakraborty, S. Dasgupta, C. Massera, D. Escudero and D. Das, *Inorg. Chem.*, 2017, 56, 12893-12901.

[39] S.M. Borisov, R. Pommer, J. Svec, S. Peters, V. Novakova and I. Klimant, *J. Mater. Chem. C Mater.*, 2018, 6, 8999-9009.

[40] G. Peng, Y. Chen and B. Li, *New J. Chem.*, 2020, 44, 7270-7276.

[41] P. Gawryszewska and J. Lisowski, *Inorg. Chim. Acta*, 2012, 383, 220-229.

[42] N. K. Al-Rasbi, H. Adams, F. O. Suliman, *Dyes Pigm.*, 2014, 104, 83-88.

[43] J. T. Groves, R. C. Haushalter, M. Nakamura, T. E. Nemo, B. Evans, *J. Am. Chem. Soc.*, 1981, 103, 2884-2886.

[44] S. Bhakta, A. Nayek, B. Roy and A. Dey, *Inorg. Chem.*, 2018, 58, 2954-2964.

[45] Y. Hitomi, K. Hiramatsu, K. Arakawa, T. Takeyasu, M. Hata and M. Kodera, *Dalton Trans.*, 2013, 42, 12878-12882.

[46] M. Á. Vázquez-Fernández, M. R. Bermejo, M. I. Fernández-García, G. González-Riopedre, M. J. Rodríguez-Doutón, M. Maneiro, *J. Inorg. Biochem.*, 105 (2011) 1538-1547.

[47] L. Z. Gao, J. Zhuang, L. Nie, J. B. Zhang, Y. Zhang, N. Gu, T. H. Wang, J. Feng, D. L. Yang, S. Perrett and X. Yan, *Nat. Nanotechnol.*, 2007, 2, 577-583.

[48] J. Mu, Y. Wang, M. Zhao and L. Zhang, *Chem. Commun.*, 2012, 48, 2540-2542.

[49] Y. Hu, H. Cheng, X. Zhao, J. Wu, F. Muhammad, S. Lin, J. He, L. Zhou, C. Zhang, Y. Deng, P. Wang, Z. Zhou, S. Nie and H. Wei, *ACS Nano*, 2017, 11, 5558–5566.

[50] M. Ma, Y. Zhang and N. Gu, *Colloid Surface A*, 2011, 373, 6-10.

[51] T. Zhang, Y. Xing, Y. Song, Y. Gu, X. Yan, N. Lu, H. Liu, Z. Xu, H. Xu, Z. Zhang and M. Yang, *Anal. Chem.*, 2019, 91, 10589–10595.

[52] Q. Wang, Z. Yang, X. Zhang, X. Xiao, C. K. Chang and B. Xu, *Angew. Chem., Int. Ed.*, 2007, 46, 4285.

[53] M. Sono, M. P. Roach, E. D. Coulter and J. H. Dawson, *Chem. Rev.*, 1996, 96, 2841.

[54] J. W. Zhang, H. T. Zhang, Z. Y. Du, X. Wang, S. H. Yun and H. L. Jiang, *Chem. Commun.*, 2014, 50(9), 1092-1094.

[55] A. Li, X. Mu, T. Li, H. Wen, W. Li, Y. Li and B. Wang, *Nanoscale*, 2018, 10, 11948–11954.

[56] Y. Song, K. Qu, C. Zhao, J. Ren and X. Qu, *Adv. Mater.*, 2010, 22, 2206-2210.

[57] F. Liu, J. He, M. Zeng, J. Hao, Q. Guo, Y. Song and L. Wang, *J. Nanopart. Res.*, 2016, 18, 1-9.

[58] J. Wang, Y. Hu, Q. Zhou, L. Hu, W. Fu and Y. Wang, *ACS Appl. Mater. Interfaces*, 2019, 11, 44466-44473.

[59] L. Hong, A.-L. Liu, G.-W. Li, W. Chen and X.-H. Lin, *Biosens. Bioelectron.*, 2013, 43, 1-5.

[60] Y. Song, Y. Chen, L. Feng, J. Ren and X. Qu, *Chem. Commun.*, 2011, 47, 4436-4438.

[61] Y.S. Kim and J. Jurng, *Sens.Actuators B Chem.*, 2013, 176, 253-257.

[62] P. Ni, H. Dai, Y. Wang, Y. Sun, Y. Shi, J. Hu and Z. Li, *Biosens. Bioelectron.*, 2014, 60, 286-291.

[63] G. Guan, L. Yang, Q. Mei, K. Zhang, Z. Zhang, M. Y. Han, *Anal. Chem.*, 2012, 84, 9492-9497.

[64] C. Ge, R. Wu, Y. Chong, G. Fang, X. Jiang, Y. Pan, C. Chen and J. J. Yin, *Adv. Funct.*, 2018, 28, 1801484.

[65] L. Ai, C. Zhang, L. Li and J. Jiang, *Appl. Catal. B*, 2014, 148, 191-200.

[66] G. Jiang, Z. Wang, S. Zong, K. Yang, K. Zhu and Y. Cui, *J. Hazard. Mater.*, 2021, 408, 124426.

[67] J. Q. Xie, J. Z. Li, X. G. Meng, C. W. Hu, X. C. Zeng, S .X. Li, *Transit. Met. Chem.*, 2004, 29, 388-393.

[68] K. Wang, J. Song, X. Duan, J. Mu and Y. Wang, *New J. Chem.*, 2017, 41, 8554-8560.

[69] A. L. Hu, Y. H. Liu, H. H. Deng, G. L. Hong, A. L. Liu, X. H. Lin, X. H. Xia and W. Chen, *Biosens. Bioelectron.*, 2014, 61, 374–378.

[70] M. Y. Berezin, S. Achilefu, *Chem. Rev.*, 2010, 110, 2641-2684.

[71] G.H. Lathe, C. R. J. Ruthven, *Biochem. J.*, 1956, 62, 665–674.

Chapter 2 . Cobalt and zinc complexes for ring opening polymerization

2.1 Introduction

The production of aliphatic polyesters has become a very topical area given their biodegradability and biocompatibility,[1] and given the current global issues with plastic pollution, this is likely to remain the case for the foreseeable future.[2] As mentioned in chapter 1, one viable route to such polymers is via the metal-catalyzed ring opening polymerization (ROP) of cyclic esters.[3] The choice of metal catalyst employed is influenced by a number factors, such as price, toxicity, activity and control. Frameworks that are capable of simultaneously binding numerous metal centres continue to be of great interest in various fields of catalysis, and this stems from the possible presence of favourable cooperative effects.[4] So in recent years, researchers have become interested in the use of Schiff-base macrocycles given that they possess multiple binding sites,[5] and previous studies in our group have been focusing on the simplest members of this family, the so-called Robson type macrocycles, derived from the [2+2] condensation of a diamine/dianiline with a dialdehyde.[6] In terms of catalysis (ROP of ε-CL), it was observed that beneficial cooperative effects occur when alkylaluminium centres are bound in a specific way to a Schiff-base macrocycle (**LH$_2$**, chart 1 left) derived from the dianiline [(CH$_2$CH$_2$)(2-C$_6$H$_4$NH$_2$)$_2$], whereas the presence of aluminoxane type (Al–O–Al) bonding in such a system proved detrimental.[7] Furthermore, it has been observed that manganese complexes of such macrocycles were far less active with conversions for the ROP of ε-CL < 15 %.[8] In this chapter, the metals cobalt and zinc are studied given their relatively low cost and biocompatibility. Further, it is noted that the use of Zn complexes for the ROP of ε-CL is well established,[3] whilst ROP using Co species are scant.[9]

Recent work by Williams *et al.* has shown how the use of hetero-dinuclear complexes can result in enhanced catalytic performance.[9] In particular, it was reported that an *in-situ* generated catalyst comprising the hetero-dinuclear Zn-Mg complex bearing a diphenolate tetraamine macrocycle (chart 1, right) used in conjunction with its homo-dinuclear Zn-Zn and Mg-Mg counterparts performed better for the copolymerization of CO_2 with epoxides than did the homo-dinuclear complexes alone. Given the very similar solubility properties of the three species, it was not possible to crystallize selectively the Mg-Zn hetero-dinuclear complex. However, subsequent studies by the Williams group have shown that it is possible to access such species via mono-metalation, followed by the addition of the second metal,[10a] and the molecular structures of a number of mixed-metal species were reported.[10b,c] Interestingly, Williams *et al.* also observed that for ROP of ε-CL and *r*-LA, a mixed titanium/zinc system displayed moderate/high activity whilst the mono-titanium system was inactive.[10d] It is also noted here that cooperative effects have also been observed for a homo-dinuclear zinc complex in lactide polymerization.[11]
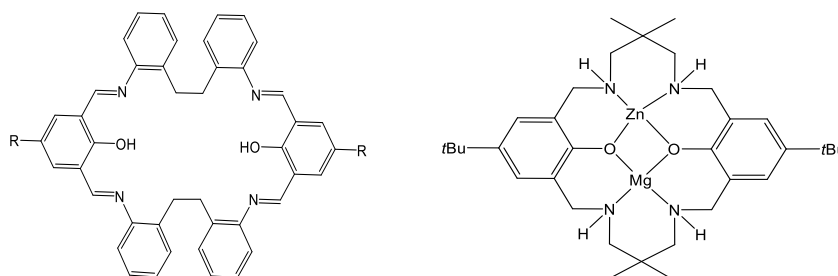
Chart 2-1. Macrocyclic ligand and the Zn-Mg complex reported by Williams *et al.*[10a]

In this chapter, homo-dinuclear cobalt and zinc complexes bearing the macrocycle **L** (**1** - **6**, chart 2-2) are found to be readily accessible. Furthermore, on reacting **1** with $ZnBr_2$ a complex **3** related to **1** was formed differing only in the composition (partial occupancy Co:Zn = 68:32) of the anion, whereas with Et_2Zn, it proved possible to isolate and structurally characterize the mixed-metal cobalt-zinc complexes **7** (chart 2 right). Interestingly, the homo-dinuclear species were inactive when screened for the ROP of ε-

CL (and virtually inactive for δ-VL), whereas the mixed-metal complexes **7** and **8** were efficient catalysts when screened under the same conditions (130 ℃, 24 h). Poly(ε-caprolactone), PCL and PVL are favoured polymers given both their biodegradability, and are considered as potential environmentally friendly commodity plastics.[12] Beyond ROP, Co-Zn species are of interest in gas sensors, semiconductors, dyes and pigments, as well as in other catalytic processes.[13]

$M^1 = M^2 = Co$ **R**=tBu (**1**) or Me (**2**)
$M^1 = Co$, $M^2 = 68\%Co/32\%Zn$ (**3**)
$M^1 = M^2 = Zn$ **R**=tBu (**4**) or Me (**5**)

(**6**)

R=tBu (**7**)
R=Me (**8**)
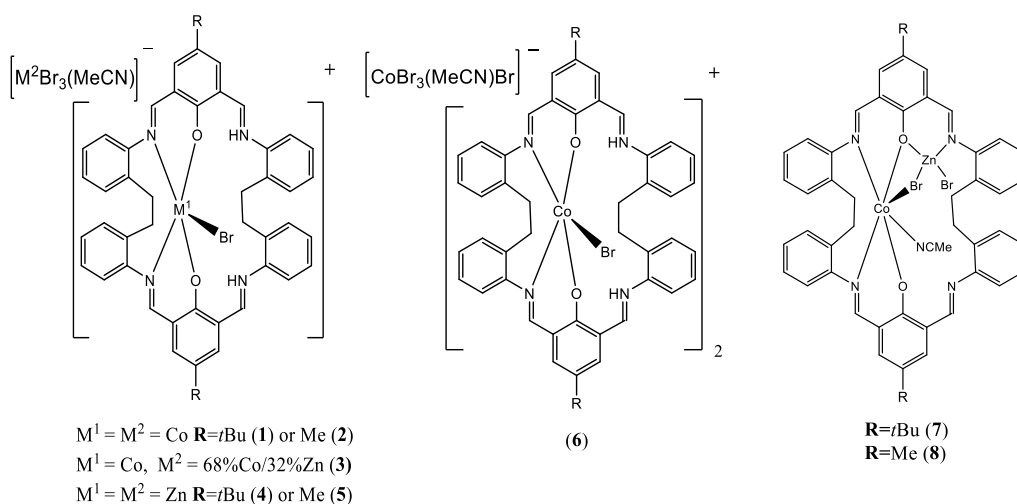
Chart 2-2. Cobalt and zinc complexes **1** – **8** prepared in this chapter.

2.2 Result and discussion

2.2.1 Cobalt compounds

Reaction of the [2+2] Schiff-base macrocycle {[2-(OH)-5-(tBu)-C$_6$H$_2$-1,3-(CH)$_2$][CH$_2$CH$_2$(2-C$_6$H$_4$N)$_2$]}$_2$ with 2.1 equivalents of CoBr$_2$ afforded, following work-up, green prisms on recrystallization from a saturated solution of acetonitrile at 0 ℃ in about 70% yield. The molecular structure of **1**·0.5MeCN is shown in Figure 2-1, with selected bond lengths and angles given in the caption. The complex is a salt of formula [CoBr**L**^{t}Bu}$][CoBr$_3$(NCMe)]·0.5MeCN (**1**·0.5MeCN). In the cation, the cobalt centre is

five-coordinate with a trigonal bipyramidal pattern; the apical sites are occupied by O atoms of phenolates, with the bromide and two N atoms in the equatorial sites. Powder X-Ray diffraction (PXRD) patterns of [(CoBr**L**$^{t\text{Bu}}$] [CoBr$_3$(NCMe)] ·MeCN (**1**·0.5MeCN) was shown in Figure 1-2.
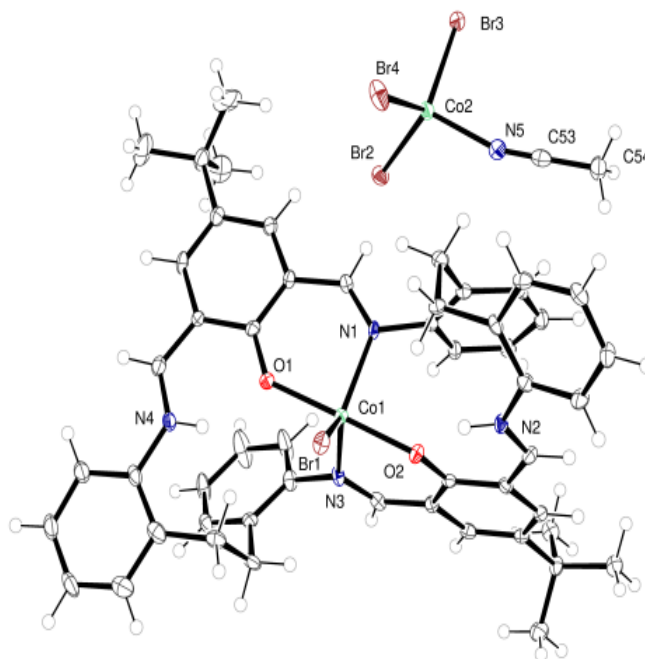
Figure 2-1. Molecular structure of [CoBr**L**$^{t\text{Bu}}$][CoBr$_3$(NCMe)]·0.5MeCN **1**·0.5MeCN. Solvent omitted for clarity. Thermal ellipsoids are drawn at the 30% probability level. Selected bond lengths (Å) and angles (°): Co(1) – Br(1) 2.4847(6), Co(1) – O(1) 2.004(2), Co(1) – O(2) 2.043(2), Co(1) – N(1) 2.088(3), Co(1) – N(3) 2.105(3); O(1) – Co(1) – O(2) 178.52(9), N(1) – Co(1) – N(3) 108.77(11), O(1) – Co(1) – Br(1) 92.98(7), N(3)-Co(1)-Br(1) 128.17(8), N(1)-Co(1)-Br(1) 122.54(8), N(1)-Co(1)-N(3) 108.77(11).
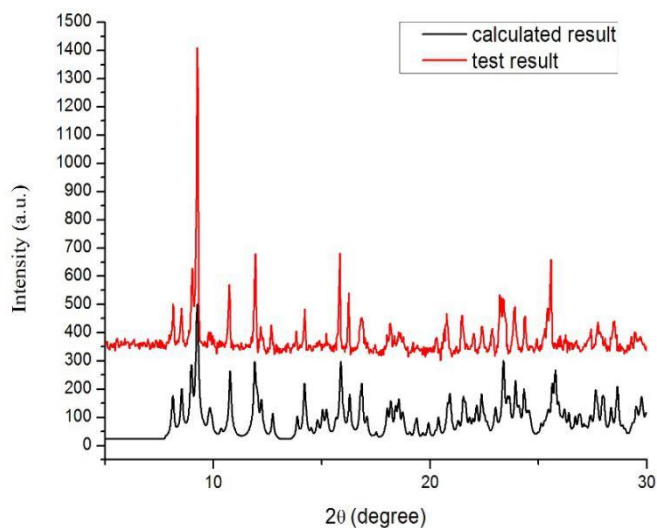
Figure 2-2. Calculated (black lines) and found powder X-Ray diffraction (PXRD) patterns of [(CoBr**L**$^{t\text{Bu}}$] [CoBr$_3$(NCMe)] ·MeCN (**1**·0.5MeCN).
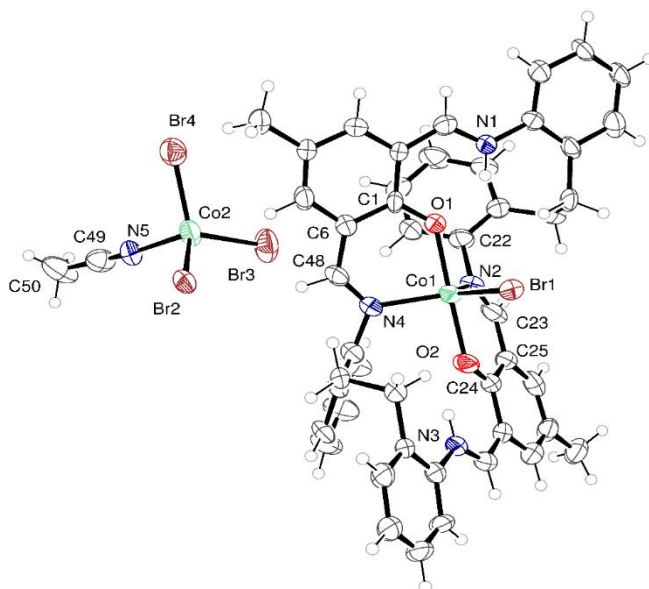
Figure 2-3. Molecular structure of minor orange product [CoBr**L**$^{\text{Me}}$][CoBr$_3$(NCMe)]·4MeCN (**2**·4MeCN). Solvent omitted for Clarity. Selected bond lengths (Å) and angles (o): Co(1) – Br(1) 2.478(2), Co(1) – O(1) 2.025(8), Co(1) – O(2) 2.014(8), Co(1) – N(2) 2.048(11), Co(1) – N(4) 2.063(9); O(1) – Co(1) – O(2) 178.6(3), N(2) – Co(1) – N(4) 114.7(4), O(1) – Co(1) – Br(1) 88.9(2), N(2)-Co(1)-Br(1) 123.9(3)º, N(4)-Co(1)-Br(1) 121.4(3)º.

Similar as the synthesize for complex **1**, reaction of the [2+2] Schiff-base macrocycle {[2-(OH)-5-(*Me*)-C$_6$H$_2$-1,3-(CH)$_2$][CH$_2$CH$_2$(2-C$_6$H$_4$N)$_2$]}$_2$ with 2.1 equivalents of CoBr$_2$ affording complex [CoBr**L^{Me}**][CoBr$_3$(NCMe)]·4MeCN (**2**·4MeCN). The cobalt centre in the cation is five-coordinate as well with a trigonal bipyramidal pattern (Figure 2-3). Powder X-Ray diffraction (PXRD) patterns of **2**·4MeCN was shown in Figure 2-4.
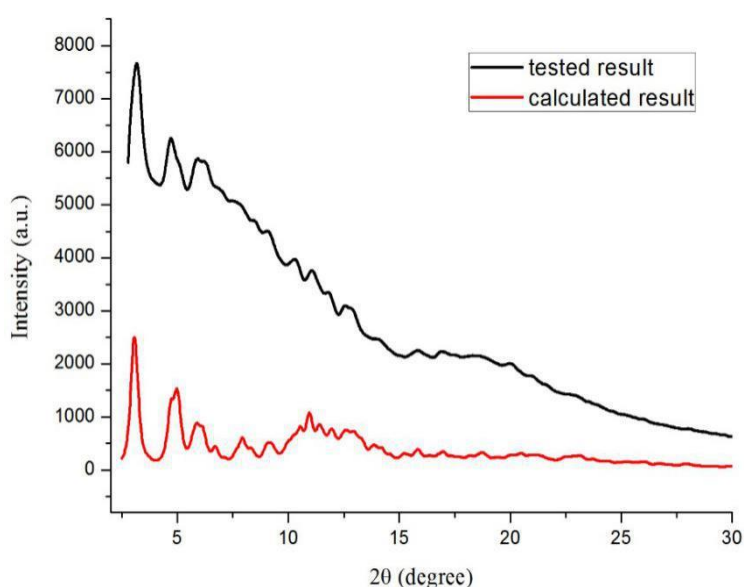
Figure 2-4. X-ray diffraction data collected from a polycrystalline sample of complex **2**·4MeCN using Mo Kα radiated diffraction data from the structure determined by single crystal diffraction.

Another Co complex was synthesized by react complex **1** was reacted with ZnBr$_2$ to afford a yellow product [CoBr**L^{tBu}**][Co$_{0.68}$Zn$_{0.32}$Br$_3$(NCMe)]·0.25MeCN (**3**·0.25MeCN), turned out to be very similar to **1** differing only in the composition of the anion, the latter having cobalt:zinc occupancy 68.4:32.6(17) (Figure 2-5).
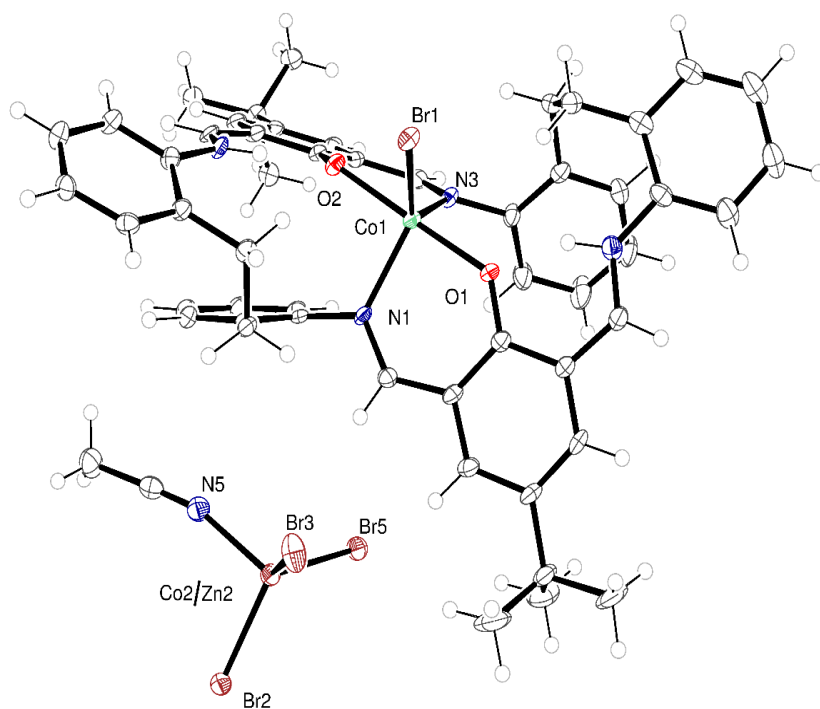
Figure 2-5. Molecular structure of [CoBr**L**^{tBu}][Co$_{0.68}$Zn$_{0.32}$Br$_3$(NCMe)]·0.25MeCN (**3**·0.25 MeCN) Solvent omitted for clarity. Thermal ellipsoids are drawn at the 30% probability level. Selected bond lengths (Å) and angles (°): Co(1)–Br(1) 2.4847(6), Co(1)–O(11) 2.004(2), Co(1)–O(14) 2.043(2), Co(1)–N(37) 2.105(3), Co(1)–N(67) 2.088(3); O(11)–Co(1)–O(41) 178.52(9), N(37)–Co(1)–N(67) 108.77(11), O(11)–Co(1)– Br(1) 92.98(7), N(3)–Co(1)–Br(1) 127.99(8), N(1)–Co(1)–Br(1) 122.75(9), N(1)–Co(1)– N(3) 108.72(11)°.

Concentration of the mother-liquor afforded more of **1**·0.5MeCN plus small amounts of an orange/red product, identified as [CoBr**L**^{tBu}]$_2$[CoBr$_3$(NCMe)][Br]·4.5MeCN (**4**·4.5MeCN), the structure of which is similar to that observed for **1**·0.5MeCN, differing mainly in the composition of the anions, namely Br$^-$ and CoBr$_3$(NCMe)$^-$; the molecular structure is shown in Figure 2-6.
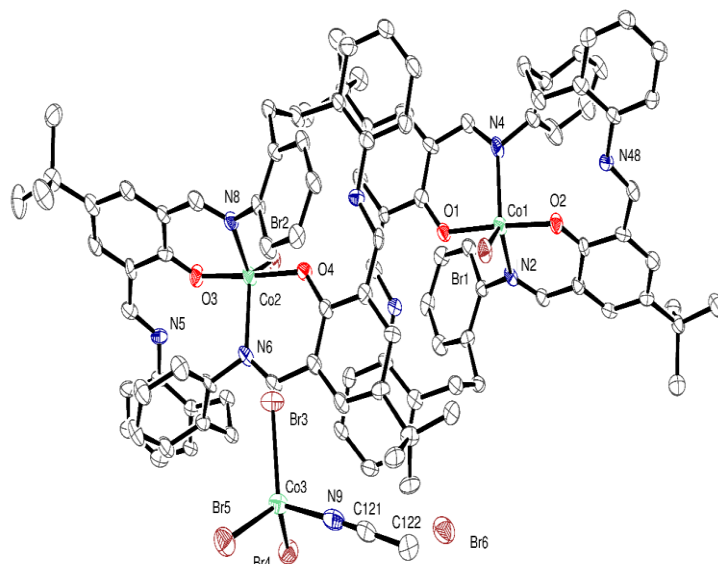
Figure 2-6. Molecular structure of minor orange product [CoB**rL**^{tBu}]$_2$[CoBr$_3$(NCMe)]

[Br]·4.5MeCN (**6**·4.5MeCN). Solvent omitted for Clarity. Selected bond lengths (Å) and

angles (°): Co(1)–Br(1) 2.4874(12), Co(1)–O(1) 2.041(4), Co(1)–O(2) 2.009(4), Co(1)–

N(2) 2.072(6), Co(1)–N(4) 2.081(6); O(1)–Co(1)–O(2) 176.64(19), N(2)–Co(1) – N(4)

110.3(2), O(1)–Co(1)–Br(1) 86.10(15), Co(2)–Br(2) 2.4917(14), Co(2)–O(3) 2.009(6),

Co(2)–O(4) 2.018(6), Co(2)–N(6) 2.085(7), Co(2)–N(8) 2.077(7); O(3)–Co(2)–O(4)

175.9(2), N(6)–Co(2)– N(8) 108.5(3), O(3)–Co(2)–Br(2) 88.77(18).

2.2.2 Zinc compounds

Reaction of **L**H$_2$ {[2-(OH)-5-(*t*Bu)-C$_6$H$_2$-1,3-(CH)$_2$][CH$_2$CH$_2$(2-C$_6$H$_4$N)$_2$]}$_2$ with 2.1

equivalents of ZnBr$_2$ afforded, following work-up, yellow prisms of

[Zn**L**^{tBu}Br][(ZnBr$_3$NCMe)]·MeCN (**5**·MeCN) (Figure 2-7) in good yield. Use of excess

ZnBr$_2$ (> 4 equivalents) also afforded **5**·MeCN as the only crystalline product. Powder

X-Ray diffraction (PXRD) patterns and ^{1}HNMR spectrum of **5**·MeCN were shown in

43

Figure 2-8 and Figure 2-9. Again, the structure is very reminiscent of **1**·0.5MeCN, with the zinc adopting a trigonal bipyramidal geometry in the cation. Similar reaction of {[2-(OH)-5-(*Me*)-C$_6$H$_2$-1,3-(CH)$_2$][CH$_2$CH$_2$(2-C$_6$H$_4$N)$_2$]}$_2$ with 2.1 equivalents of ZnBr$_2$ affording [ZnBr**L^{Me}**][ZnBr$_3$(NCMe)]·MeCN (**6**·MeCN) shown in Figure 2-10. The structures of **5** and **6** are note as analogous to the equivalent manganese complex (see CUVYID in CCDC).[7c] The ^{1}H NMR spectrum of **6**·MeCN is shown in Figure 2-11.
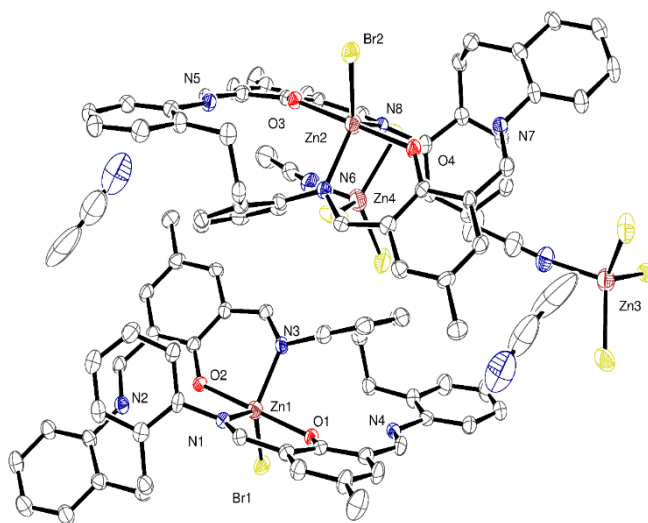
Figure 2-7. Molecular structure of [ZnBr**L^{tBu}**][ZnBr$_3$(NCMe)]·MeCN (**5**·MeCN). Solvent omitted for clarity. Solvent omitted for Clarity. Thermal ellipsoids are drawn at the 30% probability level. Selected bond lengths (Å) and angles (º): Zn(1) – Br(1) 2.4502(4), Zn(1) – O(1) 2.0464(17), Zn(1) – O(2) 2.0383(16), Zn(1) – N(1) 2.107(2), Zn(1) – N(3) 2.117(2); O(1) – Zn(1) – O(2) 178.70(7), N(1) – Zn(1) – N(3) 110.37(8), O(1) – Zn(1) – Br(1) 92.86(5), N(3)-Zn(1)-Br(1), 126.86(6), N(1)-Zn(1)-Br(1) 122.65(6), N(1)-Zn(1)-N(3) 110.37(8).
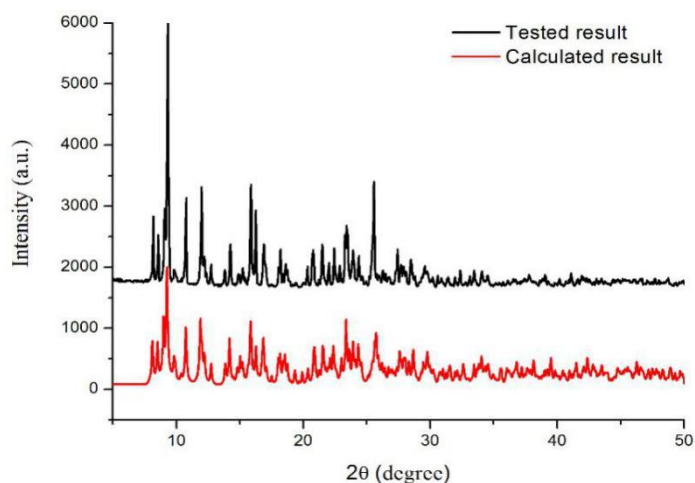
Figure 2-8. Calculated (black lines) and found powder X-Ray diffraction (PXRD) patterns of [(Zn**L**$^{t\text{Bu}}$Br)][ZnBr$_3$(NCMe)]·MeCN (**5**·MeCN).
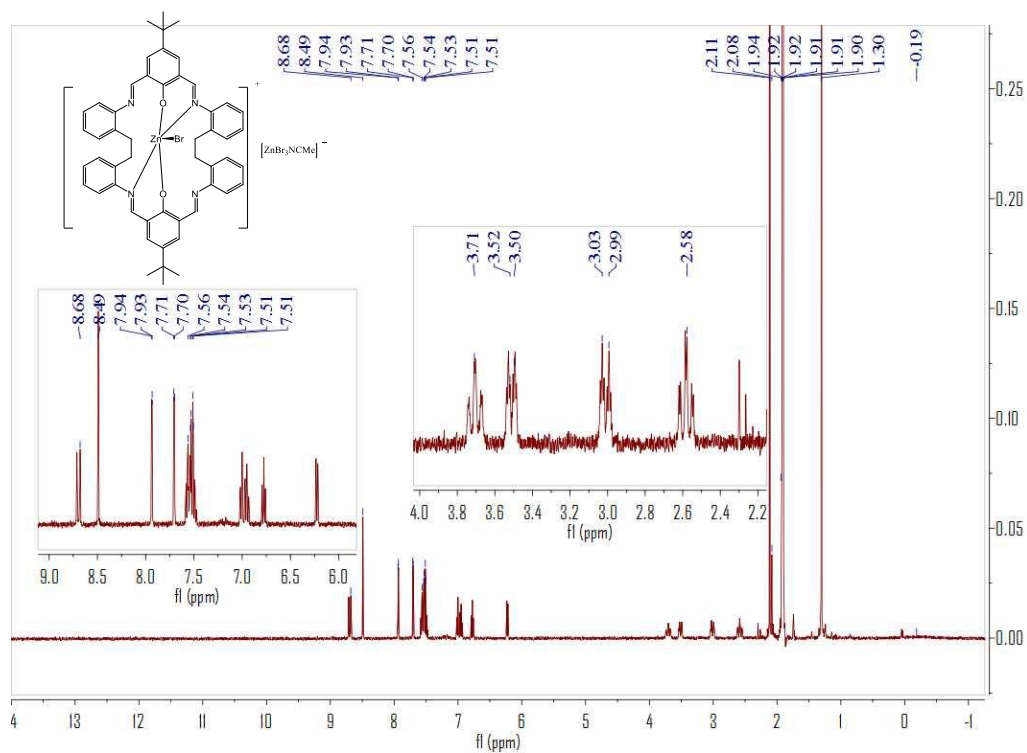
Figure 2-9. ^{1}H NMR (400 MHz CDCl$_3$) spectrum for **5**·MeCN**.**
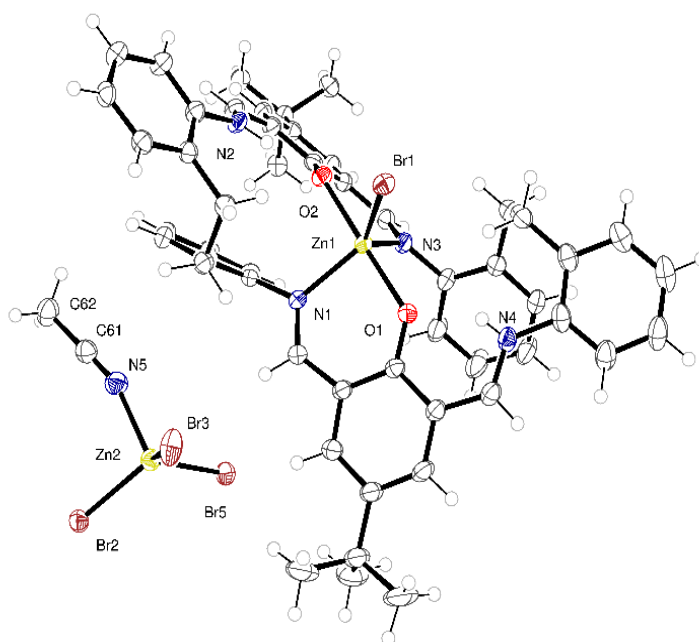
Figure 2-10. Molecular structure of [ZnBr**L**$^{\text{Me}}$][ZnBr$_3$(NCMe)]·MeCN (**6**·MeCN). Thermal ellipsoids are drawn at the 30% probability level. Selected bond lengths (Å) and angles (º): Zn(1)–Br(1) 2.4344(9), Zn(1)–O(1) 2.077(4), Zn(1)–O(2) 2.085(4), Zn(1)–N(1) 2.082(5), Zn(1)–N(3) 2.061(5); O(1)–Zn(1)–O(2) 179.74(18), N(1)–Zn(1)–N(3) 112.93(19), O(1)–Zn(1)–Br(1) 89.27(11), N(3)–Zn(1)–Br(1) 120.14(14), N(1)–Zn(1)–Br(1) 126.92(13)º.
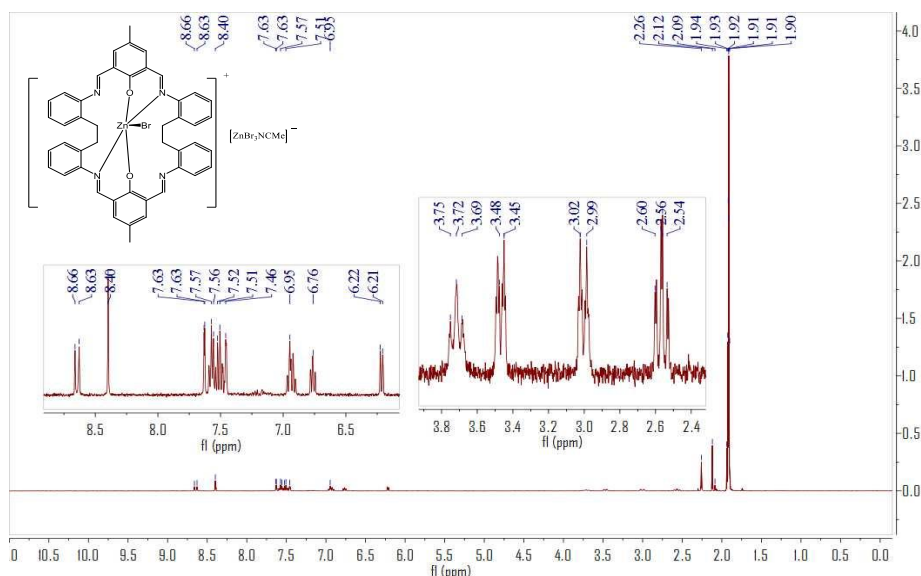
Figure 2-11. ^{1}H NMR (400 MHz CDCl$_3$) spectrum for **6**·MeCN.

2.2.3 Cobalt & Zinc compounds

To **1** was added Et$_2$Zn and refluxing in THF overnight after recrystallization affording large red/brown prisms of **7**·3.25MeCN. The molecular structure of **7**·3.25MeCN is shown in Figure 2-12, with bond lengths/angles given in the caption; for the analogous product using **L^{Me}H$_2$**, namely **8**·3MeCN, see Figure 2-14. In the asymmetric unit of **7**·3.25MeCN, there are four molecules of the complex and 13 solvent molecules. The macrocycle binds two metals (Co and Zn) in an ordered way. The Co^{2+} is bound in distorted octahedral geometry by two *cis* phenolates and two *cis* imines of the macrocycle, a rather distant bromide (Co(1)-Br(1) 2.9383(5) Å), and a single molecule of acetonitrile.
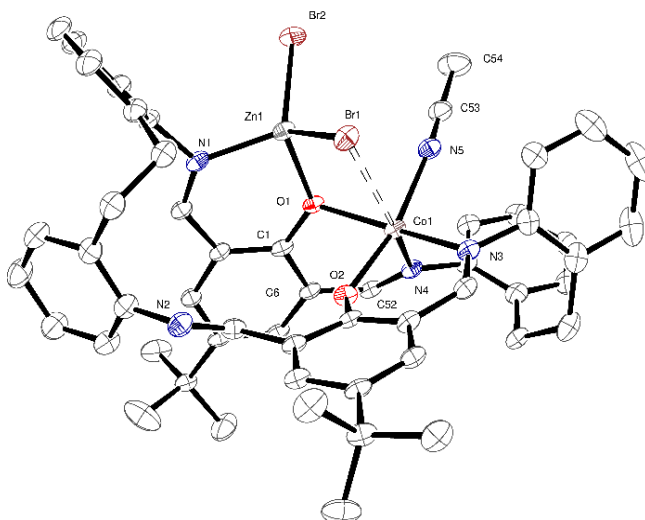
Figure 2-12. The molecular structure of [**L^{tBu}**Co(NCMe)(μ-Br)ZnBr]·3.25MeCN (**7**·3.25MeCN). Solvent omitted for clarity. Thermal ellipsoids are drawn at the 30% probability level. Selected bond lengths (Å) and angles (°): Co(1) – O(1) 2.133(2), Co(1) – O(2) 1.947(2), Co(1) – N(3) 2.058(2), Co(1) – N4) 2.126(2), Co(1) – N(5) 2.108(3), Zn(1) – Br(1) 2.3873(4), Zn(1) – Br(2) 2.3412(5), Zn(1) – O(1) 1.9792(19), Zn(1) – N(1) 2.015(3); Co(1) – O(1) – Zn(1) 103.93(8), N(3) – Co(1) – N(4) 107.92(9), O(2) – Co(1) – N(3)90.50(9), O(2) – Co(1) – N(5) 167.52(9), O(1) – Zn(1) – N(1) 93.30(9), Br(1) – Zn(1) – Br(2) 113.655(18).

The Zn ion is in close proximity to the Co ion: the bromide and one of the phenolates each coordinate to the Zn. The tetrahedral coordination about the Zn is completed by an imine and a mono-dentate bromide. One might describe the octahedron of Co(1) and the tetrahedron around Zn(1) as sharing a common edge (O(1) and Br(1)). The two metals are separated at a distance 3.2399(5) Å. Powder XRD data of **7**·3.25MeCN are shown in Figure 2-13. The magnetic moments of **7** and **8** (5.1 – 5.3) are consistent with high spin Co(II) complexes.[14]
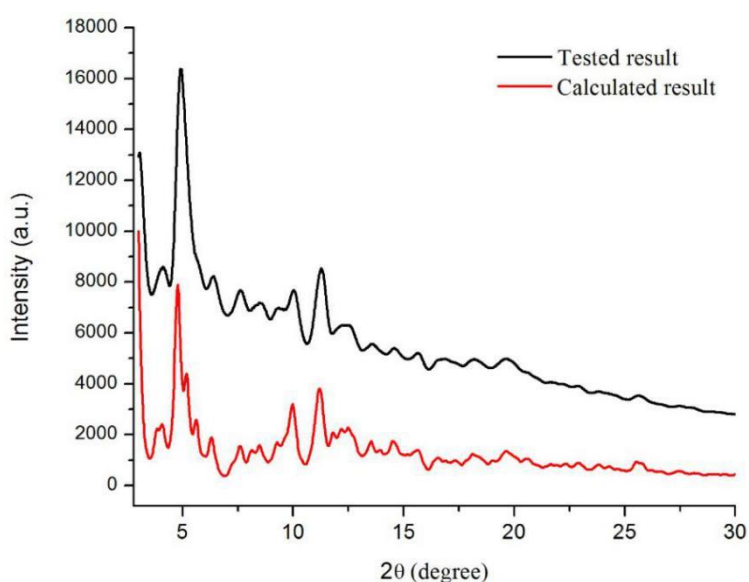
Figure 2-13. X-ray diffraction data collected from a polycrystalline sample of complex **7**·3.25MeCN using Mo Kα radiation and simulated diffraction data from the structure determined by single crystal diffraction.
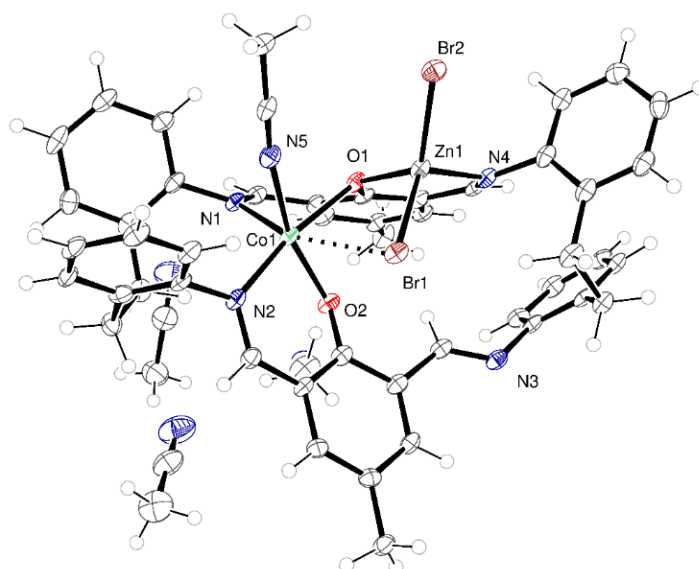
Figure 2-14. Molecular structure of [CoL**Me** (NCMe)(µ-Br)ZnBr]·3MeCN (**8**·3MeCN). Selected bond lengths (Å) and angles (°): Co(1) – O(1) 2.154(3), Co(1) – N(1) 2.108(3), Co(1) – N(2) 2.071(3), Co(1) – Br(1) 2.964(7), Zn(1) – O(1) 1.981(3), Zn(1) – Br(1) 2.3956(6), Zn(1) – Br(2) 2.3418(6), Zn(1) – N(4) 2.024(3); N(1) – Co(1) – N(2) 107.09(13), N(2) – Co(1) – O(2) 89.21(13), O(2) – Co(1) – N(5) 164.35(13), Co(1)-O(1)-Zn(1) 102.68(12)°, O(1)-Zn(1)-N(4) 93.72(13)°, Br(1)-Zn(1)-Br(2) 113.90(2)°.
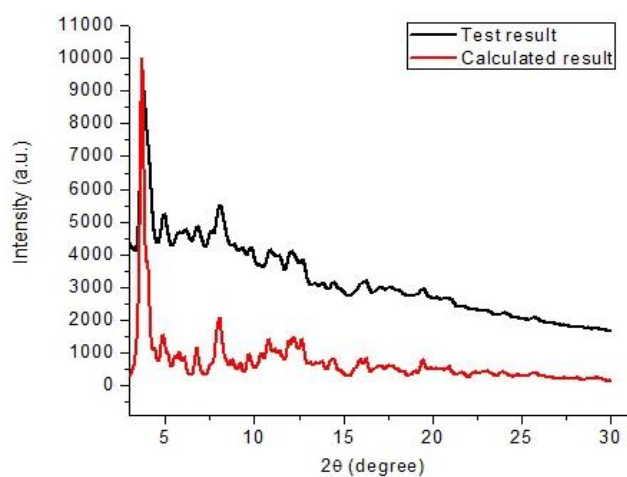
Figure 2-15. X-ray diffraction data collected from a polycrystalline sample of complex **8**·3MeCN using Mo Kα radlated diffraction data from the structure determined by single crystal diffraction.

2.2.4 Ring opening polymerization

To our knowledge, Co complexes is not an ideal catalyst towards Ring opening polymerization, whereas, several Zn complexes has been published as the catalyst for ROP reaction towards ε-CL or r-LA which got a similar M_w range as we did.[15-18]

The cobalt and zinc complexes **1**, **3**, **7** and **8** have been screened for their ability to ring open polymerize δ-VL and ε-CL exhibit in Table 2-1 and Table 2-2, respectively; runs were conducted in the presence of benzyl alcohol (BnOH).

Table 2-1. ROP of δ-VL using complexes.

Run	Cat.	[δ-VL]:[Cat] :BnOH	T (℃)	t(h)	Conv. (%)[a]	M_n ×10³[b]	M_{nCal} ×10⁴[c]	PDI[d]
1	**7**	50:1:1	130	24	75.7	0.73	0.38	1.24
2	**7**	100:1:1	130	24	92.8	2.14	0.93	1.15
3	**7**	250:1:1	130	24	98.7	5.19	2.46	1.22
4	**7**	500:1:1	130	24	99.2	4.13	4.96	1.23
5	**7**	1000:1:1	130	24	45.9	0.70	4.59	1.35
6	**7**	500:1:1	130	12	92.7	0.45	4.64	1.53
7	**7**	500:1:1 (melt）	130	24	96.2	7.11	4.82	1.79
8	**8**	50:1:1	130	24	28.4	-	0.14	-
9	**8**	100:1:1	130	24	30.7	-	0.31	-
10	**8**	250:1:1	130	24	97.0	2.68	2.43	1.30
11	**8**	500:1:1	130	24	87.2	2.84	4.36	1.28
12	**8**	1000:1:1	130	24	55.8	3.54	5.58	1.18
13	**8**	500:1:1	130	12	45.2	-	2.26	-

14	**8**	500:1:1 (melt）	130	24	85.3	3.21	4.27	1.16
15	**1**	500:1:1	130	24	38.8	0.45	1.94	1.42
16	**4**	500:1:1	130	24	4.4	-	0.22	-

[a] By ^{1}H NMR spectroscopic analysis. [b] M_n values were determined by GPC in THF *vs* PS standards and were corrected with a Mark-Houwink factors (0.58 for poly(δ-VL) [c] (F.W.[M]/[BnOH])(conversion) [d] Polydispersity index (M_w/M_n) were determined by GPC.

Data for runs is given in Table 2-1 reveals that **7** out-performs **8**, which is thought to be due to the increased solubility of the former in the reaction solvent. Highest conversion was achieved with the ratio 500:1:1, with all the runs showing good control with PDIs in range 1.15-1.30. Use of either 12h (run 6) or no solvent (i.e. a melt, run 7) was less controlled. For complexes **1** and **3**, a variety of conditions were used in the attempted ROP of δ-VL including temperatures in the range 40 to 130 ℃, differing ratios of [δ-VL]:[Cat]:[BnOH] and over different times, however on each occasion there was no sign of polymer upon work-up. However, for the mixed-metal systems, activity was observed when the temperature reached 130 ℃, in the presence of one equivalent of BnOH (at this temperature, no activity was observed for **1** and **3** – see figure 1-16 for the relative rates of the *t*Bu derivatives).

From a kinetic study (see Figure 2-16), it was observed that the polymerization rate exhibited near first order dependence of the CL concentration at 130 °C. The rate of polymerization for ϵ-CL ($K_{obs}=2.12\times10^{-3}(h^{-1})$ for **7**) was less than half that for δ-VL ($K_{obs}=6.10\times10^{-3}(h^{-1})$ for **7**), which is consistent with other reports.[16]
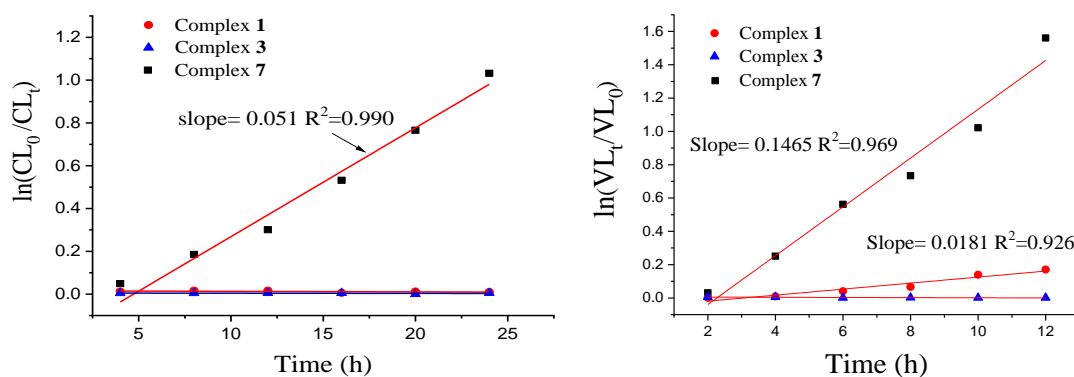
Figure 2-17. Plot of $\ln[VL]_0/[VL]_t$ *vs*. time and $\ln[CL]_0/[CL]_t$ *vs*. time using complex **1**, **3** and **7** ([monomer]:[Cat]:BnOH=500:1:1; 130 °C.

Analysis of the polymer indicated the presence of benzyloxy and hydroxyl end groups (Figure 2-20, Figure 2-21). There was evidence of significant transesterification and all observed M_n values were significantly lower than the calculated values. The MALDI-TOF spectra could be interpreted using the formula $C_6H_6\text{-}CH_2O[O(CH_2)_3CO]_nOH$ for example in the case of **7** at 130 °C (Figure 2-18, Figure 2-19). In the case of ε-CL, the situation was more pronounced with no conversion evident by ^1H NMR spectroscopy for catalyst systems **1** and **4**. By contrast, systems using **7** and **8** were efficient catalysts at 130 ºC, with best results observed using the ratio 500:1:1; below this temperature only trace polymer was observed. Most of the PDI of polycaprolactone are narrow, except for run 1(ratio 50:1:1). As for the δ-VL runs, good control was observed, except for when using either 12h or a melt.
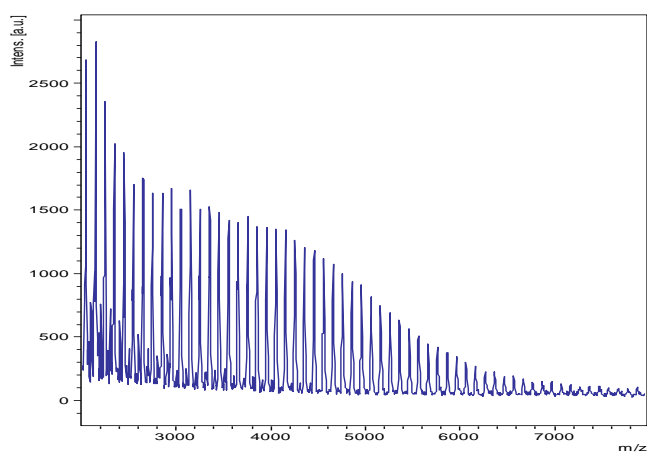
Figure 2-18. MALDI-ToF mass spectrum for PVL (δ-VL run 2, Table 2-1).
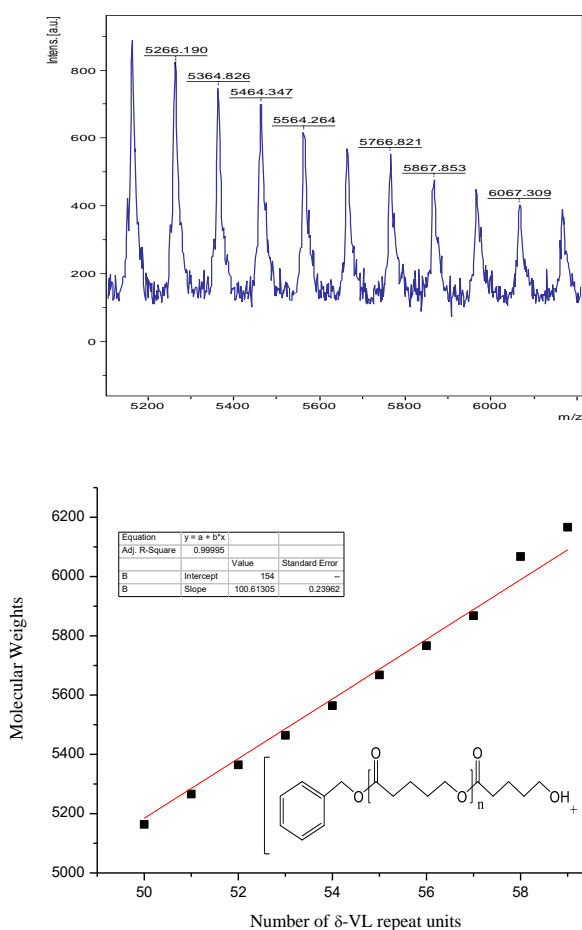
Figure 2-19. *M*$_w$ *vs* number of δ-VL repeat units (n) afforded a straight line with a slope of 100.6 and an intercept of 154; the slope corresponds to the exact mass of the δ-VL monomer, whereas the intercept corresponds to a polymer chain structure with benzyloxy chain-ends plus 2Na$^+$ (δ-VL run 2 Table 2-1).
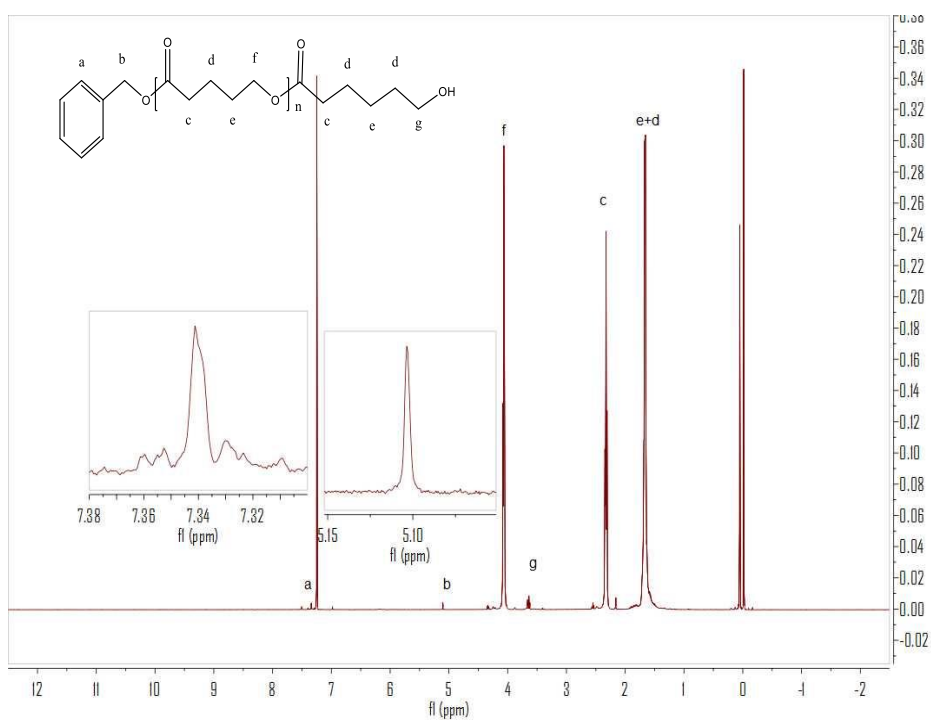
Figure 2-20. ^{1}H NMR (400 MHz, CDCl$_3$) spectrum for polymer (δ-VL run 3, Table 2-1).
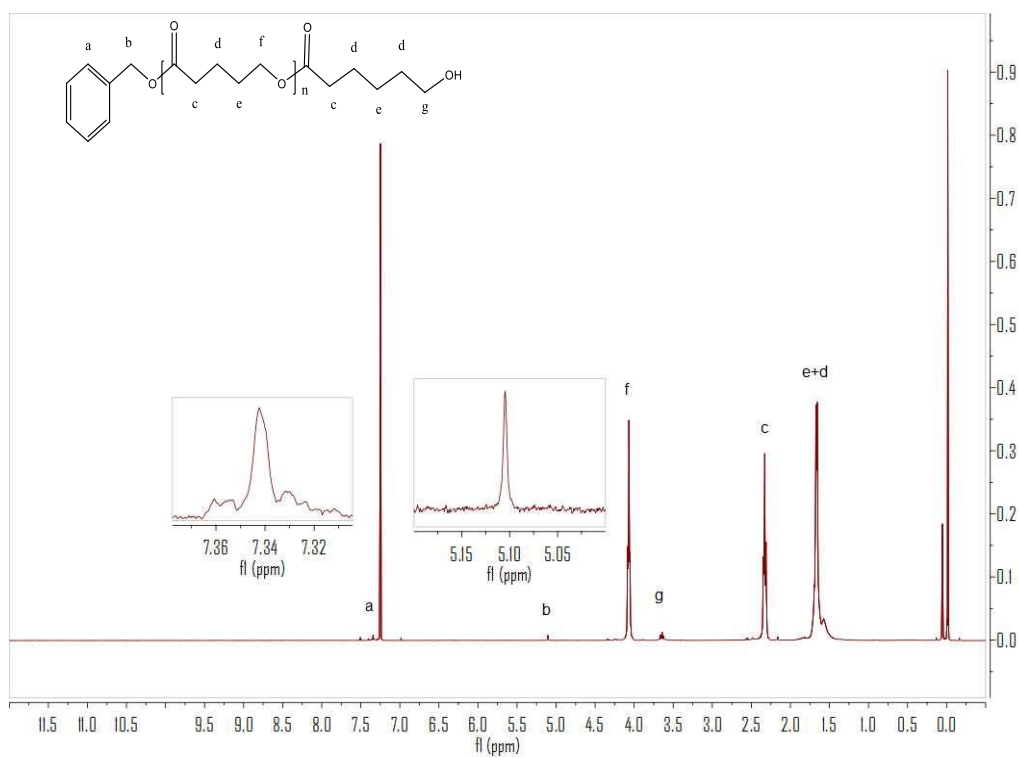
Figure 2-21. ^{1}H NMR (400 MHz, CDCl$_3$) spectrum for polymer (δ-VL run 4, Table 2-1).

Table 2-2. ROP of ε-CL using complexes.

Run	Cat.	[ε-CL]:[Cat]:BnOH	T(℃)	t/h	Conv.(%)^a	$Mn\times10^{3b}$	$Mn_{Calcd}\times10^{4c}$	PDI
1	7	50:1:1	130	24	99.7	5.40	0.57	2.14
2	7	100:1:1	130	24	99.6	7.35	1.01	1.38
3	7	250:1:1	130	24	99.0	1.16	2.84	1.10
4	7	500:1:1	130	24	99.8	5.90	5.05	1.15
5	7	1000:1:1	130	24	99.4	1.74	8.19	1.29
6	7	500:1:1	130	12	48.0	2.28	2.74	1.80
7	7	500:1:2	130	24	99.4	1.39	2.84	1.10
8	7	500:1:1 (melt)	130	24	98.2	7.87	4.98	1.66
9	7	500:1:1	70	24	98.9	-	5.63	-
10	7	500:1:1	40	24	99.1	-	5.64	-
11	8	100:1:1	130	24	99.9	4.82	1.01	1.75
12	8	250:1:1	130	24	58.2	3.68	1.67	1.12
13	8	500:1:1	130	24	52.1	3.53	2.98	1.16
14	1	500:1:1	130	24	-	-	-	-
15	2	500:1:1	130	24	-	-	-	-

^{a} By ^{1}H NMR spectroscopic analysis. ^{b} M_n values were determined by GPC in THF vs PS standards and were corrected with a Mark-Houwink factors (0.56 for poly(ε-CL) ^{c} (F.W.[M]/[BnOH])(conversion) ^{d} Polydispersity index (M_w/M_n) were determined by GPC.
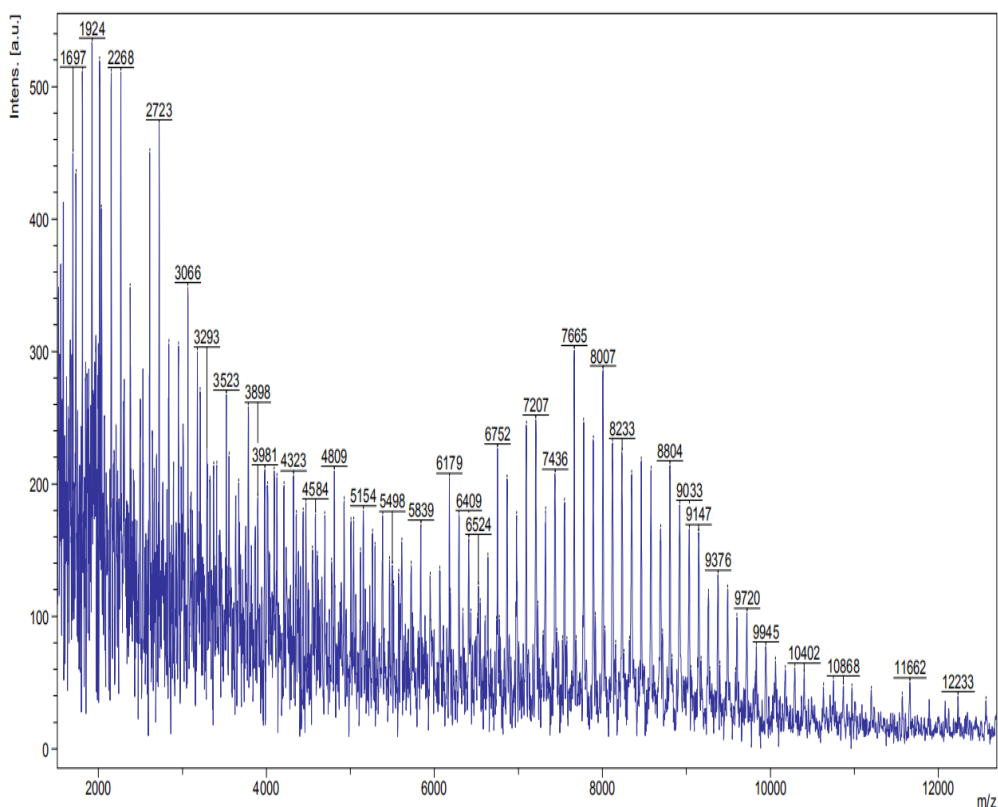
Figure 2-22. MALDI-ToF mass spectrum for polymer (ε-CL run 2, Table 2-2).

The observed molecular weights were lower than the calculated values, suggesting the presence of a chain transfer agent (H_2O or BnOH). This was also evident in the MALDI-TOF mass spectra, were a number of families of peaks were observed separated by 114 mass units (Figure 2-22, Figure 2-23). For example, in the case of **7** (run 4, table 2), peaks in the spectrum can be assigned to 4926, 5039, and 5154 using the formula C_6H_5-$CH_2O[O(CH_2)_4CO]_nOH$ for n = 42, 43 and 44 respectively.
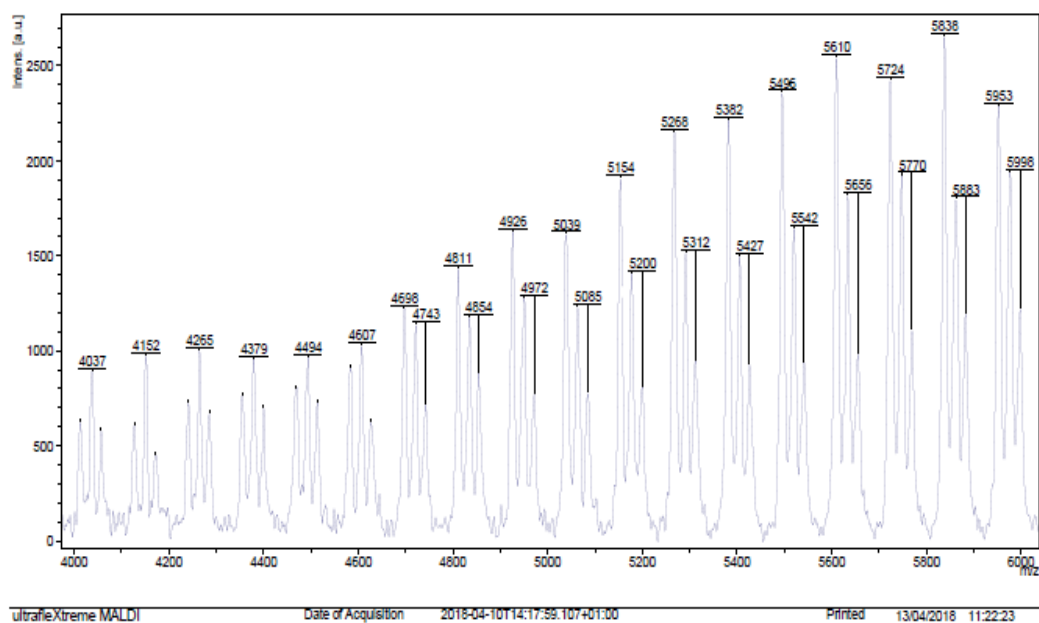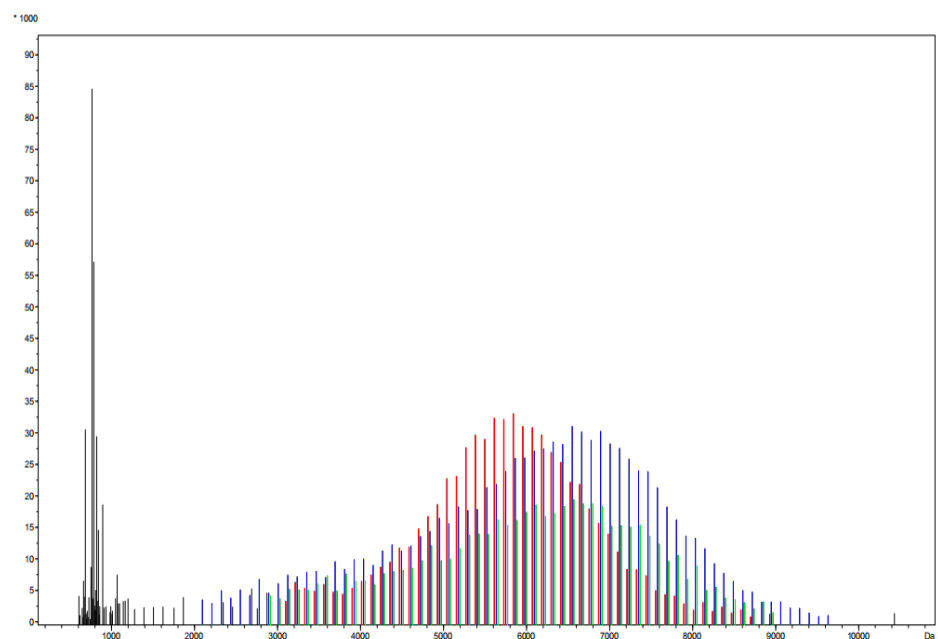
Figure 2-23. MALDI-ToF mass spectrum for PCL (ε-CL run 4, Table 2-2).
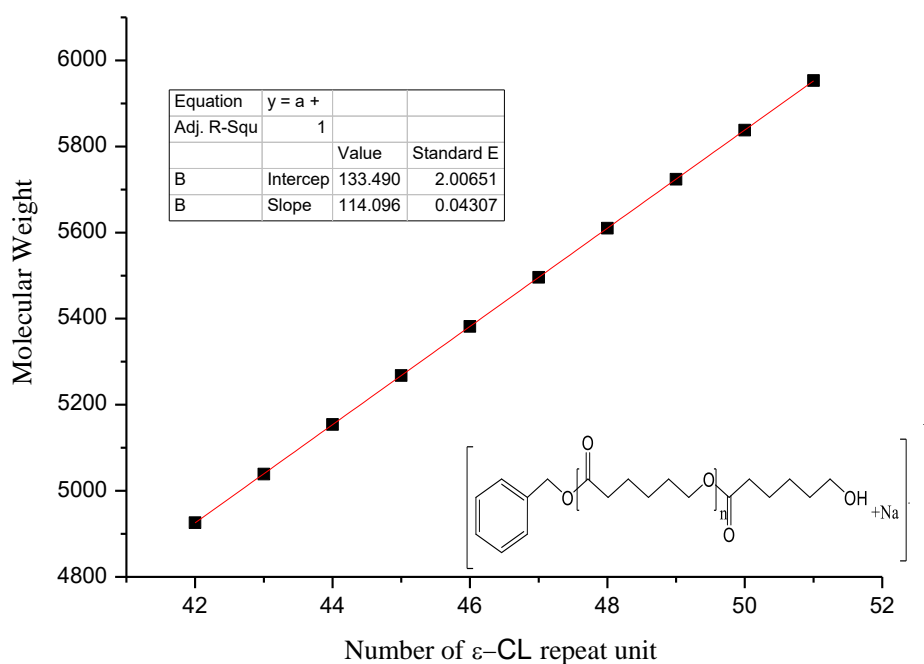
Figure 2-24. M_w vs number of ε-CL repeat units (n) afforded a straight line with a slope of 114.10 and an intercept of 133; the slope corresponds to the exact mass of the ε-CL monomer, whereas the intercept corresponds to a polymer chain structure with benzyloxy chain-ends plus one Na^+ (ε-CL run 4). The other families of peaks observed represent addition of $2Na^+$ and $3Na^+$ to the formula respectively.
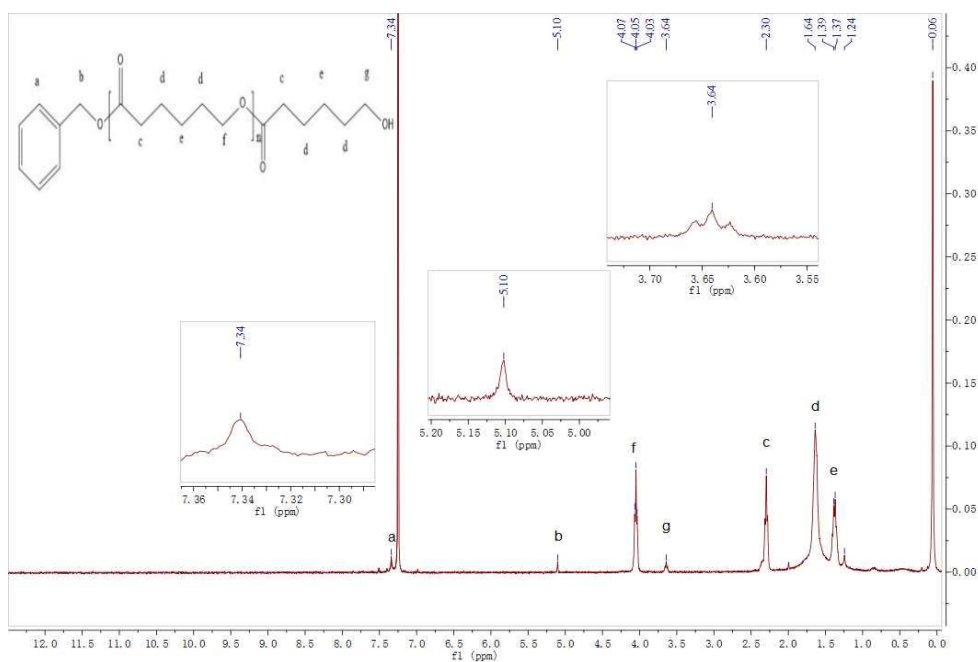
Figure 2-25. ^1H NMR (400 MHz, $CDCl_3$) spectrum for the PCL polymer (run 2, Table 2-2).
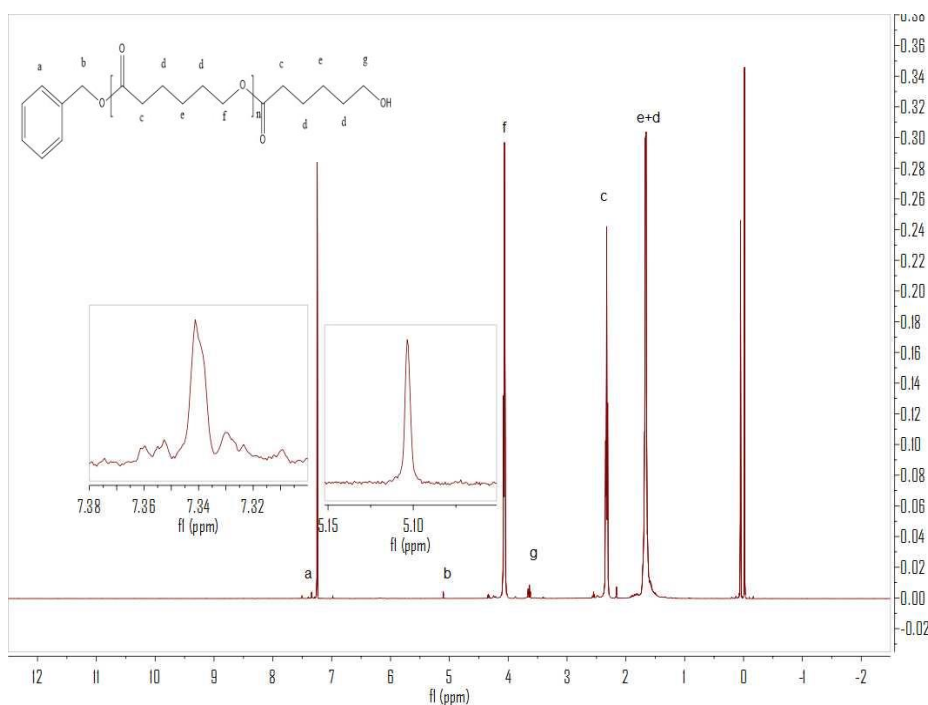
Figure 2-26. ^{1}H NMR (400 MHz, CDCl$_3$) spectrum for PCL polymer (run 4, Table 2-2).

The ^{1}H NMR spectra of the PCL (e.g. Figure 2-25 and Figure 2-26) revealed the presence of benzyloxy and OH end groups.

2.3 Conclusion

In conclusion, homo-dinuclear cobalt and zinc complexes as well as rare examples of mixed-metal (Co/Zn) complexes of a [2+2] macrocyclic Schiff-base were isolated and structurally characterized. Screening of these complexes for the ROP of the cyclic esters δ-valerolactone (δ-VL) and ε-caprolactone (ε-CL) revealed that whilst the homo-dinuclear complexes are either virtually inactive (δ-VL) or inactive (ε-CL), the mixed-metal systems are efficient catalysts at 130 ℃, suggestive that the metals are able to 'turn each other on'.

2.4 References

[1] A. C. Albertsson and I. K. Varma, *Biomacromolecules* 2003, *4*, 1466-1486.

[2] P. Villarrubia-Gómez, S. E. Cornell and J. Fabres, *Marine Policy*, 2018, *96*, 213-220.

[3] See for example (a) O. Dechy-Cabaret, B. Martin-Vaca and D. Bourissou, *Chem. Rev.*, 2004, *104*, 6147–6176; (b) M. Labet and W. Thielemans, *Chem. Soc. Rev.*, 2009, *38*, 3484–3504; (c) C. M. Thomas, *Chem. Soc. Rev.*, 2010, *39*, 165–173; (d) A. Arbaoui and C. Redshaw, *Polym. Chem.*, 2010, *1*, 801– 826; (e) Y. Sarazin, J.-F. Carpentier, *Chem. Rev.* 2015, *115*, 3564−3614 and references therein.

[4] See for example, (a) S. K. Mandal, H. W. Roesky, *Acc. Chem. Res.*, 2010, *43*, 248-259; (b) M. Delferro, T. J. Marks, *Chem. Rev.*, 2011, *111*, 2450–2485; (c) J. P. McInnis, M. Delferro, T. J. Marks, *Acc. Chem. Res.*, 2014, *47*, 2545-2557; (d) I. Bratko, M. Gómez, *Dalton Trans.*, 2013, *42*, 10664-10681.

[5] (a) N. H. Pilkington, R. Robson, *Aust. J. Chem.*, 1970, *23*, 2225–2236; (b) M. Bell, A. J. Edwards, B. F. Hoskins, E. H, Kachab, R. Robson, *J. Am. Chem. Soc.*, 1989, *111*, 3603–3610.

[6] (a) A. Arbaoui, C. Redshaw, D. L. Hughes, *Chem. Commun.*, 2008, 4717; (b) A. Arbaoui, C. Redshaw, D. L. Hughes, *Supramol. Chem.*, 2009, *21*, 35; (c) W. Yang, K. -Q. Zhao, B. –Q. Wang, C. Redshaw, M. R. J. Elsegood, J. -L. Zhao, T. Yamato, *Dalton Trans.*, 2016, *45*, 11990-12005.

[7] W. Yang, K.-Q. Zhao, B.-Q. Wang, C. Redshaw, M. R. J. Elsegood, J. -L. Zhao and T. Yamato, *Dalton Trans.*, 2016, *45*, 226–236.

[8] F. H. Allen, *Acta Crystallogr. Sect. B: Struct. Sci.*, 2002, *58*, 380.

[9] P.K. Saini, C. Romain, C. K. Williams, *Chem. Commun.*, 2014, *50*, 4164-4167.

[10] (a) J. F. Garden, P. K. Saini, C. K. Williams, *J. Amer. Chem. Soc.*, 2015, *137*, 15078-15081. (b) J. F. Garden, A. J. P. White, C. K. Williams, *Dalton Trans.*, 2017, *46*, 2532-2541; (c) A. C. Deacy, C. B. Durr, J. F. Garden, A. J. P. White, C. K. Williams, *Inorg. Chem.*, 2018, *57*, 15575-15583. (d) G. Trott, J. F. Garden, C. K. Williams, *Chem. Sci.*, 2019, *10*, 4618-4627.

[11] A. Thevenon, C. Romain, M. S. Bennington, A. J. P. White, H. J. Davidson, S. Brooker, C. K. Williams, *Angew Chem. Int. Ed.*, 2016, 55, 8680-8685.

[12] See for example, (a) M. A. Woodruff and D. W. Hutmacher, *Prog. Polym. Sci.*, 2010, *35*, 1217-1256; (b) Y. F. Al-Khafaji and F. H. Hussein in *Green and Sustainable Advanced Materials: Processing and Characterization*, Eds. S. Ahmed and C. M. Hussain, Wiley, 2018, Chapter 6.

[13] (a) T. Baird, K. C. Campbell, P. J. Holliman, R. W. Hoyle, D. Stirling, B. P. Williams, M. Morris, *J. Mater. Chem.*, 1997, *7*, 319–330; (b) X. Niu, W. Du, W. Du, *Sens. Actuators B*, 2004, *99*, 405–409; (c) N. H. Perry, T. O. Mason, C. Ma, A. Navrotsky, Kondrat, T. E. Davies, D. J. Morgan, D. I. Enache, G. B. Combes, S. H. Taylor, J. K. Bartley, G. J. Hutchings, *Catal. Sci. Technol.*, 2014, *4*, 1970-1978.

[14] K. Makiguchi, T. Satoh, T. Kakuchi, *Macromolecules,* 2011, *44*, 1999–2005.

[15] J. Wojtaszak, K. Mierzwicki, S. Szafert, N. Gulia and J. Ejfler, *Dalton Trans.*, 2014, *43(6)*, 2424-2436.

[16] C. Fliedel, V. Rosa, F. M Alves, A. M. Martins, T. Avilés and S. Dagorne, *Dalton Trans.*, 2015, 44(27), 12376-12387.

[17] C. H. Tran, L. T. T. Pham, Y. Lee, H. B. Jang, S. Kim and I. Kim, *J. Catal.*, 2019, 372, 86-102.

[18] E. D. Akpan, S. O. Ojwach, B. Omondi and V. O. Nyamori, *New J. Chem.*, 2016, 40(4), 3499-3510.

Chapter 3 . Schiff base [2+2] macrocycles derived from the dianiline [(2-NH$_2$C$_6$H$_4$)$_2$X] (X = CH$_2$CH$_2$, O); metal complexes and their ROP capability

3.1 Introduction

Fluorescent materials have become a hot research topic in areas such as optoelectronics and cellular imaging.[1-3] Such materials usually give bright emission at a specific wavelength, although certain materials exhibit solvatochromism, also the solvent polarity can cause a change in the optical properties of a material. For example, *trans*-4-dimethylamino-4′-(1-oxybutyl)stilbene (DOS) exhibits solvatochromism across the entire visible spectrum with shifts of hundreds of nanometers.[4] What is more, solvatochromic materials have potential applications in bio- and environmental sensing, and such applications (molecular recognition and ion sensing) are now well established in macrocyclic chemistry.[5] Combining solvatochromism with the inherent molecular recognition properties of macrocycles opens up the possibility of intriguing bimodal sensing possibilities. Furthermore, Schiff-base compounds have attracted more and more attention because of their biological activity,[6-10] thus macrocyclic Schiff bases are of potential interest given their multiple binding sites.[11-12] Previous studies in our group have been investigating the Robson-type Schiff-base macrocyclic family, derived from the [2+2] condensation of a diamine with a dialdehyde, specifically 1,3-diformylphenol in combination with the dianiline 2,2′-oxydianiline (see chart 3-1).[13-17] Interestingly, a series of zinc complexes bearing phenol compartmental-type ligation were recently found to exhibit controllable photophysical properties by manipulation of the substituent (Me, *t*Bu, Cl) positioned *para* to the phenolic group.[18] Based on the above-mentioned considerations, in this chapter zinc derivatives of **L^1**H$_2$ and **L^2**H$_2$ (see chart 3-2) were prepared and investigated for their emission behaviour.

L$^{1-3}$H$_2$; R=Me, *t*Bu, Cl
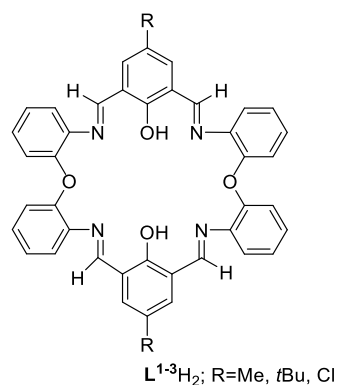
Chart 3-1. Schiff-base macrocycles **L$^{1-3}$H$_2$** used in this chapter.
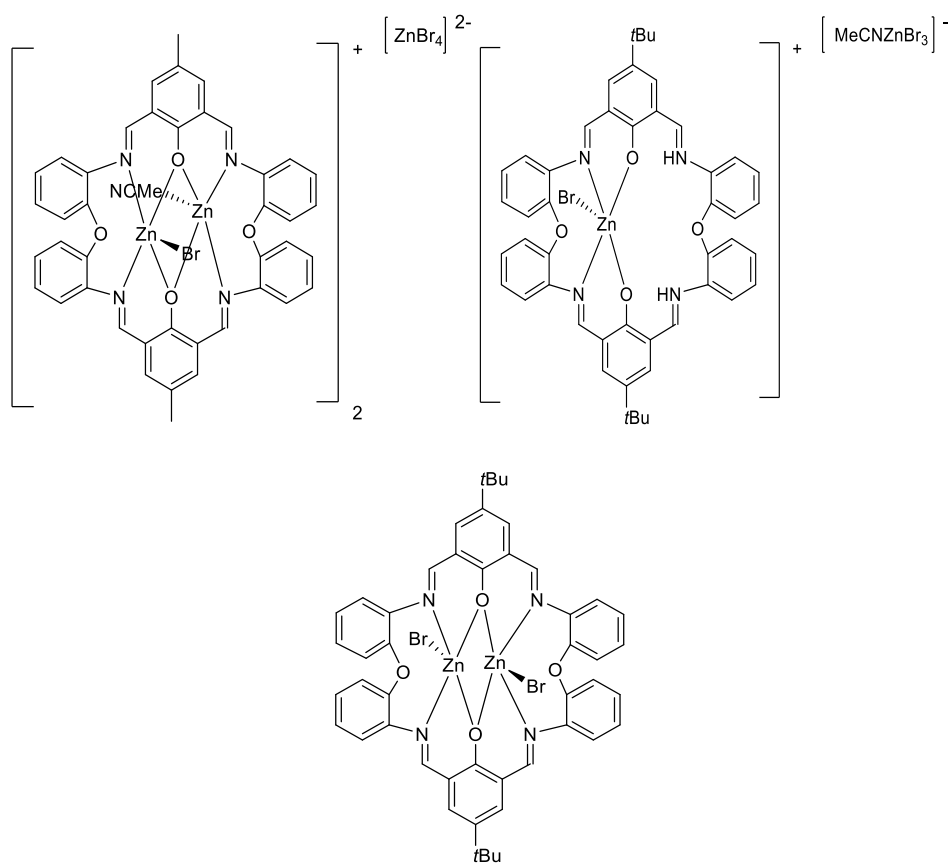
Chart 3-2. Zinc complexes **9** to **11**.

3.2 Results and Discussion

3.2.1 Emission studies on L$^{1-3}$H$_2$

Schiff base [2+2] macrocycles of type **L^{n}H$_2$** are readily available in high yield *via* the reaction of 2,6-dicarboxy-4-R-phenol, where R = Me (n = 1), *t*Bu (n = 2) or Cl (n = 3), with 2,2′-oxydianiline, (2-NH$_2$C$_6$H$_4$)$_2$O.[18] These condensation products {[2-(OH)-5-(R)-

64

C_6H_2-1,3-$(CH)_2][(O)(2-C_6H_4N)_2]\}_2$ (R = Me $\mathbf{L^1H_2}$, tBu $\mathbf{L^2H_2}$, Cl $\mathbf{L^3H_2}$) can be recrystallized from a variety of solvents.

The above-mentioned Schiff base compounds exhibit fluorescent character, and the emission spectra for $\mathbf{L^1H_2}$, $\mathbf{L^2H_2}$ and $\mathbf{L^3H_2}$ are shown in Figure 3-1. In the case of $\mathbf{L^3H_2}$, the emission spectrum displays a full hypochromic shift of the macrocycle emission in different solvents. In all cases, the 508 nm component is more pronounced in order of increasing dipole moment. The emission is typically broad, with full width at half maximum (FWHM) of 67±2 nm. Typically, the solutions with the largest dipole (acetonitrile) emit towards the blue/green end of the spectrum, whilst the macrocycle in the less polar solvents emits in the red end of the visible spectrum. Moreover, studies in DMSO (dipole moment 3.96) were also carried out, for which the spectra exhibited peaks at a) 490 and 588 nm, b) 520 nm and c) 520 and 578 nm, for $\mathbf{L^{1-3}H_2}$ respectively. These results are consistent with the observed dipole *versus* emission trend.[19] It is thought that the influence of the solvent on the intramolecular H-bonding is responsible for the observed hypochromic shifts.
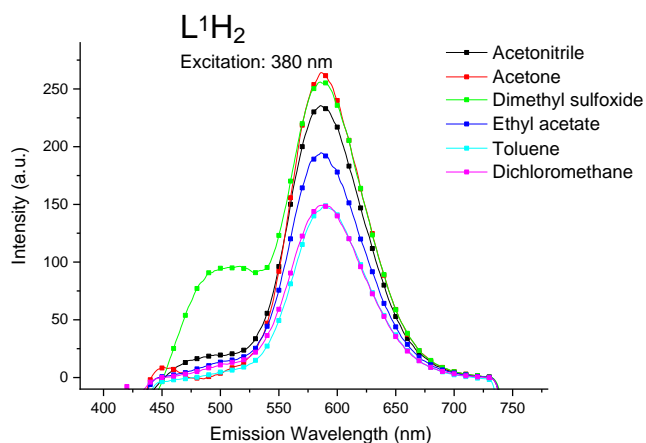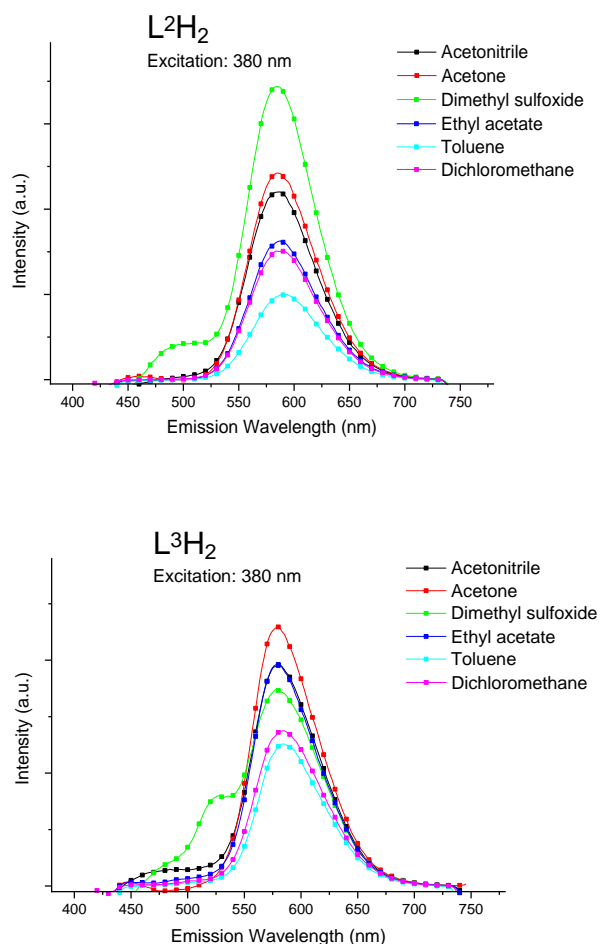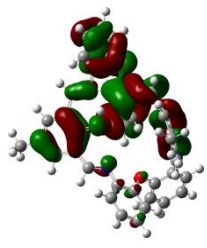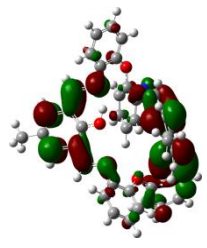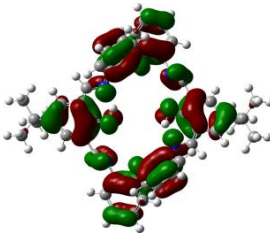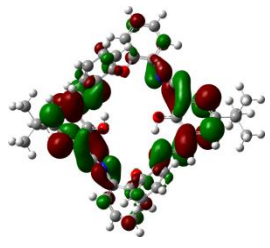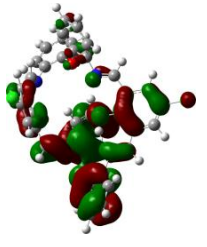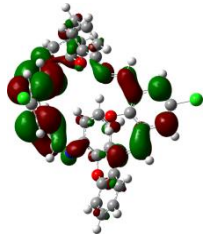
Figure 3-1. Photoluminescence emission spectra from samples L^1H_2, L^2H_2, and L^3H_2 in various solvents; Concentration: 25 mg/L.

3.2.2 DFT studies on $L^{1-3}H_2$

To provide explicit evidence for the energy states, in particular, the effect of the different solvents on the intramolecular H-bonding, the energy bandgaps of $L^{1-3}H_2$ were further evaluated by density function theory (DFT) calculations at the B3LYP/6–31G* level, collaboration with Feng's group at Guangdong University of Technology. As shown in table 3-1, the three compounds $L^{1-3}H_2$ exhibited different shapes for the HOMO/LUMO orbitals in different molecular fragments, due to the different electronic ability of the donor and acceptor groups, namely methyl, *t*-Bu group and Cl. Using L^3H_2 as an example,

the orbital distributions of the HOMO and LUMO energy levels are well separated on the parts of the naked phenyl ring and chloride-substituted phenyl ring, respectively. This push-pull system can contribute to adjust the energy gap in different solvents by intermolecular charge transfer (ICT).

Table 3-1. HOMOs and LOMOs for top L^1H_2; middle L^2H_2; bottom L^3H_2.

Compound	HOMO	LUMO
L^1H_2		
L^2H_2		
L^3H_2		

Further, the effect of solvent polarity on the molecular conformation was investigated by DFT calculations. It is noteworthy that the energy gap increases as the solvent polarity increased, and the relationship between the solvent polarity and energy gap (ΔE) is plotted in Figure 3-2. The intramolecular hydrogen bond (H-bond) was calculated from the

optimized molecular structure (Table 3-2). For example, in compound $\mathbf{L^3H_2}$, the distance for the H-bond in non-polar *n*-hexane solvent (3.44 Å) is shorter than that in the polar solvent DMF (3.60 Å). The intramolecular hydrogen bond in this system may play an important role in fixing the molecular conformation, which can make the molecule more rigid and suppress the twisted intramolecular charge transfer (TICT) and produce a hypochromic shift of the macrocycle emission in different solvent systems. These theoretical calculations are consistent with the experimental observations described above.
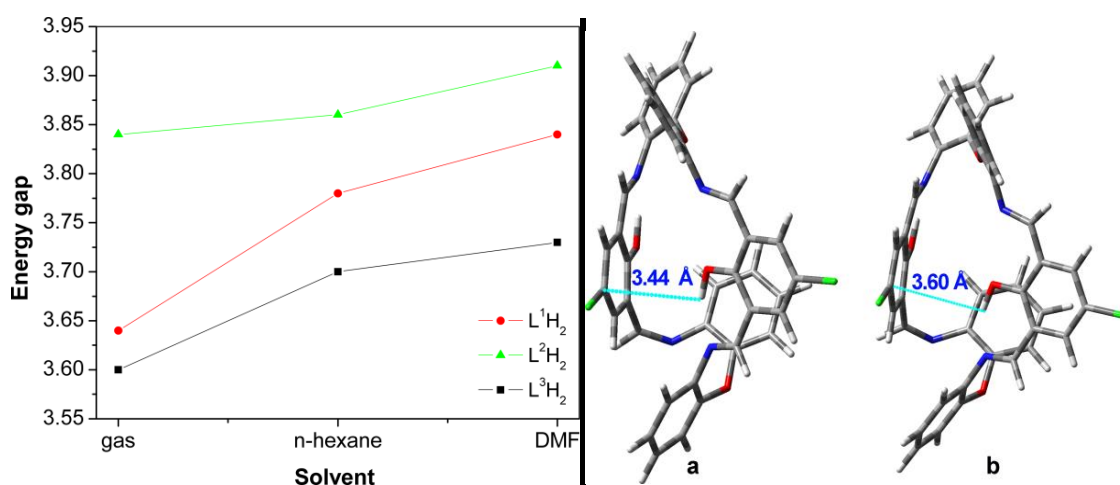
Figure 3-2. Theoretical calculations (B3LYP/6–31G* level) on the energy gap of compounds $\mathbf{L^{1-3}H_2}$ in different solvents.

Table 3-2. HOMO/LUMO energy levels for $\mathbf{L^{1-3}H_2}$

Compound	HOMO	LUMO	Energy gap	Comments
	-5.36	-1.52	3.84	In gas phase
$\mathbf{L^1H_2}$	-5.74	-1.88	3.86	In *n*-hexane
	-6.01	-2.10	3.91	In DMF
$\mathbf{L^2H_2}$	-5.33	-1.69	3.64	In gas phase
	-5.82	-2.04	3.78	In *n*-hexane

	-5.96	-2.12	3.84	In DMF
	-5.61	-2.01	3.60	In gas phase
$\mathbf{L^3H_2}$	-6.01	-2.31	3.70	In n-hexane
	-6.07	-2.34	3.73	In DMF

3.2.3 Zinc complexes

The coordination chemistry of the oxy-bridged macrocycles {[2-(OH)-5-(R)-C_6H_2-1,3-(CH)$_2$][O(2-C_6H_4N)$_2$]}$_2$ (R = Me $\mathbf{L^1H_2}$, tBu $\mathbf{L^2H_2}$) with Zn^{2+} is discussed in this chapter. Reaction of $\mathbf{L^1H_2}$ with 3 equivalents of [ZnBr$_2$] afforded, following work-up, the complex [(ZnBr)(ZnNCMe)$\mathbf{L^1}$]$_2$[ZnBr$_4$]·2.5MeCN (**9**·2.5MeCN) as orange crystals in moderate yield. Single crystals were grown from a saturated solution of acetonitrile at ambient temperature, and the molecular structure is shown in Figure 3-3; selected bond lengths and angles are given in the Table 3-3. In the cation, the zinc centre (Zn1) is five-coordinated with a distorted trigonal bipyramid geometry ($\tau = 0.57$), and is bound by two phenoxide oxygens and the two nitrogens N1 and N2 of the macrocycle plus one bromide. However, Zn2 is five-coordinated by two phenoxide oxygens two nitrogens and an MeCN ligand, which overall creates a distorted trigonal bipyramid geometry at the metal ($\tau = 0.55$).[20]
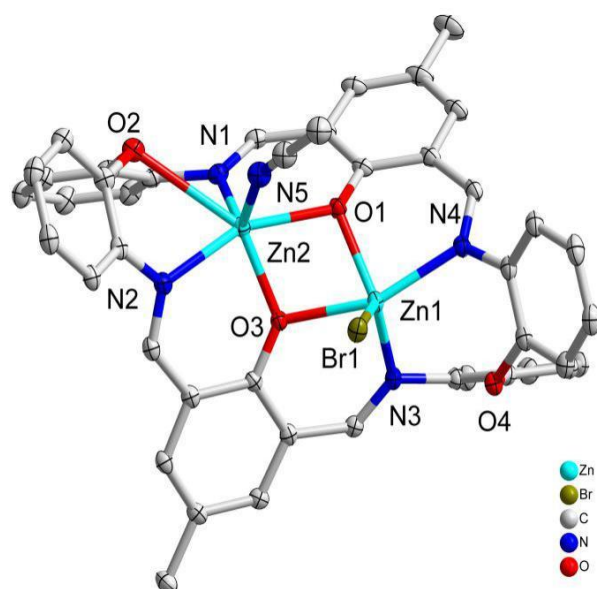
Figure 3-3. The molecular structure of $[(ZnBr)(ZnNCMe)L^1]_2[ZnBr_4]\cdot 2.5MeCN$ **9**$\cdot 2.5MeCN$. Solvent and hydrogen atoms are omitted for clarity. Thermal ellipsoids are drawn at the 30% probability level.

In the case of L^2H_2, reaction with 2 equivalents of $ZnBr_2$ afforded, following work-up, the salt complex $[(ZnBr)L^2H_2][ZnBr_3NCMe]\cdot 3MeCN$ (**10**$\cdot 3MeCN$) in *ca*. 58.4% isolated yield as shown in Figure 3-4. The Zn centre (Zn1) in complex **10** is five-coordinate and adopts a distorted trigonal bipyramid geometry with a τ value of 0.67. Notably, on adding Et_3N to the reaction between L^2H_2 and $ZnBr_2$, the orange crystalline complex $[(ZnBr)_2L^2]\cdot 4.5MeCN$ (**11**$\cdot 4.5MeCN$) which is shown in Figure 3-5, was successfully isolated in *ca*. 69.0 % yield. The zinc centres adopt distorted trigonal bipyramid geometries with a bromide at each apex (τ=0.76). The bridging phenoxide oxygens O1 and O2 and the nitrogens N1 and N4 form the basal plane. Selected bond lengths in these structures are shown in Table 3-3. In these solvates, the range of C=N bond lengths [1.287(9)–1.300(4) Å] compares favourably with those reported for the related oxygen bridged phenolic macrocycles [1.276(2)–1.381(4) Å].[20]

70
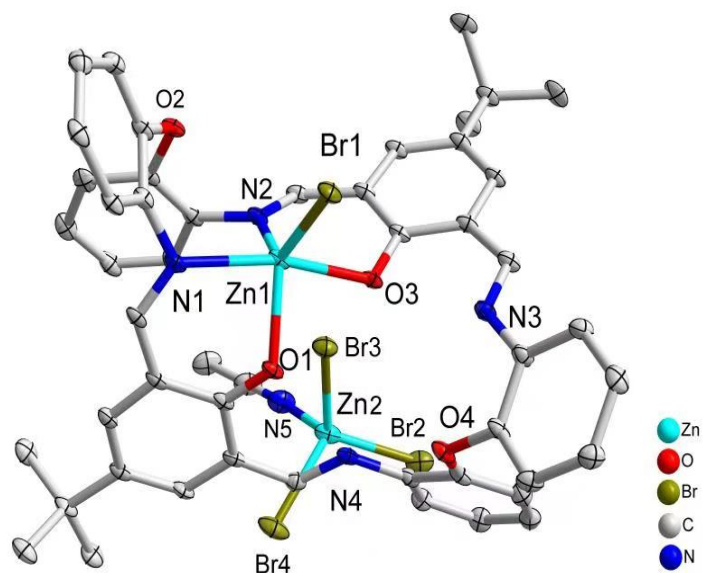
Figure 3-4. The molecular structure of $[(ZnBr)L^2H_2][ZnBr_3NCMe]\cdot 3MeCN$ ($\mathbf{10}\cdot 3MeCN$). Solvent and hydrogen atoms are omitted for clarity. Thermal ellipsoids are drawn at the 30% probability level.
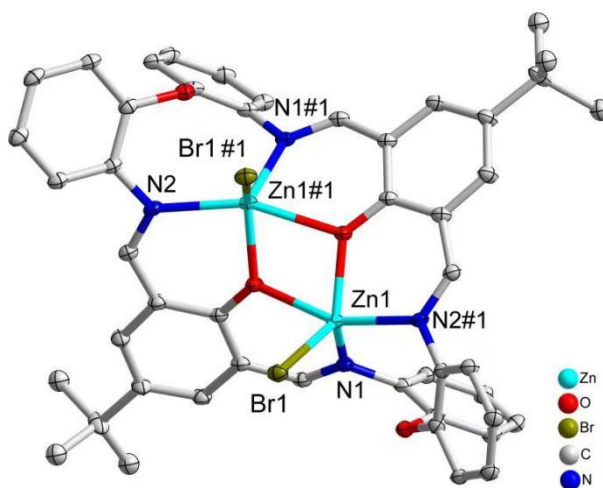
Figure 3-5. The molecular structure of $[(ZnBr)_2L^2]\cdot 4.5MeCN$ ($\mathbf{11}\cdot 4.5MeCN$). Solvent and hydrogen atoms are omitted for clarity. Thermal ellipsoids are drawn at the 30% probability level. (Symmetry Operators #a: $1-x$, y, $1.5-z$).

Table 3-3. Selected bond lengths (Å) and angles (°) in **9**, **10** and **11**.

	Selected bonds	Length (Å)	Selected angles	(°)
Complex **9**	Zn(1)-O(1)	2.054(2)	O(1)-Zn(1)-N(4)	84.15(10)
	Zn(1)-N(3)	2.098(3)	N(3)-Zn(1)-O(3)	82.90(10)
	Zn(1)-O(3)	2.121(2)	N(3)-Zn(1)-N(4)	103.42(11)
	Zn(1)-Br(1)	2.400(5)	N(4)-Zn(1)-O(3)	156.32(10)
	Zn(2)-O(3)	2.023(2)	O(1)-Zn(2)-Br(2)	92.30(2)
	Zn(2)-N(1)	2.045(3)	O(1)-Zn(2)-N(2)	156.31(10)
	Zn(2)-N(5)	2.073(4)	O(3)-Zn(2)-N(1)	110.63(10)
	Zn(2)-O(1)	2.104(2)	N(1)-Zn(2)-Br(2)	113.2(2)
	Zn(2)-Br(2)	2.571(10)	N(5)-Zn(2)-N(2)	94.63(13)
Complex **10**	N(1)-Zn(1)	2.171(5)	C(11)-N(1)-Zn(1)	122.1(4)
	N(2)-Zn(1)	2.106(5)	C(12)-N(1)-Zn(1)	121.4(3)
	N(5)-Zn(2)	2.088(7)	C(24)-N(2)-C(23)	118.2(5)
	O(1)-Zn(1)	2.001(4)	C(24)-N(2)-Zn(1)	126.2(4)
	O(3)-Zn(1)	2.136(4)	C(23)-N(2)-Zn(1)	115.6(4)
	Zn(1)-Br(1)	2.3799(9)		
Complex **11**	Zn(1)-O(1)	2.018(5)	O(1)-Zn(1)-N(3)	110.7(2)
	Zn(1)-N(3)	2.042(5)	O(1)-Zn(1)-O(3)	74.06(17)
	Zn(1)-O(3)	2.103(5)	N(3)-Zn(1)-O(3)	86.9(2)
	Zn(1)-N(2)	2.121(5)	O(3)-Zn(1)-N(2)	156.1(2)
	Zn(2)-O(3)	2.052(5)	O(1)-Zn(1)-N(5)	125.4(2)
	Zn(2)-N(1)	2.099(6)	O(3)-Zn(1)-N(4)	84.1(2)
	Zn(2)- N(4)	2.105(6)	N(1)-Zn(2)-N(4)	103.6(2)
	Zn(2)- O(1)	2.123(4)		
	Zn(2)-Br(1)	2.4011(11)		

In the infrared spectra of the Zn(II) complexes, strong stretching bands for = CH–NH-
fragment were absent, but strong, sharp bands in the range of 1623–1625 cm^{-1} can be

assigned to the azomethine C=N stretching frequency.[21] In contrast to the spectra observed for **9** and **11**, that for **10** contained an absorption band at 3419 cm^{-1} consistent with the presence of pronated amine (NH$^+$) in the structure.

The surface morphology of Zn(II) complexes was analyzed by scanning electron microscopy (SEM) as depicted in Figure 3-6 to Figure 3-8. Figure 3-6 shows a SEM micrograph of complex **9**, where stacked plate shape crystals are observed with the particle size range from 5 to 15 μm. Figure 3-7 depicts the nano rod-like structure of complex **10** with the diameter ranging from 10 to 50 μm. The SEM image of complex **11**, as shown in Figure 3-8, revealed accumulated lumpy-like crystals.
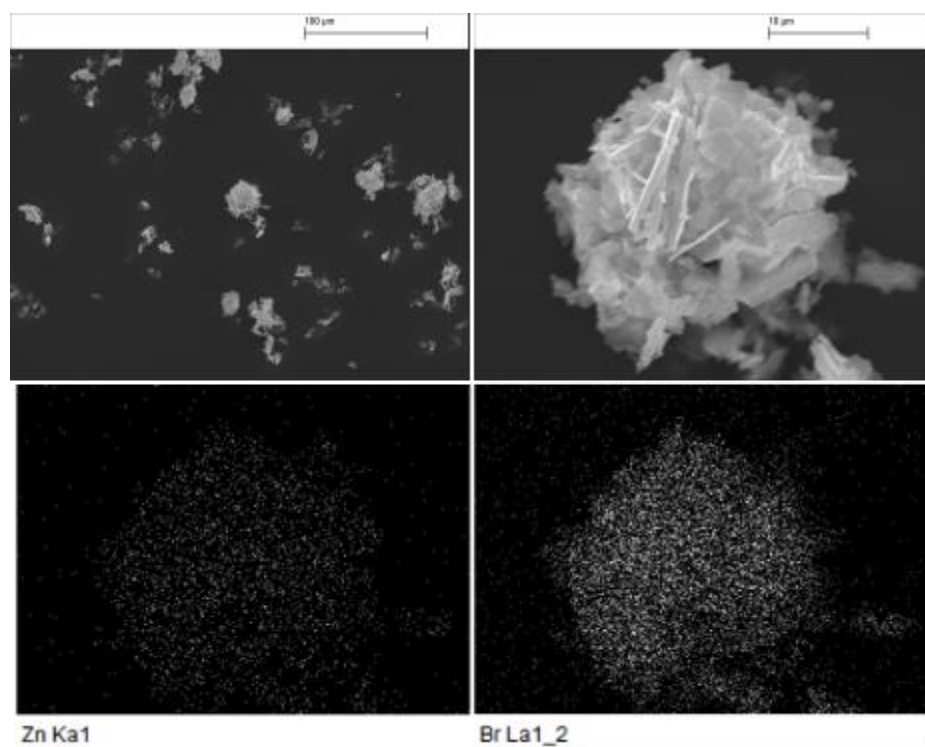
Figure 3-6. SEM and mapping images of complex **9**.
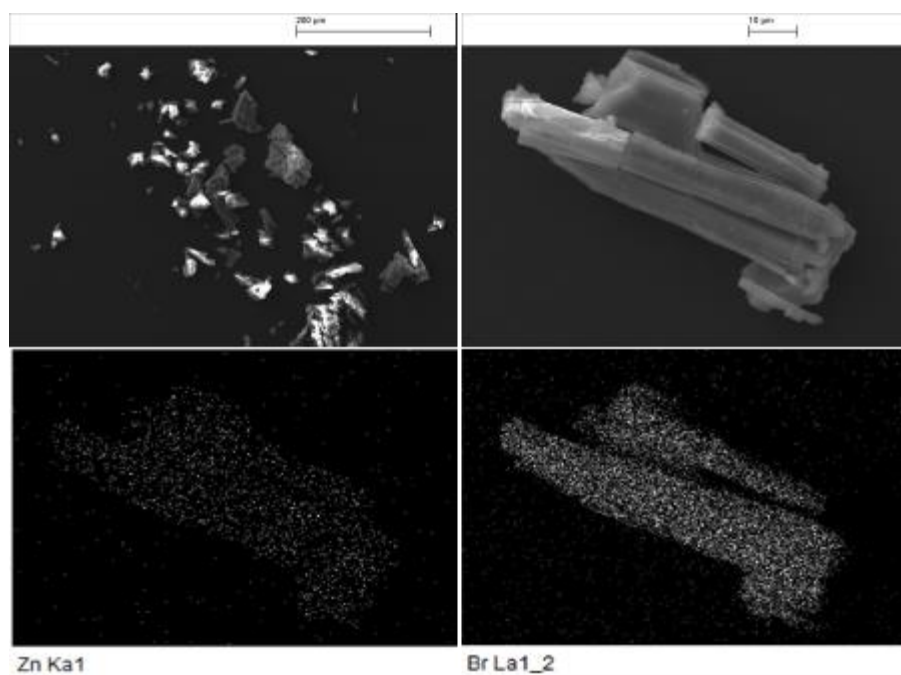
Figure 3-7. SEM and mapping images of complex **10**.
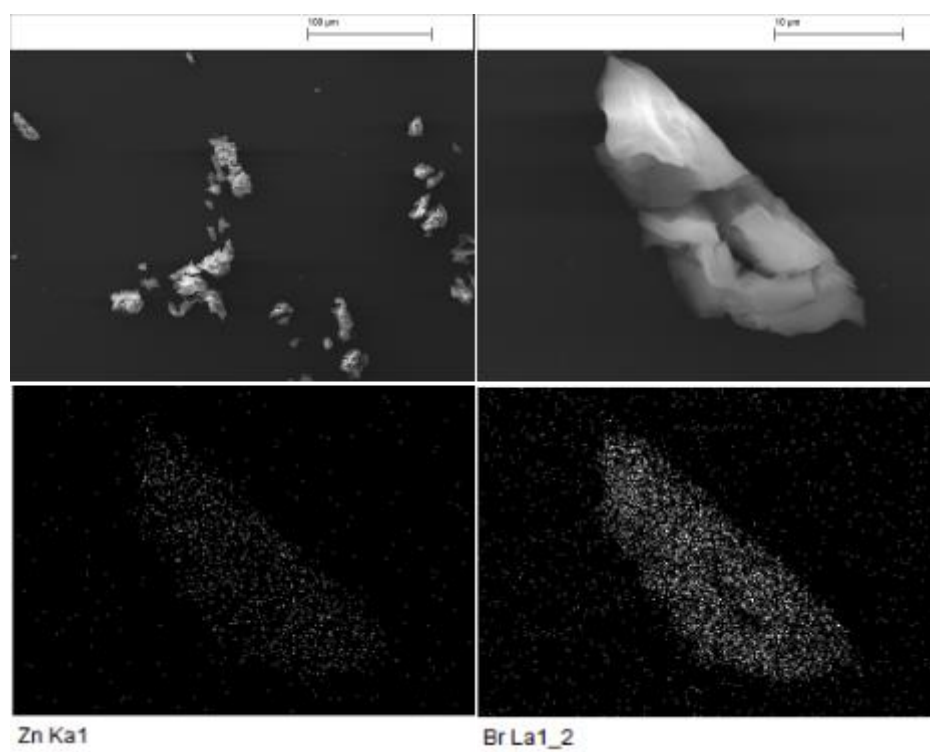
Figure 3-8. SEM and mapping images of complex **11**.

3.2.4   Emission studies on the zinc complexes

The UV-vis absorption spectra of the zinc complexes in different solvents (methanol, ethanol, chloroform, acetonitrile, acetone) were recorded at room temperature, and the data are presented in Table 3-4 and Figure 3-9. The first band centered at 280–330 nm can be assigned to a π–π^* transition of the phenyl rings. The second absorption band in the range 405–421 nm can be attributed to intramolecular interactions between metal and ligand.[22]

The photoluminescence of the zinc complexes **9**–**11** was examined as solid samples as well as in solutions of different solvents (methanol, ethanol, acetonitrile, acetone, chloroform). Selected data are summarized in Table 3-4. Complex **9** exhibited an emission maximum at 478–482 nm and green-yellow luminescence in solution except when in methanol. The maxima emission peaks are bathochromically shifted by around 50 nm in methanol compared with those in other solvents, due to the high polarity of the solvent. Similar to complex **9**, the maximum emission wavelengths of complex **10** were around 477–480 nm. Moreover, as shown in Figure 3-10, complex **11** has luminescent bands centred at 477 nm to 480 nm with green-yellow luminescence.

The luminescence properties of **9-11** were also examined in the solid state at 298 K (Figure 3-11). Complexes **9** and **11** exhibited similar luminescent bands centred at 509 and 520 nm, respectively. Notably, solid **10** exhibits a yellow emission (Figure 3-12) with λ_{max} at 564 nm. On comparing the solid-state spectra with the solution spectra, the maximum emission bands of the solid state of **9-11** are obviously red-shifted by 24-87 nm. These significant bathochromic shifts are caused by the difference in parameters like planarity, the irregular arrangement in the crystalline state and intermolecular forces such as π–π^* stacking and excimers of each molecule.[23, 24]
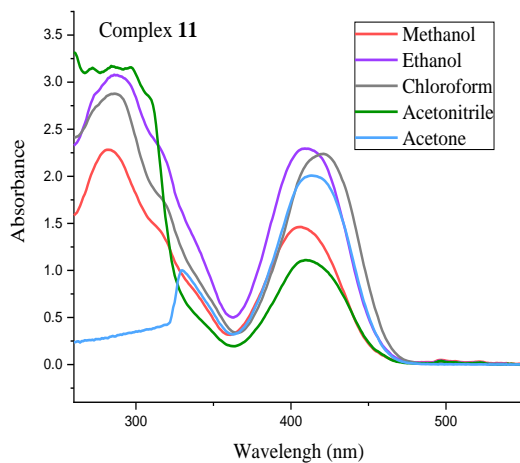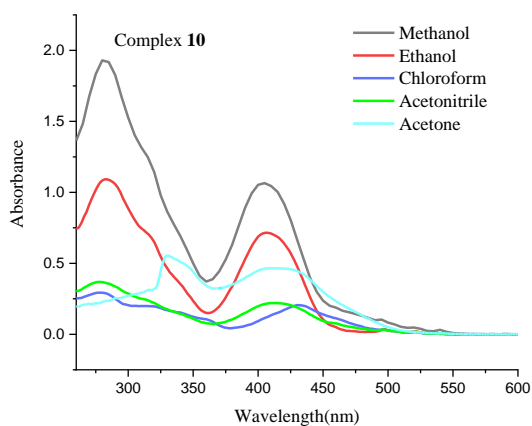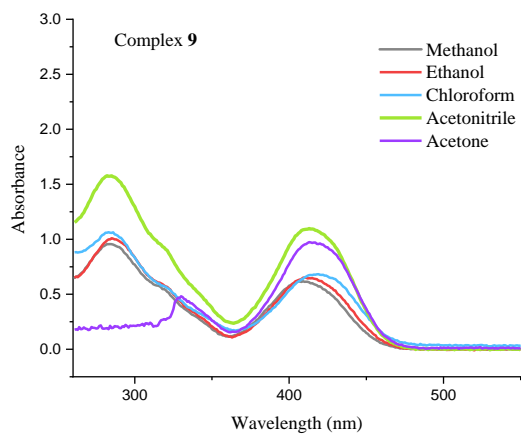
Figure 3-9. Absorption spectra of the zinc complexes **9-11** in different solvents at 298 K.
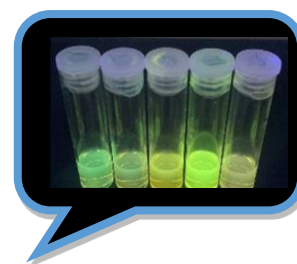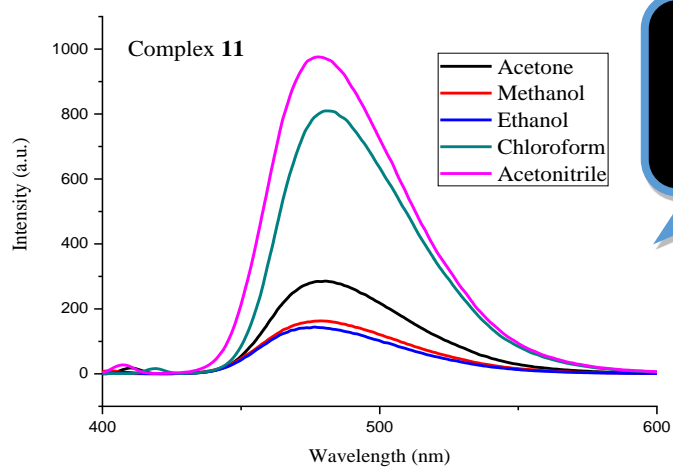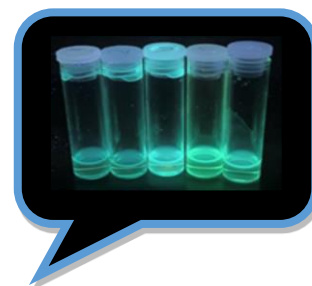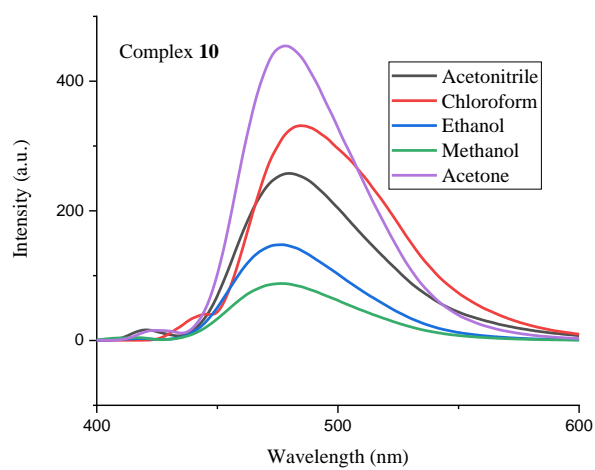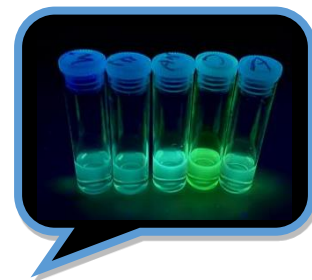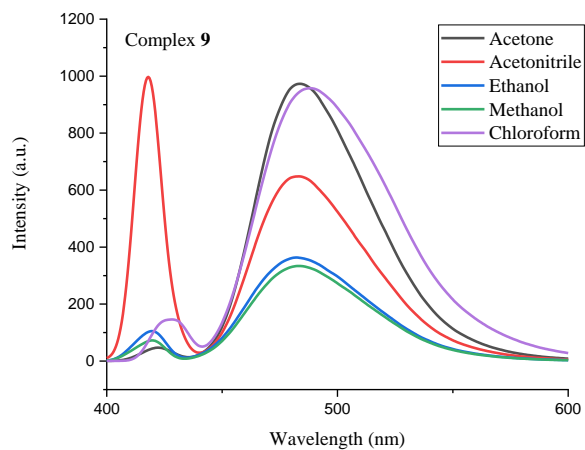
Figure 3-10. Photoluminescence emission spectra of complexes **9-11** in different solvents at 292 K and the fluorescent picture for the zinc complexes (Insert picture: Emission

pictures for zinc complexes in different solvents; From left to right is methanol; ethanol; acetonitrile; chloroform; acetone).
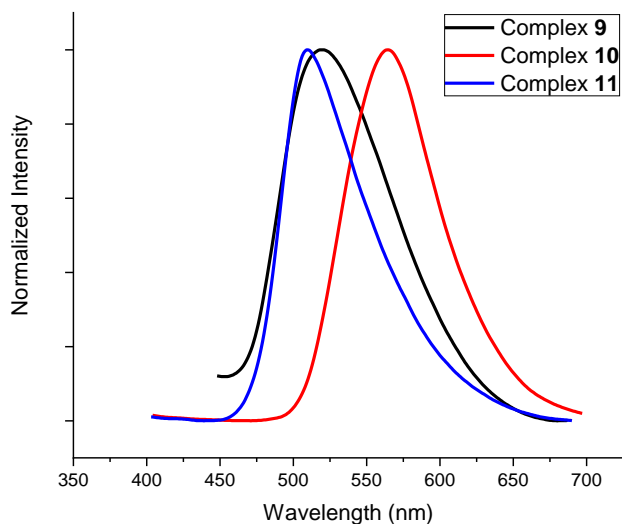
Figure 3-11. Solid Photoluminescence emission spectra of the zinc complexes.

Figure 3-12. Pictures of the zinc complexes in the solid state (from top to bottom is complex **9** to **11**, photos on the left side is the complexes under natural light, the right side is the photos under UV light).

The Commission Internationale de L'Eclairage (CIE) coordinates from the solid-state zinc complexes photoluminescence spectra are shown in Figure 3-13. It worth noting that the emission wavelength of complexes **9** and **11** are approximately the same and they

exhibit yellow fluorescence, but for complex **10** the maximum emission wavelength is 50

nm higher and it exhibits a yellow-green colour.
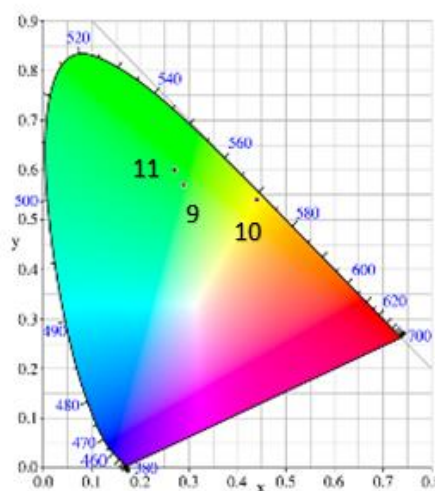
Figure 3-13. CIE diagram of the zinc complexes **9-11** in solid state. Chromaticity

parameters according to CIE 1931 colour.

Table 3-4. Emission data for zinc complexes **9-11**.

	λ_{abs}	$\lambda_{em\ (\lambda_{ex})}$	**Quantum yield (ϕ) [a]**	**fluorescence lifetime τ**
9 in methanol	284, 409	484 (409)	<0.01	0.64 ns
9 in ethanol	285, 410	482 (410)	0.76	(Solid state)
9 in acetonitrile	285, 413	483 (413)	2.34	
9 in chloroform	286, 419	488 (419)	2.50	
9 in acetone	330, 413	484 (413)	2.13	

	λ_{abs}	λ_{em} (λ_{ex})	Quantum yield (ϕ) [a]	fluorescence lifetime τ
10 in methanol	280, 405	479 (405)	<0.01	29.8 ns
10 in ethanol	284, 406	482 (406)	0.80	(Solid state)
10 in acetonitrile	290, 414	485 (414)	0.24	
10 in chloroform	284, 430	484 (430)	3.54	
10 in acetone	330, 416	478 (416)	2.75	

	λ_{abs}	λ_{em}(λ_{ex})	Quantum yield (ϕ)[a]	fluorescence lifetime τ
11 in methanol	282, 406	479 (406)	0.38	0.36 ns
11 in ethanol	286, 411	477 (411)	1.07	(Solid state)
11 in acetonitrile	284, 410	478 (410)	2.41	
11 in chloroform	286, 421	480 (421)	3.13	
11 in acetone	330, 413	480 (413)	2.96	

[a] Absolute luminescence quantum yield measured by integrating sphere.

Luminescence quantum yields were measured for both solid samples and solutions by the absolute measurement method. As shown in Table 3-4, complexes **9-11** were found to exhibit moderate fluorescence quantum yields[25] in solution. In the solid state, the quantum yields for complexes **9-11** are 2.66%, 6.90% and 1.29%, respectively, which together with the high PL lifetime makes complex **10** a good candidate as a luminescent

material. The phenomenon in which complexes show higher photoluminescence efficiency in the aggregated state than in solution is related to aggregation-induced emission enhancement (AIEE).[26]

The lifetimes for the as-prepared zinc complexes **9**-**11** as solid-state samples were also recorded. The luminescence decay spectra and their fitted curves are shown in Figure 3-14. These decay curves have been fitted with the standard biexponential decay equation and were found to agree well. The observed lifetimes are 0.64, 29.8 and 0.36 ns for the zinc complexes **9**, **10** and **11**, respectively. The measured lifetime of **10** is significantly longer than that of the other two, which can be attributed to a fast charge transfer process between the Zn(II) and the specific coordinated macrocycle. The lifetime on the nanosecond scale indicates that the zinc complexes have the fluorescent character of luminescence.[23]
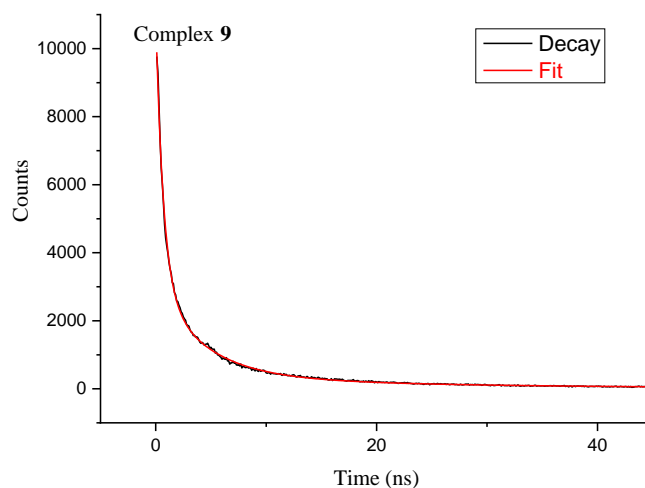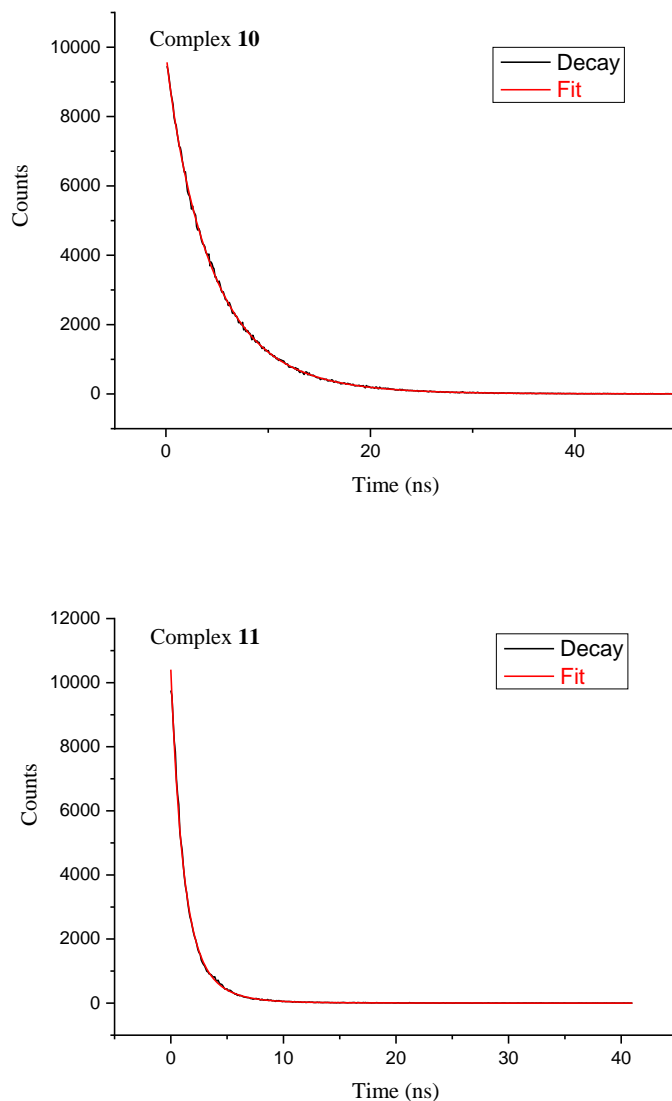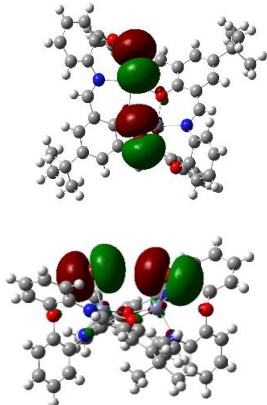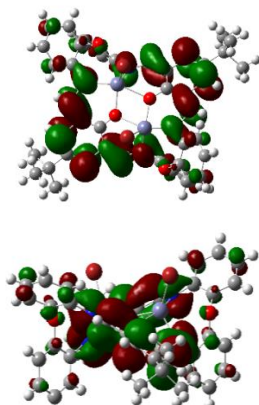
Figure 3-14. Fluorescence decay and their fitted curves for the zinc complexes **9-11** in the solid state.

3.2.5 DFT studies for complex 11

Density function theory (DFT) calculations at the B3LYP/6–31G* level are provided for the energy states discussion. As shown in table 3-5, the zinc complex **11** exhibited different shapes for the HOMO/LUMO orbitals. The orbital distributions of the HOMO energy levels mainly separated on the bromides but the LUMO energy levels were well separated over the whole macrocyclic ligand.

Table 3-5. DFT studies for complex **11**.

Complex	HOMO	LUMO
11		

3.3 Conclusion

In conclusion, the Schiff base macrocycles $L^{1-3}H_2$ exhibit hypochromic shifts of the emission bands. The features of the emission can be aligned with the dipole of the solvent system employed and is thought to be related to the influence of the solvent on the intramolecular hydrogen bonding. In the case of the zinc complexes, it was found that the Zn(II) complexes demonstrate yellow or yellow/green photoluminescence and enhanced performance *versus* the parent macrocycles. All the complexes exhibit good PL emissions and quantum yields in solutions. The lifetime measurement and solid-state quantum yields shows that complex **10** generates a longer-live fluorescence and relatively high quantum yields than the other two complexes.

3.4 References

[1] J. R. Askim, M. Mahmoudi and K. S. Suslick, *Chem. Soc. Rev.*, 2013, 42(22), 8649-8682.

[2] Z. Guo, S. Park, J. Yoon and S. Injae, *Chem. Soc. Rev.*, 2014; 43(1), 16-29.

[3] H. Zhang, T. Sun, Q. Ruan, J. L. Zhao, L. Mu, X. Zeng, Z. W. Jin, S. B. Su, Q. Y. Luo, Y. Y. Yan and C. Redshaw , *Dyes Pigm.*, 2019, 162, 257-265.

[4] C. Reichardt and T. Welton, Solvents and solvent effects in organic chemistry, *4th Ed. Weinheim*, Germany, Wiley-VCH, 2010.

[5] K. M. Mullen and P. D. Beer, *Chem. Soc. Rev.*, 2009, 38(6), 1701-1713.

[6] E. M. Hodnett and W. J. Dunn, *J. Med. Chem.*, 1970, 13(4), 768-770.

[7] S. N. Pandeya, D. Sriram, G. Nath and E. D. Clercq, *Il Farmaco*, 1999, 54(9), 624-628.

[8] A. H. El-masry, H. H. Fahmy and S. H. Ali Abdelwahed, *Molecules*, 2000, 5(12), 1429-1438.

[9] A. A. Jarrahpour and M.Zarei, *Molbank*, 2004, 2004(1), M377.

[10] H. L. Siddiqui, A. Iqbal, S. Ahmad and G. W. Weaver, *Molecules*, 2006, 11(2), 206-211.

[11] S. Brooker, *Coord. Chem. Rev.*, 2001, 222, 33.

[12] W. Radecka-Paryzek, V. Patroniak and J. Lisowski., *Coord. Chem. Rev.*, 2005, 249, 2156-2175.

[13] A. Arbaoui, C. Redshaw and D. L. Hughes, *Chem. Commun.*, 2008, 39, 4717-4719.

[14] A. Arbaoui, C. Redshaw and D. L. Hughes, *Supramol. Chem.*, 2009, 21(1-2), 35-43.

[15] W. Yang, K. Q. Zhao, B. Q. Wang, C. Redshaw, M. R. Elsegood, J. L. Zhao and T. Yamato,. *Dalton Trans.*, 2016, 45, 226-236.

[16] H. Chen, C. Huang, Y. Deng, Q. Sun, Q. L. Zhang, B. X. Zhu and X. L. Ni, *ACS Nano*, 2019, 13(3), 2840-2848.

[17] H. Chen, C. Huang, Y. Ding, Q. L. Zhang, B. X. Zhu and X. L. Ni., *Chem. Sci.*, 2019, 10, 490-496.

[18] P. Chakraborty, J. Adhikary, S. Samanta, I. Majumder, C. Massera, D. Escudero, G. Sanjib, B. Antonio, F. Antonio and D. Das, *Dalton Trans.*, 2015, 44, 20032-20044.

[19] T. Dziembowska, Z. Malarski and B. Szczodrowska, *J. Soln Chem.* 1996, 25, 179-189.

[20] A. W. Addison, T. N. Rao, J. Reedijk, J. van Rijn and G. C. Verschoor, *J. Am. Chem. Soc., Dalton Trans.*, 1984, 7, 1349-1356.

[21] F. Marchetti, C. Pettinari, C. Di Nicola, A. Tombesia and R. Pettinarib, *Coord. Chem. Rev.*, 2019, 401, 213069.

[22] A. Gusev, V. Shul'gin, E. Braga, E. Zamnius, M. Kryukova and W. Linert, *Dyes Pigm.,* 2020, 183, 108626.

[23] R. Lakshmanan, N. C. Shivaprakash and S. Sindhu, *J. Lumin.*, 2018, 196, 136-145.

[24] M. Yang, D. Xu, W. Xi, L. Wang, J. Zheng, J. Huang, J. Zhang, H. Zhou, J. Wu and Y. Tian, *J. Org. Chem.*, 2013, 78, 10344–10359.

[25] J. Xia, Z. Zhou, W. Li, H. Q. Zhang and C. Redshaw, W. H., *Inorg. Chim. Acta*, 2013, 394, 569-575.

[26] Y. Ren, W. H. Kan, M. A. Henderson, P. G. Bomben, C. P. Berlinguette, V. Thangadurai and T. Baumgartne, *J. Am. Chem. Soc.*, 2011, 133, 17014-17026.

Chapter 4 . Schiff-base [2+2] macrocycles derived from the dianiline [(2-NH$_2$C$_6$H$_4$)$_2$X] (X = CH$_2$CH$_2$, O) metal complexes and their ROP capability

4.1   Introduction

Global issues over plastic pollution continue to drive the search for alternative, more environmentally-friendly materials.[1] New catalysts for affording biodegradable polymers via the ring opening polymerization (ROP) of cyclic esters have become a hot research topic.

Previous work in our group has focused on the coordination chemistry of Schiff-base macrocycles derived from the [2+2] condensation of the dianilines [(X)(2-C$_6$H$_4$NH$_2$)$_2$] (X = CH$_2$CH$_2$, O) with the diformylphenols 2,6-(CHO)$_2$-4-R-C$_6$H$_2$OH (R = Me, tBu) (chart 4-1).[2,3] To date, alkylaluminium centres bound to the macrocycle (X = CH$_2$CH$_2$) was reported to exhibit beneficial cooperative effects in the ROP of ε-caprolactone (ε-CL), whereas aluminoxane type (Al–O–Al) bonding proved to be detrimental.[3] Manganese complexes bearing these macrocycles were far less active (conversions < 15%).[4] However, studies of mixed cobalt/zinc systems revealed interesting catalytic properties, with homo-dinuclear systems exhibiting inactivity while mixed-metal systems proved to be efficient for the ROP of ε-caprolactone and δ-valerolactone (δ-VL), this part is shown in the chapter 2 of this thesis. Given this, iron, cobalt and copper complexes bearing [2+2] macrocycles derived from the dianilines [(X)(2-C$_6$H$_4$NH$_2$)$_2$] (X = CH$_2$CH$_2$, O, chart 4-2) were revisited and subject to investigation. In this chapter, the molecular structures of these Fe, Co and Cu complexes (Chart 4-2) are presented. A number of them have been screened for their capability in the ROP of ε-CL, δ-VL and *rac*-lactide (*r*-LA), and the co-polymerization of ε-CL with *r*-LA

and *vice-versa*. These have been chosen as poly(ε-caprolactone), PCL, and poly(lactide), PLA, are favoured polymers given their biodegradability properties, and their co-polymers are considered as potential environmentally-friendly commodity plastic.[5]

$\mathbf{L^{Me}H_2}$ X =CH_2CH_2; R = Me
$\mathbf{L^{tBu}H_2}$ X =CH_2CH_2; R = tBu
$\mathbf{L^1H_2}$ X = O; R =Me
$\mathbf{L^2H_2}$ X = O; R =tBu

L^4H
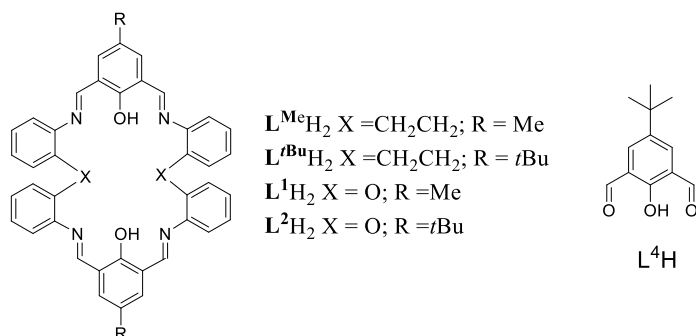
Chart 4-1. Ligands in this Chapter.

X = 0.5Br₃FeOFeBr₃; R = Me (**12**), *t*Bu (**13**)
X = Br; R = *t*Bu (**14**)

15

16   **17**   **18**

L = MeCN (**19**)

L = MeCN
M=Co (**21**)
M=Fe (**23**)

L = MeCN (**22**)

L = MeCN, X =2[CoBr₃L] (**20**)
L = MeCN, X = FeBr₃OFeBr₃ (**24**)
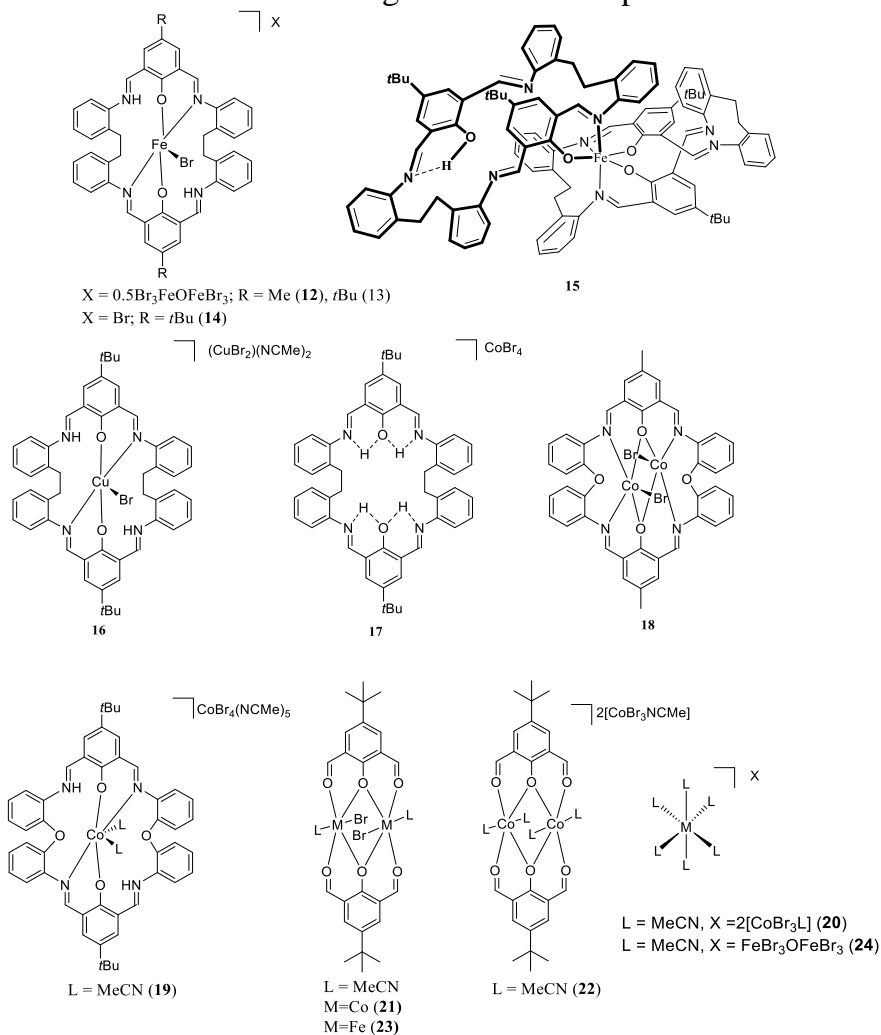
Chart 4-2. Structures of iron and cobalt complexes **12** - **24** prepared herein.

87

4.2 Results and Discussion

4.2.1 -CH₂CH₂- bridged systems

Iron

Use R = Me L¹H₂

Iron is a cheap, earth abundant metal and its complexes have shown potential in the ROP of cyclic esters.[6] The reaction of the macrocycle {[2-(OH)-5-Me-C₆H₂-1,3-(CH)₂][CH₂CH₂(2-C₆H₄N)₂]}₂ ($L^{Me}H_2$) with two equivalents of FeBr₂ in refluxing toluene afforded after work-up (recrystallization from MeCN), a brown crystalline solid in moderate yield. Single crystals were grown from a saturated solution of acetonitrile on standing at ambient temperature for 3 days. The molecular structure is shown in Figure 4-1, with selected bond lengths and angles given in the caption. There are two macrocyclic iron complexes in the asymmetric unit, related by a pseudosymmetric translation of *c*/2, plus an anion of [Br₃FeOFeBr₃] and two molecules of acetonitrile. Of the macrocyclic bound iron centres, both Fe1 and Fe2 adopt a distorted trigonal bipyramidal geometry (τ=0.69),[7] bound by a bromide and two nitrogen atoms and two oxygen atoms of the macrocycle, apical sites are occupied by O atoms, with the bromide and N atoms in the equatorial sites. The composition is thus [FeBr(L^{Me})]₂[Br₃FeOFeBr₃]·2(MeCN) (**12**·2MeCN) see Figure 4-2. In terms of charge, the 2+ available from the anion which contains two Fe(III) centres, is balanced by the two cations (2x +1), each of which contains an Fe(II) centre. There are two symmetry independent macrocyclic metal complexes in **12**·2MeCN. These are related by a pseudosymmetric translation of c/2.
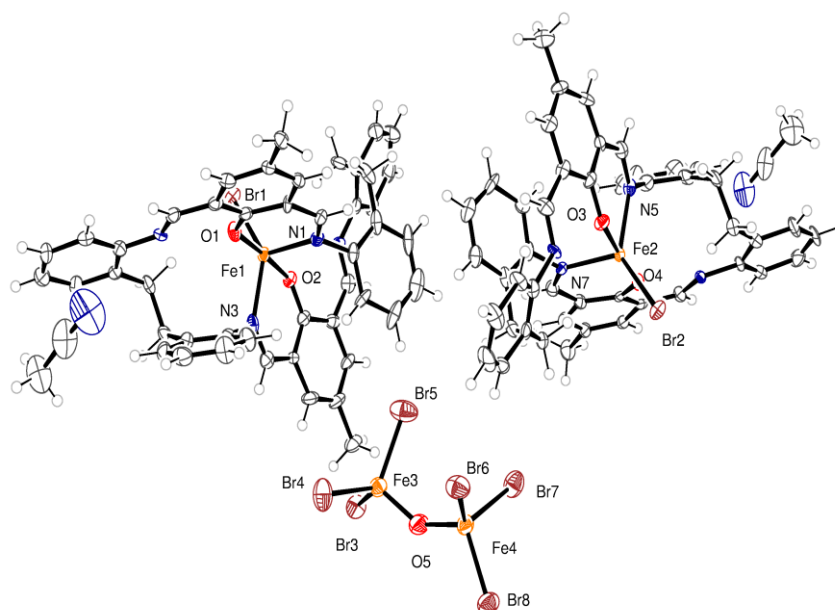
Figure 4-1. Asymmetric unit for the structure of $[FeBr(\mathbf{L^{Me}})]_2[Br_3FeOFeBr_3]\cdot$ $\cdot 2MeCN$ (**12**$\cdot$2MeCN). Thermal ellipsoids are drawn at the 50% probability level. Selected bond lengths (Å) and angles ($^{\circ}$): Fe(1) – O(1) 2.002(6), Fe(1) – O(2) 2.020(6), Fe(1) – N(1) 2.129(7), Fe(1) – N(3) 2.138(7), Fe(1) – Br(1) 2.5070(16), Fe(2) – O(3) 2.031(6), Fe(2) – N(5) 2.150(7), Fe(2) – N(7) 2.135(7), Fe(2) – Br(2) 2.5104(15); O(1) – Fe(1) – O(2) 177.0(2), N(1) – Fe(1) – N(3) 103.8(3), Br(1) – Fe(1) – N(1) 120.26(19), N(5) – Fe(2) – N(7) 102.9(3).
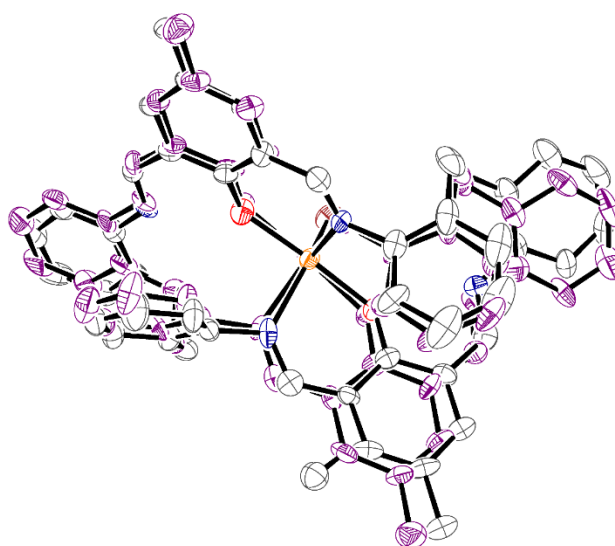
Figure 4-2. Different view showing the components of the structure **12**$\cdot$2MeCN.

Use R = tBu L²H₂

Similar reaction of $\{[2\text{-}(OH)\text{-}5\text{-}(t\text{Bu})\text{-}C_6H_2\text{-}1,3\text{-}(CH)_2][CH_2CH_2(2\text{-}C_6H_4N)_2]\}_2$ (**L**$^{t\text{Bu}}$**H₂**) with 2.1 equivalents of FeBr₂ afforded red needles [FeBr(**L**$^{t\text{Bu}}$**H₂**)], $0.5[(FeBr_3)_2O]\cdot0.5(MeCN)$ (**13**·0.5MeCN) in good yield. Crystals suitable for X-ray diffraction were grown from a saturated solution of acetonitrile at ambient temperature. A view of the molecular structure is shown in Figure 4-3, and bond lengths and angles are given in the caption. The crystal comprises FeBr(**L**$^{t\text{Bu}}$**H₂**) cations, $(FeBr_3)_2O$ anions and MeCN solvent molecules. The anions lie about a centre of symmetry and the solvent molecule sites refine best with half-occupancy; the molecular formula is therefore [FeBr(**L**$^{t\text{Bu}}$**H₂**)], $0.5[(FeBr_3)_2O]\cdot0.5(MeCN)$ (**13**·0.5MeCN), and similar as **12**·2MeCN, it is a mixed oxidation state Fe(II)/Fe(III) system. The iron atom in the cation is five-coordinate with a trigonal bipyramidal pattern (τ=0.82);[7] the apical sites are occupied by O atoms, with the bromide and N atoms in the equatorial sites. There is a pseudo two-fold symmetry axis along the Fe-Br bond. In the macrocyclic ligand, there are four N atoms, each involved in a double bond, *viz* C11=N2 1.298(5) C52=N1 1.287(6) C26=N3 1.296 (6) C37=N4 1.308 (7), N1 and N3 are coordinated to the Fe atom, while N2 and N4 are bonded to two C atoms (one with a double bond) and a hydrogen atom. The hydrogen atoms were included in the structure factor calculations in a planar, trigonal fashion, and their Uiso values were refined freely and satisfactorily; It is believed that both these groups are charged C-N⁺H=C groups. Both these hydrogen atoms are involved in intramolecular hydrogen bonds.
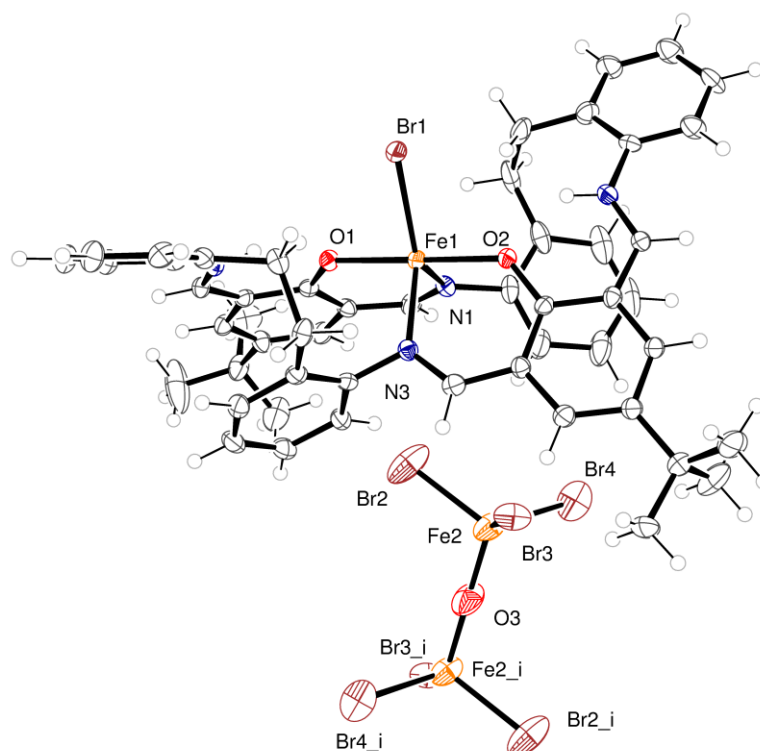
Figure 4-3. View of the [FeBr(L^{tBu})][(FeBr$_3$)$_2$O]$_{0.5}$·0.5(MeCN) (**13**·0.5MeCN) complex ion, indicating the atom numbering scheme. Thermal ellipsoids are drawn at the 50% probability level. Symmetry equivalent atoms are generated by i = 1–x, 1–y, 1–z. Selected bond lengths (Å) and angles (º): Fe(1) ‒ O(1) 2.052(3), Fe(1) ‒ O(2) 2.059(3), Fe(1) ‒ N(1) 2.131(4), Fe(1) ‒ N(3) 2.124(4), Fe(1) ‒ Br(1) 2.4967(8); Br(1) ‒ Fe(1) ‒ O(1) 89.71(9), O(1) ‒ Fe(1) ‒ N(3) 94.83(14).

The (FeBr$_3$)$_2$O anion lies about a centre of symmetry. One of the bromide ligands is disordered over two sites, in an 82:18 occupancy ratio. The nearest neighbours of the bromide atoms are atoms of the disordered *t*-butyl group.

Similar treatment of {[2-(OH)-5-(*t*Bu)-C$_6$H$_2$-1,3-(CH)$_2$][O(2-C$_6$H$_4$N)$_2$]}$_2$, but with limited FeBr$_2$ (1.1 equivalents), led to the isolation of the Fe(II) salt [FeBr(L^{tBu}H$_2$)]Br·5.5MeCN (**14**·5.5MeCN). The structure **14**·5.5MeCN contains Fe^{2+} which is five-coordinated in distorted tetrahedral geometry. The molecular structure is provided in Figure 4-4.
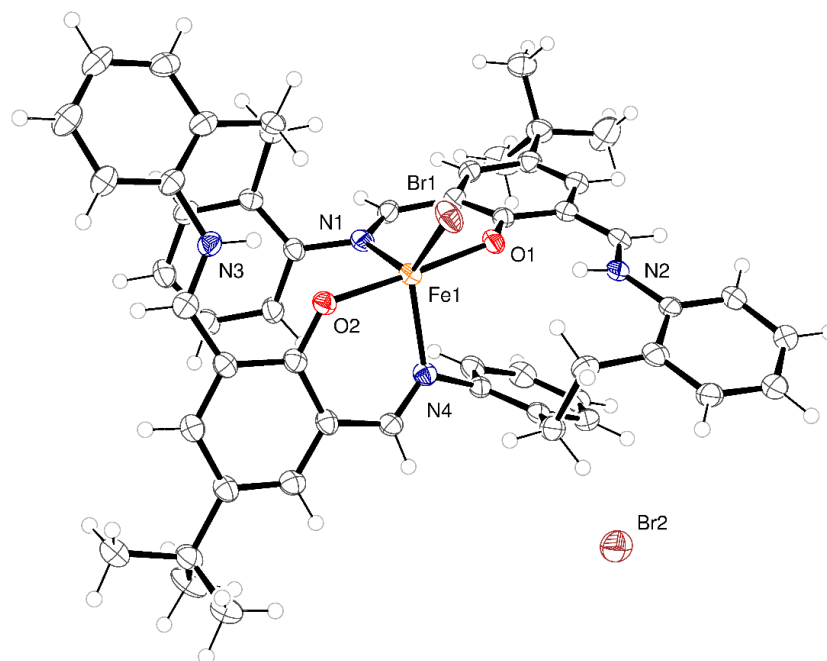
Figure 4-4. ORTEP plot of [FeBr(L^2H_2)][Br]·5.5MeCN (**14**·5.5MeCN).

Use of [KFe(O*t*Bu)$_3$(THF)]

Reaction of L^2H_2 with *in-situ* generated [KFe(O*t*Bu)$_3$(THF)] in refluxing toluene resulted, after work-up, in the isolation of a brown crystalline material. Crystals grown from a saturated solution of acetonitrile were found to be a *bis*-chelate structure [Fe(L^{tBu})(L^{tBu}H)]·3MeCN (**15**·3MeCN) (see Figure 4-5), in which a distorted octahedral iron(III) centre is bound to two of the macrocyclic ligands. The asymmetric unit contains one iron complex and 3 molecules of acetonitrile. The coordination at the iron is such that one macrocycle is bound only in chelate fashion via *N,O*-type ligation, whilst the second macrocycle utilizes four atoms to bind in 2x *N,O*-type fashion. Similar binding modes can be found in recently for aluminium.[3c]
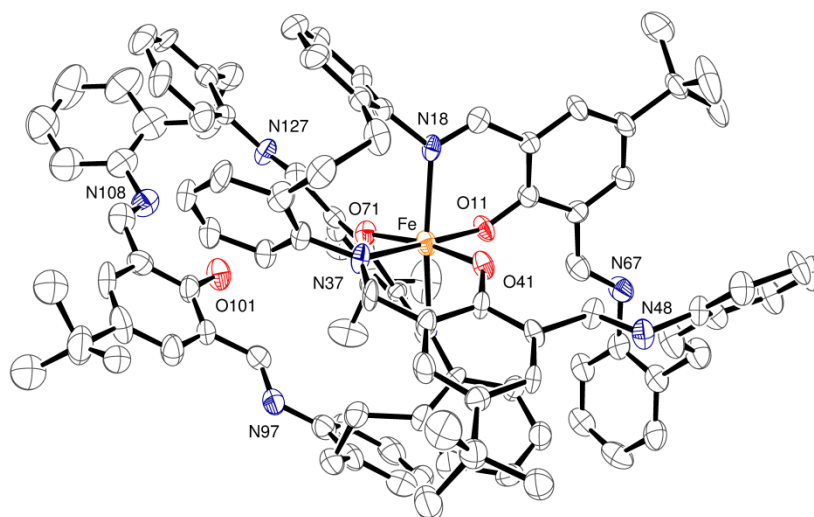
Figure 4-5. View of [Fe($\mathbf{L}^{t\mathbf{Bu}}$)($\mathbf{L}^{t\mathbf{Bu}}$H)]·3MeCN (**15**·3MeCN), indicating the atom numbering scheme. Thermal ellipsoids are drawn at the 50% probability level. For clarity hydrogen atoms are not shown. Selected bond lengths (Å) and angles (°): Fe(1) – O(11) 1.936(4), Fe – O(41) 1.931(4), Fe – O(71) 1.905(4), Fe – N(18) 2.234(5), Fe – N(37) 2.189(5), Fe – N(78) 2.240(5); O(11) – Fe – O(41) 92.1(2), O(11) – Fe – N(37) 176.6(2), N(18) – Fe – N(78) 164.0(2).

Use of copper bromide

Copper is also an earth abundant metal, though it has had only limited success in the ROP of cyclic esters.[8] For the successful systems, Schiff-base ligation appears beneficial, suggesting that interaction with the macrocyclic systems of the type herein could lead to a ROP active complex. Reaction of $\mathbf{L}^{t\mathbf{Bu}}\mathbf{H}_2$ with two equivalents of CuBr$_2$ afforded, following work-up, the orange/brown Cu salt complex [CuBr($\mathbf{L}^{t\mathbf{Bu}}\mathbf{H}_2$)][CuBr$_2$]·2MeCN (**16**·2MeCN) in good yield. In the cation, the copper centre is distorted trigonal bipyramidal with oxygens at the apex and two nitrogens and a bromide in the equatorial plane (τ=0.90).[7] The anion Cu(I)Br$_2^-$ resides close to a pocket formed by the macrocycle, see Figure 4-6.
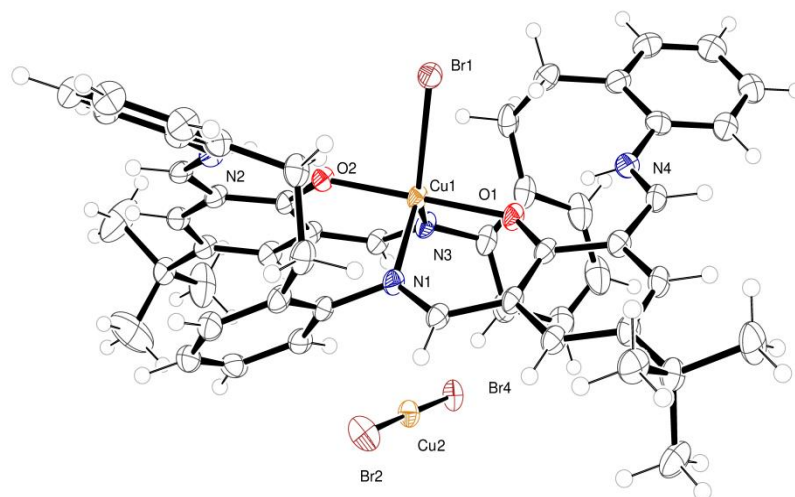
Figure 4-6. Molecular structure of [CuBr($L^{tBu}H_2$)][CuBr$_2$]·2MeCN (**16**·2MeCN) with atoms drawn as 50 % probability ellipsoids. Solvent molecules are not shown. Selected bond lengths (Å) and angles (°): Cu(1) – O(1) 1.955(3), Cu(1) – O(2) 1.948(3), Cu(1) – N(1) 2.106(3), Cu(1) – N(3) 2.074(3), Cu(1) – Br(1) 2.4790(6); O(1) – Cu(1) – O(2) 179.8(1), N(1) – Cu(1) – Br(1) 119.58(9), N(3) – Cu(1) – Br(1) 125.8(1).

Attempted mixed-metal systems

Having successfully isolated mixed cobalt/zinc systems (chapter 2 of this thesis), which were active for ring opening polymerization whereas the analogous homodinuclear species were not,[9] so the preparation of a mixed cobalt/titanium complexes was attempted. The entry point was again the cobalt complex [CoBr**L**^{tBu}H$_2$][CoBr$_3$(NCMe)], and reaction with [TiCl$_4$] resulted in [**L**^{tBu}H$_4$][CoBr$_4$]·2MeCN (**17**·2MeCN) as the only crystalline product. The molecular structure of the salt **17** comprises a protonated macrocycle **L**^{2}H$_2$ and the Co(II) containing anion [CoBr$_4$]$^{2-}$; see Figure 4-7 for details.
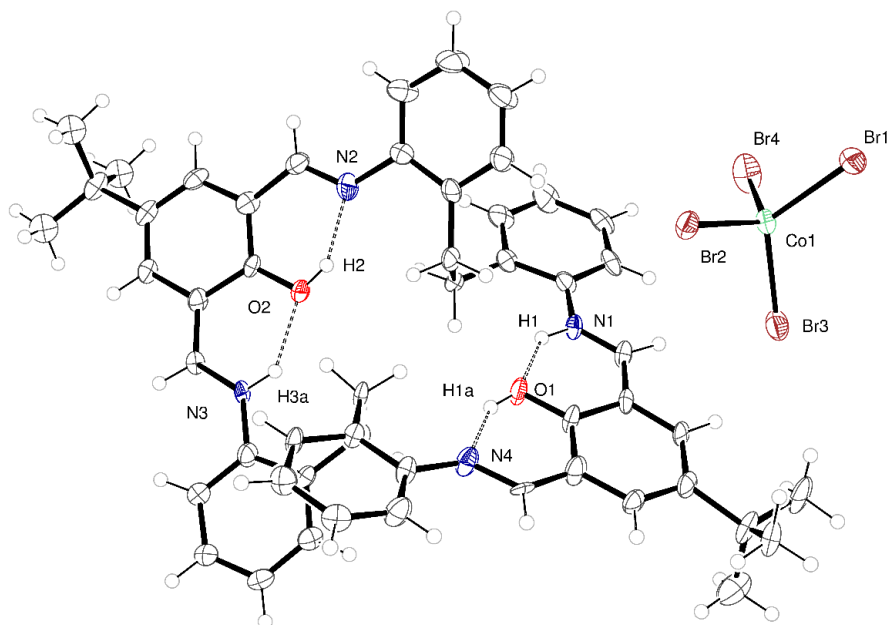
Figure 4-7. ORTEP plot of $[L^2H_2][CoBr_4] \cdot 2MeCN$ (**17**·2MeCN)

4.2.2 -O- bridged systems

Reaction of L^1H_2 $\{[2\text{-(OH)-5-Me-}C_6H_2\text{-1,3-}(CH)_2][O(2\text{-}C_6H_4N)_2]\}_2$ with two equivalents of $CoBr_2$ afforded, following work-up (acetone), the complex $[(CoBr)_2L^1] \cdot 2C_3H_6O$ (**18**·2C₃H₆O), containing two Co(II) centres, as black crystals in *ca*. 40 % isolated yield. Single crystals can be grown from a saturated solution of acetone at ambient temperature, and the molecular structure is shown in Figure 4-8; selected bond lengths and angles are given in the caption. Both cobalt centres adopt distorted trigonal bipyramidal with a bromide at each apex (τ=0.59 and 0.53 for Co1 and Co2, respectively).[7]
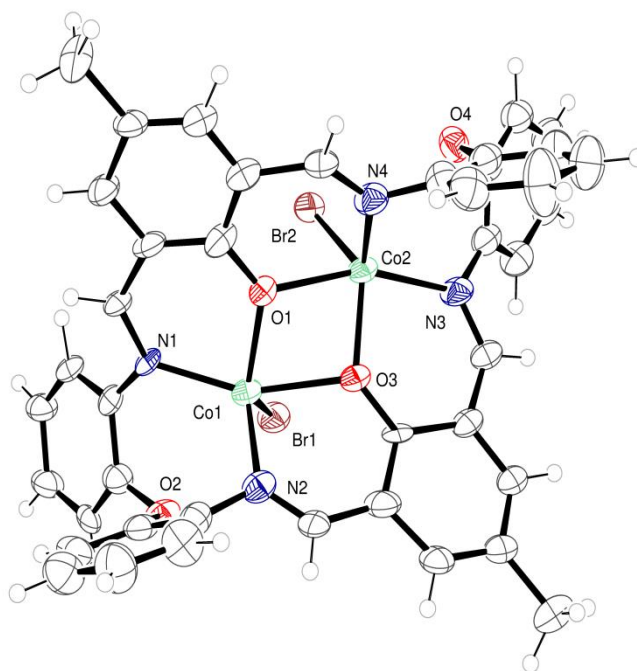
Figure 4-8. Molecular structure of $[(CoBr)_2(\mathbf{L^1})]\cdot 2C_3H_6O$ ($\mathbf{18}\cdot 2C_3H_6O$) with atoms drawn as 50 % probability ellipsoids. Selected bond lengths (Å) and angles (°): Co(1) – O(1) 1.982(11), Co(1) – O(3) 2.216(11), Co(1) – N(1) 2.067(12), Co(1) – N(2) 2.091(13), Co(1) – Br(1) 2.421(3), Co(2) – O(1) 2.179(11), Co(2) – O(3) 1.977(11), Co(2) – N(3) 2.102(14), Co(2) – N(4) 2.079(13), Co(2) – Br(2) 2.421(3); O(1) – Co(1) – O(3) 70.0(4), N(1) – Co(1) – N(2) 112.3(5), O(1) – Co(1) – Br(1) 122.2(3), O(1) – Co(2) – N(3) 157.8(5), N(4) – Co(2) – Br(2) 111.2(4).

In the case of $\mathbf{L^2}H_2$ {[2-(OH)-5-tBu-C_6H_2-1,3-(CH_2)][O(2-C_6H_4N)$_2$]}$_2$, reaction with CoBr$_2$ afforded, following work-up (MeCN), two sets of crystals (~90:10). Both sets were subjected to single crystal X-ray diffraction, and the major product, as shown in Figure 4-9, was found to be the Co(II) containing salt [Co(NCMe)$_2$($\mathbf{L^2}H_2$)][CoBr$_4$]·5MeCN ($\mathbf{19}\cdot 5$MeCN). In the cation, the cobalt centre is distorted octahedral, and is bound by two phenoxide oxygens and the two nitrogens N(1) and N(3) of the macrocycle plus two bound acetonitrile ligands. In the solid-state, there are C-H $\cdots$ Br interactions present. The minor product was

96

found to be Co(II) containing salt $[Co(NCMe)_6][CoBr_3NCMe]_2\cdot 2MeCN$ (**20**$\cdot$2MeCN), details of this structure can be found in Figure 4-10.
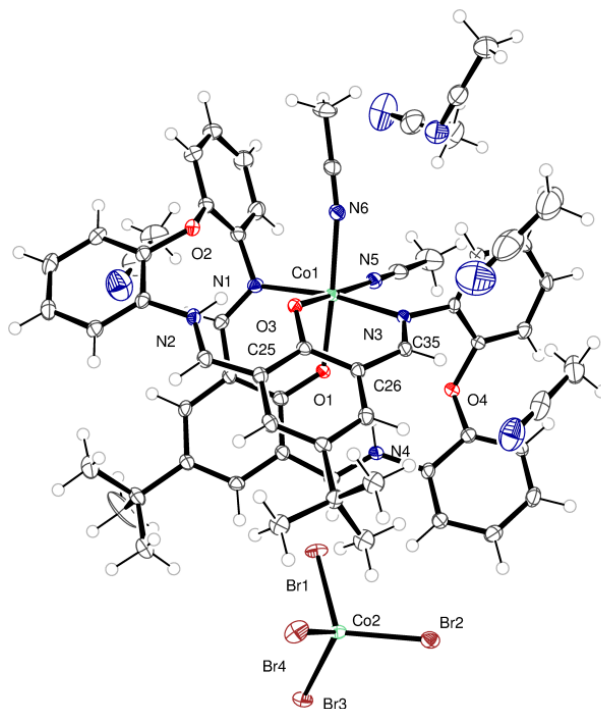
Figure 4-9. Molecular structure of $[Co(NCMe)_2(\mathbf{L^2})][CoBr_4]\cdot 5MeCN$ (**19**$\cdot$5MeCN) with atoms drawn as 50 % probability ellipsoids. Selected bond lengths (Å) and angles (°): Co(1) – O(1) 2.016(3), Co(1) – O(3) 2.056(3), Co(1) – N(1) 2.156(3), Co(1) – N(3) 2.156(3), Co(1) – N(5) 2.121(3), Co(1) – N(6) 2.114(3); O(1) – Co(1) – O(3) 91.98(11), N(1) – Co(1) – N(3) 169.15(12), O(1) – Co(1) – N(6) 174.71(13), O(3)-Co(1)-N(5) 174.77(13)°.
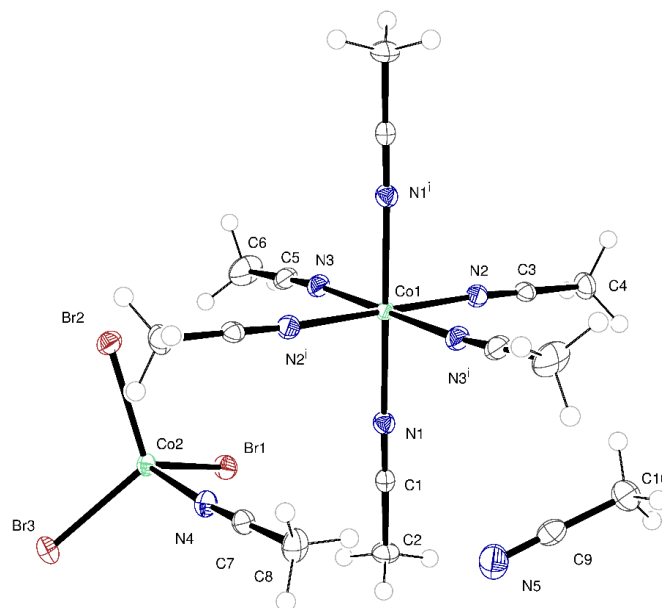
Figure 4-10. ORTEP plot of expanded asymmetric unit [Co(NCMe)$_6$][CoBr$_3$NCMe]$_2$·2MeCN (**20**·2MeCN); atoms labelled I are generated by the symmetry operator 4/3-x, 2/3-y, 2/3-z. Selected bond lengths (Å) and angles (°): Co(1)–Br(1) 2.4874(12), Co(1)–O(11) 2.041(4), Co(1)–O(14) 2.009(4), Co(1)–N(37) 2.072(6), Co(1)–N(67) 2.081(6); O(11)–Co(1)–O(41) 176.64(19), N(37)–Co(1)–N(67) 110.3(2), O(11)–Co(1)–Br(1) 86.10(15).

4.2.3 'Dialdehyde' systems

To probe the role played by the presence of the macrocycle during catalysis (see ROP section at the end of this chapter), cobalt complexes bearing chelate ligands derived from the 4-*tert*-butyl-2,6-diformylphenol 2,6-(CHO)$_2$-4-*t*Bu-C$_6$H$_2$OH (**L^{4}H**) were also prepared. Reaction of **L^{4}H** with CoBr$_2$ in the presence of excess Et$_3$N afforded, after work-up (MeCN), the Co(II) complex {[CoBr(NCMe)]**L^4**}$_2$·2MeCN (**21**·2MeCN) as orange/brown prisms in good yield. The molecular structure is shown in Figure 4-11, with selected bond lengths and angles given in the caption. Each cobalt centre is distorted octahedral, and are

bound by oxygens from two ligands and a bromide and acetonitrile ligand. The ligand arrangement is such that one bromide and an MeCN ligand reside above the Co_2O_6 plane and one bromide and an MeCN ligand are below this plane.
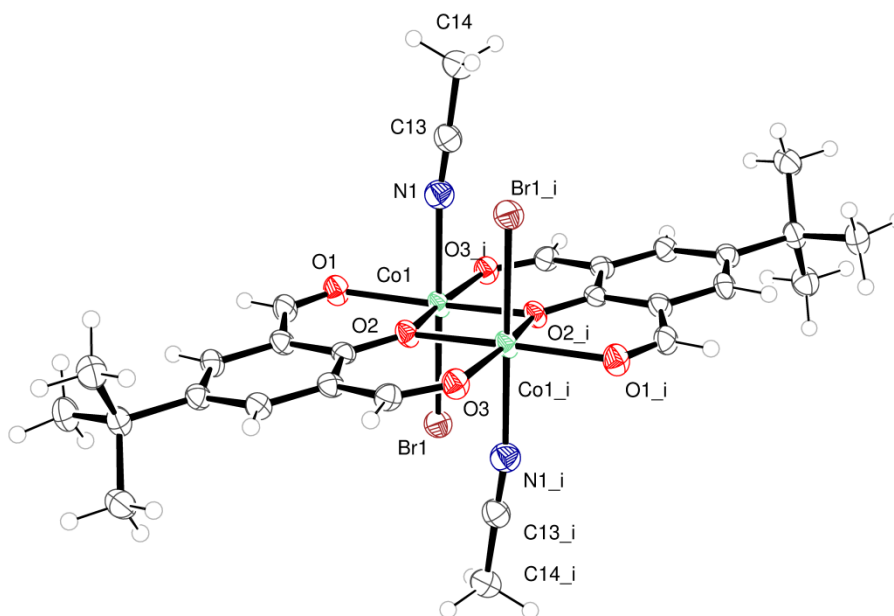
Figure 4-11. Molecular structure of $\{[CoBr(NCMe)]L^4\}_2 \cdot 2MeCN$ (**21**·2MeCN) with atoms drawn as 50% probability ellipsoids. (Unbound solvent not shown) Selected bond lengths (Å) and angles (°): Co(1) – O(1) 2.052(2), Co(1) – O(2) 2.079(2), Co(1) – Br(1) 2.5751(6), Co(1) – N(1) 2.163(3); O(1) – Co(1) – O(2) 87.17(8), Co(1) – O(2) – Co(1_i) 100.59(9), Br(1) – Co(1) – N(1) 169.51(8).

The structure **21**·2MeCN contains Co^{2+} in both octahedral and distorted tetrahedral geometry. The $[Co(NCMe)_6]^{2+}$ ion resides on an inversion centre and is a little distorted from a perfect octahedron despite the six identical ligands. $[CoBr_3NCMe]$ formally has C_{3v} symmetry at the metal centre.

If the same reaction is conducted in the absence of Et_3N, then, following work-up (MeCN), green prisms are isolated in good yield. The molecular structure (see

Figure 4-12 for the cation) revealed the structure of the complex to be the Co(II) containing salt [Co(NCMe)$_2$**L^4**]$_2$[CoBr$_3$(NCMe)]$_2$ (**22**). The dimer is centrosymmetric – the second half of the dimer is generated by the symmetry operation –x, 1-y, 1-z. Each cobalt centre in the cation is distorted octahedral, but unlike **21**, there is no bound bromide.
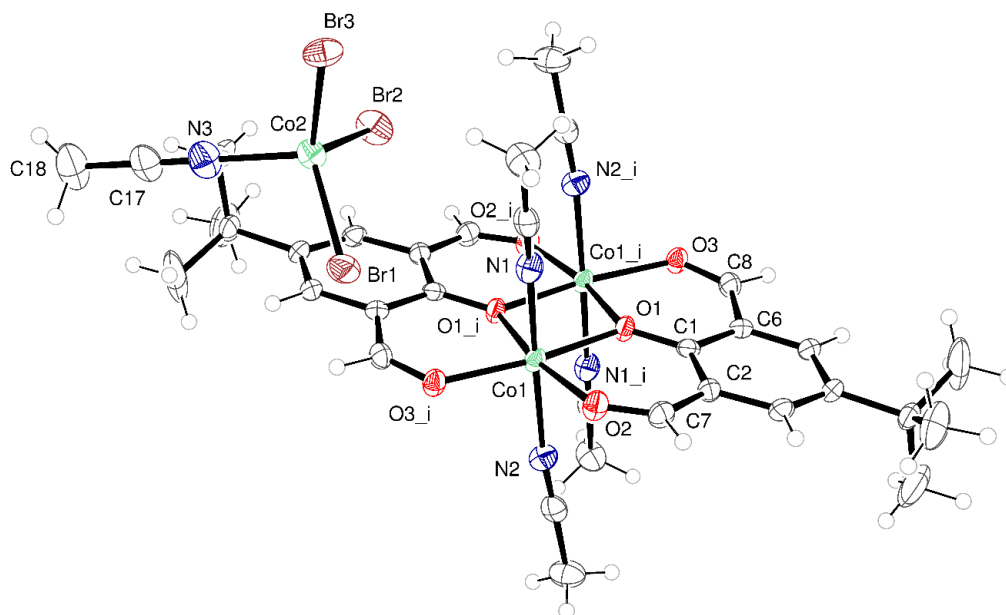
Figure 4-12. Molecular structure of [Co(NCMe)$_2$**L^4**]$_2$[CoBr$_3$(NCMe)]$_2$ (**22**) with atoms drawn as 50 % probability ellipsoids. Symmetry operation used to generate equivalent atoms: i = –x, 1–y, 1–z. Selected bond lengths (Å) and angles (°): Co(1) – O(1) 2.046(2), Co(1) – O(2) 2.050(2), Co(1) – N(1) 2.108(3), Co(1) – N(2) 2.143(3); O(1) – Co(1) – O(2) 88.56(9), Co(1) – O(2) – Co(1i) 99.59(9), N(1) – Co(1) – N(2) 172.07(11).

If a similar reaction is conducted with FeBr$_2$ in the presence of Et$_3$N, then, following work-up (MeCN), black prisms are isolated in good yield. The molecular structure revealed the structure of the Fe(II) complex to be [FeBr(NCMe)**L^4**]$_2$·2MeCN (**23**·2MeCN). Each iron centre in the cation is distorted

100

octahedral, bound by oxygens from two L ligands, a bromide and an acetonitrile ligand, see Figure 4-13.
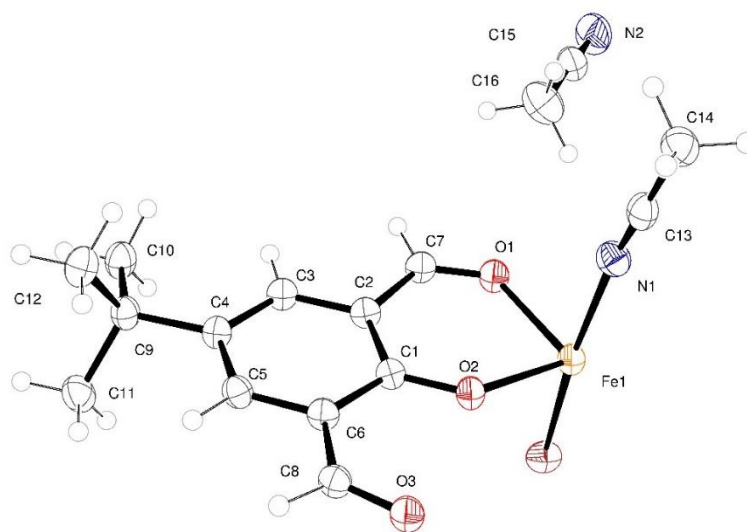
Figure 4-13. ORTEP plot of [FeBr(NCMe)$\mathbf{L^4}$]$_2$·2MeCN (**23**·2MeCN); N(1) – Fe(1) 2.210(2), O(1) – Fe(1) 2.0488(16), Fe(1) – Br(1) 2.6034(4), C(13) – N(1) – Fe(1) 171.5(2), C(7) – O(1) – Fe(1) 128.99(15), C(1) – O(2) – Fe(1) 129.84(13), Fe(1) – O(2) – Fe(1) 99.86(6), O(1) – Fe(1) – O(3) 105.97(6).

Finally, for comparative catalytic studies, the salt [Fe(NCMe)$_6$][FeBr$_3$OFeBr$_3$] (**24**) was prepared from $\mathbf{L^1}$H$_2$ and FeBr$_3$ (see Figure 4-14).
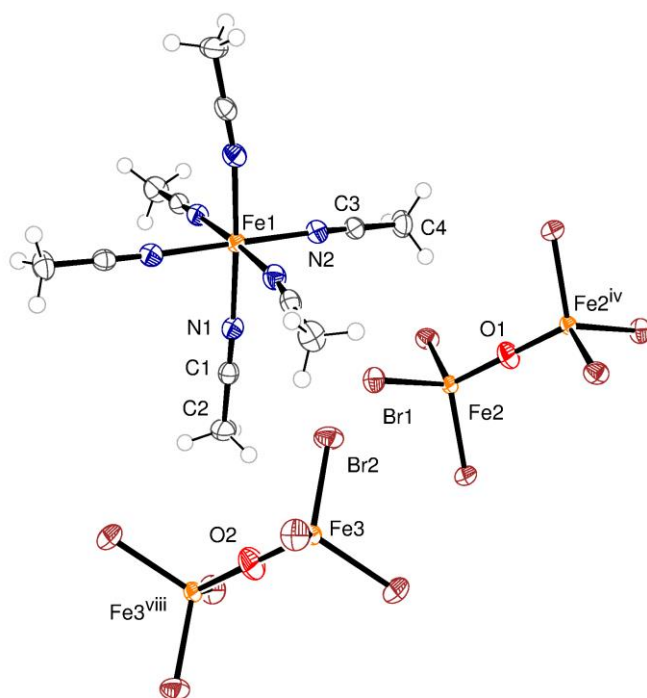
Figure 4-14. ORTEP plot of [Fe(NCMe)$_6$][FeBr$_3$OFeBr$_3$] (**24**); atoms labelled I are generated by the symmetry operator 2-x, 2-y, 1-z. Selected bond lengths (Å) and angles (°): Fe(1) – N(1) 2.159(2), Fe(1) – N(2) 2.162(2), Fe(1)–Br(1) 2.3634(3), Fe(2) – O(1) 1.7664(6), Fe(3) – O(2) 1.7625(6); N(1) – Fe(1) – N(2) 89.77(7).

4.2.4 Ring opening polymerization (ROP) of ε-CL or δ-VL

The Fe, Cu and Co complexes **12**, **13**, **15**, **16**, **20** - **24** have been screened for their ability to ring open polymerise ε-caprolactone (ε-CL) and δ-valerolactone (δ-VL); runs were conducted in the presence of benzyl alcohol (BnOH). For complexes **12**, **13** and **15**, a variety of conditions were used in the attempted ROP of ε-CL including differing ratios of [ε-CL]:[Cat]:[BnOH] and run times, and it was found that the Fe compounds were far more active than the other metal complexes screened in this chapter. ROP systems based on Fe[6], Cu[8] and Co[10] have been reported with mixed success.

Table 4-1. Synthesis of polycaprolactone from using Fe complexes.

Run	Cat.	[monomer]:[Cat] :BnOH	T(℃)	t/h	Conv.(%)[a]	$Mn \times 10^{3b}$	$Mn_{Calcd} \times 10^{4c}$	PDI[d]
1	12	500:1:1	130	24	63.2	3.70	3.61	1.95
2	12	250:1:1	130	24	88.7	2.95	2.54	3.28
3	12	500:1:1	130	12	79.4	0.97	4.53	1.11
4	12	500:1:1	130	12	66.3	0.70	3.79	1.17
5	13	500:1:1	130	24	99.3	5.92	5.66	1.56
6	13	250:1:1	130	24	55.0	2.60	1.58	1.06
7	15	500:1:1	130	24	68.9	8.67	3.94	1.75
8	15	250:1:1	130	24	87.6	7.52	2.50	1.58
9	20	500:1:1	130	24	-	-	-	-
10	21	500:1:1	130	24	-	-	-	-
11	22	500:1:1	130	24	-	-	-	-
12	23	500:1:1	130	24	8.4	-	0.45	-
13	24	500:1:1	130	24	15.3	-	0.87	-

[a] Conversion was confirmed by ^{1}H NMR spectroscopy. [b] Determined by GPC analysis calibrated with polystyrene standards and multiplied by correction factor of 0.56. [c] F.W.[M]/[BnOH])(conversion)+BnOH [d] Polydispersity index (M_w/M_n) were determined by GPC.

The polymerization data for the ε-CL runs is given in Table 4-1. Highest conversion was achieved using 13 in run 5 using the ratio 500:1:1 at 130 ℃ over 24h, albeit with less control than observed in run 6 using 250:1:1. Systems employing 12 and 15 were also less controlled, whilst the non-macrocyclic cobalt systems 20 - 22 proved to be inactive under the conditions employed herein. Interestingly, the non-macrocyclic iron complexes 23 and 24 proved to be poorly active with low conversions for ε-CL. However, for δ-VL, a 32% conversion (affording small molecular weight oligomers) was observed for 24, whereas 23 was inactive. Most of the runs showing good control with PDIs besides run 2.

Table 4-2. Synthesis of polyvalerolactone using Fe complexes.

Run	Cat.	[VL]: [Cat] :BnOH	T(℃)	t/h	Conv.%[a]	$Mn \times 10^{3b}$	$Mn_{Calcd} \times 10^{4c}$	PDI[d]
1	12	500:1:1	130	24	98.6	2.52	4.94	1.14
2	12	250:1:1	130	24	94.3	3.10	2.36	1.28
3	12	500:1:1	130	12	39.7	-	2.00	-
4	13	500:1:1	130	24	96.1	6.00	4.92	1.38
5	13	250:1:1	130	24	93.2	4.53	2.41	1.23
6	13	500:1:1	130	12	83.8	-	4.20	-
7	15	500:1:1	130	24	34.5	2.59	1.84	1.25
8	15	250:1:1	130	24	23.5	2.51	0.60	1.27
9	16	500:1:1	130	24	-	-	-	-
10	20	500:1:1	130	24	-	-	-	-
11	21	500:1:1	130	24	-	-	-	-
12	22	500:1:1	130	24	-	-	-	-
13	23	500:1:1	130	24	-	-	-	-
14	24	500:1:1	130	24	32.0	0.76	2.18	1.26

[a] Conversion was confirmed by ^{1}H NMR spectroscopy. [b] Determined by GPC analysis calibrated with polystyrene standards and multiplied by correction factor of 0.58. [c] F.W.[M]/[BnOH])(conversion)+BnOH [d] Polydispersity index (M_w/M_n) were determined by GPC.
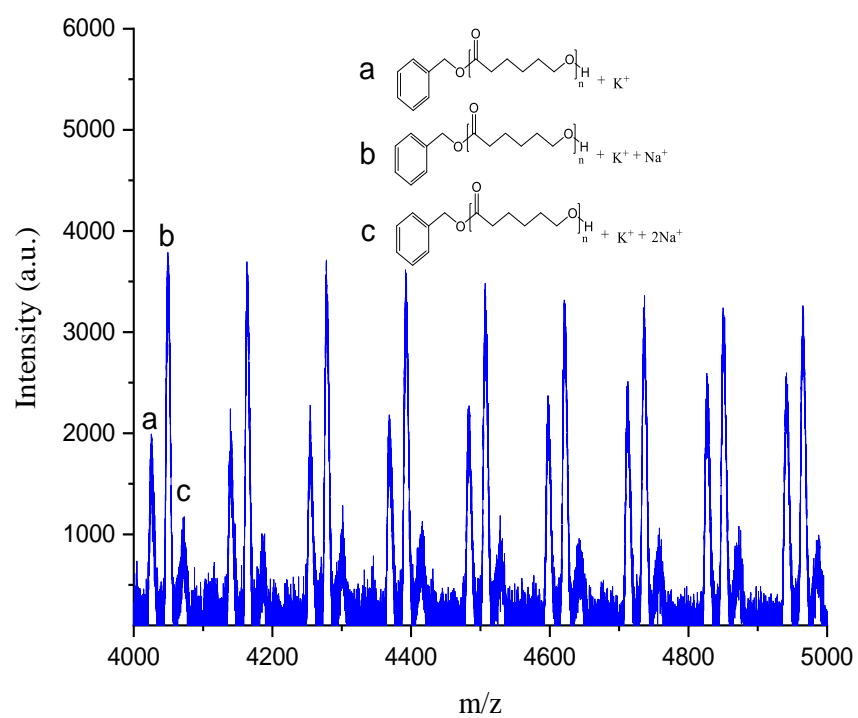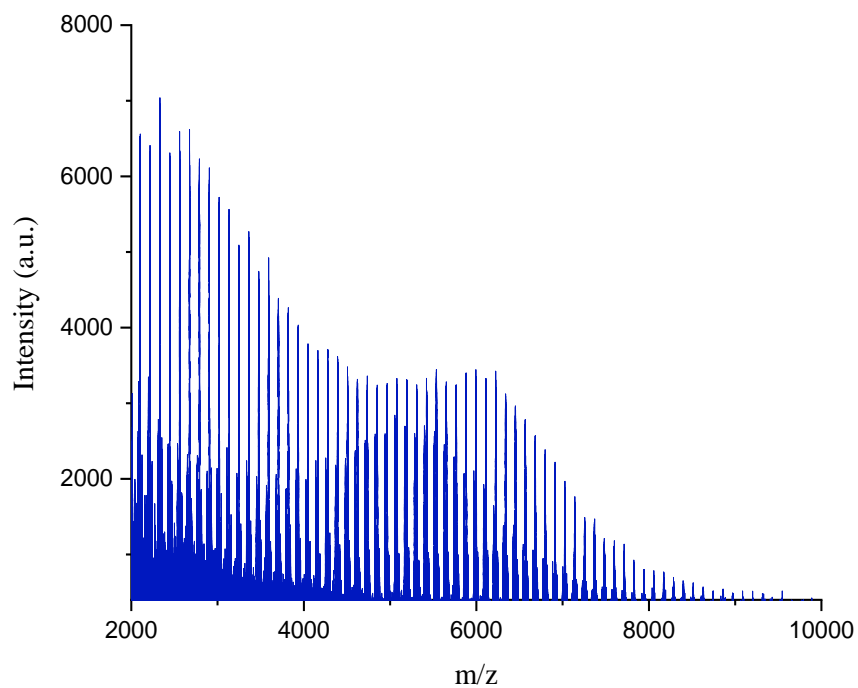
Figure 4-15. MALDI-ToF mass spectrum for polycaprolactone (run 5, Table 4-1).

The MALDI-TOF spectra can be interpreted using the formula $C_6H_5\text{-}CH_2O[O(CH_2)_5CO]_nOH$, for example see run 5 in table 4-2 (Figure 4-15). The ^{1}H NMR spectrum of the PCL indicated the presence of benzyloxy and hydroxyl end groups (Figure 4-16). There was evidence of significant transesterification, whilst all observed M_n values were significantly lower than the calculated values.

In the case of δ-VL, complexes **12** and **13** exhibited better conversions *versus* **15** and **23**, whilst **16**, **20**, **21** and **22** proved to be inactive (Table 4-2). From a kinetic study (Figure 4-17 and Figure 4-18), it was observed that the polymerization rate exhibited near first order dependence on the ε-CL or δ-VL concentration at 130 °C, and complex **13** displayed the best rate in both δ-VL [$K_{obs}=7.29\times10^{-3}(h^{-1})$] and ε-CL polymerizations [$K_{obs}=4.70\times10^{-3}(h^{-1})$]. The ^{1}H NMR spectra of the PVL (e.g Figure 4-19) revealed the presence of benzyloxy and OH end groups. The observed molecular weights were lower than the calculated values, suggesting the presence of a chain transfer agent (H_2O or BnOH). In the MALDI-TOF mass spectra of the PVL, a number of families of peaks were observed separated by 100 mass units (Figure 4-20) can be assigned by the formula $C_6H_6\text{-}CH_2O[O(CH_2)_4CO]_nOH$; the highest were typically about 6000 (run 4, Figure 4-21). All the runs showing good control with PDIs in range 1.14-1.38.
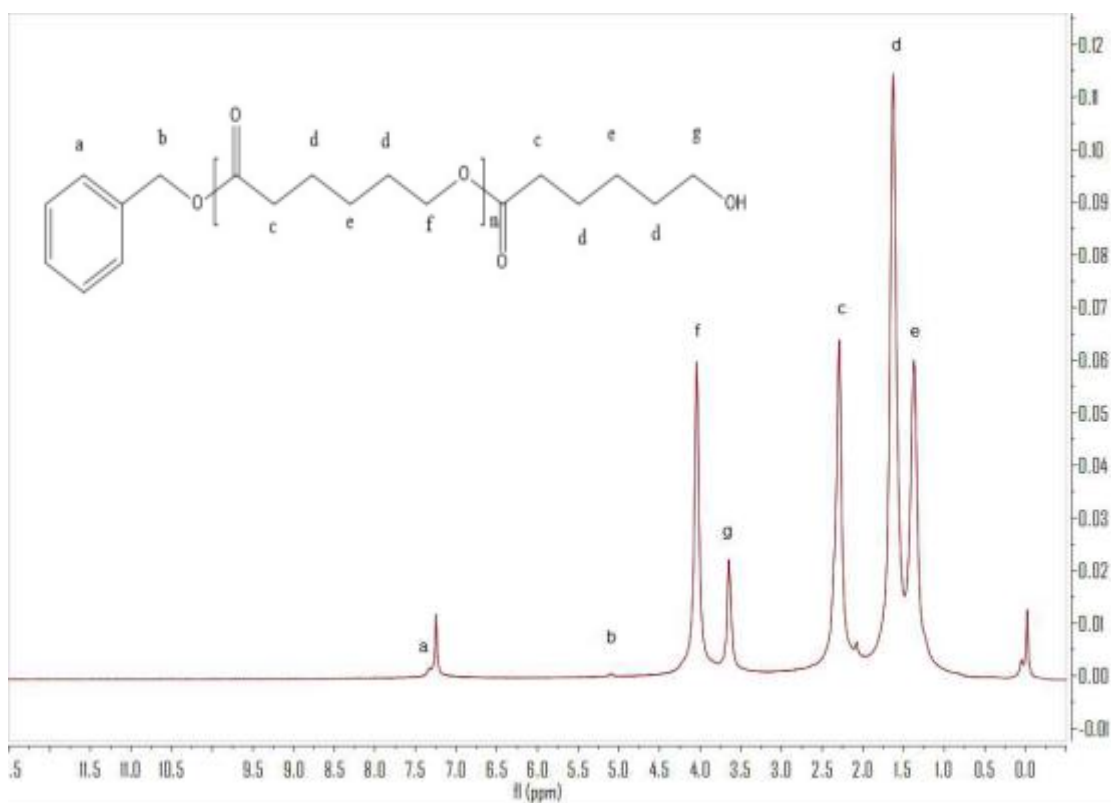
Figure 4-16. ^{1}H NMR (400 MHz, CDCl$_3$) spectrum for polycaprolactone (run 5, Table 4-1).
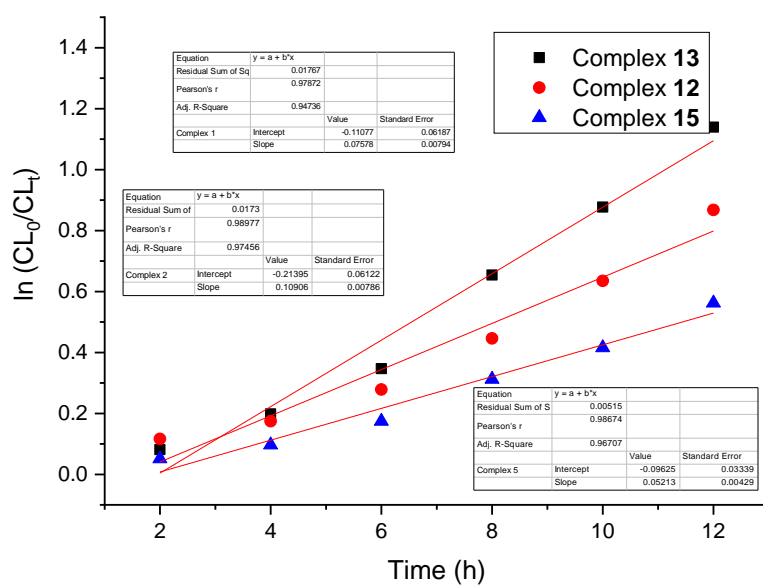
Figure 4-17. Plot of ln [CL]$_0$/[CL]$_t$ *vs*. time using Fe complexes ([monomer]:[Cat] :BnOH=500:1:1; 130 °C).
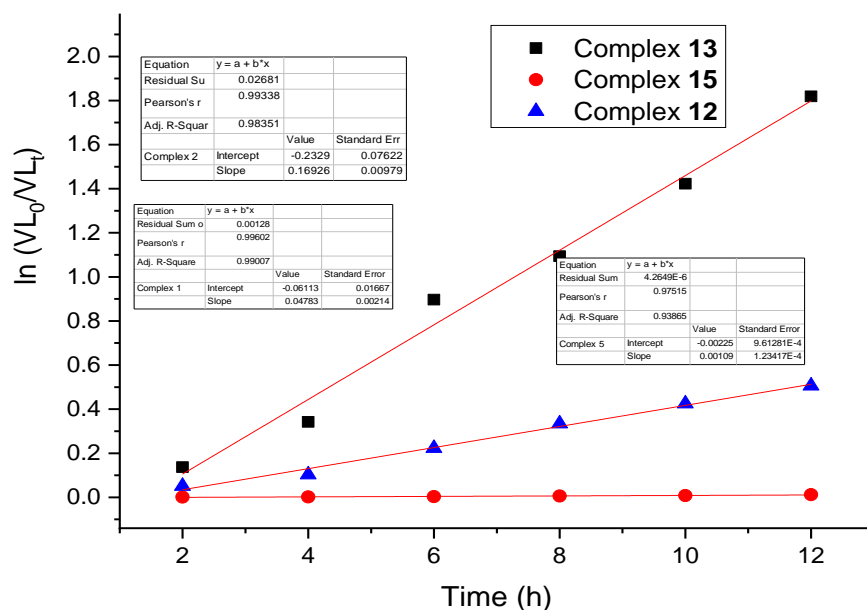
Figure 4-18. Plot of ln [VL]$_0$/[VL]$_t$ *vs*. time using Fe complexes ([monomer]:[Cat]:

BnOH=500:1:1; 130 ℃).
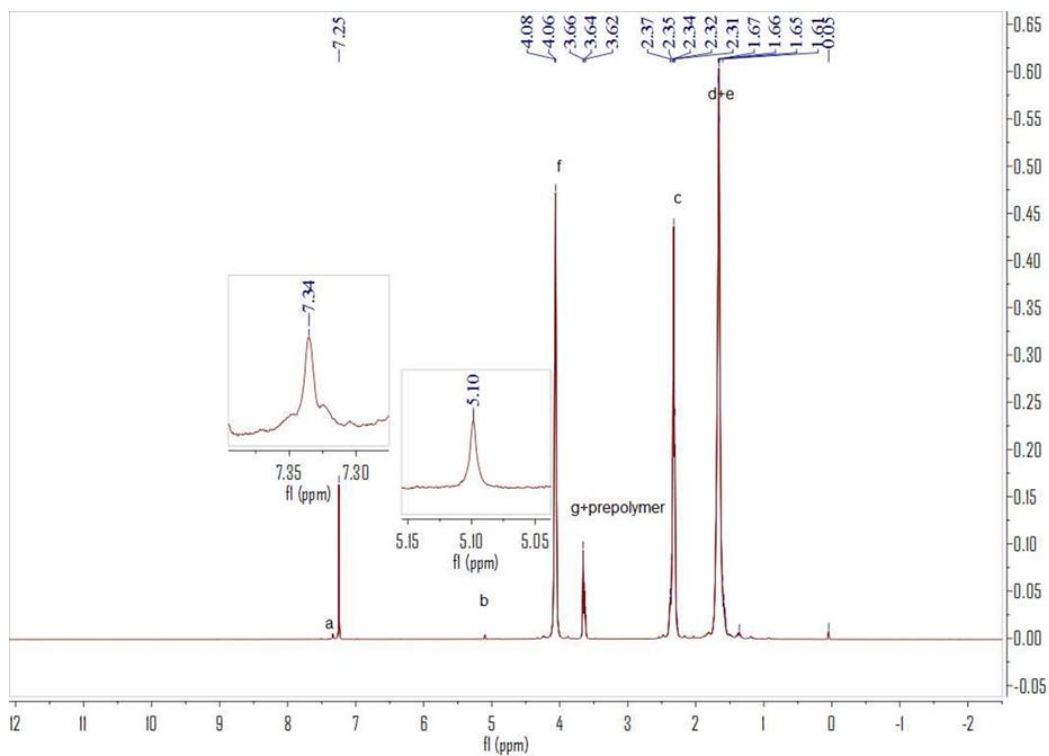
Figure 4-19. ^{1}H NMR (400 MHz, CDCl$_3$) spectrum for polyvalerolactone (run 4, Table

4-2).

Figure 4-20. M_w *vs* number of δ-VL repeat units (n) afforded a straight line with a slope of 100.6 and an intercept of 131; the slope corresponds to the exact mass of the δ-VL monomer, whereas the intercept corresponds to a polymer chain structure with benzyloxy chain-ends plus Na^+ (δ-VL run 4, Table 4-2).
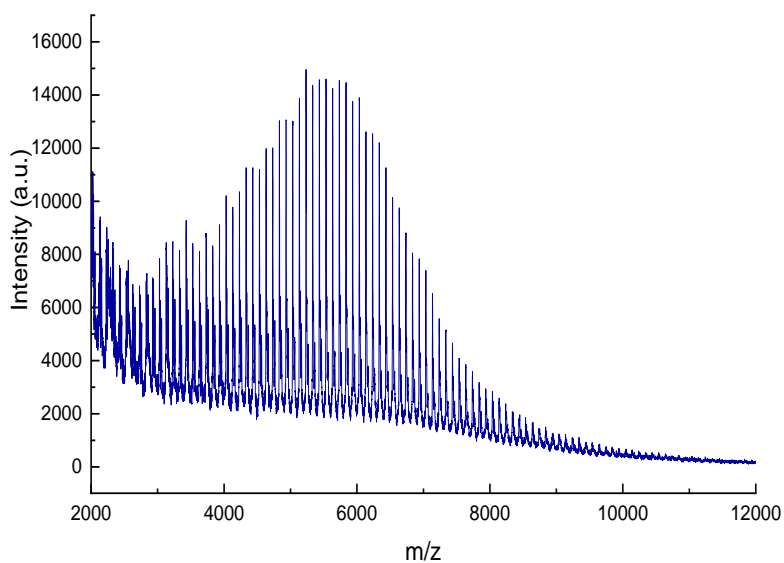
Figure 4-21. MALDI-ToF mass spectrum for polyvalerolactone (run 4, Table 4-2).

Synthesis of block co-polymers

The co-polymerization of ε-CL with *r*-LA and of δ-VL with *r*-LA was also examined (Table 4-3). Noteworthy, the co-polymerization of ε-CL with *r*-LA is much easier than δ-VL with *r*-LA when using the Fe complexes. In the presence of complex **13**, the M_n of the block co-poly(ε-CL+ *r*-LA) reached around 12000. From the MALDI-ToF mass spectrum (positive mode) of poly(ε-CL+*r*-LA) a gap of 114 corresponding to the molecular weight of ε-CL was evident, whilst running the spectra in negative method revealed a gap of 144 corresponding to the molecular weight of *r*-LA (Figure 4-22 and Figure 4-23). Complexes **12** and **15** were less active in these co-polymerizations. As observed by ^{1}H NMR spectroscopy (Figure 4-24 and Figure 4-28), the co-polymers were also capped by benzyloxy and hydroxyl end groups. The 2D J-resolved ^{1}H NMR spectrum for the copolymer was also recorded and the peaks were assigned to the corresponding tetrads (see Figure 4-26 and Figure 4-27) according to literature reports,[11] which revealed an atactic LA-LA-LA chain. The composition of the copolymer was further illustrated by

110

^{13}C NMR spectroscopy (Figure 4-25 and Figure 4-29). The MALDI-ToF mass spectrum for co-poly (δ-VL+r-LA) was also recorded, see Figure 4-30.

Table 4-3. Synthesis of block copolymers from cyclic ester monomers using the Fe complexes.

Run	Composition	Catalyst	t(h)	Incorporated amount[a]	$M_n \times 10^{3[b]}$	PDI
1	Poly (ε-CL+ r-LA) [ε-CL]:[r-LA]:[cat]:[BnOH]= 500:500:1:1	12	24+24	ε-CL: r-LA= 47:53	3.75	2.22
2	Poly (δ-VL+r-LA) [δ-VL]:[r-LA]:[cat]:[BnOH]= 500:500:1:1	12	24+24	δ-VL: r-LA= 14:86	5.51	1.73
3	Poly (r-LA+ ε-CL) [r-LA]:[ε-CL]:[cat]:[BnOH]= 500:500:1:1	13	24+24	r-LA: ε-CL= 49:51	10.55	1.51
4	Poly (r-LA+ ε-CL) [ε-CL]:[r-LA]:[cat]:[BnOH]= 250:250:1:1	13	24+24	r-LA: ε-CL= 93:7	6.20	1.82
5	Poly (ε-CL+ r-LA) [ε-CL]:[r-LA]:[cat]:[BnOH]= 500:500:1:1	13	24+24	ε-CL: r-LA= 60:40	9.31	1.64
6	Poly (ε-CL+ r-LA) [ε-CL]:[r-LA]:[cat]:[BnOH]= 250:250:1:1	13	24+24	ε-CL: r-LA= 63:37	12.63	3.02
7	Poly (δ-VL+r-LA) [δ-VL]:[r-LA]:[cat]:[BnOH]= 500:500:1:1	13	24+24	δ-VL: r-LA= 55:45	3.40	1.26

8	Poly (δ-VL+*r*-LA) [δ-VL]:[r-LA]:[cat]:[BnOH]= 250:250:1:1	**13**	24+24	δ-VL: *r*-LA= 88:12	2.57	2.56
9	Poly (ε-CL+ *r*-LA) [ε-CL]:[r-LA]:[cat]:[BnOH]= 500:500:1:1	**15**	24+24	ε-CL: *r*-LA= 100:0	4.61	1.23
10	Poly (ε-CL+ *r*-LA) [ε-CL]:[r-LA]:[cat]:[BnOH]= 250:250:1:1	**15**	24+24	ε-CL: *r*-LA= 90:10	3.61	1.18

[a] Conversion was confirmed by ^{1}H NMR spectroscopy. [b] Determined by GPC analysis calibrated with polystyrene standards and multiplied by correction factor of 0.56.
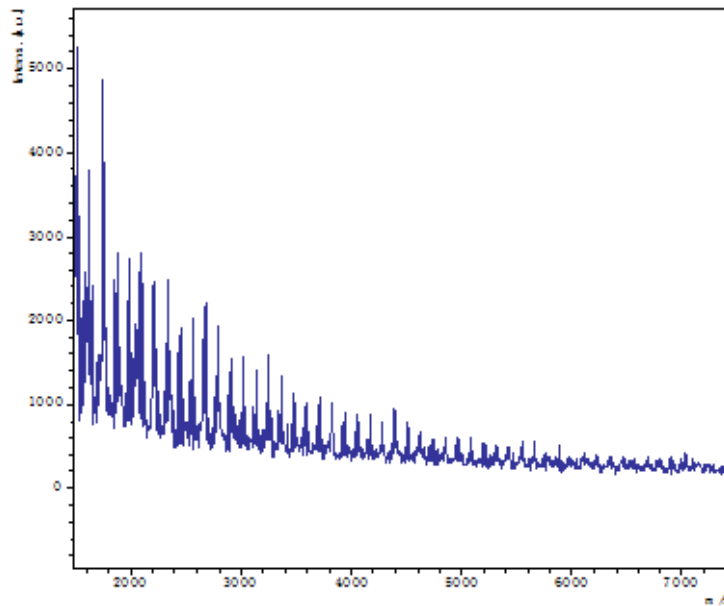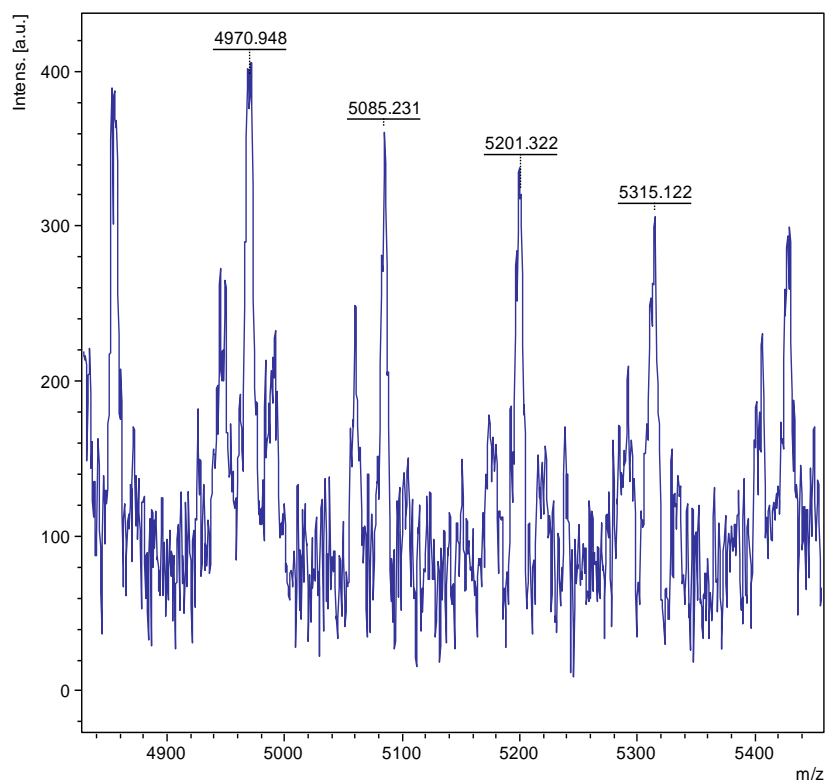
Figure 4-22. MALDI-ToF mass spectrum positive method for co-poly (ε-CL+ *r*-LA) (run 5, Table 4-3). The gap of 114 corresponds to the molecular weight of ε-CL.
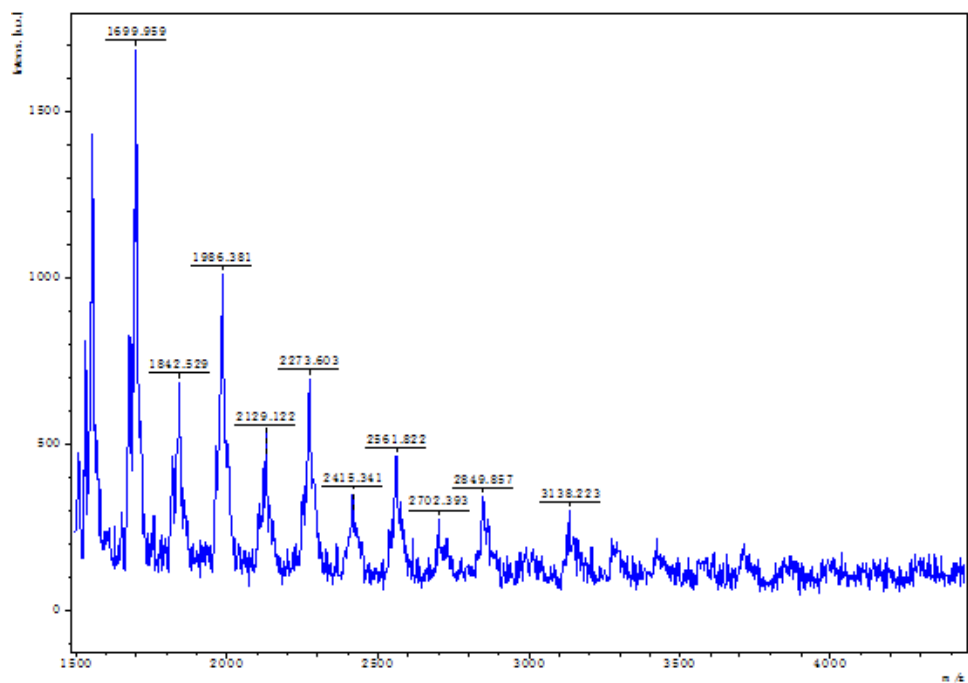
Figure 4-23. MALDI-ToF mass negative method spectrum for co-poly (ε-CL+ *r*-LA) (run 5, Table 4-3). The gap of 144 corresponds to the molecular weight of *r*-LA.
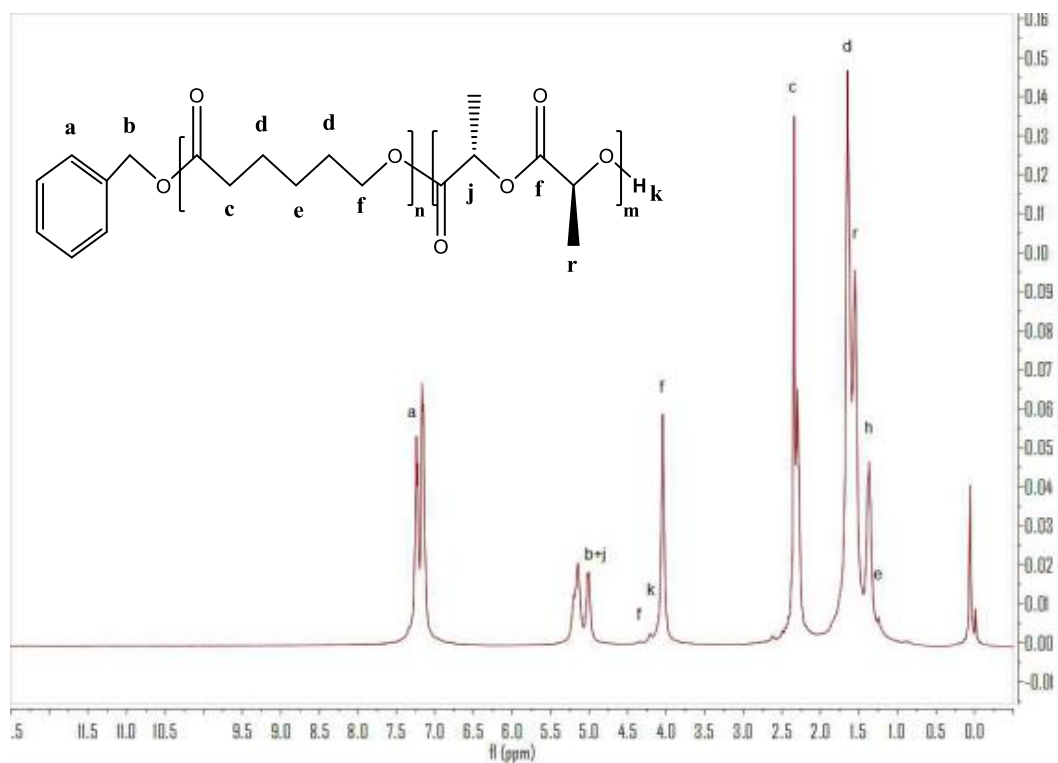
Figure 4-24. ^{1}H NMR spectrum for co-poly (ε-CL+ r-LA) (run 5, Table 4-3).
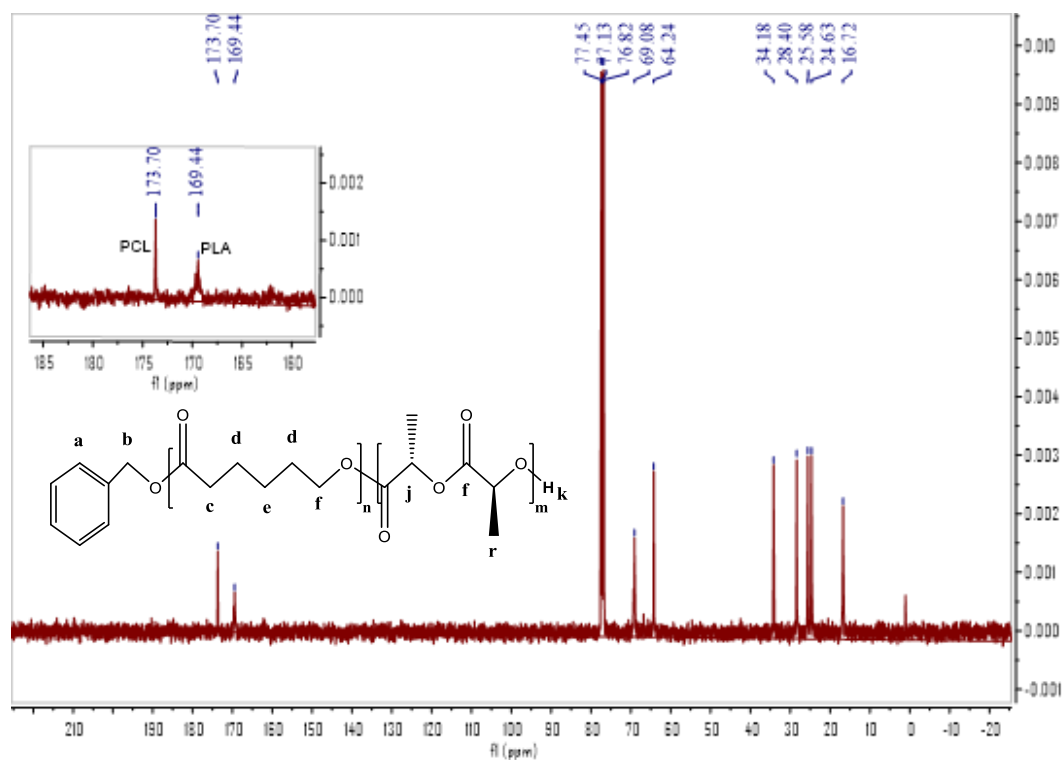
Figure 4-25. ^{13}C NMR spectrum for co-poly (ε-CL+ r-LA) (run 5, Table 4-3).
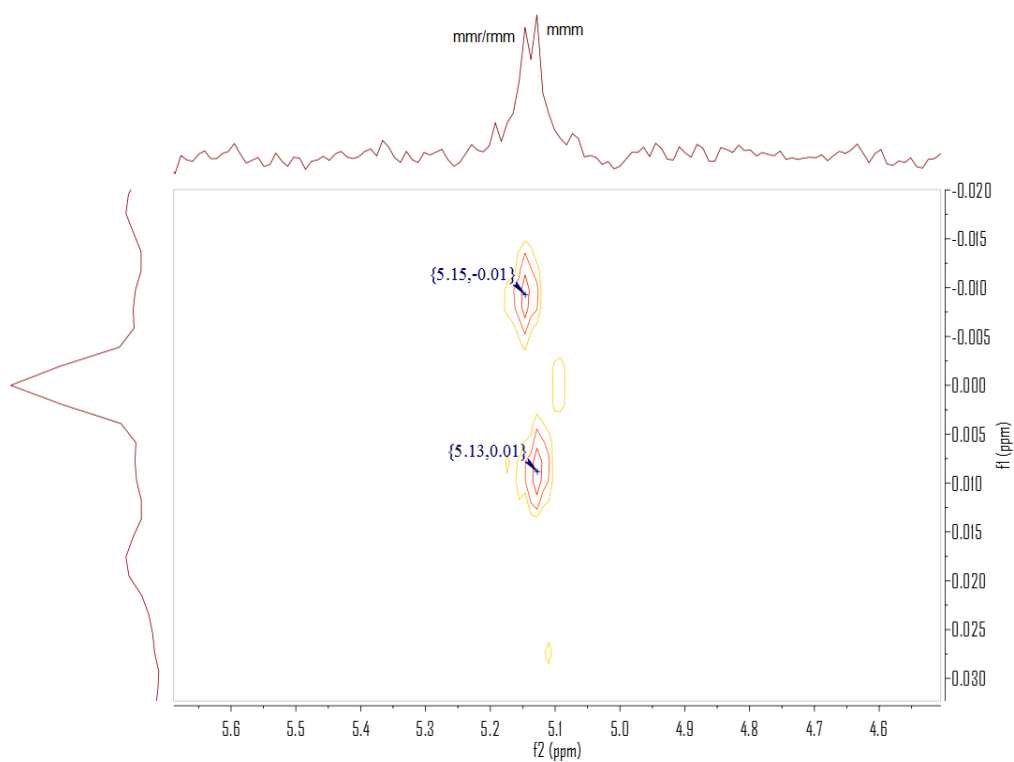
Figure 4-26. 2D J-Resolved ^{1}H NMR spectrum for co-poly (ε-CL+ *r*-LA) (run 5, Table 4-3).
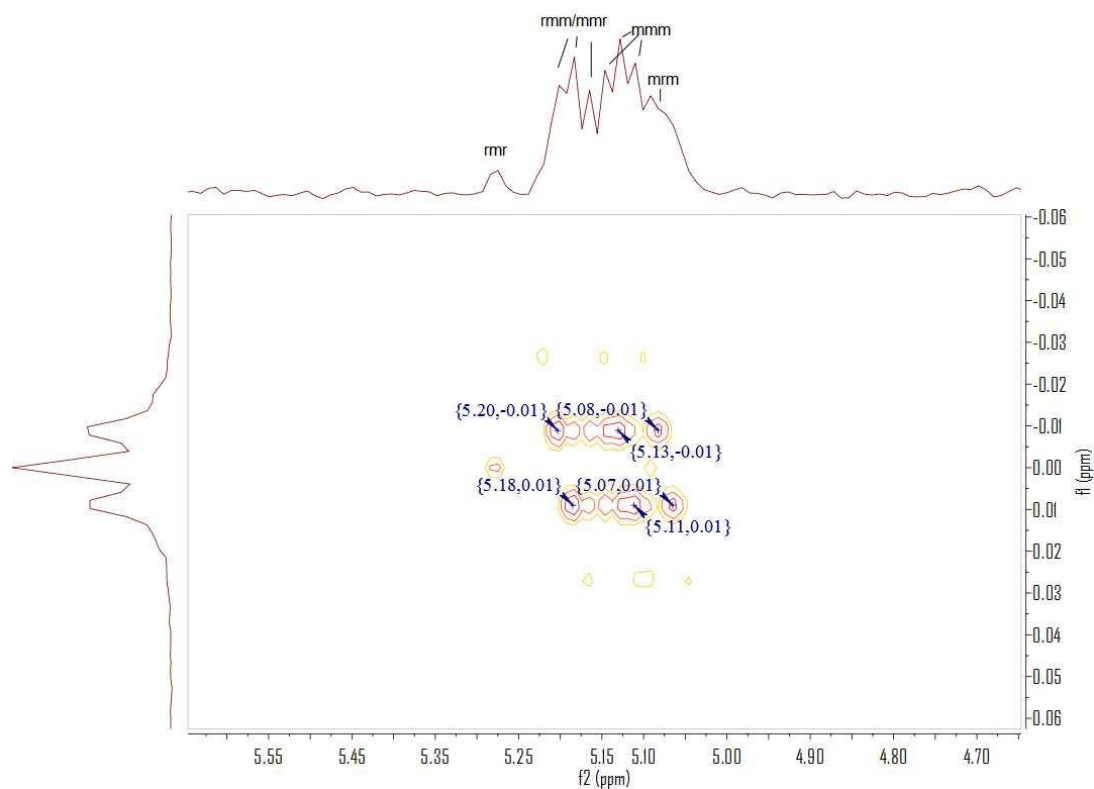
Figure 4-27. 2D J-Resolved ^{1}H NMR spectrum for co-poly (δ-VL+*r*-LA) (run 7, Table 4-3).
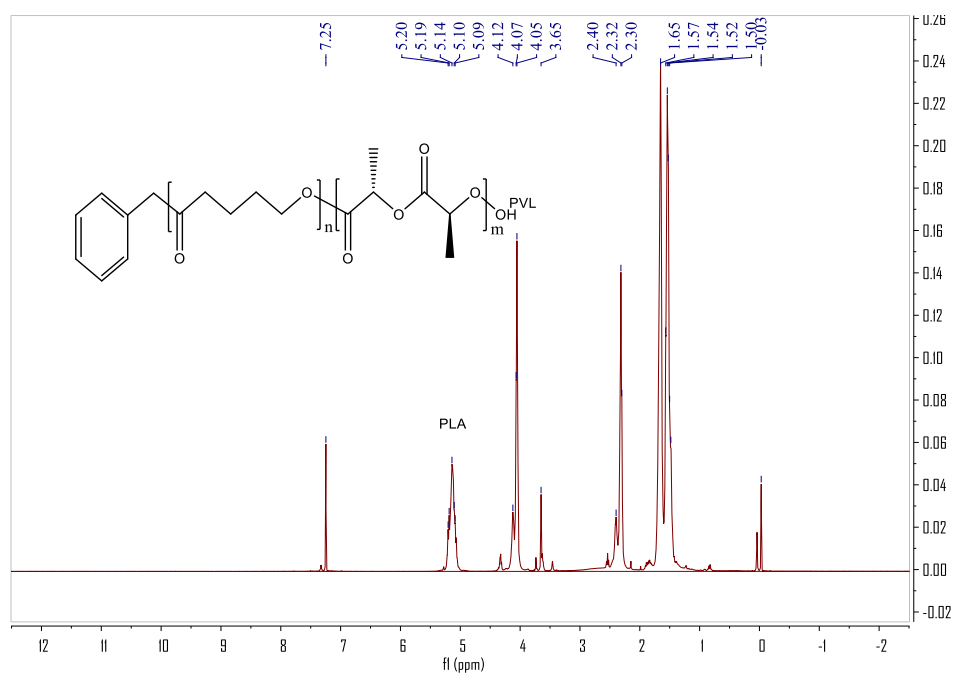
Figure 4-28. ^{1}H NMR spectrum for co-poly (δ-VL+r-LA) (run 7, Table 4-3).
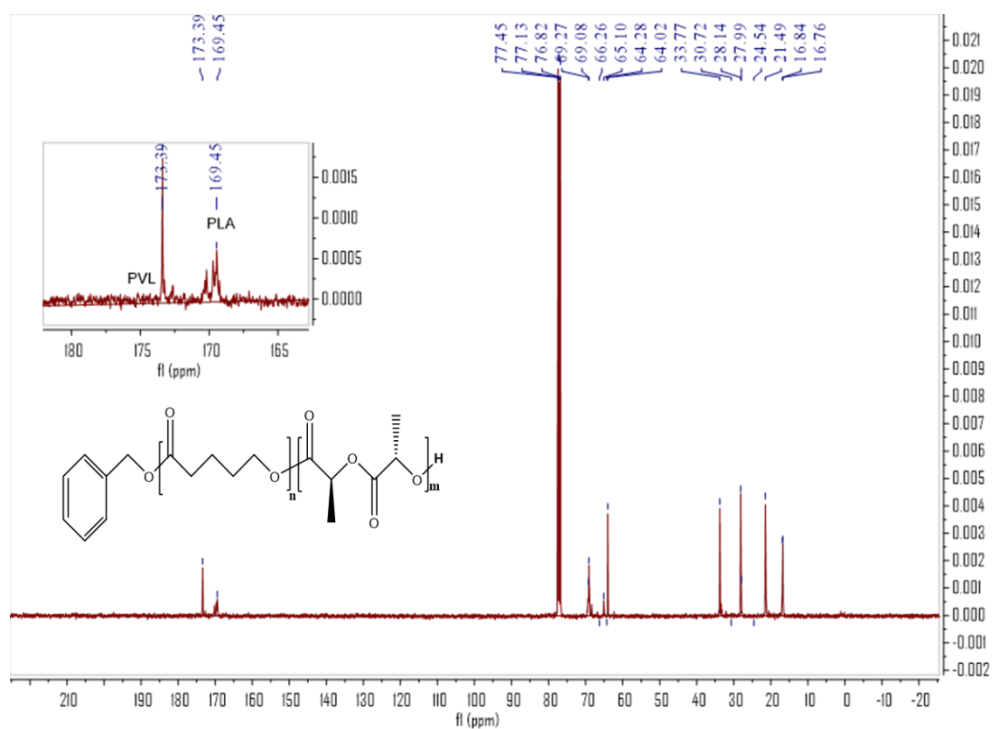
Figure 4-29. ^{13}C NMR spectrum for co-poly (δ-VL+r-LA) (run 7, Table 4-3).

116
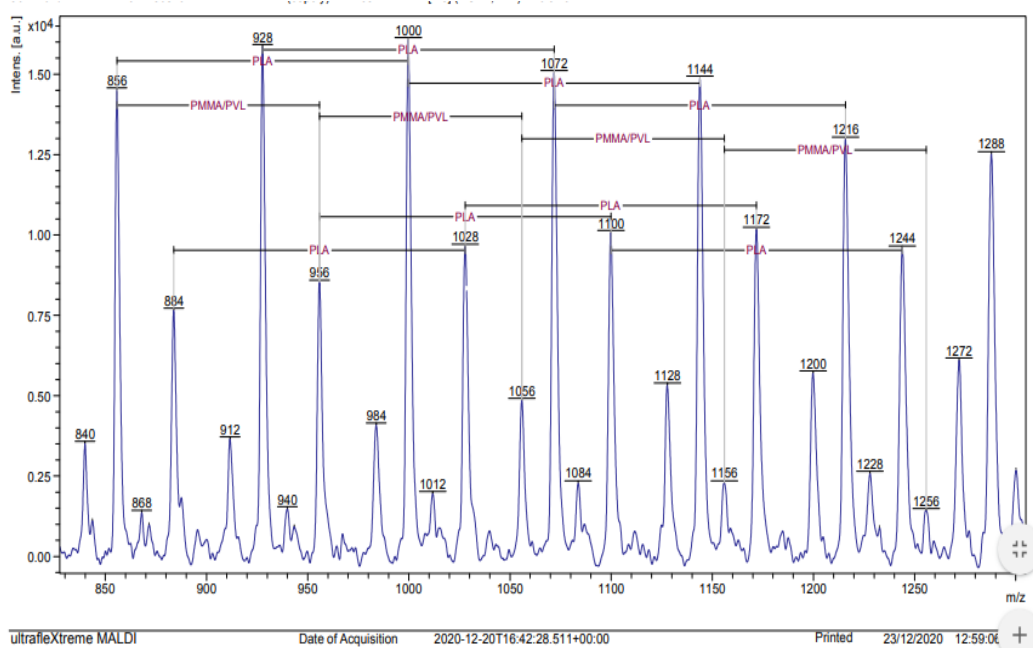
Figure 4-30. MALDI-ToF mass spectrum for co-poly (δ-VL+*r*-LA) (run 7, Table 4-3).

4.3 Conclusion

In conclusion, iron, cobalt and copper complexes bearing [2+2] Schiff-base macrocycles derived from dianilines containing -CH$_2$CH$_2$- bridges were successfully synthesised. Cobalt complexes were also prepared from a related dianiline containing an oxy bridge. A number on non-macrocyclic Fe and Co complexes were also prepared for comparative catalytic studies. The iron complexes outperformed the other metal systems herein for the ring opening polymerization of both ε-caprolactone and δ-valerolactone. Best results were obtained using the iron salt **13**, however the non-macrocyclic system **23** also performed well. Complex **13** was also capable of the copolymerization of ε-CL (or δ-VL) with *rac*-lactide, affording copolymers appreciable amounts of each monomer incorporated.

4.4 References

[1] L. M. Heidbreder, I. Bablok, S. Drews and C. Menzel, *Sci. Total. Environ.,* 2019, 668, 1077-1093.

[2] (a) C. Redshaw, *Catalysts,* 2017, 7, 165. (b) O. Santoro, X. Zhang and C. Redshaw, *Catalysts* 2020, 10, 800.

[3] (a) A. Arbaoui, C. Redshaw and D. L. Hughes, *Chem. Commun*. 2008, 4717-4719. (b) A. Arbaoui, C. Redshaw and D. L. Hughes, *Supramol. Chem*. 2009, 21, 35-43. (c) W. Yang, K.-Q. Zhao, T. J. Prior, D. L. Hughes, A. Arbaoui, T. Bian, M. R. J. Elsegood and C. Redshaw, *Dalton Trans*., 2016, 45, 11990-12005.

[4] W. Yang, K. -Q. Zhao, B. -Q. Wang, C. Redshaw, M. R. J. Elsegood, J. -L. Zhao and T. Yamato, *Dalton Trans*., 2016, 45, 226-236.

[5] (a) S. Brooker, *Coord. Chem. Rev*., 2001, 222, 33-56. (b) W. Radecka-Paryzek, V. Patroniak and J. Lisowski, *Coord. Chem. Rev*., 2005, 249, 2156-2175.

[6] For examples of iron-based ROP systems see: (a) B. J. O'Keefe, S. M. Monnier, M. A. Hillmyer and W. B. Tolman, *J. Am. Chem. Soc*., 2001, 123, 339-340. (b) B. J. O'Keefe, L. E. Breyfogle, M. A. Hillmyer, W. B. Tolman, *J. Am. Chem. Soc*., 2002, 124, 4384-4393. (c) K. R. Delle Chiaie, A. B. Biernesser, M. A. Ortuño, B. Dereli, D. A. Iovan, M. J. T. Wilding, B. Li, C. J. Cramer, J. A. Byers, *Dalton Trans*. 2017, 46, 12971-12980. (d) S. -L. Lee, F. -L. Hu, X. -J. Shang, Y. -X. Shi, A. L. Tan, J. Mizera, J. K. Clegg, W. -H. Zhang, D. J. Young and J. -P. Lang, *New J. Chem*., 2017, 41, 14457-14465. (e) E. Fazekas, G. S. Nichol, J. A. Garden and M. P. Shaver, *ACS Omega*, 2018, 3, 16945-16953. (f) M. Cozzolino, V. Leo, C. Tedesco, M. Mazzeo, M. Lamberti, *Dalton Trans*. 2018, 47, 13229-13238. (g) M. A. Ortuño, B. Dereli, K. R. D. Chiaie, A. B. Biernesser, M. Qi, J. A. Byers and C. J. Cramer, *Inorg. Chem*., 2018, 57, 2064-2071.

[7] A. W. Addison, T. N. Rao, J. Reedijk and G. C. van Rijn J, Verschoor, *J. Chem. Soc., Dalton Trans*., 1984, 7, 1349-1356.

[8] For examples of copper-based ROP systems see: (a) A. Routaray, N. Nath, T. Maharana, A.K. Sutar, *J. Macromol. Sci., Part A: Pure Appl. Chem*., 2015, 52, 444−453. (b) M. Mandal, K. Oppelt, M. List, I. Teasdale, D. Chakraborty, U. Monkowius, *Chem. Mon*., 2016, 147, 1883-1892. (c) M. Zikode, S. O. Ojwach and M. P. Akerman, *Appl. Organomet. Chem*., 2017, 31, e3556. (d) J. Rueda-Espinosa, J. F. Torres, C. V. Gauthier, L. Wojtas, G. Verma, M. A. Macias and J. Hurtado, *Chem. Select*. 2017, 2, 9815-9821.

[9] K. Wang, T. J. Prior and C. Redshaw, Chem. Commun., 2019, 55, 11279-11282.

[10] For examples of cobalt-based ROP systems see: (a) H. J. Jeon, Y. C. You, J. H. Youk. *J. Polym. Sci., Part A: Polym. Chem.*, 2009, 47, 3078-3085. (b) J. Zhang, B. Wang, L. Wang, J. Sun, Y. Zhang, Z. Cao and Z. Wu, *Appl. Organomet. Chem*. 2018, 32, e4077. (c) P. Marin, M. J. -L. Tschan, P. Haquette, T. Roisnel, I. del Rosal, L. Maron and C. M. Thomas, *Eur. Polym. J*. 2019, 120, 109208. (d) H. C. Pradhan, S. Mantri, A. Routaray, T. Maharaba, A. K. Sutar, *J. Chem. Sci*. 2020, 132, 25-31. (e) N. Shen, F. Tian, J. Chang, K. L. Huang, Z. H. Zhang, X. Feng, J. Gu, S. C. Chen, M. Y. He, Q. Chen, *CrystEngComm*, 2020, 22, 3656-3663.

[11] (a) Z. Zhong, P. J. Dijkstra and J. Feijen, *J. Am. Chem. Soc*., 2003, 125, 11291-11298. (b) R. M. Slattery, A. E. Stahl, K. R. Brereton, A. L. Rheingold, D. B. Green and J. M. Fritsch, *J. Polym. Sci., Part A: Polym. Chem.*, 2019, 57, 48-59.

Chapter 5 . Robust peroxidase mimic properties of iron complexes of [2+2] and [6+6] Schiff-base macrocycles

5.1 Introduction

Natural enzymes have been the focus of lots of attention due to their specificity and efficiency, but these natural enzymes are difficult to extract, purify and are easily deactivated. Because of these intrinsic drawbacks, artificial enzyme mimics have become an increasingly researched topic, In recent years, increasing numbers of materials have been discovered which possess enzyme mimic activity, e.g. transition metal oxides (Fe_3O_4, Co_3O_4),[1-2] precious metals (Au, Ag),[3-4] composite materials ($Pt@CeO_2$, AuPt/MOF−Graphene),[5-6] heme,[7] and porphyrin,[8] metal organic frameworks (MOFs)[9] and their derivatives have been employed as ligands in such systems.[10] Given the easy acquisition, such artificial mimetics can be used as electrochemical sensors or for the colorimetric detection of H_2O_2,[11-13] dopamine,[14-15] glucose,[16-19] cholesterol,[20, 21] etc. They have also been used for the degradation of pollutants in waste water such as dyes,[22] pesticides,[23] and phenol.[24]

Iron complexes can be used as peroxidase-like mimetics especially iron porphyrin complexes,[25-27] for example, the group of Abhishek described a biomimetic iron porphyrin complex present in the active site of HRP.[28] What's more, an iron(III) tetradentate monoamido complex was found to catalyse the degradation of dyes such as Orange II, ABTS in the presence of H_2O_2.[29] Schiff base iron chemistry has received interest, and macrocyclic [2+2] iron systems have been reported.[30] However, literature on [6+6] macrocycles is scant.[31-33] In terms of applications, iron Schiff-base complexes have been reported as good catalysts for many reactions such as oxidation of

cyclohexane,[34] and ring opening polymerizations,[35] whereas their use as enzyme mimetics remain rare.[36] Motivated by the above considerations, herein, three iron Schiff-base complexes have been prepared from [2+2] or [6+6] macrocycles (charts 5-1 and 5-2), and the complexes were used as peroxidase mimetics. The mechanistic aspects of their performance were also investigated in two ways. Furthermore, a colorimetric H_2O_2 detection method was successfully established with high accuracy and good selectivity.

5.2 **Result and discussion**

5.2.1 **Synthesis and characterization of Fe Schiff-base macrocyclic complexes 25-27.**
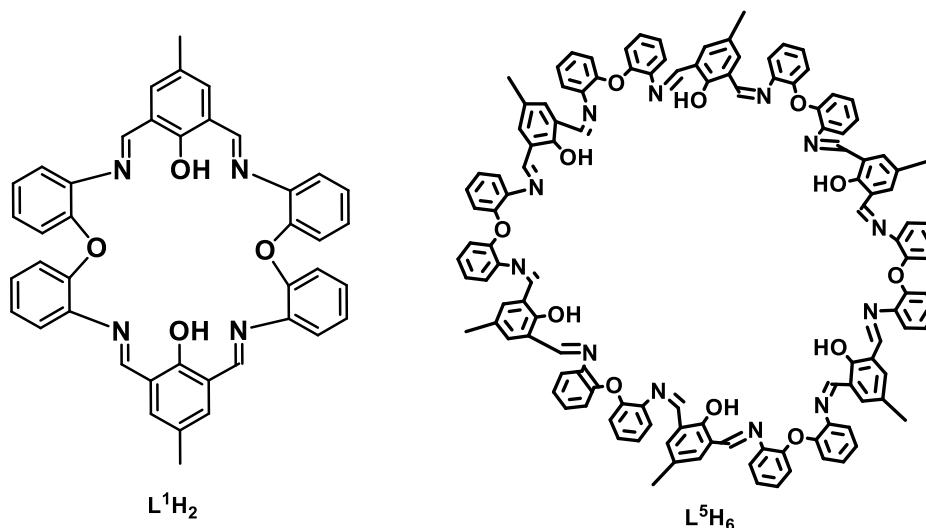
Chart 5-1. Macrocycles L^1H_2 and L^5H_6 used in this chapter.

Reaction of L^1H_2 {[2-(OH)-5-Me-C_6H_2-1,3-$(CH)_2$][O(2-$C_6H_4N)_2$]}$_2$ with 2.1 equivalents of $FeBr_2$ in toluene, followed by recrystallization from MeCN at ambient temperature afforded the black crystalline solid $[L^1H_2FeBr_2]_2[FeBr_3OFeBr_3]\cdot7MeCN$ (**25**·7MeCN). The formation of Fe(III) is likely due to adventitious oxygen, and appears also to promote salt formation (also see complex **27**). The molecular structure of **25**·7MeCN is exhibited in Figure 5-1, bond lengths and angles are shown in table 5-1.

The asymmetric unit comprises two cations, an anion and three solvents (MeCN) of crystallization. In the cation, the iron centre adopts a distorted octahedral geometry and bound in *N, O, N, O*-fashion by the macrocycle with phenoxides of **L¹** providing the O ligation; two *cis*-bromides complete the coordination sphere.
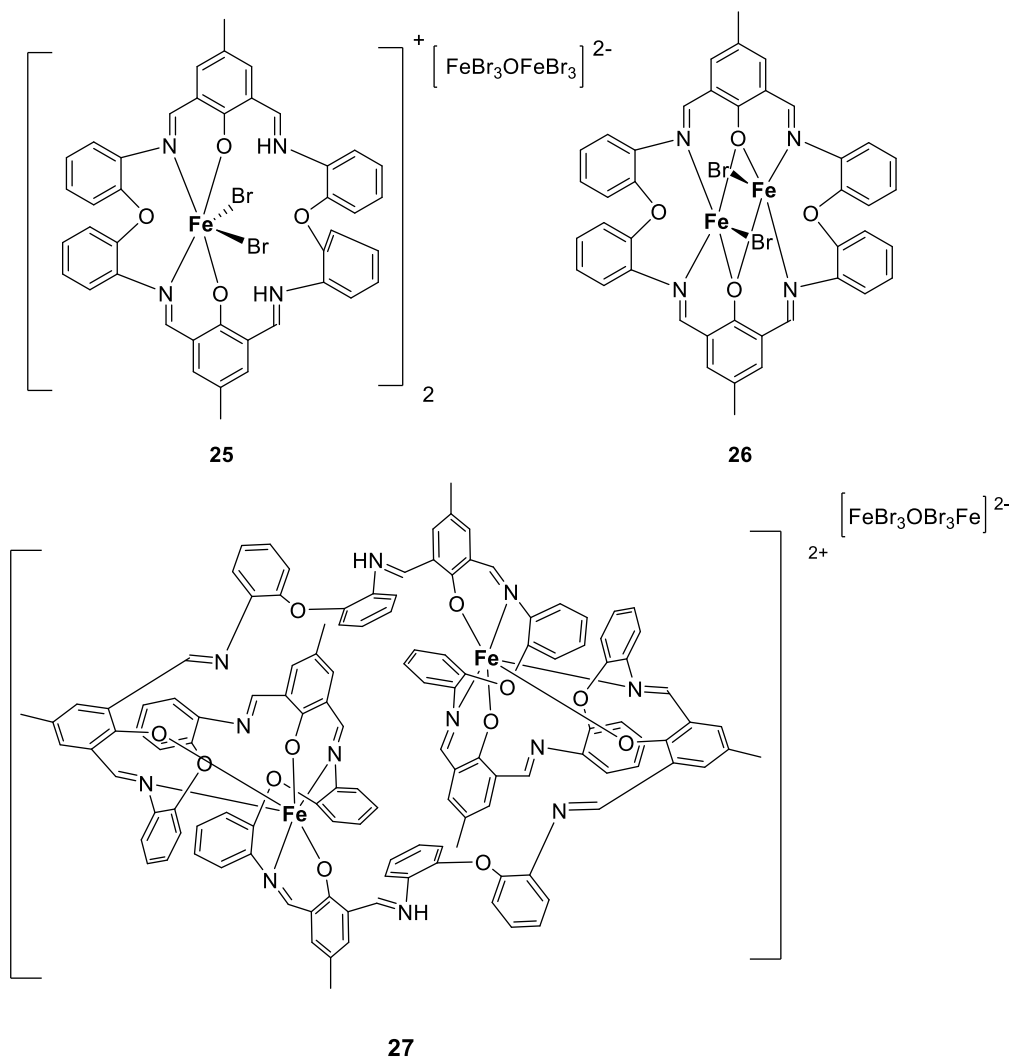
Chart 5-2. Complexes **25** to **27** prepared herein.
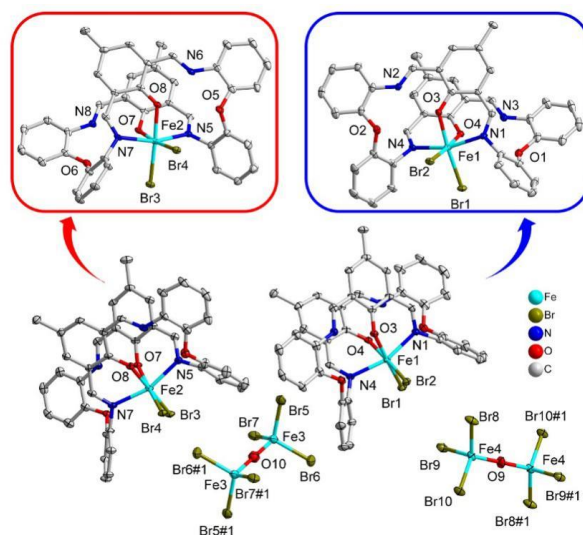
Figure 5-1. Molecular structure of [**L**^{1}H$_2$FeBr$_2$]$_2$[FeBr$_3$OFeBr$_3$]·7MeCN (**25**·7MeCN). Solvent molecules omitted for clarity.
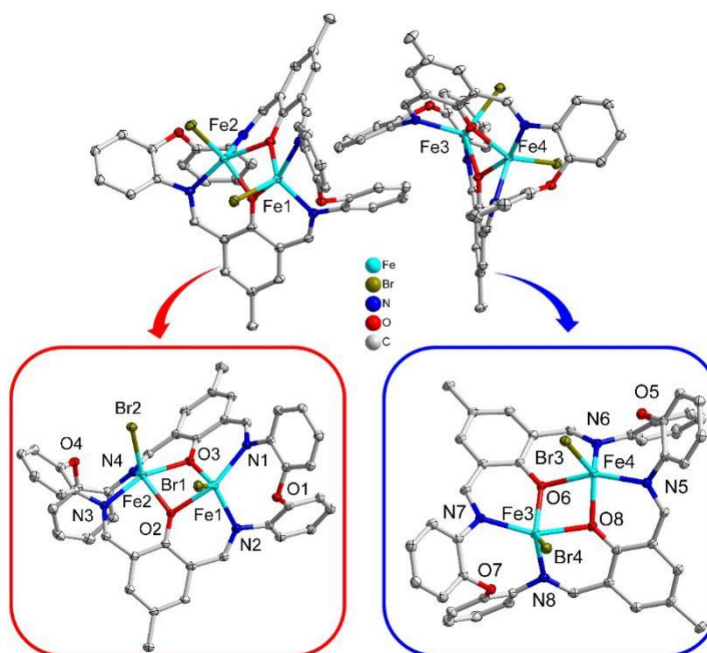
Figure 5-2. Molecular structure of [**L**^{1}(FeBr)$_2$]·3MeCN (**26**·3MeCN). Solvent molecules omitted for clarity.

Reaction of **L**^{1}H$_2$ {[2-(OH)-5-Me-C$_6$H$_2$-1,3-(CH)$_2$][O(2-C$_6$H$_4$N)$_2$]}$_6$ with 2.1 equivalents of FeBr$_2$ in refluxing toluene, in the presence of Et$_3$N, following work-up using acetonitrile, afforded the black crystalline Fe(II) complex [Fe$_2$Br$_2$**L**^{1}]$_2$·3MeCN

(**26**·3MeCN). In this case, the asymmetric unit included two dinuclear iron complexes and three molecules of acetonitrile (Figure 5-2). Each iron centre is five-coordinate, in which a distorted trigonal bipyramidal iron centre Fe1 (τ=0.55) and a distorted square pyramidal Fe2 (τ=0.42) was observed.

As reported previously,[37] the [2+2] macrocycle $\mathbf{L^1H_2}$ is readily available via a double condensation reaction in refluxing methanol. However, on changing the solvent to toluene, and hence the reflux temperature, the product isolated is the [6+6] macrocycle $\mathbf{L^5H_6}$. Reaction of $\mathbf{L^5H_6}$ $\{[2\text{-}(OH)\text{-}5\text{-}Me\text{-}C_6H_2\text{-}1,3\text{-}(CH)_2][O(2\text{-}C_6H_4N)_2]\}_2$ with 4.1 equivalents of FeBr$_2$ afforded, following work-up (acetonitrile), black needles suitable for an X-ray diffraction study. The molecular structure of [Fe$_2$($\mathbf{L^5H_2}$)][FeBr$_3$OFeBr$_3$]·4MeCN (**27**·4MeCN) is shown in Figure 5-3; bond lengths and angles can be found in table 5-1. The structure is comprised of a dinuclear Fe(III) cation, an [FeBr$_3$OFeBr$_3$] anion and four MeCN solvent molecules. In the cation of complex **27**, the iron centre adopts a distorted octahedral geometry and is bound by three imine nitrogens and three phenoxide oxygens. There are many noteworthy intermolecular interactions including C–H···π interactions, Br-H interactions and anion···π interactions shown in Figure 5-4. These interactions connect two neighbouring macrocycles, the C-H···π interactions are around 3.455 Å and C-H-imine interactions are around 3.667 Å. Moreover, as shown in Figure 5-4c, Br-H interactions (2.807 Å -3.309 Å) and anion···π interactions (3.475 Å) were found between the anion and macrocycle.[38]
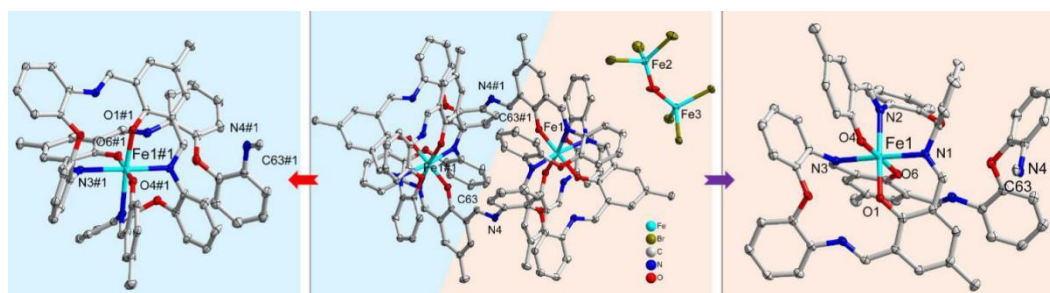
Figure 5-3. Molecular structure the [Fe$_2$($\mathbf{L^5H_2}$)]·[FeBr$_3$OFeBr$_3$]·4MeCN (**27**·4MeCN).

Table 5-1. Selected bond lengths (Å) and angles (°) in **25**, **26** and **27**.

	Selected bonds	Length (Å)	Selected angles (°)	
	Fe(1)-O(3)	2.021(3)	O(3)-Fe(1)-O(4)	86.96(13)
	Fe(1)-O(4)	2.041(3)	O(3)-Fe(1)-N(1)	82.00(14)
	Fe(1)-N(1)	2.176(4)	N(3)-Fe(1)-N(4)	161.53(16)
	Fe(1)-N(4)	2.180(4)	O(3)-Fe(1)-Br(1)	174.19(10)
Complex **25**	Fe(1)-Br(1)	2.436(9)	O(7)-Fe(2)-N(7)	84.64(14)
	Fe(2)-O(7)	2.018(3)	O(7)-Fe(2)-N(5)	81.71(14)
	Fe(2)-N(7)	2.176(4)	N(7)-Fe(2)-N(5)	161.07(15)
	Fe(2)-Br(3)	2.437(9)	N(7)-Fe(2)-Br(4)	97.08(11)
	Fe(3)-O(10)	1.721(17)	O(10)-Fe(3)-Br(5)	109.73(11)
	Fe(1)-O(3)	2.003(4)	O(3)-Fe(1)-N(2)	114.59(16)
	Fe(1)-O(2)	2.190(4)	O(3)-Fe(1)-N(1)	83.46(16)
	Fe(1)-N(1)	2.188(5)	N(2)-Fe(1)-N(1)	111.38(17)
Complex **26**	Fe(1)-N(2)	2.136(4)	O(3)-Fe(1)-O(2)	72.33(14)
	Fe(1)-Br(1)	2.441(10)	O(3)-Fe(1)-Br(1)	122.67(12)
	Fe(2)-Br(2)	2.414(9)	O(2)-Fe(2)-Br(2)	134.19(12)
	Fe(3)-O(6)	2.016(4)	O(6)-Fe(3)-N(7)	84.25(16)
	Fe(1)-O(4)	1.886(4)	O(4)-Fe(1)-O(6)	178.53(16)
	Fe(1)-O(6)	1.967(4)	O(4)-Fe(1)-O(1)	89.53(16)
	Fe(1)-O(1)	1.974(4)	O(6)-Fe(1)-O(1)	90.09(15)
	Fe(1)-N(1)	2.157(4)	O(1)-Fe(1)-N(2)	173.58(15)
Complex **27**	Fe(1)-N(2)	2.183(4)	O(1)-Fe(1)-N(2)	92.88(17)
	Fe(1)-N(3)	2.185(4)	N(1)-Fe(1)-N(3)	172.19(16)
	Fe(2)-O(7)	1.724(4)	N(2)-Fe(1)-N(3)	86.13(16)
	Fe(2)-Br(4)	2.342(15)	Br(4)-Fe(2)-Br(5)	103.21(5)
	Fe(2)-Br(5)	2.364(13)	O(7)-Fe(2)-Br(6)	106.02(18)
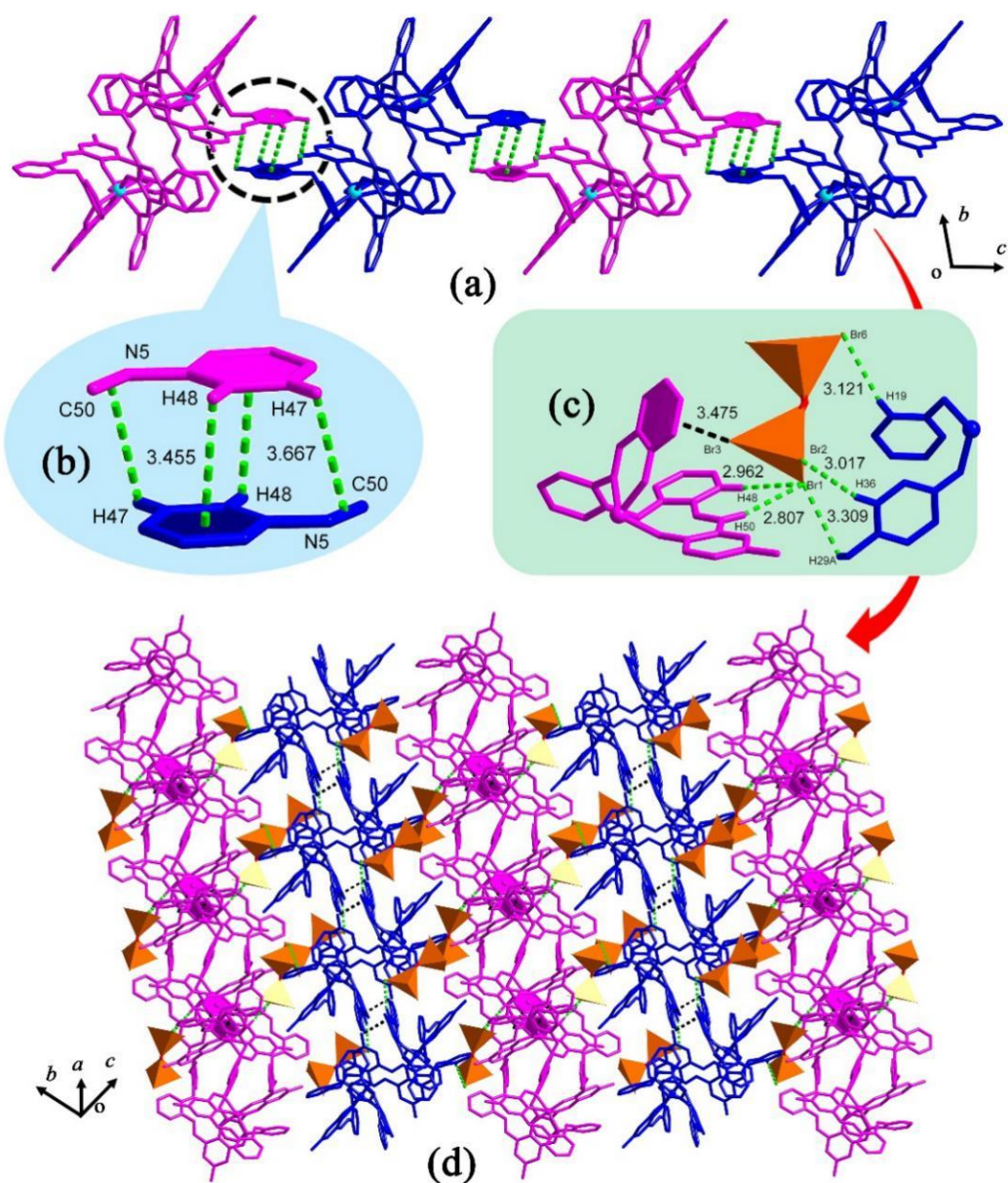
Figure 5-4. (a) The 1D chain of complex **27** constructed by the non-covalent interaction (b) and (c) the interaction between the adjacent [Fe$_2$**L^5**H$_2$] units in **27**; (C-H···π. Br-H bond, interaction and anion···π interaction); (e) the interaction between the adjacent [Fe$_2$**L^5**H$_2$] units from different adjacent chains in **27**; (d) the 2D network linked via the C-H···π interaction between the adjacent [Fe$_2$**L^5**H$_2$] units from different adjacent chains in **27**.
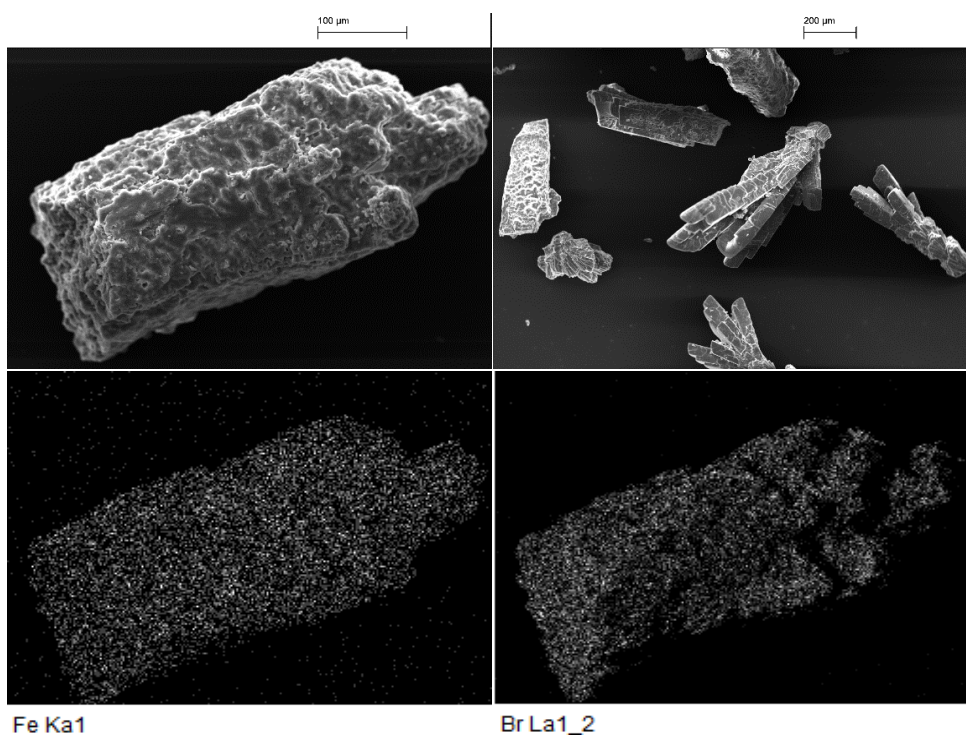
Figure 5-5. SEM images of the Fe complex **25**.
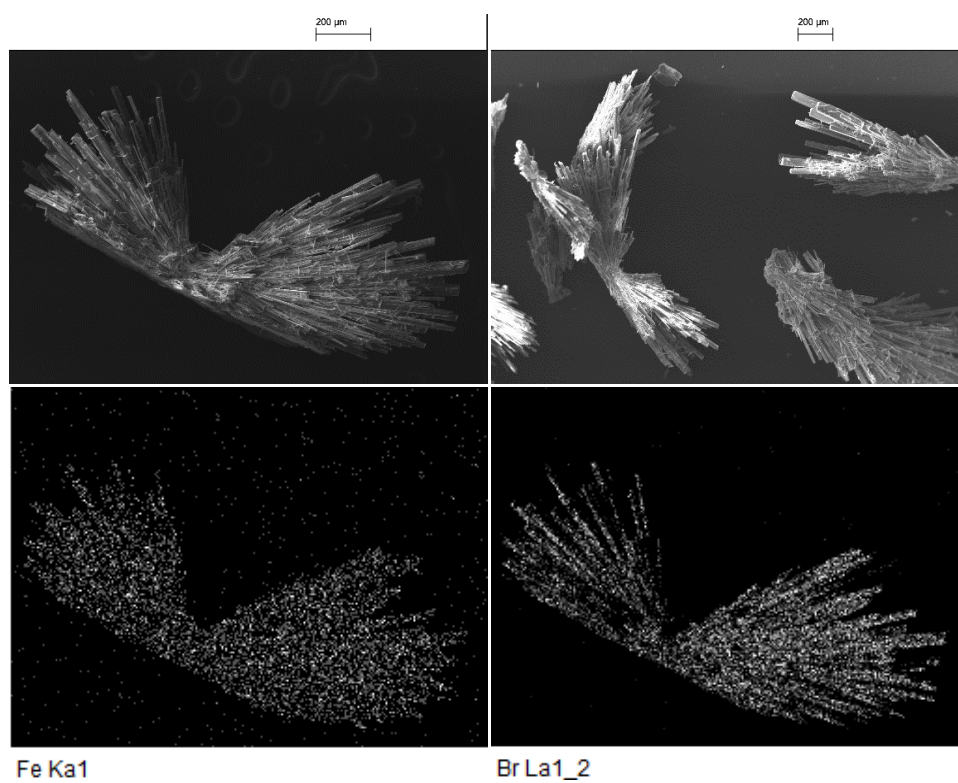
Figure 5-6. SEM images of the Fe complex **26**.
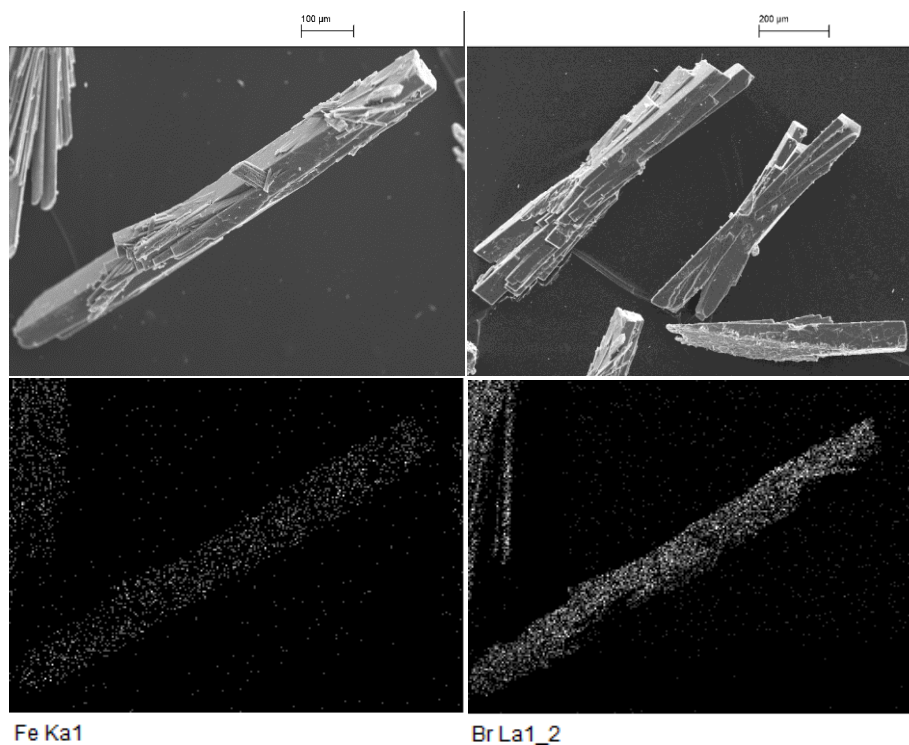
Figure 5-7. SEM images of the Fe complex **27**.

The morphology of the Fe complexes **25-27** was analysed using scanning electron microscopy (SEM) and is shown in Figure 5-5 to Figure 5-7 respectively. Figure 5-5 and Figure 5-7 reveal SEM micrographs where nano rod-like morphology are observed. Interestingly, the SEM image of **26**, as depicted in Figure 5-6, revealed homogeneous "wing" shapes composed of needle-like crystals.

5.2.2 Peroxidase-like activity of complexes 25-27.

The peroxidase-like activity of complexes **25-27** was tested via the oxidation of substrate (TMB) in the presence of H_2O_2, H_2O_2 can oxidize TMB in the presence of catalysts **25-27** forming the oxTMB product which exhibits a blue colour with absorption at 652 nm. The catalytic activity is shown in Figure 5-8, with TMB oxidation only found

in the Fe complex-TMB-H_2O_2 system, whereas no oxidation is observed in either the Fe complex-TMB system or TMB-H_2O_2 system.
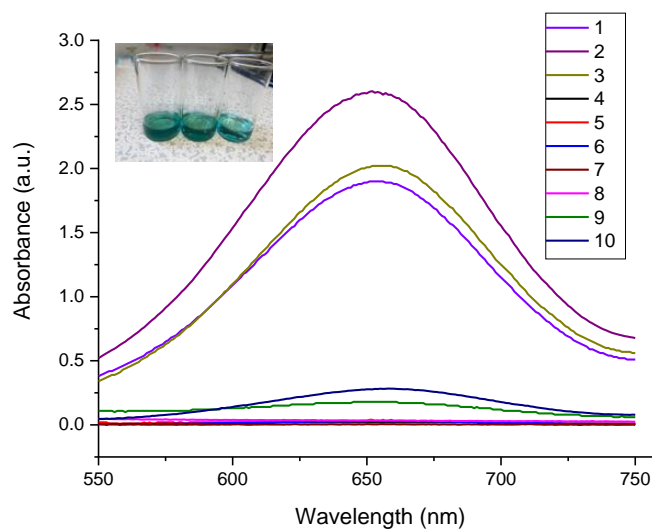
Figure 5-8. Absorbance spectra of oxTMB in different reaction conditions: 1) **25** + TMB + H_2O_2; 2) **26** + TMB + H_2O_2; 3) **27** + TMB+ H_2O_2; 4) **25** leaching solution + TMB + H_2O_2; 5) **26** leaching solution + TMB + H_2O_2; 6) **27** leaching solution + TMB+ H_2O_2; 7) TMB + H_2O_2; 8) **26** leaching solution + TMB; 9) **26** + TMB; 10) **27** + TMB; Insert shows the colour change of samples (from left to right: reaction using complexes **25**, **26** and **27**, respectively.)

The optimization of pH and temperature for the TMB oxidation reaction is shown in Figure 5-9. The oxidation of TMB was found to be pH-dependent, and pH = 4 is the optimum pH condition. Moreover, the effect of temperature was investigated over the temperature range from room temperature to 60 °C, and it was found that the maximum absorbance was obtained at 45 °C for complexes **25** and **26**, whereas for **27**, the highest activity was observed at 50 °C.
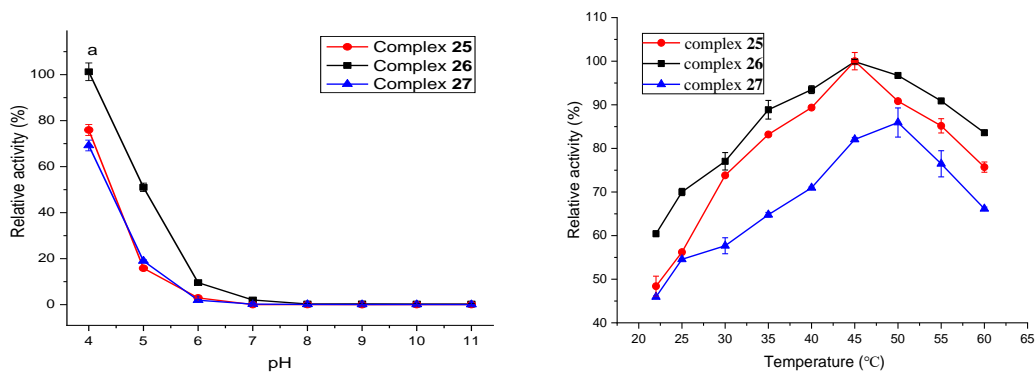
Figure 5-9. Effects of (a) pH and (b) temperature on the peroxidase-like activity of the iron complexes **25**-**27**.

5.2.3 Kinetic studies

Steady-state kinetic measurements were carried out to shed light on the kinetic process of the peroxidase-like catalytic activity of these Fe complexes. The Linewaver–Burk plot for **25**-**27** are shown in c) and d) of Figure 5-10 to Figure 5-12, in which the double reciprocal plot is near linear, suggesting a "ping–pong" mechanism for TMB oxidation.[28] The calculated V_{max} values as well as K_m values for **25**-**27** towards H_2O_2 and TMB are presented in Table 5-2. The V_{max} values of these iron complexes are higher than HRP and Fe_3O_4, suggesting a high performance as peroxidase-like mimetics. The initial reaction rate was calculated using the Beer–Lambert law:

Eq.1. $V = \dfrac{\Delta c}{\Delta t} = \dfrac{\frac{\Delta A}{\varepsilon b}}{\Delta t}$

In the above formula, A is the absorbance, b is the thickness of the solution, c is the substrate concentration, V is the reaction rate and ε is the molar attenuation coefficient (value of 39000 M^{-1} cm^{-1}).

The Michaelis–Menten equation was used to calculate the Michaelis–Menten constant (K_m) and the maximal reaction velocity (V_{max}):

Eq.2. $V_0 = \frac{V_{max}[S]}{K_m + [S]}$

where V_0 corresponds to the initial velocity, V_{max} is the maximal reaction velocity, K_m is the Michaelis constant and $[S]$ represents the concentration of substrates. The Michaelis constant (K_m) is a parameter to evaluate the binding affinity between the enzyme and the substrate, and a low value of K_m represents a higher combination ability between the artificial enzyme and the substrate and *vice versa*.[14]

The Michaelis–Menten constant was determined by fixing the concentration of one substrate and changing that of the other, and the fixed concentrations of TMB and H_2O_2 were 0.5 mM and 50 mM, respectively a) and b) in Figure 5-10 to Figure 5-12.
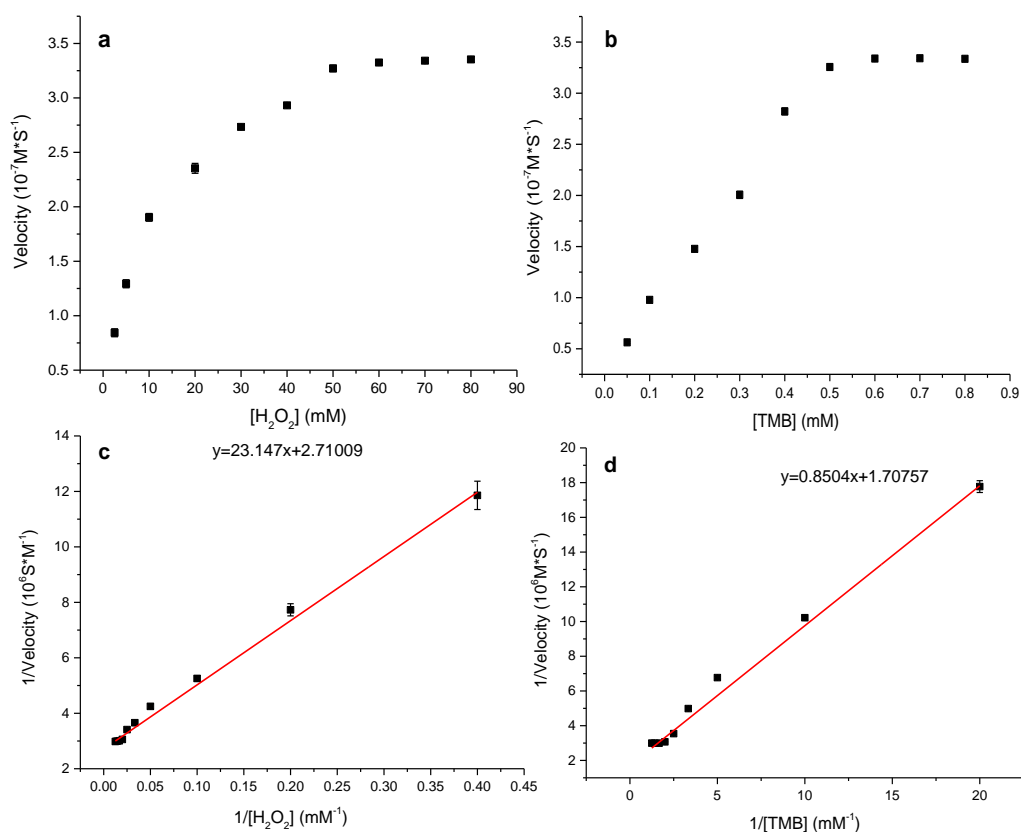
Figure 5-10. Steady state kinetic assay of **25**. (a) Constant concentration of H_2O_2 (50 mM) and the TMB concentration was varied (b) Constant concentration of TMB (0.5 mM) and the H_2O_2 concentration was varied. Double reciprocal plot of peroxidase mimic activity of **25** with the (c) constant concentration of H_2O_2 (50mM) and varying concentrations of

TMB (d) constant concentration of TMB (0.5mM) and varying concentrations of H_2O_2. The reactions were carried out with 0.1mg/mL **1** in 3 mL of 100mM NaAc-HAc buffer at pH=4.0.
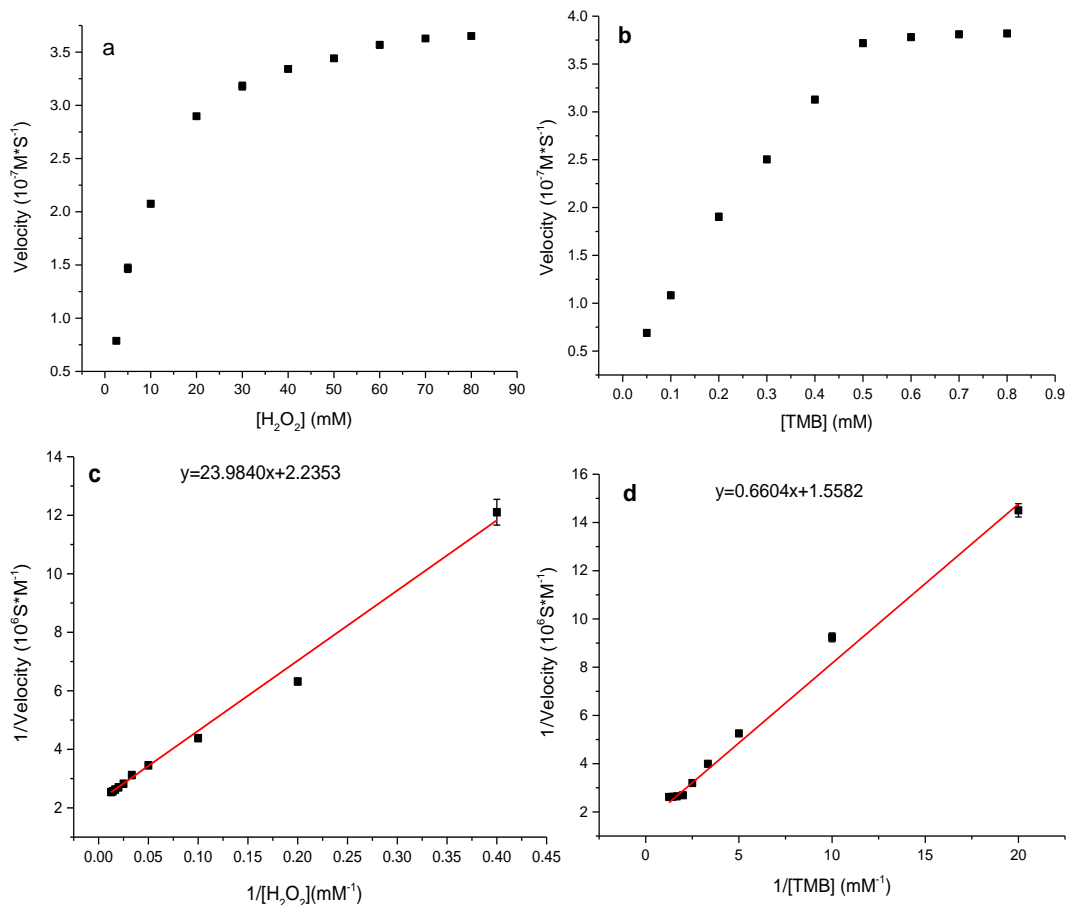
Figure 5-11. Steady state kinetic assay of **26**. (a) Constant concentration of H_2O_2 (50 mM) and the TMB concentration was varied (b) Constant concentration of TMB (0.5 mM) and the H_2O_2 concentration was varied. Double reciprocal plot of peroxidase mimic activity of **26** with the (c) constant concentration of H_2O_2 (50mM) and varying concentrations of TMB (d) constant concentration of TMB (0.5mM) and varying concentrations of H_2O_2. The reactions were carried out with 0.1 mg/mL **2** in 3 mL of 100mM NaAc-HAc buffer at pH=4.0.
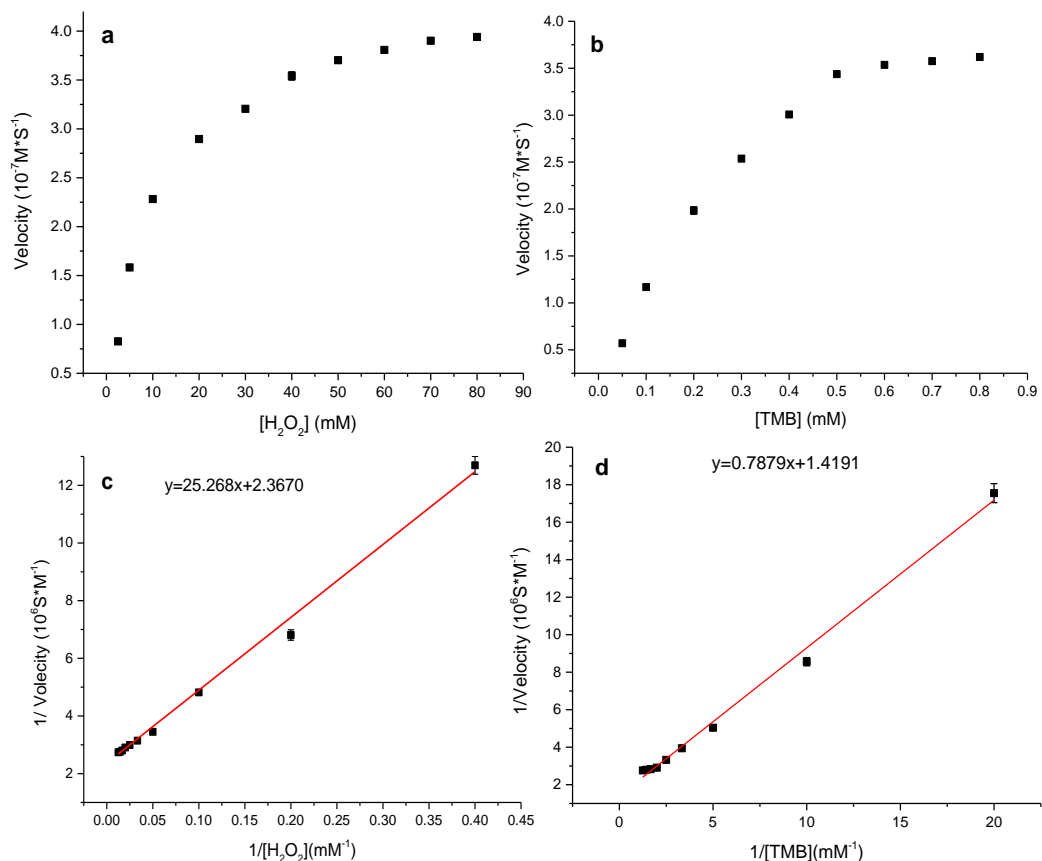
Figure 5-12. Steady state kinetic assay of **27**. (a) Constant concentration of H_2O_2 (50 mM) and the TMB concentration was varied (b) Constant concentration of TMB (0.5 mM) and the H_2O_2 concentration was varied. Double reciprocal plot of peroxidase mimic activity of **27** with the (c) constant concentration of H_2O_2 (50mM) and varying concentrations of TMB (d) constant concentration of TMB (0.5mM) and varying concentrations of H_2O_2. The reactions were carried out with 0.1mg/mL **27** in 3 mL of 100mM NaAc-HAc buffer at pH=4.0.

Table 5-2. Kinetic parameters of different artificial peroxidase and HRP using TMB as substrate.

catalyst	K_m (mM)		V_{max} (10^{-8} M·s^{-1})		reference
	H_2O_2	TMB	H_2O_2	TMB	Ref.
HRP	3.7	0.43	8.71	10	1
Fe_3O_4	154	0.098	9.78	3.44	1
25	7.20	0.118	33.5	33.3	This work
26	6.28	0.116	39.4	38.1	This work
27	6.35	0.107	36.5	36.1	This work

5.2.4 Mechanism study of peroxidase-like activity complexes 25-27.

a) Electron transfer discussion

The possible electron transfer processes of the Fe complex-TMB-H_2O_2 systems was investigated by cyclic voltammograms. Reduction currents of H_2O_2 were found using an Fe complex modified GCE as working electrode. It can be deduced that complexes **25-27** can accelerate the electron transfer process between TMB and H_2O_2 (Figure 5-13, bottom).[14] As shown in Figure 5-14, it is evident that the system employing either **25** or **27** exhibits the best reduction current, which were assigned to the presence of the Fe(III) centres in complexes **25** and **27** (*versus* the Fe(II) in **26**).
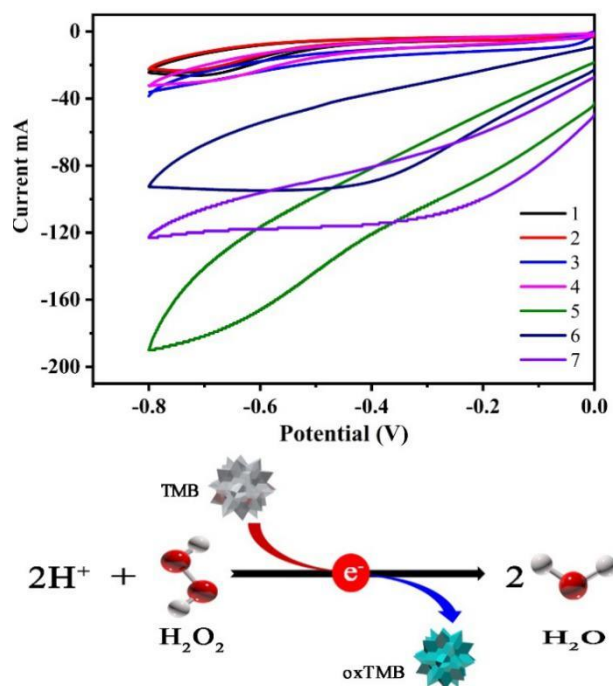
Figure 5-13. Cyclic Voltammograms of complexes **25-27** of 1) buffer (pH=4.0); 2) **25** modified GCE + buffer (pH=4.0); 3) **26** modified GCE + buffer (pH=4.0); 4) **27** modified GCE + buffer (pH=4.0); 5) **25** modified GCE + buffer (pH=4.0) + 20mM H_2O_2; 6) **26** modified GCE + buffer (pH=4.0); 7) **27** modified GCE + buffer (pH=4.0).

b) Hydroxyl radical detection
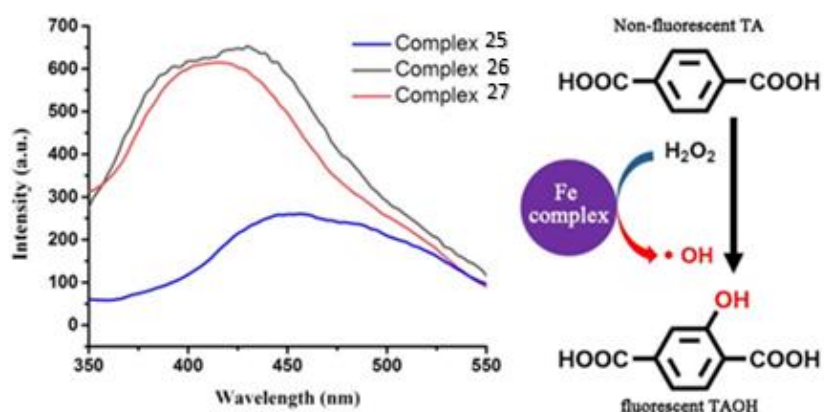
Figure 5-14. Hydroxyl radical detection using **25-27**.

The formation rate of the hydroxyl radical at the interfaces of these Fe complex was detected using TA (terephthalic acid) as a probe molecule.[39] As peroxidase mimetics, the Fe complexes can break up the O–O bond of H_2O_2 into two hydroxyl radicals,[40] then TA readily reacts with hydroxyl radical to produce the fluorescent product (hydroxyterephthalate) TAOH. In Figure 5-14, it was observed that TAOH can be found in the TA–Fe complex-H_2O_2 system, and **26** and **27** generated more ·OH than **25**.

5.2.5 Determination of H_2O_2.
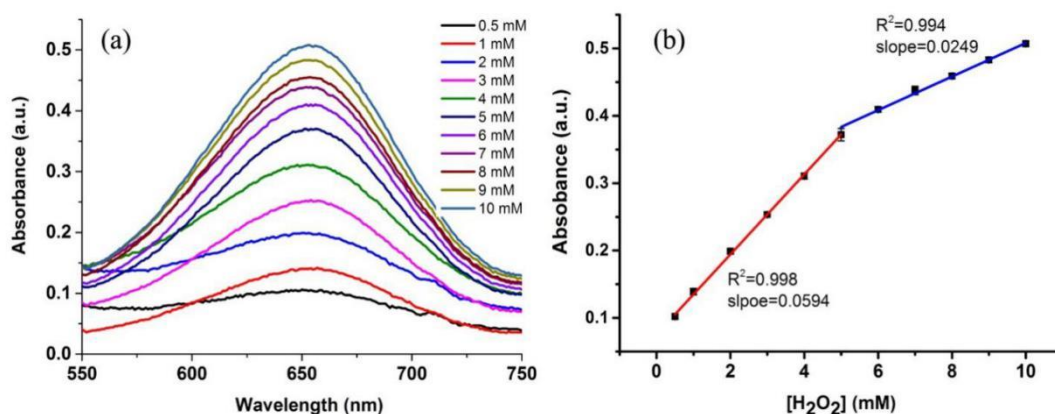
Figure 5-15. H_2O_2 determination using complex **27** as peroxidase mimetic. (a) The UV-vis absorption spectra of different H_2O_2 concentrations. (b) Linear calibration plot for H_2O_2 detection.
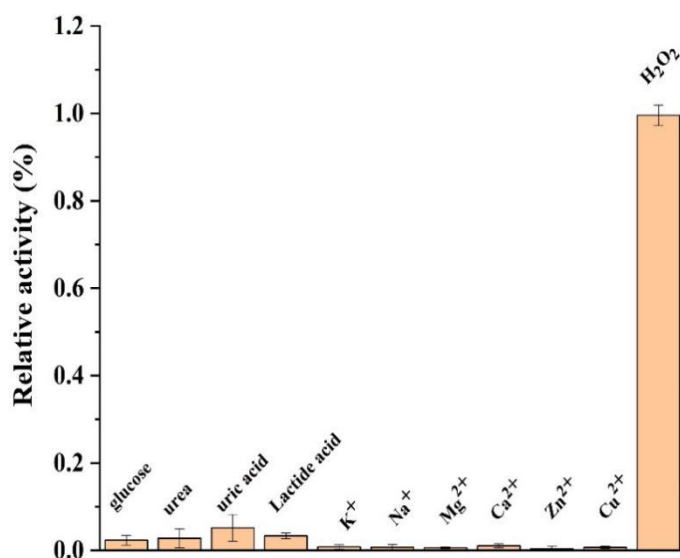
Figure 5-16. Selectivity of the H_2O_2 detection method.

Based on these findings, a colorimetric method for H_2O_2 determination is established. The colorimetric method for H_2O_2 sensing was based on the amount of blue oxTMB product and was proportional to the amount of H_2O_2. As shown in Figure 5-15, two linear ranges were obtained, namely 0.5-5 mM, and 6-10 mM, with a limit of detection (LOD) of 0.05 mM. The selectivity was tested with 5 mM of H_2O_2 and the concentration for other interferences are 4-fold of H_2O_2 (Figure 5-16). These results indicate this method is very efficient even in the presence of potentially competing contaminants.

Table 5-3. Comparison of the linear range and the detection limit of different H_2O_2 sensors.

Catalyst	Linear range	Detection limit	Ref.
FePt-Au HNPs	20-700 μM	12.33 μM	[41]
$Cu_2(OH)_3Cl$-CeO_2	20-50 μM	10 μM	[42]
CoS	50-800 μM	20 μM	[43]
Fe_3O_4@Cu@Cu_2O	4-50 mM	2000 μM	[44]
GO-FeTPyP NCs	20-500 μM	72 μM	[45]
Fe Schiff base complex	0.5-5; 6-10 mM	50 μM	This work

5.3 Conclusion

In conclusion, [2+2] or [6+6] Schiff-base macrocycles have been complexed with Fe, and used as horseradish peroxidase mimetics. When the reaction pH is 4.0, the systems exhibit the highest absorbance at 652 nm, suggesting the best catalytic activity. Whilst 45°C is the optimal temperature for **25** and **26**, that for **27** is 50°C. From the kinetic studies, the complexes all exhibit Michaelis−Menten type kinetics and a "ping−pong"

mechanism. The process of electron transfer between TMB and H_2O_2 was found to be greatly accelerated by the presence of the Schiff-base iron complex. The ·OH radical is found to be an intermediate in the catalytic process in the presence of H_2O_2. Based on the peroxidase mimic activity, a colorimetric determination method for H_2O_2 using complex **27** was established. The approach exhibits good selectivity toward H_2O_2 with linear range of 0.5-5 mM and 6-10 mM and a low detection limit of 0.05 mM, which may have potential applications in biosensors. Overall, these results reveal that iron complexes bearing [2+2] or [6+6] Schiff-base macrocycles (derived from 2,2'-oxydianiline), show robust peroxidase mimic properties, and have the potential to replace natural horseradish peroxidase and other artificial enzymes in biosensing, pollutant degradation and so on.

5.4 References

[1] L. Z. Gao, J. Zhuang, L. Nie, J. B. Zhang, Y. Zhang, N. Gu, T. H. Wang, J. Feng, D. L. Yang, S. Perrett and X. Yan, *Nat. Nanotechnol.*, 2007, 2, 577-583.

[2] J. Mu, Y. Wang, M. Zhao and L. Zhang, *Chem. Commun.*, 2012, 48, 2540-2542.

[3] Y. Hu, H. Cheng, X. Zhao, J. Wu, F. Muhammad, S. Lin, J. He, L. Zhou, C. Zhang, Y. Deng, P. Wang, Z. Zhou, S. Nie and H. Wei, *ACS Nano*, 2017, 11, 5558–5566.

[4] X. Fang, H. Ren, H. Zhao and Z. Li, *Microchim. Acta*, 2017, 184, 415–421.

[5] C. Fu, Y. Sun, C. Huang, F. Wang, N. Li, L. Zhang and J. Yu., *Talanta*, 2021, 223, 121719.

[6] T. Zhang, Y. Xing, Y. Song, Y. Gu, X. Yan, N. Lu, H. Liu, Z. Xu, H. Xu, Z. Zhang and M. Yang, *Anal. Chem.*, 2019, 91, 10589–10595.

[7] Q. Wang, Z. Yang, X. Zhang, X. Xiao, C. K. Chang and B. Xu, *Angew. Chem., Int. Ed.*, 2007, 46, 4285.

[8] M. Sono, M. P. Roach, E. D. Coulter and J. H. Dawson, *Chem. Rev.*, 1996, 96, 2841.

[9] J. W. Zhang, H. T. Zhang, Z. Y. Du, X. Wang, S. H. Yun and H. L. Jiang, *Chem. Commun.*, 2014, 50, 1092-1094.

[10] A. Li, X. Mu, T. Li, H. Wen, W. Li, Y. Li and B. Wang, *Nanoscale*, 2018, 10, 11948–11954.

[11] Y. Ding, B. Yang, H. Liu, Z. Liu, X. Zhang, X. Zheng and Q. Liu, *Sens. Actuators, B*, 2018, 259, 775–783.

[12] X. M. Chen, B. Y. Su, Z. X. Cai, X. Chen and M. Oyama, *Sens. Actuators, B*, 2014, 201, 286–292.

[13] C. Song, W. Ding, W. Zhao, H. Liu, J. Wang, Y. Yao and C. Yao, *Biosens. Bioelectron.*, 2020, 151, 111983.

[14] K. Wang, J. Song, X. Duan, J. Mu and Y. Wang, *New J. Chem.*, 2017, 41, 8554–8560.

[15] J. Wang, Y. Y. Hu, Q. Zhou, L. Z. Hu, W. S. Fu and Y. Wang, *ACS Appl. Mater. Interfaces*, 2019, 11, 44466–44473.

[16] L. Rastogi, D. Karunasagar, R. B. Sashidhar and A. Firi, *Sens. Actuators, B*, 2017, 240, 1182.

[17] H. J. Cheon, M. D. Adhikari, M. Chung, T. D. Tran, J. Kim and M. I. Kim, *Adv. Healthcare Mater.*, 2019, 8, 1801507.

[18] B. S. Batule, K. S. Park, S. Gautam, H. J. Cheon, M. I. Kim and H. G. Park, *Sens. Actuators, B*, 2019, 283, 749–754.

[19] J. Yu, D. Ma, L. Mei, Q. Gao, W. Yin, X. Zhang, L. Yan, Z. Gu, X. Ma and Y. Zhao, *J. Mater. Chem. B*, 2018, 6, 487–498.

[20] V. Sharma and S. M. Mobin, *Sens. Actuators, B*, 2017, 240, 338–348.

[21] J. Hassanzadeh and A. Khataee, *Talanta*, 2018, 178, 992–1000.

[22] Q. M. Chen, X. D. Zhang, S. Q. Li, J. K. Tan, C. J. Xu and Y. M. Huang, *Chem. Eng. J.*, 2020, 395, 125130.

[23] P.-K. Boruah and M.-R. Das, *J. Hazard. Mater.*, 2020, 385, 121516–121579.

[24] J. Li, X. Li, W. Feng, L. Huang, Y. Zhao, Y. Hu and K. Cai, *Mater. Lett.*, 2018, 229, 193–197.

[25] R. Ricoux, R. Dubuc, C. Dupont, J. D. Marechal, A. Martin, M. Sellier and J. P. Mahy, *Bioconjugate Chem.*, 2008, 19, 899.

[26] P. Zucca, G. Mocci, A. Rescigno and E. Sanjust, *J. Mol. Catal. A: Chem.*, 2007, 278, 220–227.

[27] T. T. Liu, J. Tian, L. Cui, Q. Y. Liu, L. L. Wu and X. M. Zhang, *Colloids Surf., B*, 2019, 178, 137.

[28] S. Bhakta, A. Nayek, B. Roy and A. Dey, *Inorg. Chem.*, 2019, 58, 2954–2964.

[29] Y. Hitomi, K. Hiramatsu, K. Arakawa, T. Takeyasu, M. Hata and M. Kodera, *Dalton Trans.*, 2013, 42, 12878–12882.

[30] G. Kumar, S. Devi, R. Johari and D. Kumar, *Eur. J. Med. Chem.*, 2012, 52, 269–274.

[31] J. K. H. Hui and M. J. MacLachlan, *Chem. Commun.*, 2006, 23, 2480.

[32] S. Srimurugan, P. Suresh and H. N. Pati, *J. Inclusion Phenom. Macrocyclic Chem.*, 2007, 59, 383–388.

[33] J. Gregoliński, K. Ślepokura, T. Paćkowski and J. Lisowski, *Org. Lett.*, 2014, 16, 4372.

[34] D. S. Nesterov, O. V. Nesterova, M. F. C. Guedes da Silva and A. J. L. Pombeiro, *Catal. Sci. Technol.*, 2015, 5, 1801–1812.

[35] Y. Y. Kang, H.-R. Park, M. H. Lee, J. An, Y. Kim and J. Lee, *Polyhedron*, 2015, 95, 24–29.

[36] A. Bocian, M. Szymańska, D. Brykczyńska, M. Kubicki, M. Wałęsa-Chorab, G. N. Roviello and V. Patroniak, *Molecules*, 2019, 24, 3173.

[37] W. Yang, K. Q. Zhao, T. J. Prior, D. L. Hughes, A. Arbaoui, T. Bian, M. R. J. Elsegood and C. Redshaw, *Dalton Trans.*, 2016, 45, 11990-12005.

[38] K. Chen, Z. Y. Hua, R. Li, Y. Y. Peng, Q. Z. Zhu, J. L. Zhao and C. Redshaw, *CrystEngComm*, 2021, 23, 465-481.

[39] A. L. Hu, Y. H. Liu, H. H. Deng, G. L. Hong, A. L. Liu, X. H. Lin, X. H. Xia and W. Chen, *Biosens. Bioelectron.*, 2014, 61, 374–378.

[40] W. Chen, L. Hong, A. L. Liu, J. Q. Liu, X. H. Lin and X. H. Xia, *Talanta*, 2012, 99, 643-648.

[41] Y. Ding, B. Yang, H. Liu, Z. Liu, X. Zhang, X. Zheng and Q. Liu, *Sens.Actuators B Chem.*, 2018, 259, 775-783.

[42] N. Wang, J. C. Sun, L. J. Chen, H. Fan and S. Y. Ai, *Microchim. Acta.*, 2015, 182, 1733–1738.

[43] H. Yang, J. Zha, P. Zhang, Y. Xiong, L. Su and F. Ye, *RSC Adv.*, 2016, 6, 66963.

[44] Z. Wang, M. Chen, J. Shu and Y. Li, *J. Alloys Compd.*, 2016, 682, 432–440.

[45] C. Socaci, F. Pogacean, A.R. Biris, M. Coros, M.C. Rosu, L. Magerusan, G. Katona and S. Pruneanu, *Talanta*, 2016, 148, 511–517.

Chapter 6 . Schiff-base double layer macrocycles derived from 2,2'-ethylenedianiline and a Pd@Schiff base composite: synthesis, structures and use as peroxidase mimetics

6.1 Introduction

Enzymes are biocatalysts produced in living cells,[1] which can catalyze various biological and chemical processes efficiently by reducing their activation energy. However, the limitations of natural enzymes, such as high isolation costs, low stability and storage difficulties, have led to the emergence of various artificial enzymes. Recently, varieties of artificial enzymes have been developed, such as peroxidase,[2] catalase,[3] superoxide dismutase,[4] lipase,[5] etc., whilst Horseradish peroxidase (HRP) has become a hot topic of research because of its diverse applications. Over the last decade, increasing numbers of materials have been utilized as peroxidase-like mimetics, for example, metal oxides,[6] precious metals,[7] quantum dots,[8] MOFs,[9] composites,[10] and so on. Such systems have been widely applied in many fields such as analytical chemistry,[11] antibacterial[12] and in the degradation of dyes or other pollutants.[13] Given their ease of acquisition, high efficiency and stability, such artificial mimetics are of great interest.

Schiff base macrocycles are considered as ''privileged ligands''[14] because of their ease of preparation, *i.e.* condensation between aldehydes and imines to form the "-RC=N-" linkage. This has led to Schiff-base chemistry receiving much attention over the years, and such compounds have been widely employed in luminescence sensing,[15] biomaterial,[16] catalytic chemistry,[17] and so on. Of note is the discovery by Ni *et al* of a Schiff-base macrocyclic host that can serve as a probe for Cu^{2+} and Fe^{3+} ion sensing by using those macrocycles.[18] Schiff base compounds can adopt a variety of structural types, and macrocycles,[19] cages,[20] helices[21] are well established.

In recent years, interest in Pd-based heterogeneous catalysts has increased because of the wide range of potential applications and their good reusability. For instance, palladium nanoparticles (PdNPs) using an organic molecular cage as template has been synthesized and can be utilized as an efficient catalyst in Suzuki–Miyaura coupling reactions.[22] In 2017, Nasrollahzadeh *et al.* reported the synthesize of a GO/Pd nanocomposite that was found to be an excellent heterogeneous catalyst for dyes degradation in the presence of NaBH$_4$.[23] Moreover, the incorporation of Pd and enzymes within porous Schiff base molecular cages was reported by Jiang *et al.*, and the resulting composite materials exhibited high efficiency in semi-heterogeneous chemoenzymatic catalysis.[24] Such results have stimulated the demand for new Pd-based composites as heterogeneous catalysts. Despite the plethora of chemistry on Schiff-bases, reports concerning the structures and properties of double layered Schiff base macrocycles and their Pd metal composites, particularly systems exhibiting enzyme-like activity, are rare. Herein, we report a series of [2+2], [2+3] and [2+4] Schiff-base double layer macrocycles derived from 2,2'-ethylenedianiline. It is noteworthy that the [2+2] and [2+3] double layer macrocycles were synthesized in high yield via a one-pot procedure, whilst the [2+4] macrocycle was prepared in two steps and required the presence of a metal. For the first time, we report a Pd composite of a [2+3] double-layer macrocycle, and investigate its enzyme-like activity and apply in the sensing of H$_2$O$_2$.
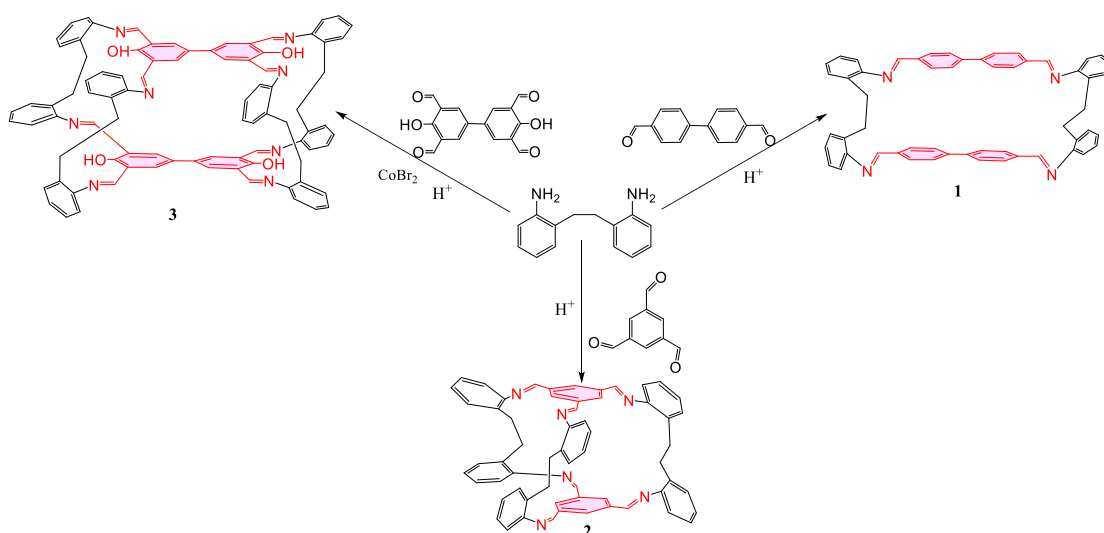
Scheme 6-1. Preparation of **28-30**.

6.2 Results and Discussion

6.2.1 Structures of the double-Layer macrocycles

The double-layer [2+2] macrocycle was synthesized with good yield (*ca.* 70%) via a one-step solvent-mixing method. The reaction of 4,4'-biphenyldicarboxaldehyde with one equivalent of 2,2'-ethylenedianiline at room temperature in the presence of trifluoroacetic acid afforded the [2+2] structure. The double layer [2+2] macrocycle was characterized by multinuclear ^{1}H NMR and FT-IR spectroscopies, elementary analysis, ESI-MS analyses and by single crystal X-ray diffraction. The formation of [2+2] assembled molecule was unambiguously established by the peak at m/z =773.4 corresponding to [M+H]$^+$ in the ESI-MS spectrum (Figure 6-1). Single crystals suitable for X-ray diffraction were grown from a saturated toluene/CH$_2$Cl$_2$ solution (1:1) at room temperature. Various views of the molecular structure are shown in Figure 6-2.

The [2+2] macrocycle crystallises in the centrosymmetric space group *P*2$_1$/*c* with two symmetry-unique molecules in the asymmetric unit that are related by a pseudo-translation of *b*/2. The molecular conformation of the two molecules is very similar; these

145

differ only in the conformation of one -CH$_2$CH$_2$ link. There is simple primitive packing of these pairs of molecules according to the space group symmetry. No classical hydrogen bonds are present but there are numerous C–H···π interactions connecting neighbouring macrocycles as shown in Figure 6-2b.
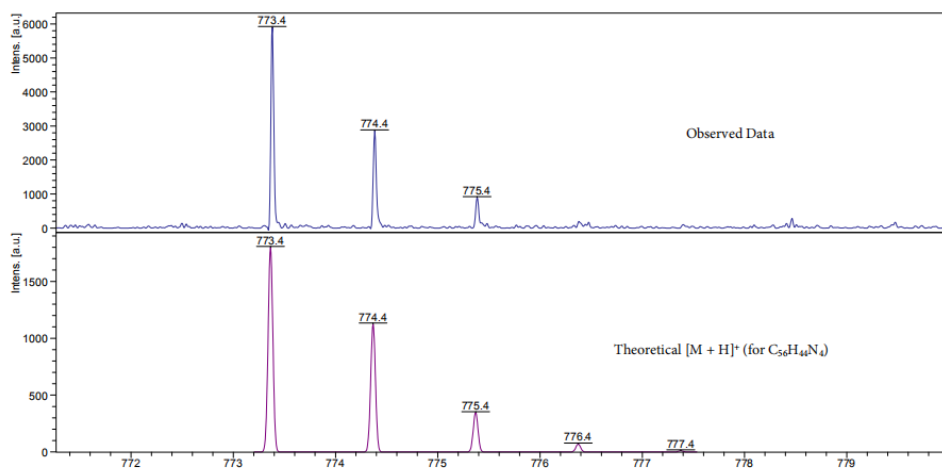
Figure 6-1. Mass spectrum for the [2+2] macrocycle **28**.
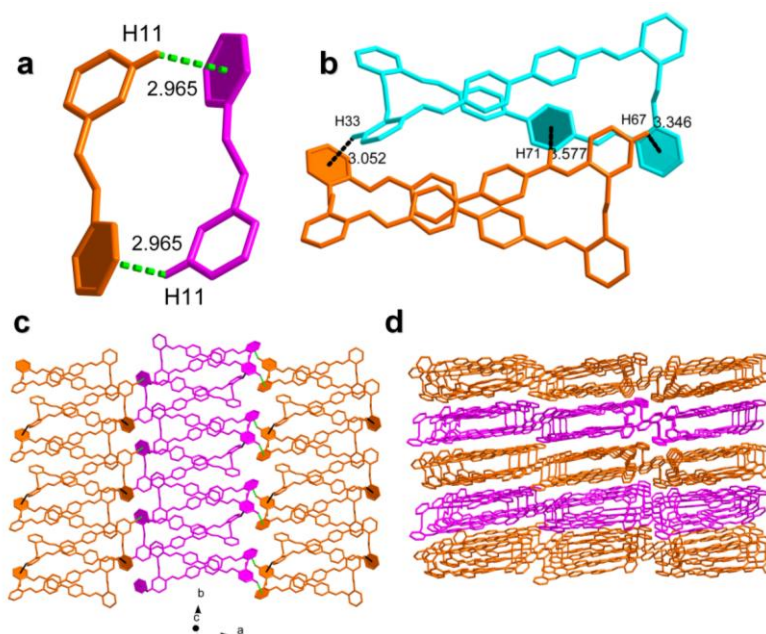
Figure 6-2. Structure of the [2+2] macrocycle **28**. a) and b) C-H···π interactions; c) the 2D network linked via the C-H···π interactions; d) 3D packing pictures for [2+2] macrocycle.

By treating 1,3,5-triformylbenzene with 2,2'-ethylenedianiline in a 2:3 stoichiometric ratio in dichloromethane, in the presence of trifluoroacetic acid, a [2+3] double layer macrocycle was isolated. The [2+3] macrocycle is enthalpically favoured because of the least angle strain, and is entropically favoured due to it been comprised of the minimum number of building blocks compared to all the possible 3D architectures.[25] The [2+3] macrocycle was characterized by multinuclear NMR (^{1}H, ^{13}C), ^{1}H-^{1}H COSY, HBMC and FT-IR spectroscopies, elementary analysis and ESI-MS analysis (Figure 6-4 to Figure 6-8). Single crystals suitable for X-ray diffraction were grown from a saturated dichloromethane solution at room temperature. Various views of the molecular structure are shown in Figure 6-3. The {2+3} macrocycle crystallises in the centrosymmetric space group *Pbca* with a single macrocycle and one dichloromethane in the asymmetric unit. The molecules are arranged in columns parallel to the crystallographic *b*-axis (Figure 6-3b) with numerous C–H⋯π interactions and π⋯π interactions connecting neighbouring macrocycles (Figures 6-3a-d). The dichloromethane molecules appear to reside in pockets between macrocyclic molecules (Figure 6-3e) rather than in channels. There are C–H⋯π and C-H⋯Cl interactions between the dichloromethane and surrounding macrocycles. The peak at m/z =853.4 in the ESI-MS spectrum (Figure 6-4) corresponds to [M – CH_2Cl_2] illustrating the formation of the double layer macrocycle.
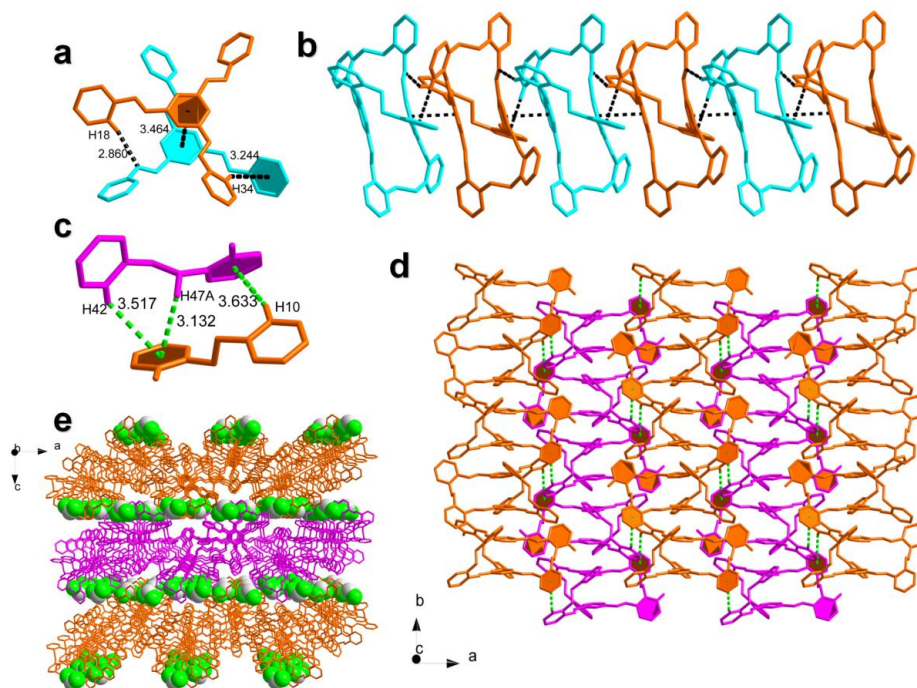
Figure 6-3. Structure of the [2+3] macrocycle **29**. (a) C-H···π and π ···π interactions; b) The 1D chain along [010]; c) C-H···π and π ···π between molecules; d) 2D network linked via the C-H···π interactions; e) packing of the [2+4] macrocycle with CH_2Cl_2 between macrocyclic molecules.
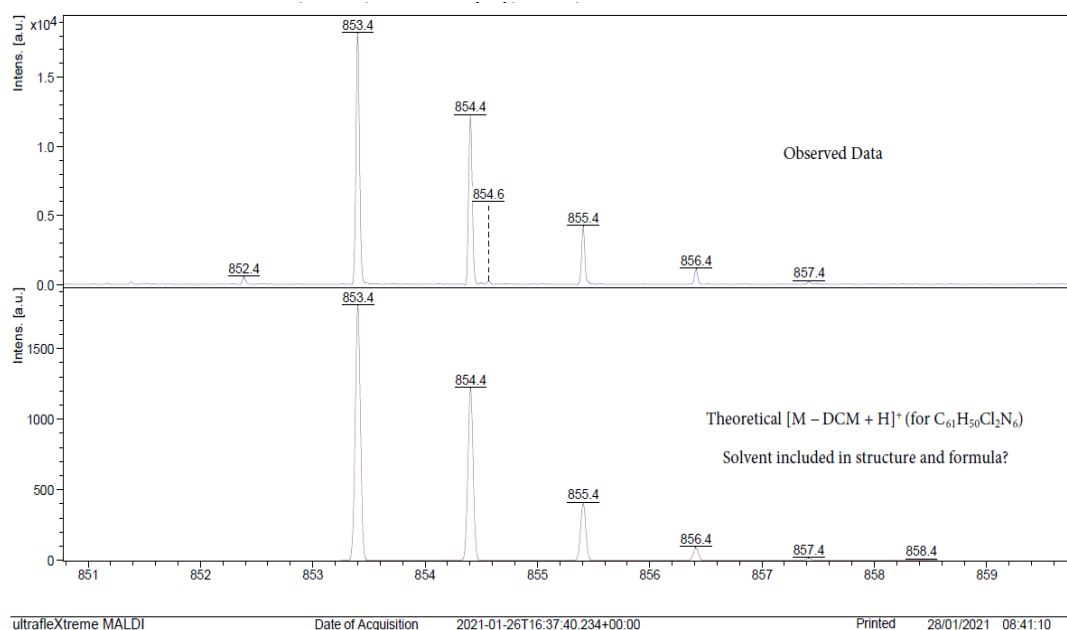
Figure 6-4. Mass spectrum for the [2+3] macrocycle **29**.

148
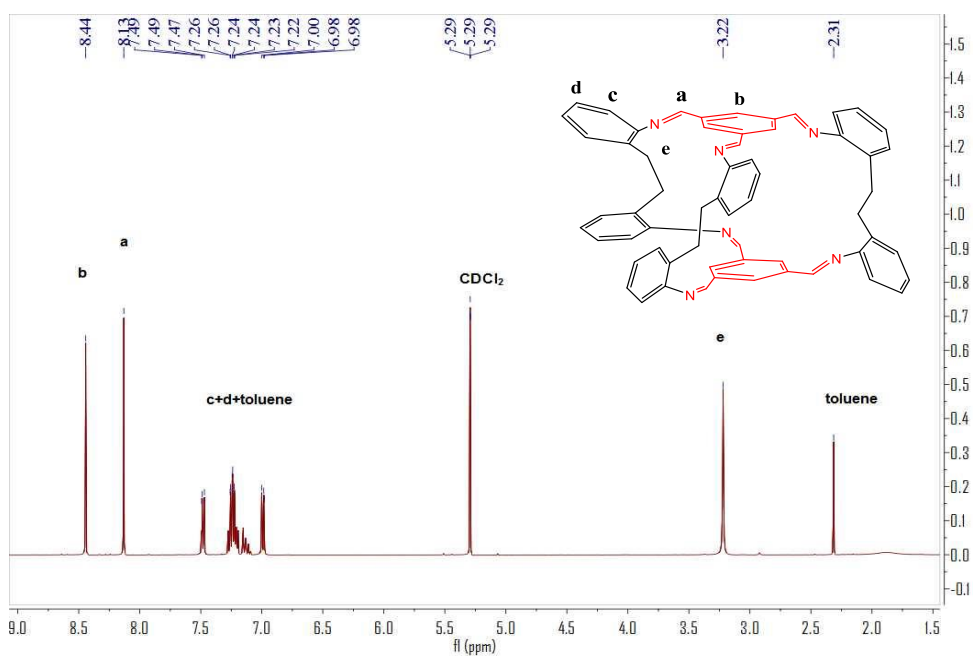
Figure 6-5. ^{1}H NMR spectrum of the [2+3] macrocycle **29**.
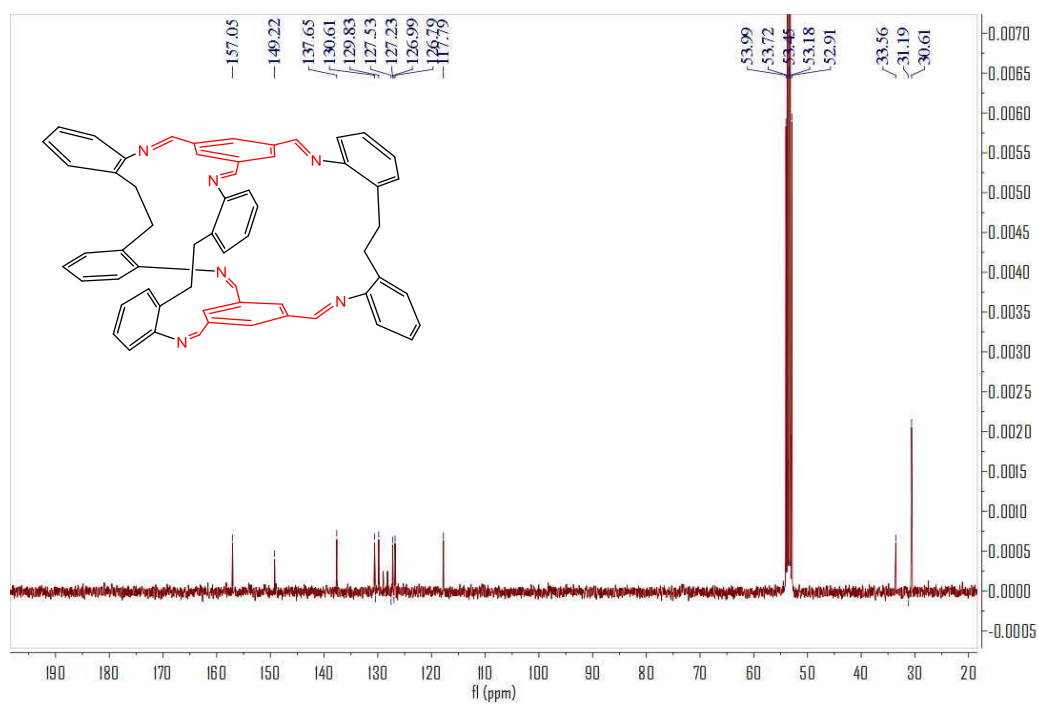
Figure 6-6. ^{13}C NMR spectrum of the [2+3] macrocycle **29**.
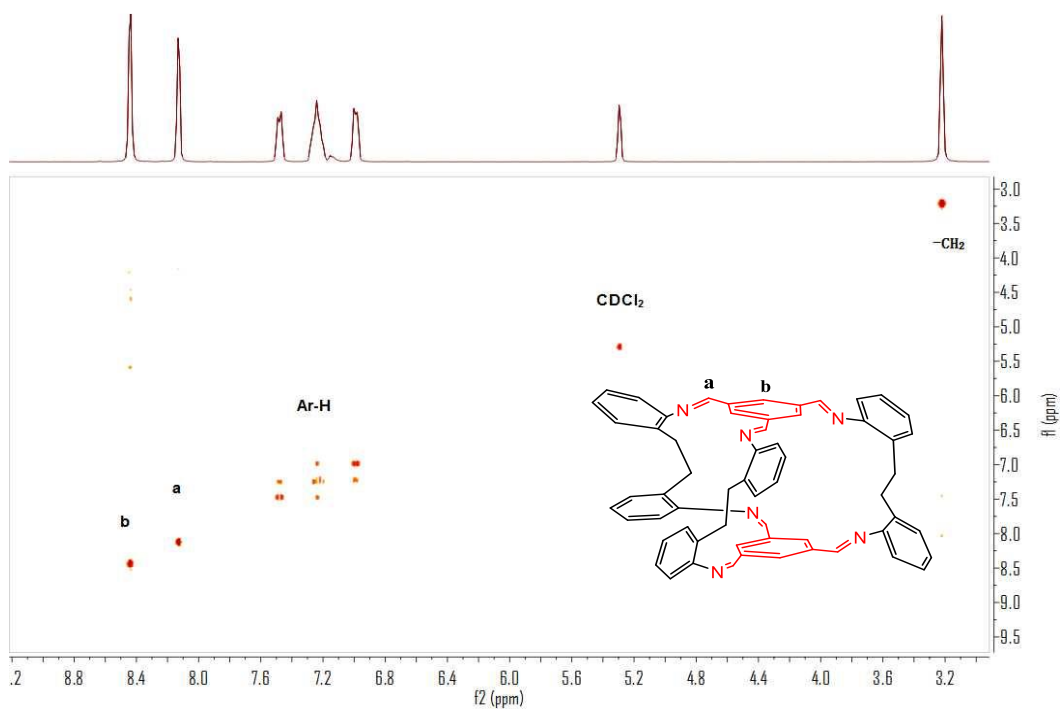
Figure 6-7. ^{1}H-^{1}H COSY NMR spectrum of the [2+3] macrocycle **29**.
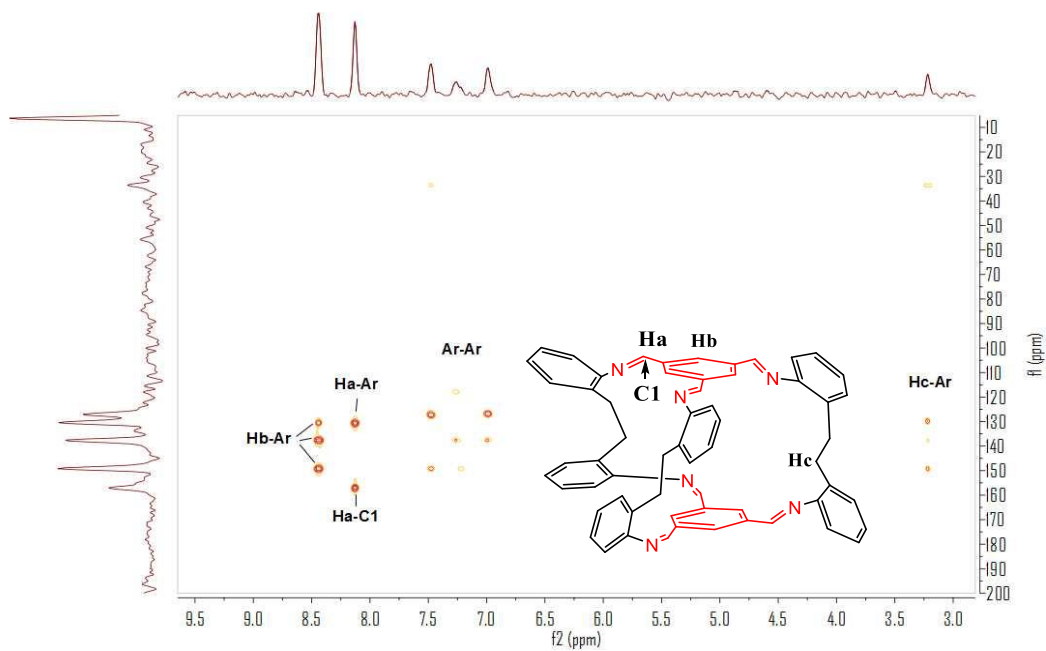
Figure 6-8. ^{1}H-^{13}C HMBC NMR spectrum of the [2+3] macrocycle **29**.
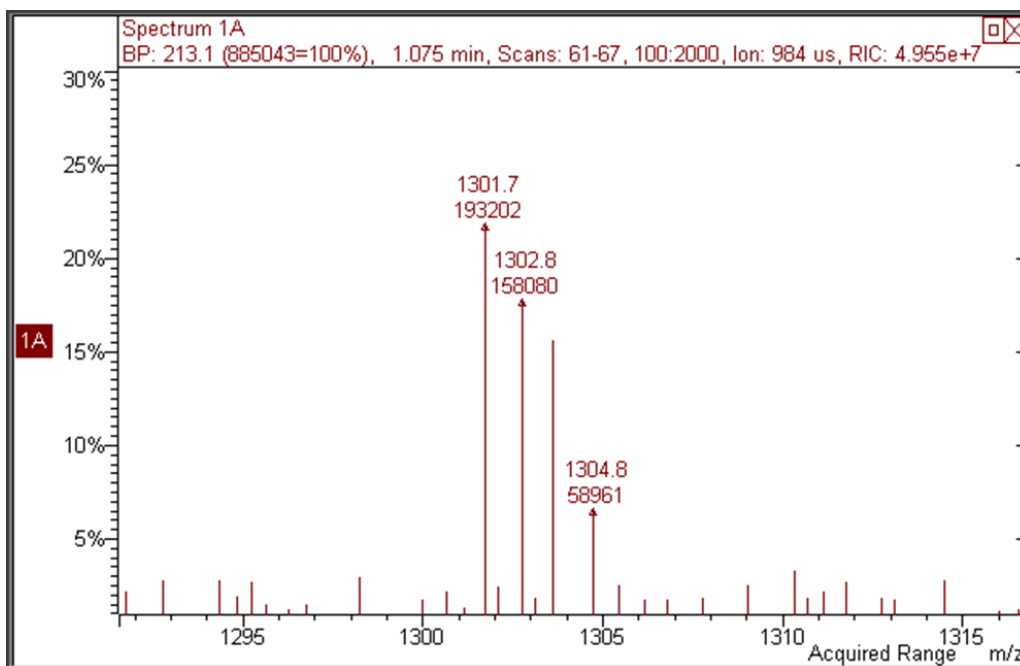
Figure 6-9. Mass spectrum for the [2+4] macrocycle **30**.
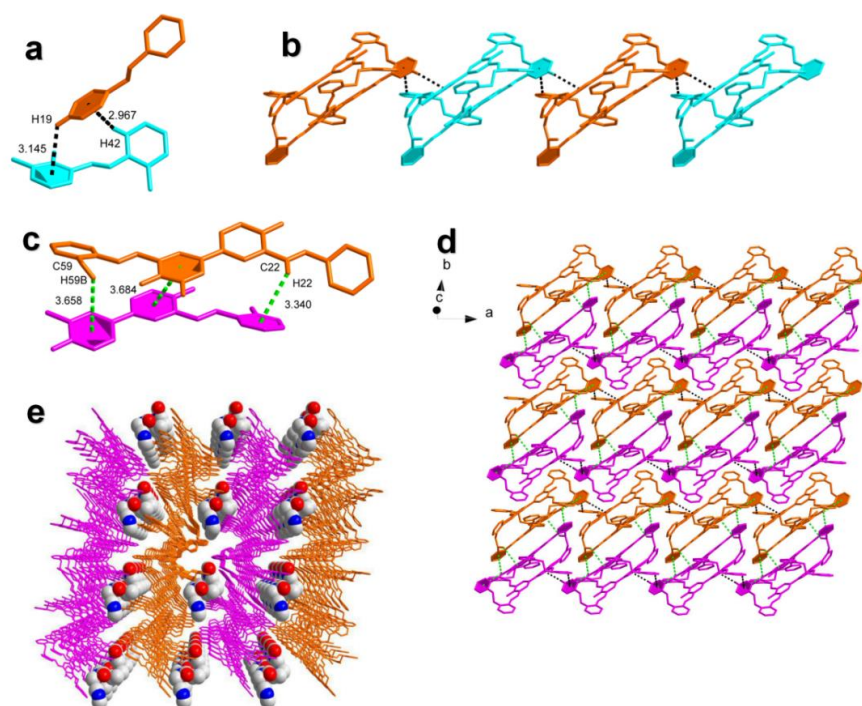
Figure 6-10. Structure of the [2+4] macrocycle **30**. (a) C-H⋅⋅π interactions between molecules; b) 1D chain by non-covalent interactions along [010]; c) C-H⋅⋅π and π ⋅⋅π interactions between neighbouring macrocycles; d) the 2D network linked via the C-H⋅⋅π

interactions; e) packing of the [2+4] macrocycle with DMF between macrocyclic molecules.

In the case of the [2+4] macrocycle, it proved necessary to employ a two-step procedure. Firstly, 4,4'-dihydroxy-[1,1'-biphenyl]-3,3',5,5'-tetracarbaldehyde and 2 equivalents of 2,2'-ethylenedianiline were refluxed in toluene in the presence of formic acid. After the toluene was removed and the residue washed using acetonitrile, the system was refluxed in toluene again with 6 equivalents of $CoBr_2$ (note $ZnBr_2$ or $FeBr_2$ can also be employed), affording after work-up (recrystallization from hot DMF), a red crystalline solid. The limited solubility of this macrocycle prevented characterization by NMR spectroscopy, however, FT-IR spectroscopy, elementary analysis and ESI-MS analyses (Figure 6-9) were possible. Moreover, single crystals suitable for X-ray diffraction were grown from a saturated DMF solution at room temperature. Various views of the molecular structure are shown in Figure 6-10.

The large macrocycle crystallises in the centrosymmetric space group P-1 with a single macrocycle and five DMF molecules and one MeCN in the asymmetric unit. The solid-state structure helps to define the topology of this macrocycle; if the 3-connected aromatic rings are taken as nodes, then this molecule is seen as a tetrahedron. There are intermolecular O-H···N hydrogen bonds present and as for the [2+3] structure, C–H···π interactions and π···π interactions were found between neighbouring macrocycles (Figure 6-10a); DMF molecules were found to be present in the intermolecular spaces (Figure 6-10e).

6.2.2   DFT studies on the double layer macrocycles

In order to discuss the electron distribution of the double layer Schiff base macrocycles, density function theory (DFT) calculations at the RB3LYP/6-311G(d,p) level was carried out using a Gaussion 09 program. The energy gap (ΔE) is, 3.54 eV for **28**, 3.81 eV for **29** and, 3.18 eV for **30**, respectively.

The different electronic structures and energy levels lead to the differences in the electronic spectra between those compounds (shown in Table 6-1). The optimized molecular structures and the corresponding HOMO-LUMO levels are shown in Table 6-2 using the single-crystal structure as a model. For the [2+2] structure **28**, the HOMO and LUMO levels are separated on two diphenyl rings groups, respectively, whilst the HOMO and LUMO energy level of [2+3] structure **29** is only centralized on the salicylaldehyde groups.
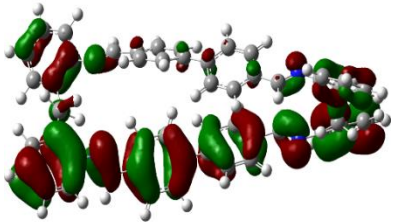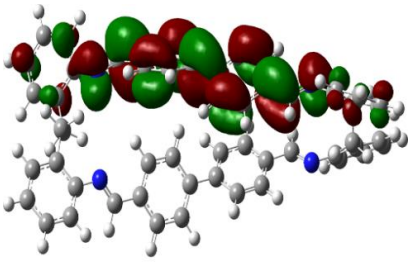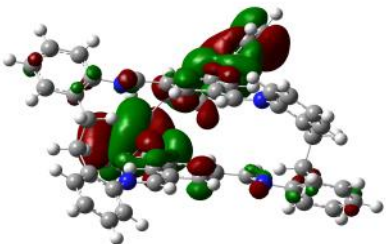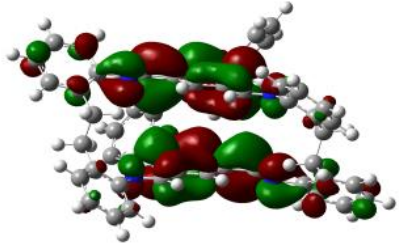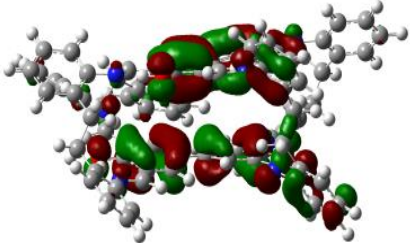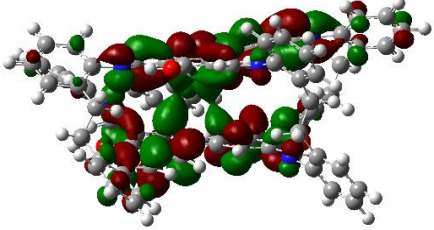
Table 6-1. HOMO/LOMO energy level for the macrocycles **28**-**30**.

Macrocycle	HOMO (eV)	LOMO (eV)	Eg (eV)
[2+2] (28)	-5.85	-2.31	3.54
[2+3] (29)	-6.01	-2.20	3.81
[2+4] (30)	-5.63	-2.45	3.18

In the [2+4] macrocycle **30**, the HOMO and LUMO level are mostly localized on the salicylaldehyde and a bridging imine group. The difference in the electronic distribution may be due to the presence of the charge delocalization of the six-membered ring consisting of intramolecular hydrogen bonds formed by O atoms, hydrogen atoms and

adjacent N atoms in **30**. Compared to **29**, the intramolecular H-bonding in **30** and the extended π-conjugation in **29** could enhance the HOMO energy level and lower the LUMO energy level.

Table 6-2. Optimized geometry and electronic distribution of the frontier orbitals for the macrocycles.

Complex	HOMO	LOMO
[2+2](28)		
[2+3](29)		
[2+4](30)		

6.2.3   Preparation and characterization of Pd@Schiff base

The [2+3] macrocycle was chosen for the incorporation Pd because of its high yield and facile synthesis. As can be seen from the Figure 6-11a, in the PXRD pattern, the diffraction peaks at 2θ = 40.0, 46.6, 68.4° can be assigned to the (111), (200), (220) reflections of the Pd metallic phase, consistent with the successfully immobilization of the Pd. Moreover, SEM was used to study the morphology of Pd@Schiff base and is exhibited in Figure 6-11. Figure 6-11b reveals the nano rod-like morphology of the [2+3] macrocycle; the SEM image of Pd@Schiff base composite was depicted in Figure 6-11c. The SEM elemental mappings further illustrated that Pd were uniformly distributed over the Schiff base structure (Figure 6-11d).
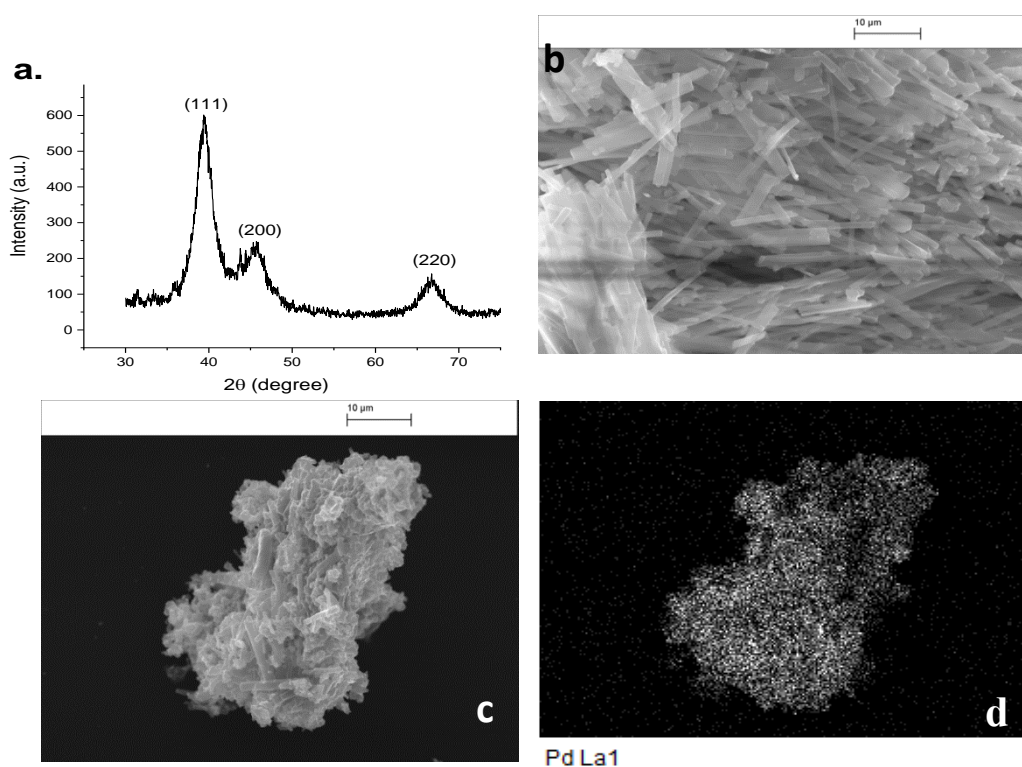
Figure 6-11. a) PXRD of the Pd@Schiff base product; b) SEM of the [2+3] macrocycle; c) SEM of the Pd@Schiff base composite; d) Pd mapping for the Pd@Schiff base composite.

155

6.2.4 Peroxidase-like activity of Pd@Schiff base

The peroxidase-like catalytic activity of the Pd@Schiff base composite was investigated via the oxidation of TMB in the presence of H_2O_2. Hydrogen peroxide can oxidize TMB in the presence of the Pd@Schiff base composite forming a blue coloured product (oxTMB) and exhibits an absorption at 652 nm. As shown in Figure 6-12, the colour change can only be observed in the Pd@Schiff base-TMB-H_2O_2 system, whereas no oxidation was observed in the Pd@Schiff base-TMB system. The Pd@Schiff base leach liquor- TMB-H_2O_2 system or TMB-H_2O_2 system, reveals that the peroxidase-like activity was generate from our Pd@Schiff base material and not the leaching of the Pd ion into the solution.
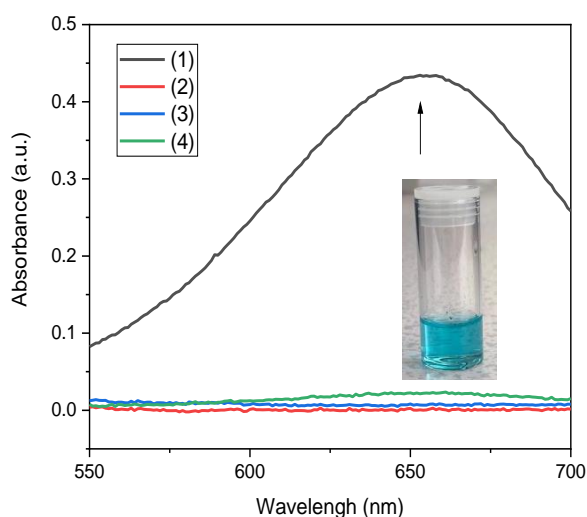
Figure 6-12. Absorbance spectra of oxTMB in different reaction conditions: 1) Pd@Schiff base + TMB + H_2O_2; 2) Pd@Schiff base + TMB; 3) Pd@Schiff base leaching liquor solution + TMB + H_2O_2; 4) TMB + H_2O_2.

The pH conditions for the peroxidase-like activity of Pd@Schiff base were optimized as shown in Figure 6-13. The pH played an important role in the catalytic

process, and the Pd@Schiff base was not active under alkaline conditions, whilst pH = 4 was found to be the optimum condition. In addition, the effect of temperature was also addressed, and the peroxidase-like properties were found to be enhanced as the temperature increased from room temperature to 60 °C.
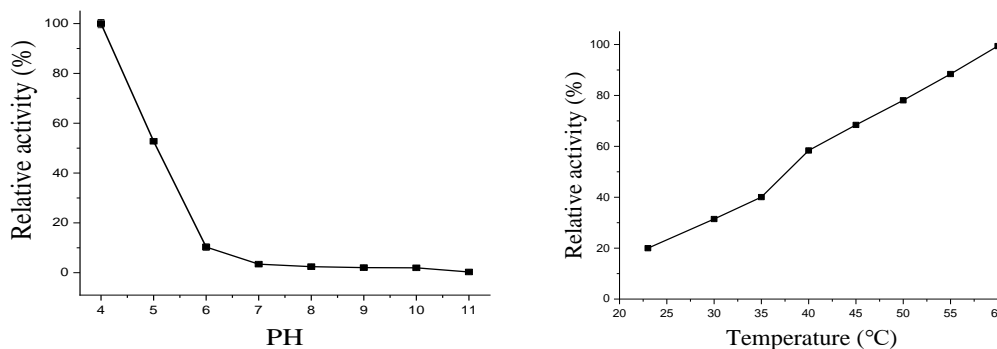
Figure 6-13. Effects of (a) pH and (b) temperature on the peroxidase-like activity of Pd@Schiff base composite.

6.2.5   Kinetic studies

Steady-state kinetic measurements were carried out to evaluate the kinetic process of the peroxidase-like activity of the Pd@Schiff base composite. The oxidation process follows the "ping–pong" mechanism because the double reciprocal plot is near linear (Figure 6-14 c) and d)).[26] The calculated K_m and V_{max} values for the Pd@Schiff base toward H_2O_2 and TMB are shown in Table 6-3.

The synthesized Pd@Schiff base composite possesses relatively small K_m values illustrating the good combining capacity towards H_2O_2 as peroxidase-like mimetics.

Table 6-3. Kinetic parameters of HRP and other Pd based peroxidase mimetics using TMB as substrate.

Catalyst	K_m (mM)		V_{max} (10^{-8} M·s^{-1})		Reference
	H$_2$O$_2$	TMB	H$_2$O$_2$	TMB	
HRP	3.7	0.43	8.71	10	[27]
MoS$_2$-PPy-Pd	6.4	0.93	-	-	[28]
Fe$_3$O$_4$@SiO$_2$-NH$_2$-Au@Pd$_{0.30}$	3.5	0.090	6.76	11.20	[29]
Pd$_1$Cu$_{1.7}$ NAFs	7.782	0.377	69.04	53.24	[30]
Pd NAFs	13.768	0.040	29.06	16.89	[30]
Pd@Schiff base	1.17	8.86	3.67	3.72	This work
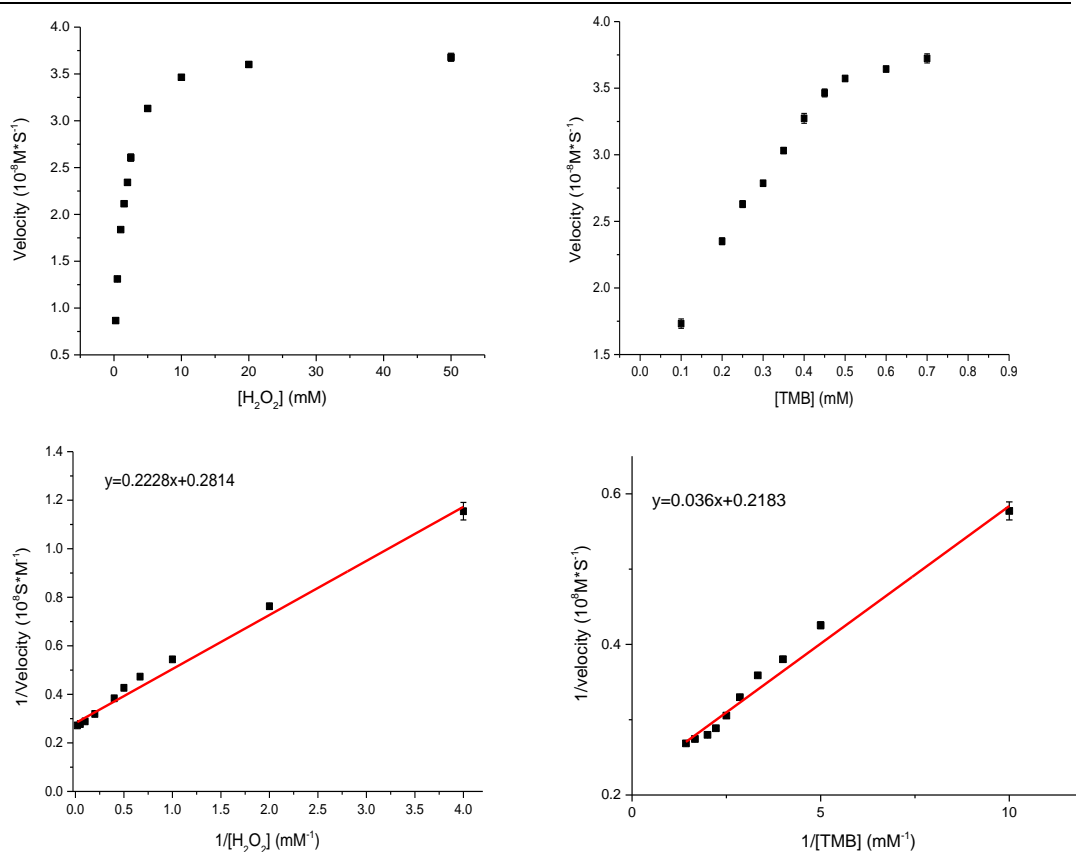
Figure 6-14. Steady state kinetic assay of synthesized Pd composite. (a) Constant concentration of H$_2$O$_2$ (50 mM) and the TMB concentration was varied (b) Constant concentration of TMB (0.5 mM) and the H$_2$O$_2$ concentration was varied. Double reciprocal plot of peroxidase mimic activity of Pd composite with the (c) constant

concentration of H_2O_2 (50mM) and varying concentrations of TMB (d) constant concentration of TMB (0.5mM) and varying concentrations of H_2O_2. The reactions were carried out with 0.1mg/mL Pd composite in 3 mL of 100mM NaAc-HAc buffer at pH=4.0.

6.2.6 H_2O_2 determination
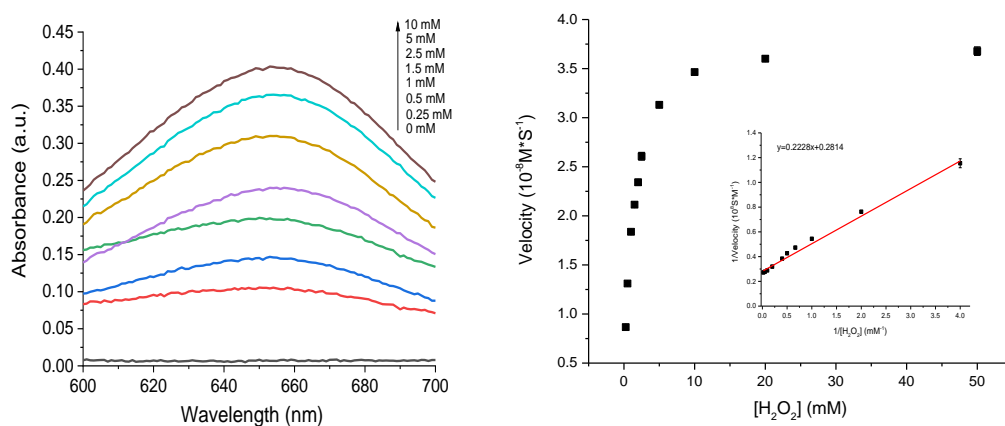
Figure 6-15. H_2O_2 determination using Pd@Schiff base as a peroxidase mimetic. (a) The UV-vis absorption spectra for different H_2O_2 concentrations; (b) Linear calibration plot for H_2O_2 detection.
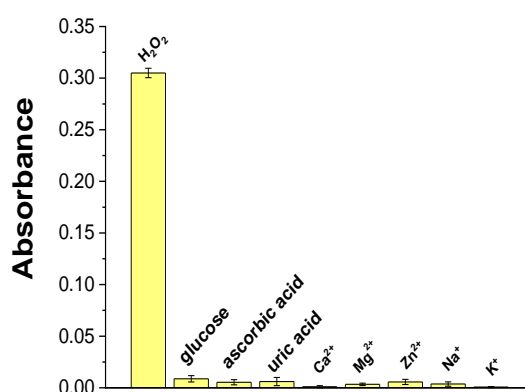
Figure 6-16. Selectivity test of the H_2O_2 detection method. The concentrations used were as follows: 2 mM H_2O_2, 10 mM glucose, ascorbic acid, uric acid, Ca^{2+}, Mg^{2+}, Zn^{2+}, Na^+, K^+.

Based on the above-mentioned findings, a colorimetric sensor for H_2O_2 is constructed using the peroxidase-like activity of the Pd@Schiff base composite. The absorbance of the system was proportional to the amount of H_2O_2. As shown in Figure 6-15, linear ranges for our H_2O_2 detection were 0.5-10 mM with a limit of detection (LOD) of 29.7 µM. In order to test the selectivity of the constructed H_2O_2 detection method, the absorbance of H_2O_2 and some other interferences (glucose, ascorbic acid, uric acid, Ca^{2+}, Mg^{2+}, Zn^{2+}, Na^+, K^+) were evaluated, see Figure 6-16. The concentration of the potential interferences is 5-fold H_2O_2 and these interferents showed very weak colour changes, which indicates that our Pd@Schiff system exhibits good selectivity toward H_2O_2 determination.

6.3   Conclusion

In conclusion, three new [2+2] [2+3] and [2+4] double layer Schiff-base macrocycles derived from condensation reactions involving 2,2'-ethylenedianiline and di-, tri- or tetra-aldehydes have been synthesized and structurally characterized. The [2+3] derivative formed a composite with Pd, and was used as a horseradish peroxidase mimetic. When the reaction pH was 4.0, the system exhibited the highest absorbance at 652 nm, indicating optimum catalytic activity. From the kinetic studies, the peroxidase-like activity of the Pd@Schiff base composite exhibited Michaelis−Menten type kinetics and a "ping−pong" mechanism. Based on the peroxidase mimic activity, a colorimetric method for H_2O_2 detection using the Pd@Schiff base macrocycle was developed. The approach exhibits good selectivity toward H_2O_2 with a linear range of 0.5-10 mM and a low detection limit of 0.05 mM, which may have potential applications in biosensors.

6.4 References

[1] L. A. Underkofler, R. R. Barton and S. S. Rennert, *Appl. Microbiol.*, 1958, 6, 212-221.

[2] K. Wang, J. Song, X. Duan, J. Mu and Y. Wang, *New J. Chem.*, 2017, 41, 8554–8560.

[3] Z.W. Chen, J.J. Yin, Y.T. Zhou, Y. Zhang, L. Song, M. J. Song, S.L. Hu and N. Gu, *ACS Nano*, 2012, 6, 4001-4012.

[4] L. Lewandowski, M. Kepinska and H. Milnerowicz, *Eur. J. Clin. Invest.*, 2018, 49, e13036.

[5] L. Youngjun and N. K. Devaraj. *Chem. Sci.*, 2021, 12, 1090-1094.

[6] L. Z. Gao, J. Zhuang, L. Nie, J. B. Zhang, Y. Zhang, N. Gu, T. H. Wang, J. Feng, D. L. Yang, S. Perrett and X. Yan, *Nat. Nanotechnol.*, 2007, 2, 577-583.

[7] Y. Hu, H. Cheng, X. Zhao, J. Wu, F. Muhammad, S. Lin, J. He, L. Zhou, C. Zhang, Y. Deng, P. Wang, Z. Zhou, S. Nie and H. Wei, *ACS Nano*, 2017, 11, 5558–5566.

[8] V. K. Singh, P. K. Yadav, S. Chandra, D. Bano, M. Talat and S. H. Hasan, *J. Mater. Chem. B*, 2018, 6, 5256–5268.

[9] J. W. Zhang, H. T. Zhang, Z. Y. Du, X. Wang, S. H. Yun and H. L. Jiang, *Chem. Commun.*, 2014, 50(9), 1092-1094.

[10] T. Zhang, Y. Xing, Y. Song, Y. Gu, X. Yan, N. Lu, H. Liu, Z. Xu, H. Xu, Z. Zhang and M. Yang, *Anal. Chem.*, 2019, 91, 10589–10595.

[11] J. Wang, Y. Y. Hu, Q. Zhou, L. Z. Hu, W. S. Fu and Y. Wang, *ACS Appl. Mater. Interfaces*, 2019, 11, 44466–44473.

[12] C. Ge, R. Wu, Y. Chong, G. Fang, X. Jiang, Y. Pan, C. Chen and J.-J. Yin, *Adv. Funct. Mater.*, 2018, 28, 1801484

[13] Q. M. Chen, X. D. Zhang, S. Q. Li, J. K. Tan, C. J. Xu and Y. M. Huang, *Chem. Eng. J.*, 2020, 395, 125130.

[14] T. P. Yoon, E. N. Jacobsen, *Science*, 2003, 299, 1691-1693.

[15] Y. W. Choi, G. J. Park, Y. J. Na, H. Y. Jo, S. A. Lee, G. R. You and C. Kim, *Sens. Actuators, B,* 2014, 194, 343–352.

[16] S. Li, M. Pei, T. Wan, H. Yang, S. Gu, Y. Tao, X. Liu, Y. Zhou, W. Xu, P. Xiao, 2020, *Carbohyd. Polym.*, 250, 116922.

[17] K. Wang, T. J. Prior and C. Redshaw, *Chem. Commun.*, 2019, 55, 11279–11282.

[18] Q. Yu, X. Zhang, S. T. Wu, H. Chen, Q. L. Zhang, H. Xu, Y. L. Huang, B. X. Zhu and X. L. Ni, *Chem. Commun.*, 2020, 56, 2304–2307.

[19] K. Wang, T. J. Prior, D. L. Hughes, A. Arbaoui and C. Redshaw, *Dalton Trans.*, 2021, 50, 8057-8069.

[20] P. Li, S. Xu, C. Yu, Z.-Y. Li, J. Xu, Z.-M. Li, L. Zou, X. Leng, S. Gao, Z. Liu, X. Liu and S. Zhang, *Angew. Chem., Int. Ed.*, 2020, 59, 7113–7121.

[21] X. P. Yang, R. A. Jones, M. M. Oye, A. L. Holmes and W. K. Wong, *Cryst. Growth Des.*, 2006, 6, 2122-2125.

[22] L. Qiu, R. McCaffrey, Y. Jin, Y. Gong, Y. Hu, H. Sun, W. Park and W. Zhang, *Chem. Sci.*, 2018, 9, 676-680.

[23] A. Omidvar, B. Jaleh and M. Nasrollahzadeh, *J. Colloid. Interface. Sci.*, 2017, 496, 44-50.

[24] S. Gao, Y. Liu, L. Wang, Z. Wang, P. Liu, J. Gao and Y. Jiang, *ACS Catal.*, 2021, 11, 5544–5553.

[25] Y. Jin, B. A. Voss, A. Jin; H. Long, R. D. Noble and W. Zhang, *J. Am. Chem. Soc.*, 2011, 133, 6650−6658.

[26] S. Bhakta, A. Nayek, B. Ro and A. Dey, *Inorg. Chem.*, 2019, 58, 2954–2964.

[27] L. Z. Gao, J. Zhuang, L. Nie, J. B. Zhang, Y. Zhang, N. Gu, T. H. Wang, J. Feng, D. L. Yang, S. Perrett and X. Yan, *Nat. Nanotechnol.*, 2007, 2, 577-583.

[28] M. Chi, Y. Zhu, L. Jing, C. Wang and X. Lu, *Anal. Chim. Acta*, 2018, 1035, 146–153.

[29] O. Adeniyi, S. Sicwetsha and P. Mashazi, *ACS Appl. Mater. Interfaces*, 2020, 12, 1973−1987.

[30] W. Liu, J. Guo, C. Chen, P. Ni, Y. Jiang, C. Zhang, B. Wang and Y. Lu, *Microchim. Acta*, 2021, 188, 114–114.

Chapter 7 Experimental Section

7.1 Co and Zn complexes for ring opening polymerization

7.1.1 General

All manipulations were carried out under an atmosphere of dry nitrogen using conventional Schlenk and cannula techniques or in a conventional nitrogen-filled glove box. Toluene was refluxed over sodium. Acetonitrile was refluxed over calcium hydride. THF was dried over sodium benzophenone. All solvents were distilled and degassed prior to use. IR spectra (nujol mulls, KBr windows) were recorded on a Nicolet Avatar 360 FT-IR spectrometer; ^{1}H NMR spectra were recorded at room temperature on a Varian VXR 400 S spectrometer at 400 MHz or a Gemini 300 NMR spectrometer or a Bruker Advance DPX-300 spectrometer at 300 MHz. The ^{1}H NMR spectra were calibrated against the residual protio impurity of the deuterated solvent. Magnetic moments were determined using an Evans balance.[1] Elemental analyses were performed by the elemental analysis service at the Department of Chemistry, the University of Hull. The pro-ligands $L^{tBu}H_2$ and $L^{Me}H_2$ were prepared as described previously.[2] All other chemicals were purchased from Sigma Aldrich or TCI, UK.

7.1.2 Synthesis of Co and Zn complexes

Synthesis of $[CoBrL^{tBu}][CoBr_3(NCMe)]\cdot0.5MeCN$ (**1**·0.5MeCN)

$L^{tBu}H_2$ (0.50 g, 0.65 mmol) and $CoBr_2$ (0.29 g, 1.33 mmol) were weighed out in a dry box. After transferring to a Schlenk line, toluene (20 mL) was added and the system was refluxed for 12 h. On cooling, the volatiles were removed *in-vacuo*, and the residue was extracted into warm MeCN (20 mL). On cooling (0 °C), green prisms were formed which were isolated and dried *in-vacuo* to afford **1**·0.5MeCN (1.13 g, 69% yield). Elemental analysis calculated for $C_{110}H_{106}Br_8Co_4N_{11}O_4$ C 52.40, H 4.24, N 6.11%. Found: C 51.94,

H 4.24, N 5.84%. IR: 3534 (w), 3415 (w), 3051 (m), 2925 (s), 2855 (s), 2729 (m), 2307 (m), 2280 (w), 2251 (w), 1973 (w), 1892 (m), 1886 (w), 1633 (s), 1619 (s), 1584 (m), 1558 (w), 1537 (s), 1502 (w), 1484 (m), 1462 (s), 1395 (s), 1377 (s), 1360 (m), 1335 (s), 1299 (m), 1283 (m), 1241 (s), 1218 (s), 1180 (m), 1165 (w), 1159 (w), 1137 (m), 1102 (m), 1063 (s), 1047 (s), 1020 (s), 955 (m), 945 (w), 939 (w), 912 (m), 843 (m), 828 (m), 794 (m), 766 (s), 725 (w), 688 (m), 675 (w). M. S. (MALDI-ToF): 1041 [M-(MeCN)-Br$_2$], 961 [M-(MeCN)-Br$_3$], 822 [M-Br-anion]. Mag moment: μ_{eff} 6.66 B.M.

Synthesis of [CoBr**L**$^{\textbf{Me}}$][CoBr$_3$(NCMe)]·4MeCN (**2**·4MeCN)

L$^{\textbf{Me}}$H$_2$ (0.50 g, 0.73 mmol) and CoBr$_2$ (0.32 g, 1.47 mmol) were weighed out in a dry box. After transferring to a Schlenk line, toluene (20 mL) was added and the system was refluxed for 12 h. On cooling, the volatiles were removed *in-vacuo*, and the residue was extracted into warm MeCN (20 mL). On cooling (0 °C), green prisms were formed which were isolated and dried *in-vacuo* to afford **2**·4MeCN (0.66 g, 69% yield). Elemental analysis calculated for C$_{48}$H$_{41}$Br$_4$Co$_2$N$_5$O$_2$ (**2**): C 49.73, H 3.57, N 6.05%. Found: C 49.24, H 3.63, N 5.50%. IR: 2923 (s), 2854 (s), 2726 (w), 1634(s), 1589(s), 1532 (s), 1463 (s), 1377(s), 1335 (m), 1281 (m), 1240 (m), 1214 (m), 1181 (m), 1104 (m), 1067 (m), 1049 (w), 966 (m), 892 (w), 871 (m), 840 (w), 810 (s), 788 (w), 754 (s), 739 (w), 722 (s), 672 (w), 615 (w), 595 (w), 574 (w), 549 (w), 533 (m), 521 (s), 499 (s), 467 (m). M. S. (MALDI-ToF): 1051 (M-Co-MeCN), 961 (M-Br-MeCN), 871 (M-Br$_3$-MeCN), 855 (M-CoBr$_3$), 818 (M-anion), 738 (M-Br - anion). Mag moment: μ_{eff} 6.77 B.M.

Synthesis of [ZnBr**L**$^{\textit{t}\textbf{Bu}}$][ZnBr$_3$(NCMe)]·MeCN (**3**·MeCN)

As for **1**·0.5MeCN, but using **L**$^{\textit{t}\textbf{Bu}}$H$_2$ (0.50 g, 0.65 mmol) and ZnBr$_2$ (0.30 g, 1.33 mmol) affording yellow prisms of **3**·MeCN. Yield 0.62 g, 76%. Elemental analysis calculated for C$_{54.25}$H$_{55}$Br$_4$N$_5$O$_{2.25}$Zn$_2$: C 51.63 H 4.39 N 5.54%; found: C 51.50, H 4.41, N 5.67%. IR: 2956 (s), 2924 (s), 2854 (s), 2728 (m), 2349 (w), 2293 (m), 1634 (s), 1621 (s), 1587

(s), 1574 (w), 1556 (w), 1535 (s), 1502 (w), 1480 (m), 1463 (s), 1396 (m), 1377 (s), 1366 (m), 1329 (s), 1297 (w), 1284 (w), 1260 (m), 1240 (s), 1217 (m), 1182 (m), 1154 (m), 1101 (m), 1060 (m), 1048 (w), 1021 (m), 953 (w), 934 (w), 909 (w), 890 (m), 877 (w), 841 (w), 794 (s), 754 (s), 723 (m), 688 (w). M. S. (MALDI-ToF): 909 [M-anion], 827 [M-Br-anion], 765.4 [M-ZnBr-anion]. ^{1}H NMR (CD$_3$CN, 400 MHz): δ 8.70 (d, 2H, J=13.2, Ar-H), 8.50 (s, 2H, CH=N), 7.94 (d, 2H, J=2.8, Ar-H), 7.70 (d, 2H, J=2.8, Ar-H), 7.54 (m, 6H, Ar-H), 7.01 (d, 2H, J=6.8, Ar-H), 6.95 (td, 2H, J$_1$=8.0, J2=1.2, Ar-H), 6.78 (td, 2H, J$_1$=7.6, J$_2$=2.4, Ar-H), 6.23 (d, 2H, J=6.4, CH=N), 3.71 (t, 2H, J=13.2, CH_2), 3.52 (dt, 2H, J$_1$=14.0, J$_2$=4.4, CH_2), 3.01 (dt, 2H, J$_1$=14.4, J$_2$=4.0, CH_2), 2.58 (td, 2H, J$_1$=13.6, J$_2$=3.2, CH_2), 2.11 (s, 18H, C(CH_3)$_3$).

Synthesis of [ZnBr**L**^{Me}][ZnBr$_3$(NCMe)]·MeCN (**4**·MeCN)

As for **2**·4MeCN, but using **L**^{Me}H$_2$ (0.50 g, 0.73 mmol) and ZnBr$_2$ (0.30 g, 1.33 mmol) affording yellow prisms of **4**·MeCN. Yield 0.53 g, 61%. Elemental analysis calculated for C$_{47}$H$_{41}$Br$_4$N$_5$O$_2$Zn$_2$: C 49.26, H 3.53, N 5.98%; found: C 49.02, H 3.32, N 6.06 %. IR (KBr) cm^{-1}: 2918 (s), 2853 (s), 2727 (m), 2672 (m) , 2349 (w), 1727 (w), 1709 (w), 1692 (w) , 1633 (m), 1591 (m), 1532 (m), 1299 (m), 1280 (m), 1261 (s), 1212 (w), 1196 (w), 1180 (m), 1154 (m), 1101 (s), 1066 (m), 1019 (m), 891 (w), 872 (w), 801 (s), 754 (m), 722 (s), 671 (w), 659 (w), 595 (w), 574 (w), 531 (w), 496 (w), 464 (w). M. S. (MALDI-ToF): 825 (M-anion), 765 (M-Br-anion) 681 (M-ZnBr-anion). ^{1}H NMR (CD$_3$CN, 400 MHz): δ 8.63 (d, 2H, J=13.2, Ar-H), 8.40 (s, 2H, CH=N), 7.63 (d, 2H, J=2.0, Ar-H), 7.52 (m, 8H, Ar-H), 6.95 (m, 6H, Ar-H), 6.76 (td, 6H, J$_1$=8.0, J$_2$=2.0, Ar-H), 6.21 (d, 2H, J=7.2, CH=N), 3.72 (t, 2H, J=14.8, CH_2), 3.45 (dt, 2H, J$_1$=14.4, J$_2$=3.6, CH_2), 2.99 (dt, 2H, J$_1$=14.8, J$_2$=4.8, CH_2), 2.56 (td, 2H, J$_1$=13.4, J$_2$=3.2, CH_2), 2.26 (s, 6H, CH_3).

Synthesis of [CoBr**L**^{tBu}]$_2$[Co$_{0.68}$Zn$_{0.32}$Br$_3$(NCMe)]·0.25MeCN (**5**·0.25MeCN)

To **1**·0.5MeCN (1.00 g 0.80 mmol) was added ZnBr$_2$ (0.18 g, 0.80 mmol) and the system

was refluxed for 12 h. On cooling, the volatiles were removed *in vacuo* and the residue was extracted into MeCN (30 mL). Prolonged standing at ambient temperature afforded green/brown prisms of **5**·0.25MeCN. Yield 0.53 g, 53%. Elemental analysis calculated for $C_{54.50}H_{55}Br_4N_{5.25}O_2Co_{1.68}Zn_{0.32}$: C 52.15 H 4.41 N 5.86%, C 52.34, H 4.56, N 5.85%. IR (KBr) cm^{-1}: 2955 (s), 2925 (s), 2854 (s), 2727 (w), 2305 (w), 1748 (w), 1632 (s), 1618 (s), 1537 (s), 1462 (s), 1395 (w), 1377 (s), 1366 (m), 1299 (w), 1260 (s), 1217 (w), 1180 (m), 1101 (s), 1063 (s), 1020 (s), 884 (m), 798 (s), 757 (m), 723 (m), 688 (m), 598 (m), 576 (m), 540 (m), 497 (m), 476 (w). M.S. (ASAP, positive mode): 1135 [M – Br - MeCN], 1037 [M - $Zn_{0.33}$ - Br_2 -MeCN], 969 [M - Br_3 - MeCN], 939 [M - $Zn_{0.33}$ - Br_3 - MeCN], 904 [M - anion], 822 [M - Br-anion].

For [CoBr**L**^{tBu}]$_2$[CoBr$_3$(NCMe)][Br]·4.5MeCN (**6**·4.5MeCN): On concentration of the mother-liquor and further cooling, small red prisms **6**·4.5MeCN were also isolated in low yield (*ca.* 10%). For $C_{115}H_{113.5}Br_6Co_3N_{13.5}O_4$: C 57.43, H 4.76, N 7.86%; found: C 57.79, H 4.67, N 6.44%. IR: 2957 (s), 2924 (s), 2854 (s), 2728 (m), 1633 (m), 1584 (m), 1537 (m), 1462 (s), 1261 (s), 1094 (s), 1020 (s), 875 (m), 799 (s), 757 (w), 722 (m), 660 (w), 598 (w), 540 (w), 466 (w). M. S. (MALDI-ToF): 904 (M$^+$), 822 (M$^+$ - Br).

Synthesis of [Co**L**^{tBu}(NCMe)(μ-Br)ZnBr]·3.25MeCN (**7**·3.25MeCN)

To **1**·0.5MeCN (1.00 g, 0.80 mmol) in THF (30 mL) at -78 °C was added Et$_2$Zn (0.66 mL, 1.2 M, 0.80 mmol) and the system was slowly allowed to warm to ambient temperature and left to stir for 12 h. Volatiles were then removed *in-vacuo*, and the residue was extracted in MeCN (20 mL). Cooling to 0 °C afforded large red/brown prisms of **7**·3.25MeCN. Yield: 0.64 g, 66%. Elemental analysis calculated for $C_{242}H_{251}Br_8Co_4N_{33}O_8Zn_4$: C 59.49, H 5.18, N 9.46%. found: C 59.74, H 4.89, N 9.30%. IR (KBr) cm^{-1}: 2925 (s), 2855 (s), 2726 (w), 2304 (w), 2275 (w), 2246 (w), 1615 (s), 1591 (m), 1537 (m), 1464 (s), 1378 (m), 1332 (m), 1311 (m), 1287 (w), 1263 (m), 1248 (w), 1234 (w), 1211 (m), 1187 (m), 1156 (w), 1141 (w), 1125 (w), 1088 (w),1059 (m), 1034

(w), 1023 (w), 1013 (w), 982 (m), 964 (w), 917 (w), 895 (w), 863 (w), 799 (w), 774 (m), 754 (m), 739 (m), 726 (m), 690 (w), 655 (w), 631 (w), 581 (w), 553 (w), 525 (m), 507 (m), 482 (m), 466 (w). M. S. (MALDI-ToF): 1041 [M-5MeCN], 961 [M-Br-5MeCN], 822 [M-ZnBr$_2$-5MeCN], 766 [M-ZnCoBr$_2$-5MeCN]. Mag moment: μ_{eff} 5.23 B.M.[3]

Synthesis of [Co**L**^{Me}(NCMe)(μ-Br)ZnBr]·3MeCN (**8**·3MeCN)

To **2**·4MeCN (1.00 g, 0.76 mmol) in THF (30 mL) at -78 °C was added Me$_2$Zn (0.76 mL, 1.0 M, 0.76 mmol) and the system was slowly allowed to warm to ambient temperature and left to stir for 12 h. Volatiles were then removed *in-vacuo*, and the residue was extracted in MeCN (20 mL). Cooling to 0 °C afforded large red/brown prisms of **8**·3MeCN (-3MeCN, sample dried *in vacuo* for 12h). Yield: 0.42 g, 49%. Further crops of **8**·3MeCN can be obtained from the mother-liquor (total isolated yield 61%). Elemental analysis calculated for C$_{48}$H$_{41}$Br$_2$CoN$_5$O$_2$Zn: C 57.42, H 4.12, N 6.98%. Found: C, 57.20, H 3.95, N 7.13%. IR (KBr) cm^{-1}: 2922 (s), 2853 (s), 1634 (s), 1589 (s), 1535 (s), 1463 (s), 1377 (s), 1341 (s), 1297 (s), 1104 (s), 1069 (s), 1041 (s), 1017 (s), 919 (s), 869 (s), 839 (s), 801 (s), 754 (m), 740 (w), 722 (m), 672 (m), 615 (w), 597 (w), 574 (w), 554 (w), 533 (m), 521 (w), 499 (m), 467 (m). M. S. (MALDI-ToF): 1050 [M-2MeCN]. Mag moment: μ_{eff} 5.10 B.M.[3]

7.1.3 Ring opening polymerization

Typical polymerization procedures are as follows. A toluene solution of catalyst (0.010 mmol, in 1.0 mL toluene) was added into a Schlenk tube in the glove-box at room temperature. The solution was stirred for 2 min, and then the appropriate amount of ε-CL or δ-VL (e.g. 2.5 mmol) along with 1.5 mL toluene was added to the solution. The reaction mixture was then placed into an oil bath pre-heated to the required temperature, and the solution was stirred for the prescribed time. The polymerization mixture was then quenched by addition of an excess of glacial acetic acid (0.2 mL) into the solution, and

the resultant solution was then poured into cold methanol (200 mL). The resultant polymer was then collected on filter paper and was dried *in vacuo*.

Co-polymerizations

a) Poly (δ-VL+ ε-CL):

A toluene solution of catalyst (0.010 mmol, in 1.0 mL toluene) was added into a Schlenk tube in the glove-box at room temperature. The solution was stirred for 2 min, and then 1 equivalent of BnOH (from 1 mmol BnOH in 100 mL toluene) and 5 mmol of δ-VL were added, after 24h ε-CL was added to the solution. The reaction mixture was then placed into an oil bath pre-heated to the 130°C, and the solution was stirred for another 24h. The polymerization mixture was then quenched by addition of an excess of glacial acetic acid (0.2 mL) into the solution, and the resultant solution was then poured into cold methanol (200 mL). The resultant polymer was then collected on filter paper and was dried *in vacuo*.

b) Poly (ε-CL + δ-VL):

A toluene solution of catalyst (0.010 mmol, in 1.0 mL toluene) was added into a Schlenk tube in the glove-box at room temperature. The solution was stirred for 2 min, and then 1 equivalent of BnOH (from 1 mmol BnOH in 100 mL toluene) and 5 mmol ε-CL of were added, after 24h δ-VL was added to the solution. The reaction mixture was then placed into an oil bath pre-heated to the 130°C, and the solution was stirred for another 24h. The polymerization mixture was then quenched by addition of an excess of glacial acetic acid (0.2 mL) into the solution, and the resultant solution was then poured into cold methanol (200 mL). The resultant polymer was then collected on filter paper and was dried *in vacuo*.

c) *Poly (ε-CL+r-LA):*

169

A toluene solution of catalyst (0.010 mmol, in 1.0 mL toluene) was added into a Schlenk tube in the glove-box at room temperature. The solution was stirred for 2 min, and then 1 equivalent of BnOH (from 1 mmol BnOH in 100 ml toluene) and 5 mmol ε-CL of were added, after 24h r-LA was added to the solution. The reaction mixture was then placed into an oil bath pre-heated to the 130°C, and the solution was stirred for another 24h. The polymerization mixture was then quenched by addition of an excess of glacial acetic acid (0.2 mL) into the solution, and the resultant solution was then poured into cold methanol (200 mL). The resultant polymer was then collected on filter paper and was dried *in vacuo*.

Kinetic studies

The polymerizations were carried out at 130 °C in toluene (2 mL) using 0.010 mmol of complex. The molar ratio of monomer to initiator was fixed at 500:1, and at appropriate time intervals, 0.5 µL aliquots were removed (under N_2) and were quenched with wet $CDCl_3$. The percent conversion of monomer to polymer was determined by ^{1}H NMR spectroscopy.

Mass Spectrometry

PVL and co-polymer samples were run at the University of Hull using MALDI-TOF MS analysis. Samples were dissolved in THF, and the matrix, 2-(4-hydroxyphenylazo) benzoic acid (HPABA) with added NaOAc was employed, which was dissolved in THF to give a saturated solution. 50 µL of the sample solution was then mixed with 50µL matrix solution, and 1µL of the mixed solution applied to the sample target. The sample was allowed to dry in air before analysis. The PCL samples were tested at the EPSRC National Mass Spectrometry Service (Swansea), by MALDI ToF in both positive-linear and –reflectron modes using a dithranol matrix and NaOAc as additive.

7.1.4 Crystal Structure Determinations

Single crystal X-ray diffraction data were collected by the EPSRC UK National Crystallography Service for the majority of samples. Data collections were performed from crystals held at 100K, data for **1**·0.5MeCN were collected using a Mo rotating anode source and a Rigaku Oxford Diffraction 2015; Data for **2**·4MeCN and **3**·MeCN were collected using a Cu rotating anode source and a Rigaku HyPix 6000 detector; data for **6**·4.5MeCN and **4**·MeCN were collected using a Mo rotating anode source and a Rigaku HG Saturn724+ detector; data for **8**·3MeCN were collected using a Mo rotating anode source and a Rigaku HyPix 6000; data for **7**·3.25MeCN were collected using a Mo rotating anode source and a Rigaku Oxford Diffraction 2017;. Data were processed using Rigaku Oxford software. Single crystal X-ray diffraction data for **5**·0.25MeCN were collected using a Stoe IPDS2 image plate diffractometer operating with Mo radiation. The crystal was held at 150 K for the data collection. Raw data were processed using the Stoe X-AREA suite of programmes. Diffraction data were treated for the effects of absorption.

Structures were solved using dual-space methods within SHELXT and refined against F^2 using all unique reflections with the program SHELXL-2018.[4] All non-hydrogen atoms were refined using anisotropic displacement parameters. Hydrogen atoms were placed using a riding model.

For **2**·4MeCN and **6**·4.5MeCN small scale disorder was modelled using standard techniques. **4**·MeCN is a non-merohedral twin (fractions 0.161(4): 0.839(4)); the refinement was conducted using data from both twin components. The structure is pseudo body centred. For reflections with h+k+l even, $<I/\sigma_I> = 22.55$. For reflections with h+k+l odd, $<I/\sigma_I> = 4.75$. These are systematically weak but not systematically absent. It is not possible to undertake a stable refinement in I-1.

7.2 Schiff-base [2+2] macrocycles derived from the dianiline [(2-NH$_2$C$_6$H$_4$)$_2$X] (X = CH$_2$CH$_2$, O); metal complexes and their ROP capability

7.2.1 General

Solvents were dried using standard protocols, for example, toluene was refluxed over sodium/benzophenone, acetonitrile and dichloromethane were refluxed over calcium hydride,[5] acetone was dried over magnesium sulfate, ethylacetate was dried over molecular sieves and dimethylsulfoxide was stored over barium oxide and distilled over calcium hydride prior to use. The precursors 2,6-(CHO)$_2$-4-R-C$_6$H$_2$OH and (2-NH$_2$C$_6$H$_4$)$_2$O and the Schiff-base macrocycles were prepared by the literature methods.[2]

^{1}H NMR spectra were recorded on a Varian VXR 400 S spectrometer at 400 MHz at room temperature and were calibrated against the residual protio impurity of the deuterated solvent. UV-vis absorption spectra were recorded by JENWAY 7315 spectrophotometer. Photoluminescence emission spectra were collected in a quartz cuvette (10 × 10 mm), using a PerkinElmer LS55 spectrophotometer with an excitation slit width of 10 nm and an emission slit width set at 5 nm. The measurements were performed at standard pressure and room temperature. The sample was recorded on a Carl Zeiss Evo-60 SEM instrument and Imaging was performed with a LaB6 emitter. The absolute lifetime measurements were carried out with a FLS1000 photoluminescence spectrometer. The decay curves were analysed by deconvoluting the observed decays with the instrument response function (IRF) to obtain the intensity decay function, manifested as a sum of two exponentials for the present study. IR spectra were recorded on a Nicolet Avatar 360 FT-IR spectrometer. Elemental analyses were performed by the elemental analysis service at

the University of Hull and Nanjing University of Information Science & Technology. Mass spectrometry was performed in a Bruker HCT-Ultra mass spectrometer.

7.2.2 Synthesis of Zn complexes 9-11

Synthesis of [(ZnBr)(ZnNCMe)**L**^{1}]$_2$[ZnBr$_4$]·2.5MeCN (**9**·2.5MeCN)

To **L**^{1}H$_2$ (1.00 g, 1.52 mmol) and 3 equivalents of ZnBr$_2$ (1.03 g, 4.56 mmol) was added toluene (20 mL) and the system was refluxed for 12 h in the presence of 2 equivalents of Et$_3$N. On cooling, volatiles were removed *in vacuo*, and the residue was extracted into MeCN (20 mL). Standing at ambient temperature afforded yellow prisms of **9**. Yield 0.43 g, 24.5%. ^{1}H NMR (C$_6$D$_6$, 400 MHz): δ 8.18 (s, 2H, C*H*=N), 8.04 (s, 2H, C*H*=N), 7.84-6.34 (m, 20H, Ar-*H*), 1.80 (s, 6H, *Me*). IR (KBr, cm^{-1}): 2923 (s), 2853 (s), 2726 (w), 2349 (w), 2307 (w), 1623 (m), 1605 (m), 1590 (m), 1546 (m), 1462 (s), 1377 (s), 1304 (m), 1261 (m), 1235 (m), 1216 (m), 1150 (w), 1094 (m), 1071 (m), 1020 (m), 873 (w), 841 (w), 800 (s), 760 (w), 722 (s), 663 (w), 527 (w). M. S. Found (ESI): 899 [M-MeCN-Zn$_3$Br] 865 [M$^+$-MeCN]. Elemental analysis calculated for C$_{85.8}$H$_{57}$Br$_{6.10}$N$_{8.9}$O$_8$Zn$_5$ (sample dried *in vacuo* for 12 h): C 46.90, H 2.61, N 5.67%. Found C 47.82, H 2.92, N 5.41%.

Synthesis of [(ZnBr)**L**^{2}H$_2$][ZnBr$_3$NCMe]·3MeCN (**10**·3MeCN)

To **L**^{2}H$_2$ (1.00 g, 1.36 mmol) and 2 equivalents of ZnBr$_2$ (0.69 g, 2.72 mmol) was added toluene (20 mL) and the system was refluxed for 12 h. On cooling, volatiles were removed *in vacuo*, and the residue was extracted into MeCN (20 mL). Standing at ambient temperature afforded orange prisms of **10**. Yield 1.08 g, 58.4 %. ^{1}H NMR (C$_6$D$_6$, 400 MHz): δ 7.70 (s, 2H, C*H*=N), 7.62 (s, 2H, C*H*=N),7.30-6.06 (m, 20H, Ar-*H*), 1.94 (s, 1H, C=N-H), 1.71 (s, 1H, C=N-H), 1.02. (s, 18H, *t*Bu). IR (KBr, cm^{-1}): 3419(s) 2923 (s), 2854 (s), 2726 (s), 2671 (w), 2306 (w), 2279 (w), 2245 (w), 1637 (s), 1623 (s), 1593 (m), 1533 (m), 1463 (s), 1377 (s), 1336 (w), 1326 (w), 1309 (w), 1261 (m), 1237 (m), 1221 (m), 1180 (m), 1152 (m), 1097 (m), 1060 (m), 1021 (w), 980 (m), 934 (w), 942 (w), 904

(w), 875 (w), 849 (m), 805 (m), 773 (w), 754 (m), 740 (m), 723 (m), 695 (w), 622 (w), 569 (m), 554 (m), 524 (m), 507 (m), 478 (m), 453 (m), 445 (w). M. S. Found (ESI) 929 [M-ZnBr$_3$] 887 [M$^+$]. Elemental analysis calculated for C$_{48}$H$_{43.87}$Br$_4$N$_4$O$_4$Zn$_{2.07}$ (sample dried *in-vacuo* for 12 h): C 48.18, H 3.68, N 4.68%. Found C 48.28, H, 3.77, N 4.72%.

Synthesis of [(ZnBr)$_2$**L^2**]·4.5MeCN (**11**·4.5MeCN)

To **L^2**H$_2$ (1.00 g, 1.36 mmol) and 2 equivalents of ZnBr$_2$ (0.69 g, 2.72 mmol) was added toluene (20 mL) and the system was refluxed for 12 h in the presence of 2 equivalents of Et$_3$N. On cooling, volatiles were removed *in vacuo*, and the residue was extracted into MeCN (20 mL). Standing at ambient temperature afforded orange prisms of **11**. Yield 0.96 g, 69.0 %.^{1}H NMR (C$_6$D$_6$, 400 MHz): δ 7.76 (s, 2H, CH=N), 7.62 (s, 2H, C*H*=N), 7.29-6.37 (m, 20H, Ar-*H*), 1.03. (s, 18H, *t*Bu). IR (KBr, cm^{-1}): 2923 (s), 2854 (s), 2727 (w), 1624 (m), 1606 (m), 1587 (m), 1463 (s), 1377 (s), 1322 (m), 1259 (s), 1222 (m), 1181 (m), 1099 (m), 1063 (s), 1021 (m), 979 (m), 843 (w), 800 (s), 754 (m), 738 (m), 701 (w), 630 (w), 571 (w), 525 (m), 474 (m). M. S. Found (ESI): 951 [M-Br], 804 [M-ZnBr$_2$], 765 [M-Zn$_2$Br$_2$]. Elemental analysis calculated for C$_{48}$H$_{42}$Br$_2$N$_4$O$_4$Zn$_2$ (sample dried *in vacuo* for 12 h): C 56.00, H 4.11, N 5.44%. Found C 56.08, H 4.19, N 5.58%.

7.2.3 Emission studies

Zn complexes (2 mg) were dissolved in 10 mL of the various named solvents (the concentration for the solutions for Zn complex **9**, **10** and **11** is 0.09 mmol/L, 0.19 mmol/L and 0.15 mmol/L, respectively), and then 1 ml was taken from the above solution, diluted to 5 mL and then used to record the UV-vis spectra. The fluorescence spectra test employed half the concentration of the solution which was used for the UV-vis test. For complex **9** the emission and excitation slit width is 15 nm and 7 nm, respectively. The emission and excitation slit width for complex **10** is 6 nm and 6 nm, respectively. For complex **11** the emission and excitation slit width is 7 nm and 3.5 nm, respectively.

7.2.4 X-ray Crystallography

Single crystal X-ray diffraction data were collected at the UK National Crystallography service using Rigaku Oxford Diffraction ultra-high intensity instruments employing modern areas detectors. In all cases standard procedures were employed for integration and processing of data.

Crystal structures were solved using dual space methods implemented within SHELXT.[4] Completion of structures was achieved by performing least squares refinement against all unique F^2 values using SHELXL-2018.[6] All non-H atoms were refined with anisotropic displacement parameters. Hydrogen atoms were placed using a riding model. Where the location of hydrogen atoms was obvious from difference Fourier maps, C-H and O-H bond lengths were refined subject to chemically sensible restraints. Minor disorder was treated using standard methods. SQUEEZE[7] was used to model the disordered solvent in structure **9** and **11**.

7.3 Schiff-base [2+2] macrocycles derived from the dianiline [(2-$NH_2C_6H_4)_2X$] (X = CH_2CH_2, O) metal complexes and their ROP capability

7.3.1 General

All manipulations were carried out under an atmosphere of nitrogen using standard Schlenk and cannula techniques or in a conventional nitrogen-filled glove-box. Toluene was refluxed over sodium, whilst acetonitrile was refluxed over calcium hydride. IR spectra (nujol mulls, KBr windows) were recorded on a Nicolet Avatar 360 FT-IR spectrometer; ^1H and ^{13}C NMR spectra were recorded at room temperature on a Varian VXR 400 S spectrometer at 400 MHz or a Gemini 300 NMR spectrometer

or a Bruker Advance DPX-300 spectrometer. The ^{1}H NMR spectra were calibrated against the residual protio impurity of the deuterated solvent. Elemental analyses were performed by the elemental analysis service at the London Metropolitan University, the Chemistry Department at the University of Hull or Nanjing University. The precursors 2,6-$(CHO)_2$-4-R-C_6H_2OH and 2,2$^/$-ethylenedianiline (or 2,2$^/$-oxydianiline) and the Schiff-base pro-ligands were prepared by the literature.[2, 8-11] For the iron and cobalt complexes, all manipulations were carried out under an atmosphere of dry nitrogen using conventional Schlenk and cannula techniques or in a conventional nitrogen-filled glove box. All solvents were distilled and degassed prior to use.

7.3.2 **Synthesize of metal complexes**

Synthesis of [FeBr($\mathbf{L^1}H_2$)]$_2$[(FeBr$_3$)$_2$O]·2(MeCN) (**12**·2MeCN)

$\mathbf{L^1}H_2$ (0.52 g, 0.77 mmol) and FeBr$_2$ (0.34 g, 1.58 mmol) were combined in a Schlenk and toluene (20 mL) was added. After refluxing for 12h, the volatiles were removed *in-vacuo*, and the residue was extracted into MeCN (20 mL). Prolonged standing at room temperature afforded orange/brown prisms. Yield: 0.72 g, 78 %. Elemental analysis calculated for $C_{96}H_{82}Br_8Fe_4N_{10}O_5$: required: C 49.32% H 3.60% N 5.00% Found: 49.88 % H 3.58% N 5.09%. IR (KBr, cm^{-1}): 3378 (s), 2923 (s), 2726 (w), 2671 (w), 2360 (w), 1633 (m), 1585 (m), 1538 (m), 1462 (s), 1377 (s), 1300 (w), 1280 (w), 1238 (m), 1102 (m), 977 (w), 873 (w), 801 (m), 754 (m), 722 (m), 688 (w), 622 (w), 574 (w), 534 (w), 502 (m), 486 (w), 455 (w). M. S. (MALDI-ToF): 817 (M$^+$). Magnetic moment: 6.35 B.M.[12]

Synthesis of [FeBr($\mathbf{L^2}H_2$)]$_2$[(FeBr$_3$)$_2$O]·0.5MeCN (**13**·0.5MeCN)

To the pro-ligand $\mathbf{L^2}H_2$ (0.50 g, 0.65 mmol) in toluene was added 2.1 equivalents of FeBr$_2$ (0.30 g, 1.39 mmol), and the system was refluxed for 12 h. On cooling,

the volatiles were removed under vacuo, and the residue was extracted into acetonitrile (30 ml) to afford **13**·MeCN as red needles (0.48 g, 56 %). Elemental analysis calculated for $C_{106}H_{107}Br_8Fe_4N_9O_5$: C 51.97, H 4.40, N 5.15%; found: C 51.21, H 4.43, N 5.55%. IR (KBr, cm^{-1}): 3168 (m), 2925 (s), 2854 (s), 2726 (w), 1704 (m), 1620 (m), 1587 (m), 1542 (s), 1462 (s), 1377 (s), 1317 (w), 1260 (w), 1233 (m), 1214 (m), 1180 (m), 1130 (w), 933 (w), 890 (w), 839 (w), 799 (m), 744 (m), 722 (m), 526 (m), 449 (m). M.S. (MALDI-ToF): 901 (M - anion). Magnetic moment: 5.86 B.M.[12]

Synthesis of [FeBr(**L²**H₂)]Br·3MeCN (**14**·5.5MeCN)

As for **13**, but using **L²**H₂ (0.52 g, 0.68 mmol) and FeBr₂ (0.16 g, 0.74 mmol) affording **14**·5.5MeCN as brown prisms. Yield: 0.52 g, 65%. IR (KBr, cm^{-1}): 3168 (m), 2925 (s), 2854 (s), 2726 (w), 1636 (s), 1619 (s), 1599 (m), 1587 (m), 1537 (s), 1463 (s), 1377 (s), 1333 (m), 1283 (w), 1241 (m), 1183 (m), 1101 (m), 1063 (s), 1007 (m), 976 (m), 880 (s), 794 (m), 753 (s), 722 (m), 689 (m), 622 (w), 595 (w), 575 (w), 535 (w), 513 (m), 494 (m), 476 (w). M.S. (MALDI-ToF): 901 (M - 5.5 MeCN-anion).

Synthesis of [Fe(**L²**)(**L²**H)]·3MeCN (**15**·3MeCN)

To FeBr₂ (1.00 g, 4.64 mmol) was added KO*t*Bu (1.04 g, 9.27 mmol) in THF (30 ml) at 0 °C and the system was stirred for 5 h. Following removal of the volatiles, **L²**H₂ (3.57 g, 4.64 mmol) and toluene (20 ml) was added and the system was refluxed for 12 h. On cooling, the volatiles were removed and the residue was extracted into cold acetonitrile (30 ml), where upon **4**·3MeCN formed. Yield 1.62 g, 41 %. Elemental analysis calculated for $C_{104}H_{101}FeN_8O_4$ (sample dried *in-vacuo* for 2 h): C 78.92, H 6.43, N 7.08%. Found C 79.09, H, 6.49, N On prolonged standing at ambient dark brown block. Yield: 1.84g, 46.6%. IR (KBr, cm^{-1}):

3377(w), 2958 (s), 2924 (s), 2854 (s), 2726 (w), 1630 (m), 1587 (m), 1461 (s), 1415 (w), 1377 (s), 1260 (s), 1202 (w), 1093 (s), 1019 (s), 863 (m), 800 (s), 755 (w), 740 (w), 723 (m), 705 (w), 662 (w), 566 (w), 530 (w), 504 (w), 465 (w). MS (Maldi): 1584 (M + H)$^+$. Magnetic moment: 5.07 B.M.[12]

Synthesis of [CuBr($\mathbf{L^2H_2}$)][CuBr$_2$]·2MeCN (**16**·2MeCN)

As for **12**, but using $\mathbf{L^2H_2}$ (0.52 g, 0.68 mmol) and CuBr$_2$ (0.30 g, 1.34 mmol), affording **16** as brown prisms. Yield 0.69 g, 84 %. Elemental analysis calculated for C$_{52}$H$_{52}$Br$_3$Cu$_2$N$_4$O$_2$: C 55.18, H 4.63, N 4.95%. Found C 54.59, H, 4.48, N 4.93%. IR (KBr, cm^{-1}): 3171(m), 2922 (s), 2853 (s), 2727 (s), 2671 (w), 2350 (w), 1633 (s), 1618 (s), 1594 (s), 1538 (s), 1463 (s), 1377 (s), 1336 (w), 1285 (m), 1260 (w), 1249 (m), 1239 (w), 1183 (m), 1156 (w), 1103 (m), 1062 (m), 1022 (w), 977 (w), 950 (w), 938 (w), 876 (s), 846 (m), 830 (m), 794 (m), 754 (s), 738 (w), 722 (s), 688 (m), 623 (m), 594 (w), 575 (m), 558 (m), 550 (m). M.S. ESI): 908 (M-anion), 827 (M-anion-Br). Magnetic moment: 1.19 B.M.[13]

Synthesis of [$\mathbf{L^2H_4}$][CoBr$_4$]·2MeCN (**17**·2MeCN)

To [CoBr$\mathbf{L^2}$][CoBr$_3$(NCMe)] (1.00 g, 0.80 mmol) in toluene (30 mL) was added [TiCl$_4$] (0.80 mL, 1.0M, 0.80 mmol) and the system was refluxed for 12 h. On cooling, the volatiles were removed and the residue was extracted into acetonitrile (30 ml). On prolonged standing at 0 ^{o}C small red blocks of **17**·2MeCN formed. Yield: 0.38 g, 83 %. Elemental analysis calculated for C$_{52}$H$_{54}$Br$_4$CoN$_4$O$_2$: C 54.52, H 4.75, N 4.89%. Found C 53.34, H, 5.19, N 4.95%. IR (KBr, cm^{-1}): 3381 (m), 2925 (s), 2924 (s), 2854 (s), 2726 (w), 2359 (w), 1636 (w), 1618 (s), 1594 (m), 1574 (w), 1538 (s), 1462 (s), 1377 (s), 1333(s), 1285 (m), 1260 (m), 1183 (s), 1102 (m), 1063 (m), 1021 (m), 873 (m), 799 (s), 756 (m), 722 (m), 688 (w), 668 (w),

624 (w), 576 (w), 558 (w), 522 (w). M.S. (ESI): 847 (M – CoBr$_3$). 829 (M –Br$_4$). 766.97(M – CoBr$_4$). Magnetic moment: 5.05 B.M.[14]

Synthesis of [(CoBr)$_2$(**L^3**)]·2C$_3$H$_6$O (**18**·2C$_3$H$_6$O)

To the pro-ligand **L^3**H$_2$ (1.00 g, 1.52 mmol) in toluene was added 2.1 equivalents of CoBr$_2$ (0.70 g, 3.20 mmol), and the system was refluxed for 12 h. On cooling, the volatile were removed under *vacuo*, and the residue was extracted into acetone (30 ml) to afford **18**·2C$_3$H$_6$O as black crystals (0.98 g, 62%). Single crystals can also be grown from a saturated acetone solution of **18**. Elemental analysis calculated for C$_{42}$H$_{30}$Br$_2$Co$_2$N$_4$O$_4$: C 54.10, H 3.24, N 6.01%. Found C 53.88, H 3.19, N 6.25%. IR (KBr, cm^{-1}): 2924 (s), 2853 (s), 2727 (w), 1746 (w), 1693 (w), 1620 (m), 1587 (m), 1537 (m), 1463 (s), 1377 (s), 1261 (m), 1235 (m), 1215 (m), 1151 (w), 1106 (w), 1072 (m), 1030 (w), 891 (w), 867 (w), 842 (w), 800 (m), 757 (w), 722 (m), 534 (w), 478 (w), 449 (w). M.S. (ESI): 851 (M-2C$_3$H$_6$O-Br), 714 (M-2C$_3$H$_6$O-CoBr). Magnetic moment: 6.10 B.M.[14]

Synthesis of [Co(NCMe)$_2$(**L^4**H$_2$)]·[CoBr$_4$] 5MeCN (**19**·5MeCN)

To the pro-ligand **L^4**H$_2$ (1.00 g, 1.36 mmol) in toluene was added 2.1 equivalents of CoBr$_2$ (0.62 g, 2.83 mmol), and the system was refluxed for 12 h. On cooling, the volatile were removed under vacuo, and the residue was extracted into acetonitrile (30 ml) to afford **19**·3MeCN as red crystals, yield 0.86 g, 44 %, and a smaller amount of green crystals of **20**, yield *ca*. 5%. Elemental analysis calculated for C$_{62}$H$_{65}$Br$_4$Co$_2$N$_{11}$O$_4$: C 49.55, H 4.00, N 6.67% Found for **19** C, 49.35, H 3.96, N 6.61 %. IR (KBr, cm^{-1}): 3172 (m), 2956 (s), 2923 (s), 2853 (s), 2726(w), 1619 (m), 1595 (m), 1536(m), 1461 (s), 1377 (s), 1260 (s), 1155 (w), 1096 (s), 1060 (s), 1022 (s), 892 (w), 874 (w), 800 (s), 722 (s). M.S. (ESI): 933 (M-7MeCN-3Br), 817 (M-7MeCN-3Br-2Co). Magnetic moment: 6.94 B.M.[14]

Synthesis of {CoBr(NCMe)L^5}$_2$·2MeCN (**21**·2MeCN)

To L^5H (1.00 g, 4.85 mmol) and [CoBr$_2$] (1.05 g, 4.85 mmol) was added toluene (20 mL) and Et$_3$N (0.3 ml, 0.22 mmol) and the system was refluxed for 12 h. Following removal of volatiles *in-vacuo*, the residue was extracted into MeCN (20 mL), and on standing at ambient temperature large orange/brown prisms of **21**·3MeCN formed. Isolated yield: 1.41 g, 68%. Elemental analysis calculated for C$_{32}$H$_{38}$Br$_2$Co$_2$N$_4$O$_6$ (sample dried *in-vacuo* for 2 h): C 43.66, H 4.19, N 3.64. Found C 43.81, H 4.23, N 3.67%. IR (KBr, cm^{-1}): 2957 (s), 2924 (s), 2360 (s), 2342 (m), 2312 (m), 2284 (s), 1696 (m), 1641 (s), 1566 (m), 1535 (s), 1464 (s), 1402 (w), 1377 (s), 1367 (s), 1352 (w), 1259 (s), 1225 (m), 1093 (s), 1038 (s), 939 (m), 911 (m), 867 (w), 845 (m), 800 (s), 768 (s), 729 (s), 668 (m), 620 (m), 556 (s), 532 (m), 435 (m). M.S. (ESI): 733 (M-MeCN), 585 (M-3MeCN-Co), 573 (M-MeCN-2Br). Magnetic moment: 6.35 B.M.[14]

Synthesis of [Co(NCMe)$_2$$L^5$]$_2$[CoBr$_3$(NCMe)]$_2$ (**22**)

To L^5H (1.00 g, 4.85 mmol) and [CoBr$_2$] (1.05 g, 4.85 mmol) was added toluene (20 mL) and the system was refluxed for 12 h. Following removal of volatiles *in-vacuo*, the residue was extracted into MeCN (20 mL), and on standing at ambient temperature large green prisms of **22** formed. Isolated yield: 1.53 g, 46%. Elemental analysis calculated for C$_{36}$H$_{44}$Co$_4$N$_6$O$_6$ (sample dried *in-vacuo* for 2 h): C 47.43, H 4.73, N 6.91%. Found C 47.82, H 4.79, N 6.98 %. IR (KBr, cm^{-1}): 2926 (s), 2854 (s), 2360 (m), 2342 (w), 2312 (s), 2284 (m), 1641 (s), 1621 (s), 1566 (m), 1535 (s), 1464 (s), 1402 (w), 1377 (s), 1367 (s), 1352 (w), 1259 (s), 1225 (m), 1093 (s), 1038 (s), 1019 (s), 845 (s), 800 (s), 768 (m), 758 (m), 729 (s), 668 (m), 620 (m), 556 (s), 532 (s), 435 (s). M.S. (ESI): 412 (M-4MeCN-2Co). Magnetic moment: 6.69 B.M.[14]

Synthesis of [FeBr(NCMe)**L**^{5}]$_2$·2MeCN (**23**·2MeCN)

To **L**^{5}H (1.00 g, 4.85 mmol) and [FeBr$_2$] (1.06 g, 4.85 mmol) was added toluene (20 mL) and Et$_3$N (0.7 ml, 0.485 mmol) and the system was refluxed for 12 h. Following removal of volatiles *in-vacuo*, the residue was extracted into MeCN (20 mL), and on standing at ambient temperature large orange/brown prisms of **23**·2MeCN formed. Isolated yield: 0.837 g, 40%. Elemental analysis calculated for C$_{28}$H$_{32}$Br$_2$Fe$_2$N$_2$O$_6$ (sample dried *in-vacuo* for 2 h): C 44.02, H 4.22, N 3.67. Found C 44.61, H 4.52, N 3.72%. IR (KBr, cm^{-1}): 3352 (w), 2954 (s), 2923 (s), 2854 (s), 2727 (w), 2360 (w), 2341 (w), 1643 (m), 1620 (m), 1528 (m), 1462 (s), 1377 (s), 1259 (m), 1160 (m), 1037 (s), 1016 (m), 842 (w), 800 (s), 769 (w), 755 (w), 722 (m), 668 (w), 618 (m), 539 (m). M.S. (ESI): 519 (M-4MeCN-2Br). Magnetic moment: 6.70 B.M.[14]

Synthesis of [Fe(NCMe)$_6$][FeOBr$_3$]$_2$ (**24**)

L^{1}H$_2$ (0.52 g, 0.77 mmol) and FeBr$_3$ (0.47 g, 1.58 mmol) were combined in a Schlenk and toluene (20 mL) was added. After refluxing for 12h, the volatiles were removed *in-vacuo*, and the residue was extracted into MeCN (20 mL). Prolonged standing at room temperature afforded brown prisms; isolated yield 0.39 g 81%. Elemental analysis calculated for C$_{12}$H$_{18}$Br$_6$Fe$_3$N$_6$O (sample dried *in-vacuo* for 2 h): C 15.85, H 2.00, N 9.24% Found C, 15.61 H, 2.12 N 9.31%. IR (KBr, cm^{-1}): 2925 (s), 2854 (s), 2361 (s), 2339 (s), 1868 (s), 1844 (s), 1830 (m), 1792 (m), 1772 (w), 1750 (m), 1734 (m), 1717 (m), 1700 (m), 1684 (m), 1669 (m), 1653 (m), 1646 (m), 1635 (m), 1616 (s), 1576 (s), 1559 (s), 1540 (s), 1521 (s), 1506 (s), 1497 (m), 1489 (m), 1457 (s), 1419 (m), 1377 (s), 1260 (s), 1089 (s), 800 (s), 668 (s).

7.3.3 ROP procedure

a) *ε-Caprolactone and δ-valerolactone*

Typical polymerization procedure in the presence of one equivalent of benzyl alcohol (Table 1, run 1) is as follows. A toluene solution of **12** (0.010 mmol, in 1.0 mL toluene) and BnOH (0.010 mmol) were added into a Schlenk tube in the glove-box at room temperature. The solution was stirred for 2 min, and then ε-caprolactone (2.5 mmol) or δ-valerolactone along with 1.5 mL toluene was added to the solution. The reaction mixture was then placed into an oil bath pre-heated to the required temperature, and the solution was stirred for the prescribed time. The polymerization mixture was then quenched by addition of an excess of glacial acetic acid (0.2 mL) into the solution, and the resultant solution was then poured into methanol (200 mL). The resultant polymer was then collected on filter paper and was dried *in vacuo*.

b) *Co-polymerizations*

A toluene solution of catalyst (0.010 mmol, in 1.0 mL toluene) was added into a Schlenk tube in the glove-box at room temperature. The solution was stirred for 2 min, and then 1 equivalent of BnOH (from 1 mmol BnOH in 100 ml toluene) and monomer were added, after 24h the other monomer was added to the solution. The reaction mixture was then placed into an oil bath pre-heated to the 130 °C, and the solution was stirred for another 24h. The polymerization mixture was then quenched by addition of an excess of glacial acetic acid (0.2 mL) into the solution, and the resultant solution was then poured into cold methanol (200 mL). The resultant polymer was then collected on filter paper and was dried *in vacuo*.

Kinetic studies

The polymerizations were carried out at 130 °C in toluene (1 mL) using 0.010 mmol of complex. The molar ratio of monomer to initiator was fixed at 500:1, and at appropriate time intervals, 0.5 µL aliquots were removed (under N_2) and were

quenched with wet CDCl₃. The percent conversion of monomer to polymer was determined by ^1H NMR spectroscopy.

Mass Spectrometry

Polymer samples were run at the University of Hull using MALDI-TOF MS analysis. Samples were dissolved in THF, and the matrix, 2-(4-hydroxyphenylazo) benzoic acid (HPABA) with added NaOAc was employed, which was dissolved in THF to give a saturated solution. 50 µL of the sample solution was then mixed with 50µL matrix solution, and 1µL of the mixed solution applied to the sample target. The sample was allowed to dry in air before analysis. The co-poly (δ-VL+r-LA) (run 7) sample was analysed by MALDI in positive-linear and reflection modes, with DCTB matrix and NaOAc additive. The sample was fully soluble in THF at 10 mg/mL.

7.3.4   X-ray Crystallography

Single crystal X-ray diffraction data for the structures except for **15** and **22** were collected at the UK National Crystallography service on a range of Rigaku Oxford Diffraction ultra-high intensity instruments employing modern areas detectors. Samples were held at 100 K for data collection. For **15**, data were from a Rigaku Oxford Diffraction Xcalibur-3 CCD diffractometer at 140 K. For **22,** data were from a Stoe IPSD2 image plate diffractometer utilising monochromated Mo radiation (λ = 0.71073 Å). In all cases standard procedures were employed for integration and processing of data.

Crystal structures were solved using direct methods (in SHELXS[4]) or dual space methods implemented within SHELXT. Completion of structures was achieved by performing least squares refinement against all unique F^2 values using SHELXL-2018.[7] All non-H atoms were refined with anisotropic displacement parameters. Hydrogen atoms were placed using a riding model. Where the location of hydrogen atoms was obvious

from difference Fourier maps, C-H and O-H bond lengths were refined subject to chemically sensible restraints. Minor disorder was treated using standard methods.

7.4 Robust peroxidase mimic properties of iron complexes of [2+2] and [6+6] Schiff-base macrocycles and application.

7.4.1 General

3,3',5,5'-Tetramethylbenzidine (TMB) was purchased from Sigma-Aldrich (St. Louis, USA). Deionized water was used in the peroxidase-like activity discussion. Toluene and acetonitrile were distilled and degassed before use in order to remove H_2O and dissolved oxygen in the purchased solvent. IR spectra were recorded using Nicolet Avatar 360 FT IR spectrometer. The precursors $2,6\text{-}(CHO)_2\text{-}4\text{-}Me\text{-}C_6H_2OH$ and 2,2'-oxydianiline and the Schiff-base ligand L^1H_2 were prepared using the literature methods.[2] L^5H_6 was synthesized by a similar method, but using toluene instead of the methanol as the reaction solvent. Syntheses were carried out under N_2 atmosphere and using conventional Schlenk techniques. UV/VIS Spectroscopy were tested using JENWAY 7315 spectrophotometer. Fluorescent spectra were tested using a PerkinElmer LS55 spectrophotometer in 10×10 mm a quartz. Elemental analyses were performed at the Nanjing University of Information Science & Technology and University of Hull. Magnetic moments were determined using an Evans balance.[1] Mass spectrometry was obtained from the National Mass Spectrometry Centre at Swansea, UK. The morphology of the Fe complexes was recorded by using a Carl Zeiss Evo-60 machine. The cyclic voltammetry curves were measured using three-electrode system by CHI 660D (Chenhua, China) Electrochemistry workstation.

7.4.2 Synthesize procedure

Preparation of [$L^1H_2FeBr_2]_2[FeBr_3OFeBr_3]\cdot 7MeCN$ (**25**$\cdot$7MeCN)

To the pro-ligand $\mathbf{L^1H_2}$ (1.52 mmol, 1.00 g) was added 2.1 equivalents of $FeBr_2$ (3.20 mmol, 0.70 g), then the system was refluxed in toluene for 12 h. After cooling, the toluene was removed under vacuum, then recrystallization was carried out using 20 mL acetonitrile affording **25** as black crystals (Yield 1.35 g, 68%). Elemental analysis: Calculated C 42.90%, H 2.74%, N 4.76%; Found C 43.04%, H 2.66%, N 4.83%. FT-IR (KBr, cm^{-1}): 3419 (m), 2922 (s), 2853 (s), 2726 (w), 2360 (w), 1634 (m), 1617 (m), 1585 (m), 1538 (s), 1463 (s), 1377 (s), 1316 (m), 1232 (w), 1215 (w), 1206 (m), 1109 (w), 1071 (w), 1034 (w), 996 (w), 891 (w), 845 (w), 798 (m), 753 (m), 739 (m), 722 (m), 525 (m), 463 (w), 452 (w). M.S. (ESI): 2076 (M-2Fe-2Br), 874 (M_{Cation}), 792 (M_{Cation}-FeBr), 712 (M_{Cation}-FeBr$_2$). Magnetic moment (μ_{eff}): 7.01 B.M.[12]

Preparation of $[\mathbf{L^1}(FeBr)_2]\cdot 3MeCN$ (**26**·3MeCN)

To the ligand $\mathbf{L^1H_2}$ (1.52 mmol, 1.00 g) was added 2.1 equivalents of $FeBr_2$ (3.20 mmol, 0.70 g) then the system was refluxed in toluene for 12 h in the presence of two equivalents of Et_3N. After cooling, the toluene was removed under vacuum, then recrystallization was carried out using 20 mL acetonitrile affording **26** as black crystals (Yield 0.88 g, 56%). Elemental analysis: Calculated: C 54.46%, H 3.26%, N 6.05%.; Found C 54.39%, H, 3.19%, N 6.11%. FT-IR (KBr, cm^{-1}): 2955 (s), 2925 (s), 2854 (s), 2726 (w), 1633 (m), 1621 (m), 1581 (s), 1538 (s), 1464 (s), 1377 (s), 1316 (m), 1277 (w), 1263 (w), 1241 (m), 1215 (w), 1174 (m), 1109 (m), 1073 (m), 1019 (m), 938 (w), 893 (w), 873 (w), 785 (m), 749 (m), 508 (w), 452 (w). M.S. (ESI): 926 (M-3MeCN), 790 (M-3MeCN-FeBr), 711 (M-3MeCN-FeBr$_2$). Magnetic moment (μ_{eff}): 5.55 B.M.[12]

Preparation of $[2\text{-}(OH)\text{-}5\text{-}(Me)\text{-}C_6H_2\text{-}1,3\text{-}(CH)_2]_6[O(2\text{-}C_6H_4N)_2]_6$ (**L^{5}H$_6$**)

2,6-Dicarboxy-4-methyl-phenol (5.0 mmol, 0.82 g) and $(2\text{-}NH_2C_6H_4)_2O$ (5.0 mmol, 1.00 g) were refluxed in 50 mL toluene for 12 h in the presence of 100μL of formic acid. After cooling, the solvent was removed under vacuum, then washed by acetonitrile

185

affording orange powder $\mathbf{L}^5H_6$. Yield 1.30 g, 79%. Elemental analysis Calculated: C 76.42%, H 4.49%, N 8.91%; Found C 76.28%, H 4.55%, N 8.77%. FT-IR (KBr, cm^{-1}): 3447 (w), 3183(W), 2960 (s), 2924 (s), 2853 (s), 1677 (m), 1625 (m), 1600 (m), 1575 (s), 1459 (s), 1377 (m), 1314 (3), 1261 (s), 1242 (m), 1215 (m), 1192 (w), 1155 (w), 1099 (s), 1020 (s), 859 (m), 800 (s), 746 (w), 723 (w), 653 (w), 598 (w), 563 (w), 512 (w), 455 (m). M.S. (ESI): 1972 (M+3H$^+$).

Preparation of [Fe$_2$($\mathbf{L}^5$H$_2$)][FeBr$_3$OFeBr$_3$]·4MeCN (**27**·4MeCN)

To $\mathbf{L}^5$H$_6$ (1.00 g, 0.51 mmol) in toluene was added 4.1 equivalents of FeBr$_2$ (0.46 g, 2.1 mmol), and the system was refluxed in toluene for 12 h. On cooling, the toluene was removed under vacuum, then recrystallization was carried out using 20 mL acetonitrile affording **27** as black crystals (Yield 0.98 g, 69%). Elemental analysis: Calculated C 55.42%, H 3.10%, N 6.46%; Found C 55.49%, H, 3.16%, N 6.52%. FT-IR (KBr, cm^{-1}): 3440 (w), 2954 (s), 2924 (s), 2834 (s), 2726 (w), 1629 (m), 1594 (m), 1537 (m), 1463 (s), 1377 (s), 1260 (3), 1234 (m), 1214 (m), 1172 (w), 1154 (w), 1098 (m), 1071 (m), 939 (w), 872 (w), 800 (s), 749 (w), 722 (w), 508 (w), 461 (w). M.S. (ESI): 2155 (M$^+$+2Br), 2132 (M$^+$+Br+Fe), 2074 (M$^+$+Br). Magnetic moment (μ_{eff}): 9.58 B.M.[12]

7.4.3 Peroxidase mimic activity measurements

Investigation of peroxidase-like activity was conducted as follows: 60 μL of TMB (25 mM) and 100μL of H$_2$O$_2$ (3 M) were added in 2840 μL NaAc-HAc buffer (100 mM, pH=4.0) in the presence of the catalysts. Then the formation of oxidased TMB along with the absorbance change at 652 nm was used to evaluate the peroxidase mimic activity. In oreder to discuss the kinetic process, the Michaelis–Menten constant was determined in 100 mM NaAc-HAc buffer (pH=4.0) in the presence of the Fe complexes.

7.4.4 Mechanism investigation

Electrochemical measurements

Cyclic voltammetry was employed for the mechanism discussion and employed a three-electrode system. An iron complex modified glassy carbon electrode (GCE) was used as the working electrode; an Ag/AgCl electrode was used for the reference electrode; a platinum plate was auxiliary electrode. The current of the Fe complex modified electrode as well as the bare glassy carbon electrode was measured in the presence of 20 mM H_2O_2 in pH= 4.0 NaAc-HAc buffer.

Hydroxyl radical detection

At ambient temperature, 1 mg of the catalyst sample was dispersed in 2 mL of NaAc-HAc (pH=4.0) buffer solution in the presence of 50 mM H_2O_2. Terephthalic acid (TA) was dissolved in 100 mM NaOH solution to make the concentration to 10^{-3} M. After 10 mins, the solution reached an adsorption–desorption equilibrium, and the PL spectrum was measured to determine the formation of TAOH.

7.4.5 H_2O_2 detection

In order to establish the H_2O_2 determination method, 30 µL different concentrations of H_2O_2 were added to a solution included 30µL of TMB (10 mM), complex **27**, and 2800 µL of 100 mM of NaAc-HAc buffer (pH=4.0). The concentrations of H_2O_2 in final solution varied from 0.5 mM to 10 mM. The selectivity experiments were carried out at 5 mM for H_2O_2, 20 mM for alternative interfering substances glucose, urea, uric acid, lactic acid, K^+, Na^+, Mg^{2+}, Ca^{2+}, Zn^{2+}, Cu^{2+} in the presence of TMB (10 mM) in 100 mM NaAc-HAc buffer (pH = 4.0).

7.4.6 X-ray Crystallography

The crystallographic data collections for the Fe complexes were carried out at the EPSRC National Crystallographic Service (NCS) using Rigaku Oxford Diffraction ultra-high intensity instruments. All data collections were carried out at 100 K. Non-hydrogen atoms were refined anisotropically using the SHELXL-2018,[15] and hydrogen atoms

were introduced at the calculated positions. The selected bond lengths and angles for **25-27** are shown in Table 8-1. The details of the refinement information, data collection and crystal parameters for **25-27** are summarized in the Appendix.

7.5 Schiff-base double layer macrocycles derived from 2,2'-ethylenedianiline and a Pd@Schiff base composite: synthesis, structures and use as peroxidase mimetics.

7.5.1 General

All the chemicals were purchased in reagent grade and were reacted without further purification. All syntheses were carried out under nitrogen using standard Schlenk techniques. All solvents were distilled and degassed prior to use. Toluene was refluxed over sodium, and dichloromethane was dried over calcium hydride. IR spectra were recorded using the Nicolet Avatar 360 FT-IR spectrometer; NMR spectra were recorded at room temperature on a Varian VXR 400 S spectrometer at 400 MHz. Elemental analyses were determined in Nanjing University of Information Science & Technology. The mass spectrum were tested at the EPSRC National Mass Spectrometry Service (Swansea).

7.5.2 Synthesis of double layer macrocycles 28-30.

Synthesis of macrocycle $[(C_6H_4)2-4-(CH)_2]_2[CH_2CH_2(2-C_6H_4N)_2]_2$ (**28**)

4,4'-Biphenyldicarboxaldehyde (420.46 mg, 2 mmol) was dissolved in dichloromethane (25 mL), and 2,2'-ethylenedianiline (424.58 mg, 2 mmol) was dissolved in toluene (25 mL). The two solutions were mixed at room temperature without any stirring. Finally, 1 drop of trifluoroacetic acid was added to this solution as a catalyst for

188

imine bond formation. Prolonged standing at room temperature for one week afforded egg-white coloured prisms. Yield: 507 mg, 69.2%. IR (KBr, cm^{-1}): 2954 (s), 2923 (s), 2854 (s), 2726 (w), 1675 (w), 1624 (w), 1605 (w), 1590 (w), 1573 (w), 1552 (w), 1463 (s), 1377 (s), 1310 (m), 1205 (w), 1171 (w), 1153 (w), 1132 (w), 1003 (w), 969 (w), 938 (w), 886 (w), 857 (w), 817 (m), 753 (m), 722 (m). ^{1}H NMR (CD$_2$Cl$_2$): 8.47 (s, CH=N, 4H), 7.98-6.64 (s, Ar-H, 32H), 2.75 (s, -CH$_2$, 12H). MS (ES+): C$_{56}$H$_{44}$N$_4$ 773.4 (M minus CH$_2$Cl$_2$ solvent). Elemental analysis calculated for C$_{56}$H$_{44}$N$_4$ C 87.01, H 5.74, N 7.25%; found: C 86.98, H 5.91, N 7.09%.

Synthesis of macrocycle [C$_6$H$_3$-1,3,5-(CH)]$_2$[CH$_2$CH$_2$(2-C$_6$H$_4$N)$_2$]$_3$ (**29**)

1,3,5-Triformylbenzene (324 mg, 2 mmol) was dissolved in dichloromethane (25 mL), and 2,2'-ethylenedianiline (636 mg, 3 mmol) was dissolved in toluene (30 mL). The two solutions were mixed at room temperature without any stirring. Finally, 1 drop of trifluoroacetic acid was added to this solution as a catalyst for imine bond formation. Prolonged standing at room temperature for one week afforded egg-white coloured prisms. Yield: 665 mg, 72.1%. IR (KBr, cm^{-1}): 2954 (s), 2923 (s), 2854 (s), 1629 (w), 1591 (w), 1537 (w), 1462 (s), 1377 (s), 1261 (s), 1141 (m), 1093 (s), 1019 (s), 976 (w), 864 (w), 801 (s), 754 (m), 723 (m), 683 (m). ^{1}H NMR (CD$_2$Cl$_2$): δ 8.44 (s, CH=N, 6H), 8.13-6.98 (s, Ar-H, 30H), 3.22 (s, -CH$_2$, 12H). ^{13}C NMR (CD$_2$Cl$_2$): δ 157.05, 149.22 137.65, 130.61, 129.83, 127.23, 126.99, 117.79, 33.56, 33.0, 31.19, 30.61 ppm. MS (ES+): C$_{60}$H$_{48}$N$_6$ 853.4 (M minus CH$_2$Cl$_2$ solvent). Elemental analysis calculated for C$_{60}$H$_{48}$N$_6$ C 84.48, H 5.67, N 9.85%; found: C 84.53, H 5.76, N 9.94%.

Synthesis of macrocycle [4-(OH)-(C$_6$H$_4$)$_2$-3,5-(CH)$_2$]$_2$[CH$_2$CH$_2$(2-C$_6$H$_4$N)$_2$]$_4$ (**30**)

4,4'-dihydroxy-[1,1'-biphenyl]-3,3',5,5'-tetracarbaldehyde (597 mg, 2 mmol) and 2 equivalents of 2,2'-ethylenedianiline (848 mg, 4 mmol) were reacted in 50 mL toluene with adding 3 drops of formic acid. After drying and washing with acetonitrile, the residue

was refluxed in toluene (30 mL) with 6 equivalents of $CoBr_2$ (1.312g, 6 mmol) for 12h. Removal of volatiles *in-vacuo*, followed by recrystallization from hot DMF (20 mL) afforded **30** as orange crystals. Yield (452 mg, 26.8%) IR (KBr, cm^{-1}): 3440 (m), 2954 (s), 2922 (s), 2854 (s), 2726 (w), 2671 (w), 1661 (w), 1621 (m), 1588 (m), 1571 (m), 1461 (s), 1377 (s), 1261 (s), 1210 (m), 1154 (m), 1088 (m), 1018 (m), 873 (m), 800 (s), 750 (s), 722 (m), 671 (w). MS (ES^+): $C_{88}H_{68}N_8O_4$ 1301.7 (M minus solvent DMF, Acetonitrile). Elemental analysis calculated for $C_{103}H_{103}N_{13}O_9$: C 74.21, H 6.23, N 10.92%; found: C 74.33, H 6.30, N 10.99%.

7.5.3 Preparation of Pd@Schiff base

$Pd(OAc)_2$ (225 mg, 1mmol) were reacted with 1 equivalent of above-mentioned Schiff base [2+3] macrocycle (462 mg, 0.5mmol) in 30 mL methanol in the presence of Et_3N. The system has been stir overnight, then the solvent was removed, and the as-prepared solid was washed with 10 mL methanol affording black powder Pd@Schiff base composite (461 mg, 67%).

7.5.4 Experiments of peroxidase mimic activity

To evaluate the peroxidase-like activity of synthesized composite, 60 μL of 3,3',5,5'-tetramethylbenzidine TMB (25 mM) and 20 μL of H_2O_2 (0.1M) were added in 100 mM NaAc-HAc buffer (pH = 4.0) in the presence of Pd@Schiff base catalyst (0.5 mg), and the total volume of the solution was made to 3 mL. The UV-vis spectra were used to detect the absorbance change at 652 nm to detect the oxidation of TMB.

7.5.5 Kinetic measurements

The Michaelis–Menten constant was tested by fixing the concentration of one substrate and changing that of the other. The fixed concentrations of TMB and H_2O_2 were 0.5 mM and 20 mM, respectively. Then the TMB and H_2O_2 were added in 100 mM NaAc-HAc

buffer (pH = 4.0) in the presence of catalyst (0.5 mg), and the total volume of the solution was made to 3 mL.

7.5.6 H$_2$O$_2$ detection

In a typical process, H$_2$O$_2$ with different concentrations were added to a solution included TMB (0.5 mM), Pd@Schiff base (0.5 mg), and 2800 µL of HAc-NaAc buffer (100 mM pH=6.0) then 50 µL of H$_2$O$_2$ (3 M) were added at last. The concentrations of H$_2$O$_2$ in the final solution varied from 0.5 mM to 10 mM. In order to investigate the selectivity of the detection method, the influence of some interference substrates such as glucose, ascorbic acid, uric acid, Ca^{2+}, Mg^{2+}, Zn^{2+}, Na^+ and K^+ were tested by applying the same assay.

7.5.7 X-ray Crystallography

Single crystal X-ray diffraction data for all structures were collected at the UK National Crystallography service on a range of Rigaku Oxford Diffraction ultra-high intensity instruments employing modern areas detectors. Samples were held at 100 K for data collection. In all cases standard procedures were employed for integration and processing of data.

Crystal structures were solved using dual space methods implemented within SHELXT.[4] Completion of structures was achieved by performing least squares refinement against all unique F^2 values using SHELXL-2018.[15] All non-H atoms were refined with anisotropic displacement parameters. Hydrogen atoms were placed using a riding model.

7.6 References

[1] D. F. Evans, *J. Phys. E: Sci. Instrum.*, 1974, 7, 247.

[2] W. Yang, K. Q. Zhao, T. J. Prior, D. L. Hughes, A. Arbaoui, M. R. J. Elsegood and C. Redshaw, *Dalton Trans*., 2016, 45, 11990-12005.

[3] A. A. Abou-Hussein and W. Linert, *Spectrochim Acta A*., 2015, 141, 223-232.

[4] G. M. Sheldrick, *Acta Cryst*. 2015, A71, 3-8.

[5] D. B. G. Williams and M. Lawton, *J. Org. Chem.*, 2010; 75(24), 8351-8354.

[6] G. M. Sheldrick, *Acta Cryst.*, 2015, C71, 3-8.

[7] A. L. Spek., *Acta Cryst.,* 2015, C71, 9-18.

[8] A. Arbaoui, C. Redshaw and D. L. Hughes, *Chem. Commun*. 2008, 4717-4719.

[9] R. S. Drago, M. J. Desmond, B. B. Corden and K. A. Miller, *J. Am. Chem. Soc*., 1983, 105, 2287-2296.

[10] J. J. Randell, C. E. Lewis and P. M. Slagan, *J. Org. Chem.*, 1962, 27, 4098-4101.

[11] V. C. Gibson, C. Redshaw, W. Clegg, M. R. J. Elsegood, U. Siemeling and T. Türk,

[12] B. Weber, E. Kaps, *Heteroatom Chem.*, 2005, 16, 391-397.

[13] M. Kato, H. B. Jonassen and J. C. Fanning, *Chem. Rev.,* 1964, 64, 99-128.

[14] R. W. Handel, H. Willms, G. B. Jameson, K. J. Berry, B. Moubaraki, K. S. Murray and S. Brooker, *Eur. J. Inorg. Chem*., 2010, 3317–3327.

[15] G. M. Sheldrick, SHELXL-2018, Program for the crystal Structure refinement, University of Göttingen, Germany, 2018.

Appendix

Table 8-1. Crystallographic data for crystals **1**-**30**.

Compound	**1**·0.5MeCN	**2**·4MeCN	**3**·0.25MeCN	**4**·MeCN
Formula	$C_{110}H_{110}Br_8Co_4N_{11}O_4$	$C_{56}H_{55}Br_4Co_2N_9O_2$	$C_{54.50}H_{55}Br_4N_{5.25}O_2$ $Co_{1.68}Zn_{0.32}$	$C_{54.25}H_{55}Br_4N_5O_{2.25}Zn_2$
Formula weight	2525.08	1323.59	1255.07	1263.41
Crystal system	Triclinic	Monoclinic	triclinic	triclinic
Space group	P-1	$C 2/c$	P -1	P-1
Unit cell dimensions				
a (Å)	10.7727(3)	28.9470(7)	10.7788(5)	10.75900(10)
b (Å)	12.2755(4)	14.9123(3)	12.2801(6)	12.2903(2)
c (Å)	21.8766(5)	28.7611(8)	21.8831(10)	21.8932(3)
α (°)	84.154(2)	90	84.218(4)	84.0830(10)
β (°)	88.514(2)	110.451(3)	88.620(4)	88.4630(10)
γ (°)	65.975(3)	90	66.052(4)	66.072(2)
V (Å³)	2628.22(14)	11632.7(5)	2633.3(2)	2631.71(7)
Z	1	8	2	2
Temperature (K)	100(2)	100(2)	100(2)	100(2)
Wavelength (Å)	0.71075	1.54184	0.71075	1.54184
Calculated density (g.cm⁻³)	1.593	1.512	1.583	1.594
Absorption coefficient (mm⁻¹)	3.755	8.062	3.718	5.034
Crystal size (mm³)	$0.18 \times 0.15 \times 0.086$	$0.15 \times 0.07 \times 0.01$	$0.10 \times 0.05 \times 0.03$	$0.20 \times 0.16 \times 0.08$
θ(max) (°)	27.49	68.25	26.37	68.25
Reflections measured	18214	47742	33054	56562
Unique reflections	10647	11548	12015	9509
R_{int}	0.043	0.098	0.054	0.034
Number of parameters	626	628	616	621
R_1 [$F^2 > 2\sigma(F^2)$]	0.046	0.108	0.034	0.0298
wR_2 (all data)	0.096	0.295	0.072	0.0799
GOOF, S	0.851	1.055	1.022	1.068
Largest difference peak and hole (e Å⁻³)	1.022 and –0.641	2.32 and –1.08	1.144 and -0.859	1.483 and –0.620

Compound	**5**·MeCN	**6**·4.5MeCN	**7**·3.25MeCN	**8**·3MeCN
Formula	$C_{50}H_{46}Br_4N_6O_6Zn_2$	$C_{115}H_{117.5}Br_6Co_3N_{13.5}O_4$	$C_{242}H_{251}Br_8N_{33}O_8Co_4Zn_4$	$C_{48}H_{41}Br_2CoN_5O_2Zn$
Formula weight	1213.31	2408.97	4886.22	1127.14
Crystal system	Triclinic	triclinic	monoclinic	monoclinic
Space group	P-1	P-1	P 2_1/c	2_1/c
Unit cell dimensions				
a (Å)	14.8222(4)	14.2178(5)	22.6868(2)	14.6177(3)
b (Å)	16.2435(4)	15.0893(4)	12.62670(10)	17.0574(3)
c (Å)	23.2841(5)	15.4758(4)	20.6141(2)	21.1721(4)
α (°)	94.842(2)	101.542(2)	90	90
β (°)	93.195(2)	113.361(3)	103.5260(10)	108.948(2)
γ (°)	115.593(3)	106.394(3)	90	90
V (Å^3)	5011.3(2)	2734.40(16)	5741.32(15)	4993.00(17)
Z	4	1	1	4
Temperature (K)	100(2)	100(2)	100(2)	100(2)
Wavelength (Å)	0.71075	0.71075	0.71075	0.71075
Calculated density (g.cm^{-3})	1.605	1.460	1.413	1.499
Absorption coefficient (mm^{-1})	4.191	2.700	2.148	2.643
Crystal size (mm^3)	$0.01 \times 0.03 \times 0.03$	$0.06 \times 0.05 \times 0.03$	$0.50 \times 0.48 \times 0.30$	$0.14 \times 0.09 \times 0.04$
θ(max) (°)	25.36	27.49	27.48	25.03
Reflections measured	18770	46129	65868	49728
Unique reflections	18770	21759	13099	8818
R_{int}	0.064	0.042	0.054	0.065
Number of parameters	1158	1228	674	619
R_1 [$F^2 > 2\sigma(F^2)$]	0.0602	0.053	0.047	0.056
wR_2 (all data)	0.1837	0.129	0.128	0.152
GOOF, S	1.014	1.030	1.025	1.039
Largest difference peak and hole (e Å^{-3})	2.182 and –0.668	1.928 and –1.148	1.436 and –0.829	2.751 and -0.91

Compound	**9**·2.5MeCN	**10**	**11**·4.5MeCN
Formula	$C_{87.80}H_{60}Br_{6.10}N_{9.90}O_8Zn_5$+ 2.5MeCN	$C_{56}H_{55.87}Br_4N_8O_4Zn_{2.07}$	$C_{48}H_{42}Br_2N_4O_4Zn_2$ 4.5 MeCN
Formula weight	2298.45	1359.66	1029.41
Crystal system	Monoclinic	Orthorhombic	Monoclinic
Space group	$C2/c$	$P2_12_12_1$	$P2/c$
a (Å)	32.5115(3)	12.02380(10)	13.4090(2)
b (Å)	14.0969(10)	13.95690(10)	9.11430(10)
c (Å)	20.3515(2)	34.0092(2)	23.1757(3)
α (°)	90	90	90
β (°)	103.68(10)	90	103.43(10)
γ (°)	90	90	90
V (Å^3)	9092.7(14)	5707.25(7)	2754.92(6)
Z	4	4	2
Temperature (K)	100(2)	100(2)	100(2)
Wavelength (Å)	1.54178	1.54178	1.54178
Calculated density (g.cm^{-3})	1.609	1.582	1.241
Absorption coefficient (mm^{-1})	5.098	4.757	3.080
Transmission factors (min./max.)	0.8116, 1.000	0.3681, 1.000	0.7059, 1.000
Crystal size (mm^3)	$0.060 \times 0.050 \times 0.005$	$0.050 \times 0.020 \times 0.020$	$0.200 \times 0.180 \times 0.040$
θ(max) (°)	70.40	70.02	68.23
Reflections measured	50225	132576	48389
Unique reflections	8556	10763	5023
R_{int}	0.0295	0.0563	0.0296
F(000)	4334	2727	1040
Number of parameters	538	676	284
R_1 [$F^2 > 2\sigma(F^2)$]	0.0457	0.0420	0.0416
wR_2 (all data)	0.1227	0.1074	0.1040
GOOF, S	1.031	1.077	1.137
Largest difference peak and hole (e Å^{-3})	1.701 and -1.370	2.640 and -1.168	0.479 and -0.762

Compound	**12**	**13**·MeCN	**14**·Br·3MeCN	**15**·3MeCN
Formula	$C_{96}H_{86}Br_8Fe_4N_{10}O_5$	$C_{106}H_{107}Br_8Fe_4N_9O_5$	$C_{52}H_{52}BrFeN_4O_2$, Br,3(C_2H_3N)	$C_{104}H_{101}FeN_8O_4$, (3MeCN)
Formula weight	2322.42	2449.68	1103.80	1705.9
Crystal system	Monoclinic	Triclinic	Monoclinic	Monoclinic
Space group	$P2_1/n$	$P\bar{1}$	$P2_1/n$	$P2_1/c$
Unit cell dimensions				
a (Å)	15.6606(4)	13.6454(5)	14.2077(6)	12.6268(5)
b (Å)	16.0326(4)	13.9070(7)	27.6241(9)	30.3249(10)
c (Å)	37.4062(11)	15.6432(8)	15.1579(8)	24.6577(10)
α (°)	90	67.263(5)	90	90
β (°)	99.896(3)	88.642(4)	112.484(6)	100.817(3)
γ (°)	90	81.638(4)	90	90
V (Å^3)	9252.2(4)	2707.0(2)	5496.9(5)	9273.8(6)
Z	4	1	4	4
Temperature (K)	100(2)	100(2)	100(2)	140(1)
Wavelength (Å)	1.54184	0.71075	0.71073	0.71073
Calculated density (g.cm^{-3})	1.667	1.503	1.334	1.222
Absorption coefficient (mm^{-1})	9.439	3.531	1.775	0.223
T min., T max	0.755, 1.000	0.592, 1.000	0.555, 1.000	0.749, 1.185
Crystal size (mm^3)	0.08 × 0.05 ×0.02	0.3 × 0.1 × 0.015	0.26× 0.045 ×0.01	0.74 × 0.18 × 0.16
θ(max) (°)	68.2	27.5	27.5	20.0
Reflections measured	68070	59241	47920	51064
Unique reflections	16805	12341	12467	8583
R_{int}	0.107	0.067	0.056	0.143
Number of parameters	1127	603	620	1129
R_1 [$F^2 > 2\sigma(F^2)$]	0.070	0.064	0.082	0.057
wR_2 (all data)	0.178	0.178	0.226	0.123
GOOF, S	1.011	1.069	1.076	0.913
Largest difference peak and hole (e Å^{-3})	1.42 and –0.86	1.53 and –0.78	2.10 and -1.83	0.30 and –0.25

Compound	**16**·2MeCN	**17**·2MeCN	**18**·2C$_3$H$_6$O	**19**·3MeCN
Formula	C$_{56}$H$_{58}$Br$_3$Cu$_2$N$_6$O$_2$	C$_{52}$H$_{54}$Br$_4$CoN$_4$O$_2$ · 2(C$_2$H$_3$N)	C$_{42}$H$_{30}$Br$_2$Co$_2$N$_4$O$_4$ ·2(C$_3$H$_6$O)	C$_{62}$H$_{65}$Br$_4$Co$_2$N$_{11}$O$_4$
Formula weight	1213.89	1145.56	1048.56	1465.8
Crystal system	Triclinic	Triclinic	Monoclinic	Monoclinic
Space group	$P\bar{1}$	$P\bar{1}$	$P2_1$/c	I a
Unit cell dimensions				
a (Å)	10.0808(2)	12.2629(5)	11.4774(8)	15.77810(10)
b (Å)	15.0015(4)	13.2489(6)	14.5787(10)	25.0018(2)
c (Å)	18.6604(5)	17.0384(7)	26.021(3)	16.28380(10)
α (°)	71.442(2)	96.850(3)	90	90
β (°)	82.738(2)	91.115(3)	100.235(8)	91.911(10)
γ (°)	76.600(2)	99.672(4)	90	90
V (Å^3)	2598.2(1)	2707.2(2)	4284.6(6)	6420.08(8)
Z	2	2	4	4
Temperature (K)	100(2)	100(2)	100(2)	100(2)
Wavelength (Å)	1.54184	0.71075	1.54178	0.71073
Calculated density (g.cm^{-3})	1.552	1.405	1.535	1.516
Absorption coefficient (mm^{-1})	4.572	3.309	8.652	3.060
T min., T max	0.149, 1.000	0.652, 1.000	0.404, 1.000	0.698, 1.000
Crystal size (mm^3)	0.70 × 0.60 × 0.15	0.10 × 0.04 × 0.02	0.14 × 0.03 × 0.01	0.25 × 0.18 × 0.05
θ(max) (°)	68.3	21.7	68.2	28.7
Reflections measured	44092	10619	6241	147825
Unique reflections	9337	10619	3471	16480
R_{int}	0.083	0.179	0.054	0.047
Number of parameters	622	564	526	762
R_1 [$F^2 > 2\sigma(F^2)$]	0.066	0.114	0.128	0.032
wR_2 (all data)	0.184	0.297	0.371	0.064
GOOF, S	1.062	1.098	1.226	1.023
Largest difference peak and hole (e Å^{-3})	3.45 and –1.24	1.02 and –1.54	2.52 and –2.02	0.52 and –0.46

Compound	20	21·2MeCN	22·2MeCN	23·2MeCN
Formula	$C_{20}H_{30}Br_6Co_3N_{10}$	$C_{28}H_{32}Br_2Co_2N_2O_6 \cdot$ $2 (C_2H_3N)$	$C_{36}H_{44}Br_6Co_4N_6O_6$	$C_{32}H_{38}Br_2Fe_2N_4O_6$
Formula weight	1066.79	852.34	1371.95	846.18
Crystal system	Monoclinic	Triclinic	Triclinic	Triclinic
Space group	$P2_1/n$	$P\bar{1}$	$P\bar{1}$	$P\text{-}1$
Unit cell dimensions				
a (Å)	8.34720(10)	8.4718(5)	10.416(2)	8.51990(10)
b (Å)	18.8457(3)	9.2109(3)	11.156(4)	9.20980(10)
c (Å)	12.5811(2)	12.2495(5)	11.738(4)	12.1881(2)
α (°)	90	101.186(3)	78.04(3)	101.2110(10)
β (°)	108.941(2)	102.715(4)	70.59(2)	102.4660(10)
γ (°)	90	97.208(4)	87.78(2)	97.4090(10)
V (Å³)	1871.95(5)	900.47(7)	1257.8(7)	901.29(2)
Z	2	1	1	1
Temperature (K)	100(2)	100(2)	150(2)	100(2)
Wavelength (Å)	0.71075	1.54184	0.71073	1.54184
Calculated density (g.cm⁻³)	1.893	1.572	1.811	1.559
Absorption coefficient (mm⁻¹)	7.743	10.197	6.105	9.433
Transmission factors (min./max.)	0.154, 0.733	0.423, 1.000	0.725, 0.820	0.646, 1.000
Crystal size (mm³)	0.216 × 0.125 × 0.10	0.32× 0.16× 0.10	0.31× 0.13×0.09	0.30× 0.20×0.10
θ(max) (°)	27.49	68.2	29.2	70.3
Reflections measured	48302	15481	11602	32046
Unique reflections	4301	3240	6632	3387
R_{int}	0.0235	0.066	0.044	0.0342
Number of parameters	183	217	268	217
R_1 [$F^2 > 2\sigma(F^2)$]	0.017	0.042	0.035	0.0299
wR_2 (all data)	0.0037	0.119	0.072	0.0822
GOOF, S	1.17	1.072	0.82	1.091
Largest difference peak and hole (e Å⁻³)	0.79 and –0.35	0.85 and –0.83	0.84 and –0.63	0.413 and -0.69

Compound	**24**	**25**	**26**	**27**
Formula	$C_{12}H_{18}Br_6Fe_3N_6O$	$C_{98}H_{81}Br_{10}Fe_4N_{15}O_9$	$C_{90}H_{69}Br_4Fe_4N_{11}O_8$	$C_{128}H_{92}Br_6Fe_4N_{16}O_{13}$
Formula weight	909.33	2635.27	1975.60	2765.05
Crystal system	Trigonal	Monoclinic	Monoclinic	Monoclinic
Space group	*R*-3:H	*P* 21/c	*P*21	*P* 21/c
a (Å)	12.39520(10)	26.1346(2)	11.48090(4)	15.82170(10)
b (Å)	12.39520(10)	14.52490(10)	14.90374(7)	19.92400(10)
c (Å)	12.39520(10)	26.9273(2)	24.37532(10)	23.77790(10)
α (º)	30.5277(3)	90	90	90
β (º)	90	91.8510(10)	97.1486(4)	105.3340(10)
γ (º)	90	90	90	90
V (Å^3)	120	10216.34(13)	4138.40(3)	7228.71(7)
Z	4061.92(8)	4	2	2
Temperature (K)	6	100(2)	100(2)	100(2)
Wavelength (Å)	100(2)	1.54178	1.54178	1.54178
Calculated density (g.cm^{-3})	1.54184	1.713	1.585	1.663
Absorption coefficient (mm^{-1})	2.230	9.561	8.296	9.135
Crystal size (mm^3)	0.16×0.14 ×0.03	0.320 × 0.060 × 0.020	0.140 × 0.040 × 0.010	0.150×0.150×0.140
θ (max) (°)	67.80	64.99	68.24	65.00
Reflections measured	24700	82992	165800	123916
Unique reflections	1644	17341	14491	12278
R_{int}	0.0363	0.0336	0.0522	0.0462
Number of parameters	88	1257	1061	881
R_1 [$F^2 > 2\sigma(F^2)$]	0.0188	0.0544	0.0367	0.0608
wR_2 (all data)	0.0474	0.1492	0.0990	0.1833
GOOF, S	1.11	1.041	1.033	1.041
Largest difference peak and hole (e Å^{-3})	0.38 and –0.51	1.951 and -1.692	1.339 and -0.623	1.649 and -2.048

Compound	**28**	**29**	**30**
Formula	$C_{56}H_{44}N_4$	$C_{60}H_{48}N_6 \cdot 0.84CH_2Cl_2$	$C_{88}H_{68}N_8O_4 \cdot 5.5DMF$
Formula weight	772.95	924.38	1301.50
Crystal system	monoclinic	orthorhombic	triclinic
Space group	$P2_1/c$	P b c a	P -1
a (Å)	43.8480(7)	20.6377(2)	13.9050(3)
b (Å)	13.0066(2)	14.04401(12)	18.1451(78)
c (Å)	14.0972(2)	34.4443(3)	18.3196(7)
α (º)	90.0	90	79.551(4)
β (º)	91.668(2)	90	88.677(2)
γ (º)	90.0	90	84.550(2)
V (Å^3)	8036.4(2)	9983.17(16)	4524.9(3)
Z	8	8	2
Temperature (K)	100(2)	100(2)	100(2)
Wavelength (Å)	0.6889	1.54178	1.54178
Calculated density (g.cm^{-3})	1.278	1.230	0.955
Absorption coefficient (mm^{-1})	0.071	1.364	0.467
Crystal size (mm^3)	0.08 × 0.04 × 0.01	0.200 × 0.025 × 0.020	0.240 × 0.040 × 0.015
θ(max) (°)	51.006	68.246	66.593
Reflections measured	102091	128934	79604
Unique reflections	16395	9121	15882
R_{int}	0.0964	0.0955	0.0921
F(000)	3264.0	3882	1368
Number of parameters	1153	659	901
R_1 [$F^2 > 2\sigma(F^2)$]	0.0569	0.0564	0.0806
wR_2 (all data)	0.1420	0.1508	0.1123
GOOF, S	1.025	1.047	1.041
Largest difference peak and hole (e Å^{-3})	0.21 and -0.21	0.533 and -0.313	0.30 and -0.36